ACTIVE CONTROL OF ANNULAR PLATES THROUGH THE DESIGN OF EXTENSION/SHEAR MODE PFC ACTUATORS

A Thesis Submitted in
Partial Fulfillment of the Requirements
for the Degree of

DOCTOR OF PHILOSOPHY

by

Srinivas Pavan Kumar A
(Roll No: 11610330)

DEPARTMENT OF MECHANICAL ENGINEERING

INDIAN INSTITUTE OF TECHNOLOGY GUWAHATI,

GUWAHATI-781039, INDIA

February, 2018

Department of Mechanical Engineering
Indian Institute of Technology Guwahati
Guwahati-781039 INDIA

CERTIFICATE

It is certified that the work contained in the thesis entitled "**ACTIVE CONTROL OF ANNULAR PLATES THROUGH THE DESIGN OF EXTENSION/SHEAR MODE PFC ACTUATORS"** submitted by **A. Srinivas Pavan Kumar** to the Indian Institute of Technology Guwahati for the award of the degree of Doctor of Philosophy has been carried out under my supervision in the Department of Mechanical Engineering, Indian Institute of Technology Guwahati. This work has not been submitted elsewhere for the award of any other degree or diploma.

(Dr. Satyajit Panda)
Associate Professor
Department of Mechanical Engineering
Indian Institute of Technology Guwahati
Guwahati-781039
INDIA

Declaration

I Srinivas Pavan Kumar A (Roll no: 11610330) declare that the present written submission is my thoughts in my own words. I have adequately cited and referenced the original sources, where others ideas have been involved. I also declare that I have adhered to all principles of academic honesty and integrity and have neither fabricated nor falsified any idea/data/fact/source in my submission. I understand that any violation of the above will be cause for disciplinary action by the Institute and can also evoke penal action from the sources which have thus not been properly cited or from whom proper permission has not been taken when needed.

(**Srinivas Pavan Kumar A**)

Date: **Roll No: 11610330**

Dedicated to

My parents

Acknowledgment

Over the course of five years at IIT Guwahati, I have been accompanied and supported by many people that have helped to make the undertaking of this magnitude possible. First and foremost, I sincerely thank my thesis supervisor Dr. Satyajit Panda for his untiring guidance, demand for excellence, encouragement, patience and technical expertise which brought the best from me.

I am also thankful to Prof. Debabrata Chakraborty, Prof. Anjan Dutta and Dr. S. Senthilvelan for their careful review and suggestions on my thesis work as doctoral committee members.

I am also grateful to Prof. Santosha K Dwivedy, Head of the Department of Mechanical Engineering and Prof. Anoop K Dass for providing an opportunity for higher learning in Department of Mechanical Engineering, IIT Guwahati.

I would like to express my immense gratitude to my friends and Narravula Harshavardhan Reddy for their help and suggestions in need.

I express deep gratitude to my parents for their love and support.

(Srinivas Pavan Kumar A)

Abstract

This dissertation deals with the active control of flexural vibration of annular plates through the design of two new piezoelectric fiber composite (PFC) actuators in the cylindrical coordinates. The first one is an extension mode PFC actuator, and the next one is a shear mode PFC actuator. The extension mode PFC is basically a cylindrically orthotropic short piezoelectric fiber composite (SPFC) in the shape of a thin annular disc. This annular SPFC disc is comprised of unidirectional short piezoelectric fibers embedded in the epoxy matrix. The longitudinally poled short piezoelectric fibers are oriented in the radial direction so that the extension mode piezoelectric actuation appears along the radial direction in response to an externally applied coaxial electric field. The effective electro-elastic properties of this SPFC actuator are estimated by developing a finite element (FE) procedure, and the changes in the properties due to the use of unidirectional short/discontinuous fibers (SPFC) instead of the continuous fibers (CPFC) are demonstrated. A fruitful arrangement of surface-electrodes over the top and bottom surfaces of the annular SPFC/CPFC disc is proposed, and its (SPFC/CPFC) actuation capability is investigated in active control of harmonically excited flexural vibration of an annular substrate plate. The patches of the SPFC/CPFC actuator are attached to the top surface of the substrate plate, and the controlled frequency responses of the smart annular plate are evaluated by developing a closed-loop FE model. These controlled responses of the smart plate reveal indicative control capability of the SPFC actuator, and it (control capability) is compared with that of the CPFC actuator. This comparison is further extended by taking the poling direction of the fibers in the annular CPFC disc either as longitudinal or as thickness direction. For each of these poling directions, the fibers are oriented either in radial or in the circumferential direction so that four kinds of cylindrically orthotropic CPFCs appear. For each of these CPFCs, the arrangement of surface-electrodes is presented, and the optimal size and locations of the actuator-patches over the top surface of the simply-supported/fully clamped annular substrate plate are addressed through the proposition of a new numerical methodology in conjunction with the FE procedure. On the basis of this optimal configuration of actuator-patches for each of the CPFC actuators, their (four CPFCs) capabilities in inducing the active damping in the smart annular plate are quantified, and the best one among the four kinds of CPFC actuators is recommended.

The new shear mode PFC is made in the form of a thin laminated annular disc that is mainly comprised of two or more 2-2 PFC layers. The 2-2 PFC layer is composed of conventional piezoelectric fibers which are oriented in the radial direction and evenly spaced in the circumferential coordinate. The external electric field acts along the transverse direction of the longitudinally poled piezoelectric fibers, and the electrically induced shear force within the annular actuator appears in the transverse plane of radial and axial coordinates. The cylindrically periodic microstructure within this shear mode annular PFC actuator yields its radially varying electro-elastic properties. These varying properties are estimated by dividing the volume of the corresponding representative volume (RV) into a large number of asymptotically homogeneous micro-volumes of different fiber volume fractions. The effective coefficients of these micro-volumes are estimated by deriving the corresponding closed-form expressions and also by developing an FE procedure. An analysis of these varying properties of RV is performed, and two different geometric configurations of the shear mode annular PFC actuator are addressed for having its improved actuation capability. The actuation capability of this shear mode PFC actuator with any of its two different geometric configurations is investigated by means of using its patches at the core of a sandwich annular plate. A fruitful strategy for the arrangement of the actuator-patches at the core is proposed to have the equal attenuation of all the bending modes of vibration of the smart annular sandwich plate. Concurrently, a useful scheme is also presented for efficient utilization of all the patches of the shear mode PFC actuator according to the velocity feedback control law. Based on these strategies in configuring the smart annular sandwich plate, the frequency responses of the overall plate are evaluated by deriving an FE model, and these results reveal indicative control capability of the shear mode annular PFC actuator. This study is further extended by adding the viscoelastic layers at the core of the smart annular sandwich plate for investigating the performance of the shear mode annular PFC actuator in the active constrained layer damping (ACLD) treatment. This study also reveals indicative performance of the shear mode PFC actuator in the ACLD treatment provided that the viscoelastic layer is to be used with an appropriate thickness.

TABLE OF CONTENTS

Chapter 1 **INTRODUCTION**

Chapter 5 AN ANNULAR PFC ACTUATOR FOR SHEAR MODE PIEZOELECTRIC ACTUATION OF PLANE STRUCTURES OF REVOLUTION

Chapter 6 ACTIVE CONTROL OF VIBRATION OF ANNULAR PLATES USING A NEW SHEAR MODE PFC ACTUATOR WITH CYLINDRICALLY PERIODIC MICROSTRUCTURE

Chapter 7 **ACTIVE-PASSIVE DAMPING CHARACTERISTICS OF A SMART ANNULAR SANDWICH PLATE USING A NEW SHEAR MODE PFC ACTUATOR**

Chapter 8 **CONCLUSIONS**

LIST OF FIGURES

LIST OF TABLES

LIST OF SYMBOLS

List of symbols used throughout the thesis are listed. List of symbols less frequently used, or that have different meaning or different forms at different contexts, are defined where they are used.

A_e	Elemental area in r - θ plane
$\bar{\boldsymbol{A}}$	Volume-average strain concentration matrix
C_f	Elastic stiffness for fiber
C_m	Elastic stiffness for matrix phase
$\boldsymbol{d}$	Global general displacement field vector
$\boldsymbol{d}^e$	Elemental nodal displacement vector
$\boldsymbol{D}$	Electrical displacement field vector
$\boldsymbol{E}$	Electric field vector
$\bar{\boldsymbol{e}}$	Volume-average piezoelectric coefficient matrix
E	Young's modulus
$\bar{\boldsymbol{E}}$	Volume average electric field vector
h	Thickness of substrate plate
h_p	PFC layer thickness
h_v	Viscoelastic layer thickness
$\boldsymbol{I}$	Identity matrix
k	Number of layers
k_d	Feed back control gain
$\boldsymbol{K}$	Stiffness matrix
$\boldsymbol{L}$	Linear Operator matrices
$\bar{m}$	Mass per unit area
$\boldsymbol{M}$	Mass matrix
$\boldsymbol{N}$	Shape function matrix
$\boldsymbol{N}_T$	Transformation vector
p	Mechanical load
$\boldsymbol{P}_M^e$	Element mechanical load vector
δT_k	Variation of total kinetic energy
δT_p	Variation of total potential energy
u , v , w	Displacements components in coordinate directions
v_f	Fiber volume fraction
V	Applied voltage
$V_{\max}$	control voltage at peak point
$\dot{w}$	Sensing point velocity

$\boldsymbol{X}$	Global nodal displacement vector
$r\,,\theta\,,z$	Cylindrical coordinates
ν	Poisson's ratio
ρ	Mass density
ε	Strain vector
$\bar{\boldsymbol{\varepsilon}}$	Volume-average strain vector
$\boldsymbol{\sigma}$	Stress vector
$\bar{\boldsymbol{\sigma}}$	Volume-average stress vector
$\bar{\in}$	Volume-average permittivity matrix
$\phi_r\,,\phi_\theta$	Rotations of substrate plate normals to the reference plane
$\boldsymbol{\kappa}$	Bending strain vector
ω	Circular frequency
ω_0	Fundamental frequency of vibration
$[\ \ ]$	Null matrix
l	Layer

Superscript:

e	Element
E	Electrical load
i	A State of deformation
s	Sensing point
v	Velocity
T	Transpose

Subscript:

b	Bending
L	Linear
N	Nonlinear
p	Predicted
s	Shear
f	Fiber
m	Matrix

Abbreviations:

LQR: Linear Quadratic Regulator
LQG: Linear Quadratic Gaussian
ACLD: Active constrained layer damping
FGM: Functionally graded material
PFC: Piezoelectric fiber composite
MSE: Modal Strain Energy
SPFC: Short piezoelectric fiber composite
CPFC: Continuous piezoelectric fiber composite

CHAPTER

1

Introduction

Piezoelectricity is an electro-elastic coupling phenomenon that can be described by the generation of electricity due to an applied mechanical strain (direct effect) and vice versa (converse effect). Certain ceramics exhibit these characteristics, which are known as piezoelectric ceramics. These characteristics of the piezoelectric ceramics are exploited in the development of distributed piezoelectric sensors and actuators, and the same have long been used particularly for active control of deformation/vibration of thin-walled flexible structures. Generally, the piezoelectric sensors and actuators are attached to or built into the host structure for achieving the self-sensing and self-controlling capabilities of the overall structure. Such a structure is commonly known as smart/intelligent structure. In the development of the smart/intelligent structures, the monolithic piezoelectric actuators (piezoelectric ceramics) are widely utilized even though these actuators possess some drawbacks of high stiffness, low strain energy density, insufficient flexibility, poor conformability, etc. These drawbacks motivate the researchers to develop piezoelectric fiber composites (PFCs). Many kinds of PFCs are developed till the date, and the same are also employed for the development of smart structures.

This introductory chapter is concerned with the introduction and review of the literature on the piezoelectric fiber composites (PFCs). A brief review of the literature on the development of smart structures along with an introduction of piezoelectric materials is also presented. Based on the review of the literature, the scope of research for this thesis is identified and the objectives of this dissertation are presented. Also, the contributions in the field of smart structures made towards the preparation of this dissertation are delineated. In the end, organization of the chapters is outlined.

1.1 Piezoelectric materials

In 1880, it was discovered by Pierre and Jacques Curie that the positive and negative charges are produced in certain portions of the surfaces of some crystals when they are compressed in particular directions, and the appearing charges are proportional to the applied pressure. Upon removal of the pressure, the charges disappeared. This phenomenon of electric polarization or producing electricity in certain materials as an effect of applied mechanical strain/stress is known as the direct piezoelectric effect. In a reverse way, the same materials become strained in the effect of being polarized, and this phenomenon is known as the converse piezoelectric effect. The materials which exhibit these two effects are known as piezoelectric materials, and the phenomenon is termed as piezoelectricity (Cady, 1946). These direct and converse piezoelectric effects have been exploited for the development of distributed sensors and actuators particularly for active control of flexible structures, and thus the piezoelectric materials gained the credential as the valuable materials for building advanced engineering structures.

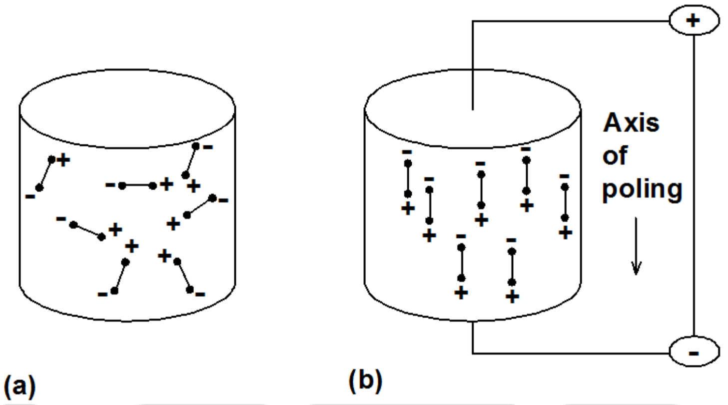

Fig.1.1 Schematic diagram of poling process in piezoelectric materials.

Piezoelectric materials either exist naturally or are prepared synthetically. The natural piezoelectric materials include quartz, Rochelle salt, paraffin, bone, ammonium phosphate, etc. The synthetic piezoelectric materials include, lead zirconate titanate ($Pb(Zr,Ti)O_3$, commonly known as PZT), barium titanate, polyvinylidene fluoride (PVDF), lead lanthanum zirconate, lithium sulphate, etc. (Jalili, 2010). Of these, PZT and PVDF are the popular ones in the active control of structural deformation/vibration. These synthetic piezoelectric materials are isotropic in nature at their raw stage where the dipoles (domains) are oriented randomly (Fig. 1.1(a)) with zero dipole density or polarization. Upon application of a strong electric field (about 10^6 V/m) in the presence of high temperature, the molecular dipoles align following the direction of the external electric field (Fig. 1.1 (b)), and this process is customarily known as poling of piezoelectric materials. On removal of the applied electric field, a permanent reorientation of the molecular dipoles appears leading to the remanent polarization, and the material then becomes anisotropic in nature with the piezoelectricity behaviour. This phenomenon of polarization of a bulk piezoelectric material is generally described by a hysteresis loop in a two-dimensional domain of the applied electric field (E) and polarization (P) as shown in Fig. 1.2(a). For a small magnitude of the applied electric field, polarization (P) is linearly related to the electric field (E) (part AB in Fig. 1.2(a)). Now, as the electric field increases, switching of molecular dipoles (domains) occurs, and the polarization reaches to its saturation stage (P_S , point C in Fig 1.2(a)). On removal of the applied electric field, back-switch of some of the domains occurs, and a nonzero polarization called as the remanent polarization (P_R) appears for zero value of the electric field. To achieve zero value of the electric potential, the electric field must be reversed to a finite value that is usually called

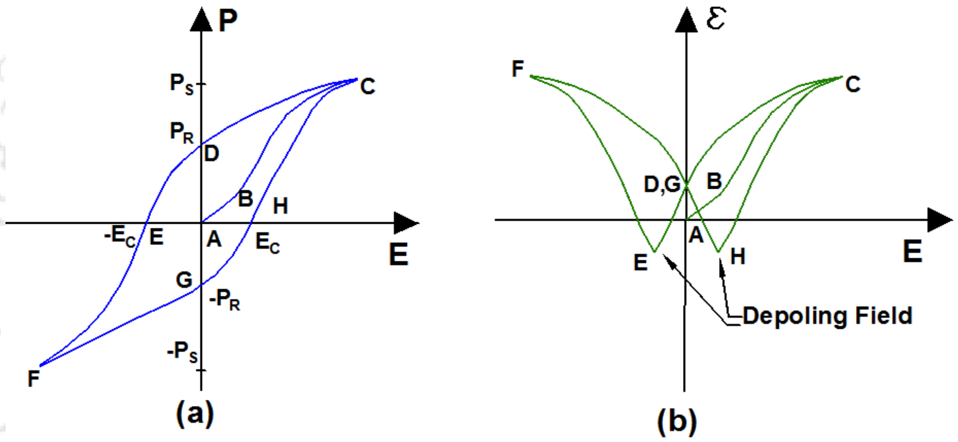

Fig. 1.2 (a) Hysteresis (electric field-polarization) loop of a typical ferroelectric material, (b) butterfly curve (electric field-strain) of a ferroelectric material.

as the coercive electric field ($-E_C$). As the electric field decreases beyond the coercive electric field, a negative maximum (saturation) polarization ($-P_S$) is reached, and a cycle continues for further decrease of the magnitude of the applied electric field as shown in Fig. 1.2(a). In parallel to the variation of polarization (Fig. 1.2(a)), the strain of the material also varies as it is illustrated typically in Fig 1.2(b). The curve in Fig. 1.2(b) is commonly known as butterfly curve due to its shape. For the decrease of the applied electric field after reaching the maximum strain through the curve ABC (Fig. 1.2(b)), the strain decreases until the depoling takes place (point E, Fig. 1.2(b)) at the coercive electric field. For a further decrease of electric field, the material expands until a physical strain limit (point F, Fig. 1.2(b)).

In the use of the piezoelectric materials for actuators, the maximum limit of the electric field is usually taken as the coercive electric field (point E or H, Fig. 1.2(b)). Moreover, in most of the applications, the linear constitutive behaviour of the piezoelectric materials is preferred, and it appears at the electric field that is well below of the coercive electric field. If the applied electric field in operation exceeds the coercive electric field, then the depoling takes place, and the material behaves differently. It is also an essential fact that the operating temperature would not exceed a certain limit that is usually known as the Curie temperature (Chaudhry and Rogers, 1995). Under these operating conditions, the linear constitutive behaviour of a piezoelectric material at a constant temperature is usually described by four field quantities, namely, stress ($\boldsymbol{\sigma}$), strain ($\boldsymbol{\varepsilon}$), electric displacement ($\boldsymbol{D}$) and electric field ($\boldsymbol{E}$). Based on these field quantities, four kinds of thermodynamic potentials can be defined as given in Eq. (1.1) (Chee, 2000) where the symbols U, H, F and G indicate internal energy, enthalpy, Helmholtz free energy and Gibbs free energy, respectively.

$$dH = \boldsymbol{\sigma} d\boldsymbol{\varepsilon} - \boldsymbol{D} d\boldsymbol{E}, \; dU = \boldsymbol{E} d\boldsymbol{D} + \boldsymbol{\sigma} d\boldsymbol{\varepsilon},$$
$$dF = \boldsymbol{E} d\boldsymbol{D} - \boldsymbol{\varepsilon} d\boldsymbol{\sigma}, \; dG = -\boldsymbol{\varepsilon} d\boldsymbol{\sigma} - \boldsymbol{D} d\boldsymbol{E}, \quad (1.1)$$

Any one of these expressions of four kinds of thermodynamic potentials can be utilized for modelling the linear constitutive behaviour of the piezoelectric materials depending on the natural variables. In the structural applications of the piezoelectric materials, the natural variables are usually taken as strain ($\boldsymbol{\varepsilon}$) and electric field ($\boldsymbol{E}$), and thus the corresponding constitutive behaviour is defined using the thermodynamic potential H as (Chee, 2000),

$$\boldsymbol{\sigma} = \boldsymbol{C\varepsilon} - \boldsymbol{eE} \quad (1.2)$$

$$\boldsymbol{D} = \boldsymbol{e}^{\mathrm{T}} \boldsymbol{\varepsilon} + \boldsymbol{\epsilon} \boldsymbol{E} \quad (1.3)$$

Equations (1.2) and (1.3) correspond to the converse and direct piezoelectric effects, respectively for the linear piezoelectric behaviour under a constant temperature. Based on these direct and converse effects, the piezoelectric sensors and actuators are developed, and the same are widely utilized for active control of flexible structures as a corresponding review of literature is furnished in the following sections.

1.2 Smart structures

Thin-walled flexible structures are extensively employed in numerous engineering constructions for aircraft, ship, automotive, transmission tower, bridge, warehouses, etc. These structures are prone to undergo large amplitude of vibration with a long settling time because of their flexibility and low damping. This often leads to structural fatigue and instability resulting in the failure of the structure or degradation of the performance of the structure. In order to improve the durability of such flexible structures and also to enhance their performance, piezoelectric sensors and/or actuators are widely utilized by means of integrating an active control system with the host structure. The active control system may be comprised of monolithic piezoelectric and actuators or piezoelectric fiber composite (PFC) sensors and actuators and a controller as it is shown typically in Fig. 1.3 considering a host beam. When the overall beam undergoes bending mode of vibration, the piezoelectric sensor provides the feedback of transverse deflection at every instant of the time. Based on this feedback, the piezoelectric actuator attenuates the vibration of the overall beam according to a control strategy that is built in the controller. This active control system does not affect the passive static/dynamic stiffness characteristics of the structure (Crawley et al., 1988). So the overall beam can sense, diagnose and control its own deflection as the external excitations are imposed on it. Such a structure is commonly known as smart structure (Bailey and Hubbard, 1985; Burke and Hubbard, 1987). In an endeavour to develop light-weight, flexible and high performing structures with the capabilities of self-sense, self-actuation and self-control, the idea of the smart structure was conceptualized and demonstrated by Clauser (1968, 1975). Subsequently, this concept of the smart structure has been utilized immensely by many researchers for active control of vibration of various structures. A brief review of the literature on the application of the concept of smart structure for active control of beams, plates, shells and other kinds of engineering structures using monolithic piezoelectric materials is furnished below.

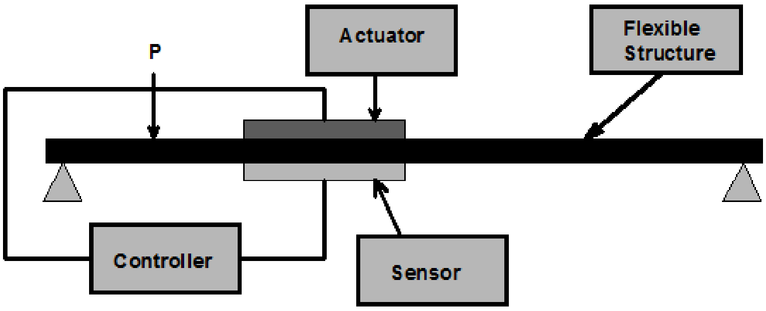

Fig. 1.3 Schematic diagram of a smart structure.

1.2.1 Analytical developments of smart structures

Crawley et al. (1988) derived analytical models of the laminated composite beams integrated with the piezoelectric actuators and reported that the performance of the piezoelectric actuators depends on the piezoelectric constants and elastic constants of the actuator-substructure system. Ray et al. (1993) presented the exact solutions of induced strain actuation for rectangular composite plates integrated with biaxially polarized PVDF sensors and actuators. Heyliger and Saravanos (1995) derived exact solutions for the natural frequencies of laminated plates comprised of elastic and piezoelectric layers. Dube et al. (1996a, 1996b) derived exact solutions for the thermo-piezo-elastic deformations of circular cylindrical panels. Batra et al. (1996) derived the exact solutions for the flexural vibration of rectangular plates integrated with piezoelectric actuators. He (1998) derived exact solutions for the axisymmetric electro-mechanical responses of laminated circular plates integrated with piezoelectric layers. Ray et al. (1998) presented the exact solutions for the forced vibration responses of laminated composite plates integrated with the piezoelectric sensor and actuator layers. Ray (1998) presented closed-form solutions for the optimum control of flexural vibration of thin laminated composite plates coupled with piezoelectric sensor and actuator layers. Aldraihem and Khdeir (2000) presented exact solutions for the deflection of laminated beams integrated with the thickness mode and extension mode piezoelectric actuators. Vel and Batra (2000) presented the analytical solutions for the static three dimensional deformations of multilayered piezoelectric rectangular plates.

Vel and Batra (2001b) analyzed the displacements and stresses of elastic bimorphs and plates with surface-bonded and embedded segmented piezoelectric actuators using the analytical solutions and classical laminate plate theory. Benjeddou and Deu (2001a) derived exact solutions for the transverse shear actuation of simply-supported piezoelectric laminated plates. The same authors (Benjeddou and Deu, 2001b) also presented the shear mode piezoelectric actuation/sensing mechanisms for a substrate of laminated composite plate. Vel and Batra (2001a) derived exact solutions for the three-dimensional deformations of thick laminated rectangular plates embedded with shear mode piezoelectric actuators. Tylikowski (2001) presented analytical solutions for the transverse vibration of annular plates integrated with piezoelectric actuators. Vel et al. (2004) provided the analytical solutions for the cylindrical bending vibrations of piezoelectric laminated composite plates. Baillargeon and Vel (2005a) derived exact solutions for control of flexural vibration of laminated composite plates using shear mode piezoelectric actuators. Kumari et al. (2007) presented exact solutions for the forced flexural response of smart laminated panels. Ebrahimi and Rastgoo (2008) and Ebrahimi et al. (2009) derived analytical solutions for nonlinear free flexural vibrations of a thin annular FG plate integrated with two uniformly distributed piezoelectric actuators, and demonstrated the effects of variation of the gradient index of the FG plate on the dynamic characteristics of the overall smart FG plate. Brischetto and Carrera (2012) presented closed-form solutions for the static deformation of smart plates under thermo-electrical loadings. Recently, Alibeigloo (2017) presented analytical solutions for the static analysis of a smart FG circular/annular plate under thermo-electro-mechanical loading.

1.2.2 Experimental developments of smart structures

Forward (1981) experimentally demonstrated active damping of two orthogonal bending modes of vibration of a cylindrical mast bonded with piezoelectric sensors and actuators. Crawley and Luis (1987) presented the experimental models for the shape and vibration control of laminated composite cantilever beams integrated with the segmented piezoelectric actuators. Miller and Hubbard (1988) demonstrated the active control of vibration of a host beam using the PVDF polymer as the material of distributed actuator and sensor. The corresponding experimental study was also carried out by Plump et al. (1987) and Tzou and Panditha (1987). Im and Atluri (1989) presented an analysis for control of nonlinear vibration of the beam using piezoelectric actuators. Baz and Poh (1988) investigated the effects of the material of bonding layer, the thickness of actuator and the location of actuator on the performance of piezoelectric actuators in control of beams. The same authors (Baz and Poh, 1990) also experimented to investigate the merits of MIMSC (Modified Independent Modal Space Control) method in comparison to Independent Modal Space Control (IMSC) and Pseudo-Inverse (PI) methods for the vibration control of a cantilever beam using piezoelectric actuators. Tzou and Gadre (1989) carried out experimental studies on the active control of vibration of a multilayered thin shell integrated with PVDF actuator. Crawley and Lazarus (1991) carried out experimental studies on the induced strain actuation of isotropic and anisotropic plates integrated with piezoelectric actuators.

Lazarus et al. (1996) presented the large bandwidth control of an aero-elastic wing cantilever structure integrated with piezoelectric actuators. The same authors also verified their analytical results through experimentation. Kim et al. (1996) carried out experimental studies of an aluminum plate integrated with piezoelectric sensors and actuators and demonstrated the relation between the electrical input admittance and response of sensor. Zemčík et al. (2007) presented the experimental results for harmonic responses of a cantilever beam bonded with the active and passive piezoelectric patches. Rao et al. (2008) presented the experimental results for optimal locations of piezoelectric actuators and sensors in control of several modes of vibration of a composite fin-tip of an aircraft. Qiu et al. (2009) presented numerical and experimental results for efficient active control of vibration of a flexible beam using non-collocated piezoelectric actuators, proportional feedback control and sliding mode variable structure control algorithms with phase shifting technology. Malgaca (2010) presented the experimental results for natural frequencies and closed-loop time responses of laminated composite beams integrated with the piezoelectric sensors and actuators. Gupta et al. (2011) presented experimental results for control of vibration of a cantilever plate at high temperature using collocated piezoelectric sensor-actuator pairs and negative velocity feedback control strategy. Kumar (2013) presented analytical, numerical (FE) and experimental studies on the active control of vibration of a smart flexible beam manipulator using LQG and PPF (Positive Position Feedback) control strategies. Qiu (2015) experimentally studied the active control of flexural and torsional vibrations of flexible cantilever plates through the optimally located piezoelectric sensors and actuators over the host plate-surface.

1.2.3 Finite element studies of smart structures

Hanagud et al. (1992) developed a finite element (FE) model for optimum vibration control of a beam bonded with piezoelectric sensors and actuators. Rao and Sunar (1993) reported significant thermal effects in the precision distributed control of a bimorph robotic finger. Lai et al. (1993) developed an FE model of a smart composite panel under aerodynamic and thermal loads. Tzou and Ye (1994) derived three-dimensional numerical models of piezoelectric laminates to investigate their controlled static and dynamic responses under a steady state thermal field. Suleman and Venkayya (1995) presented a simple FE formulation to study the sensing and actuation characteristics of cantilever laminated composite plates integrated with the piezoelectric sensor and actuator layers. Gopinathan and Pajunen (1995) developed an FE based controller to avoid spillover in control of higher modes of vibration of cantilever beams integrated with piezoelectric sensors/actuators. Smyser and Chandrashekhara (1997) designed a Neural Network controller for vibration control of laminated composite beams with embedded/surface bonded piezoelectric actuators/sensors. Saravanos et al. (1997) developed an FE model to study the static and free vibration characteristics of laminated composite plates integrated with continuous or segmented piezoelectric sensors and actuators. Peng et al. (1998) presented the effects of number and locations of piezoelectric sensors/actuators on the controlled dynamic responses of smart laminated composite beams by developing an FE model. Chee et al. (1999) developed a mixed FE model of a smart bimorph beam to investigate the deflection of the beam under different locations and/or orientations of the piezoelectric actuators. Balamurugan and Narayanan (2001) studied the geometrical and physical effects of the bonding layer on the vibration characteristics of laminated shells integrated with the piezoelectric sensor and actuator layers. Raja et al. (2002) reported significant performance of shear mode piezoelectric actuators in the active damping of laminated composite beams.

Ganapathi et al. (2004) developed a C^1 finite element to investigate the bending/torsional behavior of rectangular laminated/sandwich composite beams with integrated piezoelectric layers. Thakkar and Ganguli (2004) developed an FE model to study the control of vibration of a two-cell box beam using the shear mode piezoelectric actuators. Plagianakos and Saravanos (2005) studied the electro-elastic responses of bimorph and laminated beams comprised of active and passive piezoelectric layers. Cotoni et al. (2006) developed a finite element for the static and dynamic analyses of transversely poled piezoelectric composite plates. Narayanan and Balamurugan (2003) and Balamurugan et al. (2007) presented the active damping in smart laminated shell structures using either of the negative-velocity feedback, Lyapunov feedback and LQR control theories. Kapuria and Hagedorn (2007) developed an FE model to investigate the effects of segmentation of the electrodes on the deflection, sensory potential and natural frequencies of laminated composite cantilever beams integrated with the arbitrarily poled piezoelectric actuators and sensors. Neto et al. (2009) developed two types of finite elements for the static analysis of beams integrated with piezoelectric actuators and sensors. Yasin et al. (2010) used LQG control strategy for active control of vibration of aluminum plate using the patches of piezoelectric actuator. Kapuria and Yasin (2010) proposed an FE model of smart composite beams under impulse and step excitations for analyzing the control activities of piezoelectric actuators according to either of the velocity feedback, LQR (Linear Quadratic Regulator) and LQG (Linear Quadratic Gaussian) control strategies. Elshafei and Alraiess (2013) developed a higher order FE model to study the static and free vibration responses of smart beams integrated with piezoelectric actuators and sensors. Djojodihardjo et al. (2015) studied the effects of spillover and uncertainties on the active control of vibration of a smart Euler-Bernoulli beam under spring load.

1.2.4 Optimization studies of piezoelectric sensors/actuators on smart structures

Hwang and Park (1993) and Hwang et al. (1993) presented the effects of sizes and locations of piezoelectric sensors and actuators on the controlled vibration characteristics of a laminated composite plate. Chattopadhyay and Seeley (1994) investigated the effects of locations of actuators and structural configuration on the actively controlled dynamic responses of a box beam bonded with piezoelectric actuators. The effect of the thickness of piezoelectric actuators on their actuation capability in control of a cantilever beam was investigated by Kim and Jones (1995). Gabbert and Schultz (1996) presented a criterion for the optimal placement of piezoelectric actuator-patches over the length of a beam for effective control of vibration of the overall beam. Agrawal and Treanor (1999) presented optimum locations of piezoelectric actuator-patches over the length of a cantilever beam for achieving its (beam) desired shape of deflection. Bruant et al. (2001) studied the effects of locations of piezoelectric sensors/actuators over the length of a beam on their (sensors/actuators) control capabilities. Moon and Kim (2001) reported substantial suppression of flutter of composite plates through the use of optimally shaped and located piezoelectric actuators.

Liew et al. (2003a) presented the optimum configurations of sensor-actuator pairs for effective control of vibration of smart FGM beams. Nguyen and Tong (2004) demonstrated optimum voltage distribution over all the piezoelectric actuators for shape control of plates utilizing the PZT patches with arbitrary shapes. Trindade and Maio (2008) presented a parametric study on the optimal configuration of the shear mode piezoelectric actuators for efficient control of vibration of a sandwich beam. Ramesh Kumar and Narayanan (2008) presented optimal placement of collocated piezoelectric sensor-actuator pairs over the length of a beam for its effective control according to each of the direct proportional feedback, negative velocity feedback and LQR optimal control strategies. Kumar et al. (2014) reported optimal control of vibration of a cantilever beam by the use of collocated piezoelectric sensor-actuator pairs near the fixed end of the beam.

1.2.5 Static and Dynamic analyses of smart structures

Robbins and Reddy (1991) investigated the performance of piezoelectric actuators in control of the static deflections and transverse deflection-amplitudes of vibration of beams. Shen (1994) analyzed the static deflection and free vibration characteristics of an aluminum beam integrated with piezoelectric sensors and actuators. Chang et al. (1996) presented the harmonic vibration characteristics of an elastic beam integrated with the patches of piezoelectric actuator and sensor. Gupta et al. (1996) investigated the effects of nonlinearity and damping on the control of dynamic response of isotropic plates bonded with piezoelectric actuators and sensors. Robbins and Reddy (1996) determined the local stress fields in the surface mounted piezoelectric actuator over an unconstrained aluminum plate. Benjeddou et al. (1997) studied the static deflection and free vibration characteristics of beams integrated with extension mode and shear mode piezoelectric actuators.

Görnandt and Gabbert (2002) presented the static and dynamic responses of a smart laminated plate under the thermo-electro-mechanical excitations. Sekouri et al. (2002, 2004) presented the natural frequencies and mode shapes of piezoelectrically actuated annular plate components of space structures considering static and dynamic electro-mechanical loads. Liew et al. (2003b) studied the static and dynamic characteristics of the functionally graded (FG) plates integrated with piezoelectric sensors and actuators. Liew et al. (2004) presented the vibration characteristics of FG shells integrated with piezoelectric actuators/sensors. Moon et al. (2005) demonstrated the effective suppression of flutter of laminated composite plates using piezoelectric actuators. Wang et al. (2004) presented the dynamic stability in active control of vibration of laminated composite plates bonded with collocated and non-collocated piezoelectric sensors and actuators. Raja et al. (2006) demonstrated the active control of bending-torsion flutter instability of a cantilever composite plate using multi-layered PZT benders. Fox et al. (2007) presented the deflection characteristics of a circular plate integrated with an annular piezoelectric actuator. Ghasemi-Nejhad et al. (2006) demonstrated the active control of axial/lateral vibration of composite strut and panel structures using the piezoelectric stack and patch actuators.

Dash and Singh (2009) studied the nonlinear free vibration characteristics of smart laminated composite plates. Rao et al. (2016) presented the difference between the linear and nonlinear static deflections of piezo-laminated composite shells under large applied electric fields. Araújo et al. (2016) presented the free and forced vibration characteristics of a sandwich plate where the core is made of viscoelastic material, and the piezoelectric sensors and actuators are attached to the surface of the sandwich plate.

1.2.6 Thermo-electro-elastic behavior of smart structures

Tauchert (1992) demonstrated the control of thermally induced flexural vibration of a thin composite plate using the piezoelectric actuators. Chandrasekhara and Tenneti (1995) studied the influences of stacking sequence, boundary conditions and size of piezoelectric patches on the thermally induced transient vibration of a smart laminated composite plate. Lee and Saravanos (1995, 1997, 2000) presented the thermo-electro-mechanical behaviour of laminated shells bonded with piezoelectric sensors and actuators. Thornburgh et al. (2004) presented the transient vibration characteristics of a laminated cantilever plate integrated with piezoelectric actuators. Giannopoulous and Vantomme (2005) presented the thermo-electro-mechanical behavior of a composite plate integrated with piezoelectric layers. Jiang and Li (2008) studied the thermal effects on the deformation/vibration characteristics of laminated composite plates integrated with the piezoelectric sensors and actuators.

1.3 Piezoelectric fiber composites

The monolithic piezoelectric sensors and actuators are immensely utilized in the development of smart structures as it is observed from the review of literature in the previous section. The piezoelectric ceramics are easily available at low cost, and this may be a reason for its wide utilization in the development of smart structures. However, in the structural applications, the piezoelectric sensors and actuators are usually used in the form of the patch or the layer. The piezoelectric patch or layer is attached to the surface of the host structure or embedded in the domain of the host structure. For this kind of integration of the piezoelectric sensors/actuators with the host structure, they need to possess sufficient flexibility and conformability. The flexibility is also an important property of a piezoelectric sensor/actuator for its utilization under the circumstance of the moderate or large amplitude of vibration of a smart structure, while the conformable actuators are required for a host structure with curved boundary surfaces or complex geometry. Apart from these properties, a piezoelectric actuator is expected to be capable of providing sufficient control force as well as directional actuation. With reference to these required properties of a piezoelectric actuator, the monolithic piezoelectric actuators have several disadvantages like high stiffness, low strain energy density, insufficient flexibility and poor conformability. These actuators are also incapable of providing directional actuation. In view of these discrepancies, the piezoelectric actuators are made in the form of polymer-based composites with the inclusions of piezoelectric ceramics. The polymer constituent provides sufficient flexibility and conformability of the actuator, while the piezoelectric properties of the composite arise due to the inclusions of piezoelectric ceramics. The piezoelectric inclusions may be of different forms like particles, long fibers, short fibers, flakes etc., while most of the available piezoelectric composites are comprised of long/short piezoelectric fibers. In this section, a review of literature on the development of short/continuous (long) piezoelectric fiber-reinforced composites (PFCs) is presented.

1.3.1 Design of piezoelectric fiber composites (PFCs)

The first PFC appeared due to Chan and Unsworth (1989). Subsequently, Smith and Auld (1991) proposed a vertically reinforced 1-3 PFC that is capable of providing thickness mode actuation for an externally applied transverse electric field. Later, an exhaustive research has been carried out by many researchers and various PFCs have been developed. Bent (1999) and Bent and Hagood (1997) proposed Active Fibre Composite (AFC). In AFC, the unidirectional piezoelectric fibres are aligned in the plane of the PFC lamina. But the poling direction of the fibres is their longitudinal direction so that this PFC produces the in-plane actuation force when the external electric field is applied along the longitudinal direction through a unique arrangement of electrodes (Interdigitated Electrodes (IDEs)). After the proposition of the AFC, a similar PFC was developed at NASA using the piezoelectric fibres of rectangular cross-section (High and Wilkie, 2003) instead of the fibres of circular cross-section (Bent, 1999). This PFC (High and Wilkie, 2003) is known as Macro-Fibre Composite (MFC). As a novel contribution, Raja and Ikeda (2008) designed a shear actuated fiber composite (SAFC), and estimated its effective electromechanical behaviour for the shear mode of actuation.

1.3.2 Analytical and FE evaluation of effective properties of PFCs

Wang (1992) derived the analytical relations between the overall properties of the 0-3 PFC and the properties of its constituents. Bing et al. (1997b) and Jiang et al. (1999) derived the closed-form solutions for effective electro-elastic moduli of the piezoelectric composites comprised of ellipsoidal inclusions. Poizat and Sester (1999) estimated the effective piezoelectric constants as the functions of the fiber-volume fraction (FVF) and the fiber-aspect ratio for 1-3 and 0-3 PFCs. Pettermann and Suresh (2000) predicted all the moduli of a 1-3 PFC comprised of a dielectric matrix and piezoelectric fibers. Bowen et al. (2001) and Bowen and Kara (2002) studied the effects of FVF and elastic modulus of the polymer phase on the hydrostatic piezoelectric voltage constant and hydrostatic strain constant of 3-3 PFCs. Kari et al. (2007) investigated the effects of diameter and arrangement of fibers on the effective properties of unidirectional PFCs.

Berger et al. (2005a, 2005b, 2005c, 2006) proposed an FE procedure for estimation of effective properties of unidirectional and uniaxial periodic 1-3 PFCs. Kar-Gupta and Venkatesh (2005, 2007a, 2007b) studied the effects of fiber distribution and poling direction on the electromechanical behaviour of a 1-3 PFC. Ho et al. (2006) derived two new explicit formulae for prediction of effective piezoelectric coefficients of binary 0-3 piezoelectric composites. Ray (2006a) proposed an electrode arrangement for applying a uniform transverse electric field across the thickness of a 1-3 PFC, and derived the corresponding effective properties of the PFC. Deraemaeker et al. (2007) presented an FE procedure for estimation of effective properties of MFC actuator. The corresponding results are also compared with the similar results obtained using Uniform Fields Method

(UFM). Kar-Gupta and Venkatesh (2008) studied the effects of geometrical connectivity, volume fraction, grain size distribution and poling direction of piezoelectric inclusions on the electromechanical properties of five types of piezoelectric composites (particulate, short-fiber, long-fiber, laminate and networked composites). Using the mixing rules, Deraemaeker et al. (2009) estimated the effective piezoelectric coefficients of d_{33} and d_{31} MFCs. These estimated coefficients were also substantiated by the computation of the same coefficients using FE procedure. Deraemaeker and Nasser (2010) evaluated the properties of d_{33} and d_{31} MFCs using the FE procedure and compared the results with the similar analytical results.

Trindade and Benjeddou (2011) evaluated the effective material properties of a shear actuated d_{15} MFC using FE procedure and validated the results with the similar analytical results (Benjeddou and Al-Ajmi, 2011). Nasser et al. (2011) computed the effective electromechanical properties of MFC using UFM. Berger et al. (2010) presented the effective electromechanical behaviour of PFCs comprised of arbitrary fiber distributions. Li et al. (2011) studied the effects of geometric properties of piezoelectric phase on the electromechanical coupling coefficients of 1–3 PFCs. Chambion et al. (2011) analyzed the importance of the filler arrangement to optimize the electromechanical response of 0-3 composites (piezoelectric particle composites). Brenner et al. (2012) analytically investigated the effective piezoelectric response of 2-1-2 piezoelectric composite. Sakthivel and Arockiarajan (2010) studied thermo-electro-mechanical behaviour of 1-3 PFCs and demonstrated the thermal effect on the overall properties of 1-3 PFCs. The same authors (Sakthivel and Arockiarajan (2011, 2012)) also presented the effects of poling of matrix and fiber orientation on the thermo-electro-mechanical behaviour of 1-3-2 piezoelectric composites where both fiber and matrix are piezoelectrically active. Kalamkarov and Savi (2012) presented analytical expressions of a smart composite structure that is reinforced with a periodic grid of generally orthotropic cylindrical reinforcements. Trindade and Benjeddou (2012) proposed a novel electrode design for d_{15} thickness-shear MFC (Trindade and Benjeddou, 2011). They also carried out parametric studies to investigate the effects of FVF, epoxy elastic modulus, electrode and active layer thicknesses on the effective material properties of the shear MFC. Prasath and Arockiarajan (2013) developed an analytical model to evaluate the effective electromechanical properties of d_{33} and d_{31} MFCs. Kranz et al. (2013a, 2013b) presented FE analysis of the effective properties of d_{15} shear MFC based on the enthalpy-based homogenization method.

Iyer and Venkatesh (2014) presented an analytical model to estimate the effective properties of the 3–0 and 3–1 piezoelectric composites and validated the model by computing the properties using FE procedure. Fu et al. (2017) developed an efficient multi-scale FE procedure to investigate the nonlinear electromechanical responses of heterogeneous PFCs.

1.3.3 Effective behavior of PFCs using Micromechanical Approaches

Dunn and Taya (1993) presented the electro-elastic behaviour of PFCs by computing the effective electro-elastic moduli through the extension of dilute, self-consistent, Mori-Tanaka and differential micromechanics theories. Tungyang (1994) and Chen (1996) derived the expressions for the effective thermo-electro-elastic moduli of a PFC employing self-consistent and Mori-Tanaka methods. Benveniste and Dvorak (1992) and Benveniste (1993, 1994) derived the exact solutions for effective constants of binary and multiphase composites with arbitrary phase geometry. Huang and Kuo (1996), Kuo and Huang (1997) and Fakri et al. (2003) developed micromechanical models of PFCs consisting of spatially oriented inclusions and reported the effective electro-elastic behaviour of the PFCs. Aboudi (1998) presented micromechanical generalized method of cells model to predict the thermo-electro-elastic behavior of multiphase piezoelectric composites. . Yu (1999) developed a micromechanical model for analytic estimates of the effective electro-elastic properties of two-phase PFCs. Jiang et al. (2001) developed a generalized self-consistent micromechanical model and obtained the closed-form expressions of the effective electro-elastic coefficients of PFCs under anti-plane shear. Tan and Tong (2001a, 2001b) proposed rectangle and rectangle-cylinder micromechanical models to investigate the linear and nonlinear electro-elastic behaviour of PFCs. Ruan et al. (2002) developed a three-dimensional micromechanics model to investigate the effects of fiber orientation and matrix properties on the effective piezoelectric properties of a PFC comprised of unidirectional piezoelectric fiber yarn in a polymer matrix. Glushanin and Topolov (2003) proposed a micromechanics model to analyze the electromechanical behaviour of the 1-2 ferroelectric piezoactive ceramic (FEPC) composite comprised of ferroelectric ceramic inclusions in a polymer matrix.

Mallik and Ray (2003) proposed a unidirectional PFC comprised of transversely poled piezoelectric fibers embedded in the epoxy matrix, and derived the effective properties of the PFC using method of cells. Qin (2005) developed a micromechanics model of piezoelectric composites based on boundary element method (BEM), and presented their effective electro-elastic properties for the piezoelectric inclusions of various shapes. Della and Shu (2007, 2008) presented a micromechanics model based on the Mori-Tanaka method for analyzing the electromechanical behavior of 1-3 PFCs comprised of a porous matrix. Challagulla and Venkatesh (2009) developed a micromechanical model based on the AHM for investigating the electro-elastic behaviour of 2-2 PFCs where the constituents were elastically anisotropic and piezoelectrically active. Sabina et al. (2001) derived the closed-form expressions for the effective electro-elastic properties of PFCs employing the Asymptotic Homogenization Method (AHM). Kar-Gupta and Venkatesh (2013) developed an analytical micromechanical model to characterize the effects of phase volume fractions and orientation of the poling direction of piezoelectric inclusions on the effective properties of 2-2 PFCs. Lin and Muliana (2013, 2014) analyzed the nonlinear electromechanical responses of 0-3 and 1-3 PFCs utilizing Mori-Tanaka (MT), Self-Consistent (SC) and Unit-Cell (UC) methods. Eynbeygui and Aghdam (2015) developed a generalized plane strain (GPS) micromechanics model using the element free Galerkin method to study the electro-elastic behaviour of PFCs.

1.3.4 Experimental studies on the effective behavior of PFCs

Shindo et al. (2010) presented the experimental results for the nonlinear electromechanical responses of a 1-3 PFC consisting of the square or circular piezoelectric rods in an epoxy matrix. Lu et al. (2016) presented experimental results for the effects of voltage amplitude, operating frequency and FVF on the free strain of d_{33} PFC. Yuan et al. (2017) designed and fabricated a novel d_{15} shear PFC, and reported its good actuation capability in control of cantilever beams. Zhen et al. (2008) experimentally determined the electromechanical properties of 1-3 PFC with 10-35% volume fraction of a piezoelectric constituent. Zhou et al. (2012) fabricated and determined the electromechanical properties of a 1-3-2 piezoelectric composite. Jayendiran and Arockiarajan (2013) experimentally studied the nonlinear electromechanical behaviour of 1-3 PFC for its different FVFs and bulk piezoelectric ceramics. Dongyu et al. (2015) designed 1-3 PFCs for different distributions of piezoelectric ceramic and matrix phases, and determined their (1-3 PFCs) effective electromechanical properties. Dongyu et al. (2016) designed three types of 1-3 PFCs and addressed great improvements in the electromechanical and acoustic properties of the composites. Trindade and Benjeddou (2016) presented the dependence of the effective properties of d_{31} MFC on the electric field. Recently, Mi et al. (2017) presented a 1-1-3 piezoelectric composite along with its electromechanical behaviour.

1.4 Smart structures using PFCs

The PFCs are designed for achieving superior flexibility, conformability and actuation capability over those of the monolithic piezoelectric ceramics, and also for accomplishing directional actuation by a piezoelectric actuator. Owing to these advantages, PFCs are extensively utilized in the active control of various flexible structures. A brief review of literature is presented in this section.

1.4.1 Active vibration/ deformation control of smart structures using PFCs

Aldraihem and Wetherhold (1997) performed a study on the active control of bend-twist coupled vibration of a laminated beam integrated with the layers of PFC actuator. Mahut et al. (1998) studied the performance of PFC actuators in control of vibration of cantilever beams under static and dynamic loads. Cesnik and Shin (2001) presented a design of multi-cell composite helicopter rotor blades integrated with the layers of AFC actuator. Sodano et al. (2004) presented the control capability of MFCs in the low-frequency vibration of beams and inflatable space structures. Ray and Mallik (2004a, 2004b) studied the performance of a 1-3 PFC actuator (Mallik and Ray 2003) in active control of vibration of laminated composite plates. Park and Kim (2004) studied the aero-thermal large deflections and snap-through behavior of composite plates integrated with MFC actuators. Mallik and Ray (2004, 2005) investigated the actuation capability of a 1-3 PFC (Mallik and Ray 2003) layer for shape control of laminated composite plates. Wickramasinghe and Hagood (2004a, 2004b) presented the material and durability characterizations of AFC actuator for helicopter rotor blade applications. Park and Kim (2005) studied the active control of twist of rotor blades using MFC actuators. Brockmann and

Lammering (2006) investigated the effects of shear flexibility and torsional warping on the structural dynamics of rotating beams integrated with the layers of PFC actuator. Guennam and Luccioni (2006) derived an FE model of a closed box beam integrated with PFC patches and studied the controlled transient responses of the overall beam. Ray and his coworkers (Panda and Ray, 2006; Ray, 2006b; Ray and Sachade, 2006a; Ray and Sachade, 2006b; Reddy and Ray, 2007) studied the actuation capability of 1-3 PFC actuator (Mallik and Ray 2003) for control of rectangular FG plates. Choi et al. (2006, 2007) presented the active control of rotating beams using MFC actuators.

Zhang and Shen (2007) studied the control of vibration of laminated plates using 1-3 PFC layers. Barkanov et al. (2008) presented the optimal design of active helicopter rotor blades using MFC actuators. Kapuria and Yasin (2010) studied the effects of segmentation of electrodes, fiber orientation and FVF of PFC on the controlled responses of hybrid composite plates integrated with a PFC actuator. Mahato and Maiti (2010) reported the capability of AFC actuator in the reduction of aero-elastic flutter velocity and frequency of smart composite plates under hygro-thermal loads. Bilgen et al. (2010) studied the aerodynamic deflection of simply supported thin airfoils using MFC actuators. Maiti and Sinha (2011) developed an FE model to study the vibration characteristics of laminated plates bonded with AFC actuator-layers. Panda (2011) investigated the capability of a cylindrically orthotropic PFC actuator in control of nonlinear deformations of annular plates. Kim et al. (2011) presented the active control of vibration of cylindrical shells with surface bonded MFC actuators.

Cook and Vel (2012) developed a multi-scale analytical model to analyze the effective properties, deflections and stresses in the laminated composite plates integrated with PFC actuators. Kapuria and Yasin (2013) studied the smart flexible laminated skew plates using the layers of PFC sensor and actuator and addressed the effectiveness of directional actuation and sensing capability of PFC. Panda and Sopan (2013) performed the geometrically nonlinear thermo-electro-elastic flexural analysis of FG annular sector plates integrated with annular patches of a cylindrically orthotropic PFC, and reported the control capability of the PFC actuator for shape control of annular sector plate. Aravinda Kumar et al. (2015) performed a nonlinear frequency response analysis of smart functionally graded plates and investigated the control capability of a 1-3 PFC to control thermo-elastic deformation/vibration of functionally graded plates. Padoin et al. (2015) carried out a study on the optimal control of laminated composite cantilever plates using the MFC actuator-patches which are activated through LQR control algorithm.

Wang et al. (2016) designed and studied the tracking system for dynamic roll rate maneuver of UAV (Unmanned Aerial Vehicle) with morphing wings made of MFCs. Wang et al. (2017) presented smooth continuous morphing motion and gentle aero elastic responses by the application of optimum voltage to the wings made of MFCs. Gamble and Inman (2017) investigated the aerodynamic effects on the morphing horizontal tail made of MFCs for yaw control on a bio-inspired aircraft. Guo et al. (2017) studied the stability of the nonlinear dynamic motion of a multi-layer d_{31} MFC laminated shell.

1.4.2 Experimental active control using PFCs

Dano and Julliere (2007) presented experimental results for the active control of thermally induced deformations of composite plates using MFC actuators. Tarazaga et al. (2007) also presented experimental results for active control of an inflatable composite boom using the MFC actuators. Park et al. (2008) presented the experimental results for damage detection of railroad tracks using a MFC-impedance based wireless structural health monitoring (SHM) system. Kwak et al. (2009) carried out experiments to study the vibration characteristics of cylindrical shells integrated with the MFC actuators and sensors. Sohn et al. (2009, 2011) experimentally demonstrated the active vibration control of smart hull structures using MFC actuator. Bilgen et al. (2011) carried out experiments for increasing lift coefficient in flow control of a variable camber airfoil using MFC actuators. Zippo et al. (2015) experimentally investigated the control capability of MFC actuator for active control of vibration of a cantilever sandwich plate using PPF (Positive Position Feedback) control strategy in combinations of MIMO (Multi Input Multi Output) and SISO (Single Input Single Output) systems. Pandey and Arockiarajan (2017a) carried out experiments to study the influence of plate thickness and piezoelectric fiber angle on the performance of MFCs in actuation of a steel plate under thermal conditions. The same authors (Pandey and Arockiarajan, 2017b) also conducted experiments to study the degradation in the stiffness and strength (fatigue behavior) of the d_{31} and d_{33} MFCs under thermo-mechanical loadings.

1.4.3 Comparative studies on the control capabilities of PFC actuators

Azzouz et al. (2001) performed a comparative study on the control capabilities of MFC and traditional PZT-5A actuators in control of cantilever square and triangular plates. Nguyen and Kornamann (2006) carried out a comparative study on the capabilities of AFC, MFC and conventional PZT actuators in control of vibration of a cantilever beam. Raja et al. (2011) studied the control of shape and vibration of laminated plates using MFC and SAFC actuators. Gopinath et al. (2011a, 2011b) investigated the active control of aero-elastic flutter of a composite plate using the patches of shear mode (SAFC) and extension mode (MFC) PFC actuators. Zhang et al. (2015, 2016) carried out a comparative study on the control capabilities of d_{33} and d_{31} MFCs in control of composite and isotropic plates. Kumar et al. (2017) investigated the damping capabilities of four kinds of cylindrically orthotropic PFC laminate actuators in the active vibration control of isotropic annular plates by proposing numerical method for optimal configuration of patches corresponding to the mode of vibration.

1.5 Active constrained layer damping (ACLD)

The piezoelectric stress/strain coefficients of monolithic piezoelectric ceramics and different types of PFCs are of small magnitudes. So, the electrically induced actuation force in the actuator is not usually compatible with the high rigidity of engineering structures, and this fact results in low control capability of the piezoelectric actuators. In view of this discrepancy, the use of piezoelectric actuators along with the viscoelastic materials has been suggested by many researchers for suppression of vibration of engineering structures. The piezoelectric actuators can then be utilized to enhance the deformation of viscoelastic materials of low stiffness, and it results in improved viscoelastic damping of engineering structures.

Different kinds of arrangements of piezoelectric actuators along with the viscoelastic materials have been proposed in the literature as Electro-Mechanical Surface Damping (EMSD) (Ghoneim, (1993, 1996), Hagood and Flotow, 1991), active constrained layer damping (ACLD) (Baz and Ro, 1995; Shi et al., 2004), conventional active piezoelectric damping composites CAPDC (Gentilman et al., 1994; Reader and Sauter, 1993), active piezoelectric damping composite (APDC)

(Arafa and Baz, 2000a; Arafa and Baz, 2000b; Baz and Tempia, 2004), etc. Among all these damping arrangements, the most popular one is the ACLD arrangement as it is widely used in aircraft, naval and automobile industries (Herdic et al., 2005; Kwak et al., 1999; William, 1998). The concept of ACLD treatment was proposed by Baz and Ro (1993). In this proposition of ACLD treatment (Baz and Ro, (1993), a viscoelastic layer is sandwiched between two piezoelectric layers. The piezoelectric layers are utilised as the sensor and actuator layers through a controller to control the transverse shear deformation of the constrained viscoelastic layer for having enhanced damping in the overall structure. Instead of using two piezoelectric layers, Shen (1993, 1994) utilised one piezoelectric layer to constrain the viscoelastic layer, while the control activities of the piezoelectric constraining layer were regulated by a controller and a point-sensor.

1.5.1 Experimental investigations of ACLD

Azvine et al. (1995) presented another arrangement of ACLD treatment where the piezoelectric layer was attached to the metallic constraining layer instead of using the piezoelectric layer as the constraining layer. In the early stage of evolution of ACLD treatment, its utility as a potential damping device was substantiated through a comparative study of the available active, passive and hybrid damping treatments (Chen and Baz, 1996, Tomlinson, 1996, Veley and Rao, 1996). Baz and Ro (1996) experimentally investigated the vibration characteristics of flat plates integrated with a layer of ACLD treatment and reported superior performance of ACLD treatment than pure passive damping. Chantalakhana and Stanway (2000) experimentally investigated the vibration damping of a fully clamped plate integrated with a layer of ACLD treatment. Liu et al. (2004) experimentally demonstrated the partial ACLD treatment of plates using robust H_∞ controller and compared the efficiency of ACLD treatment with that of the pure passive damping. Ko et al. (2004) experimentally investigated the effectiveness of ACLD treatment for control of arc-type cantilever composite shells and compared the damping capacity of the ACLD treatment with that of the pure passive treatment. Shi et al. (2004) presented the experimental results for controlled and uncontrolled impulse responses at the free tip of a cantilever beam integrated with the ACLD treatment. Vasques et al. (2006) presented an experimental study on the arbitrary ACLD treatment of composite beams.

1.5.2 Analytical and numerical investigations of ACLD

Baz (1997) also studied the vibration characteristics of cantilever beams integrated with ACLD treatment and demonstrated the suitability of this active-passive damping treatment. Ray and Baz (1997) analyzed the energy dissipation characteristics of ACLD treatment of plates to determine the optimal size and control gains of the treatment. Shen (1997) presented a study on the active control of vibration of shells using ACLD treatment. Park and Baz (1999) and Gandhi and Munsky (2000) used different control strategies for achieving superior damping capacity of the ACLD treatment.

Baz and Chen (2000) used the ACLD treatment for control of axisymmetric vibration of cylindrical shells and reported its (ACLD) effectiveness in comparison to the passive viscoelastic damping. A similar study on control of cylindrical shells using ACLD treatment was carried out by Ray et al. (2001). Chattopadhyay et al. (2001) presented the influences of the number of piezoelectric actuators and their locations in the segmented ACLD treatment of composite plates. Saravanan et al. (2001) performed a semi-analytical FE analysis of ALCD of cylindrical shells of revolution and addressed the effects of axial and circumferential mode numbers, feedback factor, length to radius ratio, radius to thickness ratio of the shell, percentage area of the shell covered with collocated piezoelectric sensors/actuators and axial location of collocated sensors/actuators on the damping ratio of cylindrical shells of revolution. Lim et al. (2002) developed an FE model for the ACLD treatment of cantilever isotropic plates and addressed through a time-domain analysis that the damping in the ACLD treatment is better than that in the passive or active treatment. Batra and Geng (2002) reported that the energy of electrical deformations of shear mode PZT actuators was more than that for extension mode actuators in the ACLD treatment of thick laminated plates. Balamurugan and Narayanan (2002) used LQR optimal control strategy to activate the piezoelectric constraining layer for the ACLD treatment of beams and made an assessment of damping capability of the treatment.

Chattopadhyay et al. (2002) carried out a study to enhance the aeromechanical stability of composite rotor blades using ACLD treatment. Ro and Baz (2002) used the modal strain energy method (MSE) and self-sensing ACLD networks and addressed the optimal locations of ACLD patches in control of vibration of plates. Sun and Tong (2003) investigated the effect of debonding of

ACLD patches on its (ACLD) efficiency in the control of beams. Ray and Reddy (2004a) presented the optimal size and locations of ACLD patches over the surface of a laminated circular cylindrical shell.

Gao and Liao (2005) studied the effects of control gain, size and location of piezoelectric actuators on the modal frequencies and modal loss factors of a simply-supported beam integrated with self-sensing ACLD treatment. Ray and Reddy (2005) and Ray and Mallik (2005) investigated the performance of an extension mode 1-3 PFC as the material for constraining layer for ACLD treatment of laminated composite plates and shells. Sharnappa et al. (2007) studied the ACLD treatment of composite beam under thermal environment and addressed the effects of fiber orientation and temperature on the natural frequency and damping of the system for different boundary conditions. Liu et al. (2007) investigated the vibration characteristics of rotating cantilever plates integrated with ACLD treatment and found faster increase of the higher natural frequencies than that for lower natural frequencies as the rotating speed increases. Ray and Pradhan (2007) and Ray and Batra (2007a) investigated the performance of vertically reinforced 1-3 PFC layer as the constraining layer for ACLD treatment of laminated beams and FG plates. Li et al. (2008) studied the ACLD treatment of beams and found that the maximum value of required control voltage can be reduced by increasing the number of ACLD patches.

Providakis et al. (2008) compared the ACLD treatment with the active damping (AD) treatment based on the electromechanical impedance approach. Saini et al. (2008) addressed the optimal locations of MFC patches for ACLD treatment of first three modes of vibration of thin shells. Panda and Ray (2008, 2009a, 2009b) investigated the performance of horizontally reinforced (Mallik and Ray, 2003) and vertically/obliquely reinforced (Smith and Auld, 1991) 1-3 PFC actuators for ACLD treatment of FG plates. Kumar and Singh (2009) studied the partial ACLD treatment of beams and addressed the effects of control gain, viscoelastic layer thickness, coverage of the treatment and location of ACLD patches on the system loss factors. Yuan et al. (2010) addressed the potential of semi-analytical method over the FEM in the analysis of vibration of ACLD treated circular cylindrical shells. Zheng et al. (2011) analyzed natural frequencies, loss factors and frequency responses of cylindrical shells integrated with ACLD treatment. Kumar and Singh (2012) experimentally investigated the bending and twisting vibration characteristics of a curved panel integrated with ACLD patches.

Suresh Kumar and Ray (2012) developed a three-dimensional model of a sandwich plate integrated with ACLD treatment and studied the performance of vertically/obliquely reinforced 1-3 PFC as the material of active constraining layer. Li and Narita (2013) presented the ACLD treatment of laminated composite plates for arbitrary boundary conditions. Zhang and Zheng (2014) studied the partial ACLD treatment of plates by developing a hybrid controller where it is demonstrated that the controller effectively reduces the displacement-amplitude through the combined feed forward and feed backward control actions. Ni et al. (2013) investigated the active-passive damping in shells of revolution for ACLD treatment according to a specified control strategy and reported that the ACLD treatment is more effective at low frequency of vibration. Aravinda Kumar et al. (2016) presented nonlinear frequency responses of heated FG plates integrated with the ACLD treatment where the active constraining layer is made of an extension mode 1-3 PFC. By developing a three-dimensional FE model, Kundalwal and Ray (2016) investigated the ACLD treatment of smart fuzzy fiber reinforced composite (FFRC) plates. Li et al. (2016) studied the suppression of random vibration of laminated composite rectangular plates using ACLD treatment and 1-3 PFC for the material of active constraining layer. Lu et al. (2017) presented a theoretical study on the partial ACLD treatment for control of vibration of thin plates at low frequency, and the corresponding observations have also been verified experimentally.

1.6 Research motivation and objectives

The literature survey shows a substantial number of studies on the design and characterization of different kinds of PFCs. Among all these available PFCs, the popular ones are the extension/shear mode PFCs with the 1-3/2-2 connectivity since the applications of these PFCs are substantially reported in the literature for active control of deformation/vibration of the thin-walled flexible structures like beams, plates, shells, airfoils, etc. (Azzouz et al., 2001; Bent 1999; Bilgen et al., 2010; Cesnik and Shin, 2001; Choi et al., 2006; Kim et al., 2011; Kovalovs et al., 2007; Kwak et al., 2009; Marinaki et al., 2011; Melnykowcyz et al., 2006; Park et al., 2008; Schultz et al., 2000; Sodano et al., 2004; Sohn et al., 2006; Sohn et al., 2007; Sohn et al., 2011; Wickramsinghe and Hagood, 2004a; Wickramsinghe et al., 2004b). Similar to these structures, the plane structures of revolution like annular/circular plates are also important structural elements as these are often used in micro-valves, micro-pumps, micro-switches, implantable medical devices, oil storage tanks, brake systems of vehicles, airfoil cascades, oceanographic applications, etc. (Bambill et al., 2004; Buffum and Fleeter, 1986; Cao et al., 2001; Cha et al., 2015; Kim and Ha, 2003; Sergienko et al., 2008; Shi et al., 2017). But, it has been observed that a few studies on the active control of annular/circular plates have been reported in the literature utilizing the monolithic piezoelectric actuators. Moreover, the utilization of any of the available PFCs for active control of annular/circular plates has not yet been addressed in the literature. This may be due to the fact that the principal material coordinate system of the existing PFCs is the rectangular coordinate system, and thus these PFCs may not be well-qualified materials for distributed actuators where the mechanically induced stresses/strains arise in cylindrical coordinates. So, to employ the concept of PFC for efficient control of plane structures of revolution, the microstructure of the PFC is to be designed in the cylindrical coordinates with the special attentions on the flexibility, conformability, magnitudes of piezoelectric coefficients, strain energy density, directional actuation capability and manufacturing difficulties. The research in this line is not yet addressed in the literature. Thus, the primary objective of the present research is identified as the design of extension/shear mode PFCs with 1-3/2-2 connectivity for efficient control of plane structures of revolution like annular/circular plates. As these plates often undergo bending mode of deformation under operation, the primary intent in this design of 1-3/2-2 PFCs is to achieve the in-plane extensional/transverse shear actuation forces in the cylindrical coordinates, and also to utilize these PFCs in an appropriate manner for efficient control of annular/circular plates.

The 1-3/2-2 PFCs are usually comprised of unidirectional continuous piezoelectric fibers with a high fiber-volume fraction. The long, thin and brittle piezoelectric fibers within these PFCs may break during operation under the moderate/large amplitude of vibration or during its integration with the host structure of complex geometry. This breakage of fibers eventually degrades the actuation capability of PFC, and thus the PFCs are generally used in the form of the patch. But, the shortcoming of fiber damage may persist depending on the size of the patch and also on the complexity of geometry of the host structure. An alternative way is to compose the PFC using short piezoelectric fibers retaining their uniform orientation for directional actuation. But, one has to put particular attention in the design of this PFC because of the possibility of degraded actuation capability due to the use of the short piezoelectric fibers. In view of these practical issues in the design and applications of 1-3/2-2 PFCs, the second objective of the present research is identified as the design of an extension mode short piezoelectric fiber composite (SPFC) in the cylindrical/rectangular coordinates.

For effective control of any mode of vibration of a smart plate, the piezoelectric actuator is generally used in the form of patches. The size and locations of these patches over the plane of the plate are decided by means of an optimal algorithm. This analytical procedure for determining the appropriate configuration of the patches becomes a little difficult when several modes of vibration of the plate within an operating frequency-domain are to be attenuated effectively. In this issue, the studies have been carried out by several researchers using various optimization algorithms and extension mode piezoelectric actuators (Hwang and Park, 1993; Hwang et al. 1993; Ramesh Kumar and Narayanan, 2008; Ray, 1998). Further research in this line may be done in the quest of a simple analytical/numerical procedure for configuring the patches in such a manner that all the modes of vibration of the smart plate within an operating frequency-domain can be attenuated efficiently. Also, the same procedure may be extended for the shear mode piezoelectric actuators as this kind of study is not yet available in the literature. Thus, the third objective of this research is decided as the study on configuring the shear mode piezoelectric patches and controller for efficient control of all the bending modes of vibration of a smart annular plate in an operating frequency-domain.

The piezoelectric actuators possess low control capability with reference to the rigidity of the host structure, and this fact often results in their inefficient control activity in attenuation of structural vibration. Owing to this shortcoming, the use of the piezoelectric actuators along with the viscoelastic materials of low stiffness has been suggested by several researchers (Arafa and Baz, 2000a; Arafa and Baz, 2000b; Baz and Ro, 1995; Baz and Tempia, 2004; Gentilman et al., 1994; Ghoneim, 1993; Ghoneim, 1996; Reader and Sauter, 1993; Shi et al. 2004). In these studies, the piezoelectric actuator is primarily utilized to enhance the viscoelastic damping in a smart structure. In this context, various hybrid damping treatments of structural vibration have been proposed in the literature like Electro-Mechanical Surface Damping (EMSD) (Ghoneim, 1993; Ghoneim, 1996), Conventional Active Piezoelectric-Damping Composite (CAPDC) (Gentilman et al. 1994; Reader and Sauter, 1993), Active Piezoelectric Damping Composite (APDC)

(Arafa and Baz, 2000a; Arafa and Baz, 2000b; Baz and Tempia, 2004), Active Constrained layer damping (ACLD) (Baz and Ro, 1995; Shi et al., 2004), etc. Among these hybrid damping treatments, the ACLD treatment has gained its credential to become the most efficient means of exploiting the piezoelectric materials for achieving active control of thin-walled structures. Extensive research on the ACLD treatment of structural vibration has been reported in the literature. But, all these studies have been carried out by taking the extension mode piezoelectric actuators. Since no report on the use of shear mode piezoelectric actuator in the ACLD treatment is available in the literature, one more objective of this research is chosen as the performance of the presently designed shear mode PFC actuator in the ACLD treatment of vibration of annular plates.

In order to fulfill the aforesaid objectives in this research, the following theoretical studies have been carried out:

(a) Design of an extension mode short piezoelectric fiber composite actuator in cylindrical/rectangular coordinates.

(b) Control capability of an extension mode short piezoelectric fiber composite (SPFC) actuator in cylindrical/rectangular coordinates.

(c) A comparative study on the smart damping-capabilities of cylindrically orthotropic piezoelectric fiber composite actuators in vibration control of annular plates.

(d) An annular PFC actuator for shear mode piezoelectric actuation of plane structures of revolution.

(e) Active control of vibration of annular plates using a new shear mode PFC actuator with cylindrically periodic microstructure.

(f) Active-passive damping characteristics of a smart annular sandwich plate using a new shear mode PFC actuator.

1.7 Contributions

The following contributions in the field of smart structures have been made towards the preparation of the dissertation.

1. A new cylindrically orthotropic unidirectional short/continuous piezoelectric fiber composite (SPFC/CPFC) actuator is designed for active control of plane structures of revolution.

2. A short piezoelectric fiber composite (SPFC) actuator is designed in the rectangular coordinates, and its electromechanical behaviour is compared with the conventional continuous piezoelectric fiber composite (CPFC).

3. A microstructure-based arrangement of surface electrodes is proposed for effective utilization of the SPFC as a material of distributed actuator.

4. The control capability of the new SPFC actuator in rectangular coordinates is investigated by developing a geometrically nonlinear semi-analytical model of a simply-supported smart beam.

5. The performance of the cylindrically orthotropic SPFC/CPFC actuator in control of forced harmonic vibration of an annular plate is investigated by developing a three dimensional FE model of the smart annular plate.

6. Four kinds of cylindrically orthotropic PFC actuators are addressed for active control of vibration of plane structures of revolution, and a comparative study on their actuation-capabilities is performed.

7. A novel numerical methodology is proposed for optimal size and locations of the patches of cylindrically orthotropic extension mode PFC actuator over the surface of an annular plate.

8. A new annular PFC actuator is designed in cylindrical coordinates for shear mode piezoelectric actuation of plane structures of revolution.

9. An FE procedure is developed for numerical homogenization of the shear mode PFC actuator in cylindrical coordinates. In parallel, the closed-form expressions for the effective coefficients are also derived.

10. A fruitful strategy in configuring the smart annular plate embedded with the patches of the shear mode PFC actuator is proposed for achieving efficient control of all the modes of vibration of the smart plate.

11. The performance of shear mode annular monolithic/PFC actuator in the ACLD treatment of vibration of an annular plate is studied by developing a three dimensional FE model.

1.8 Organization of the thesis

A brief introduction and a review of the literature on the smart structures are presented in Chapter 1. The review of the literature on the design and utilization of various PFCs in the smart structures are also presented within the same chapter (Chapter 1). The literature on the development of ACLD treatment of structural vibration is also provided. Consequently, the scope and objectives of the present research are outlined.

Chapter 2 deals with the design of SPFC actuators in cylindrical and rectangular coordinates. The effective electromechanical properties of these new PFCs are estimated by developing an FE procedure. For effective use of these PFCs as the materials of distributed actuators, a special arrangement of surface-electrodes is also presented.

A nonlinear electro-elastic bending analysis of a simply-supported beam integrated with a layer of SPFC actuator is presented in Chapter 3 for investigating the actuation capability of the SPFC actuator in rectangular coordinates. A flexural vibration analysis of a simply-supported annular plate integrated with the patches of SPFC actuator in cylindrical coordinates is also carried out in the same chapter for investigating its (SPFC actuator) actuation capability.

In Chapter 4, four kinds of cylindrically orthotropic PFC actuators are addressed, and a comparative study on their control capabilities in control of vibration of a simply-supported/clamped annular plate is carried out to address the most effective one. For every kind of PFC actuator, first its patches are optimally configured over the plate-surface through the proposition of a new numerical strategy, and then its (PFC) actuation capability is evaluated for the comparative study.

A new shear mode PFC actuator in cylindrical coordinates is designed in Chapter 5. The varying effective electro-elastic coefficients of this new shear mode PFC actuator are first estimated by deriving the corresponding closed-form expressions, and then the same effective coefficients are evaluated numerically by developing an FE procedure.

The actuation capability of the new shear mode PFC actuator (designed in Chapter 5) is investigated in Chapter 6 through the flexural vibration analysis of an annular sandwich plate. The core of the sandwich plate is comprised of the patches of the shear mode PFC actuator embedded within the foam. A strategy for the distribution of the shear mode actuator-patches over the annular plane of the plate is presented for effective control of all the bending modes of vibration of the annular sandwich plate. A fruitful strategy for activation of the shear mode PFC actuator according to the velocity feedback control law is also proposed in this chapter for using all the patches effectively.

Chapter 7 is an extension of Chapter 6 where the effectiveness of ACLD treatment in control of vibration of the annular sandwich plate is investigated for the use of shear mode PFC actuator (designed in Chapter 5).

Finally, the important conclusions from work carried out, and the future scope of the present thesis work are outlined in Chapter 8. The list of references is provided at the end of the thesis.

CHAPTER
2
Design of a short piezoelectric fiber composite actuator in cylindrical/rectangular coordinates

2.1 Introduction

The literature review in the previous chapter (Chapter 1) shows different kinds of PFCs. All these PFCs are substantially employed in control of vibration of various structures like beams, plates, shells, airfoils, etc. (Azzouz et al., 2001; Bent, 1999; Bilgen et al., 2010; Choi et al., 2006; Kovalovs et al., 2007; Park et al., 2008; Ray and Reddy, 2004b; Sodano et al., 2004; Sohn et al., 2006). Similar to these structural elements, the plane structures of revolution like annular/circular plates are also equally important structural elements for their wide applications in different engineering systems like micro-valves, micropumps, micro-switches, implantable medical devices, oil storage tanks, brake systems of vehicles, airfoil cascades, oceanographic applications, etc. (Bambill et al., 2004; Buffum and Fleeter, 1986; Cao et al., 2001; Cha et al., 2015; Kim and Ha, 2003; Sergienko et al., 2008; Shi et al., 2017). For controlling bending modes of vibration of such thin-walled plane structures of revolution, any of the existing PFCs may be utilized. But, it may not be an effective use of the existing PFCs. Because, the microstructure of a PFC is based on a specific coordinate system, and also it (microstructure) is for controlling a specific mode of deformation of the host structure. Since none of the available PFCs is specially designed for controlling the flexural vibration of plane structures of revolution, a cylindrically orthotropic short/continuous piezoelectric fiber composite (SPFC/CPFC) is designed in this chapter, and its electromechanical behavior is estimated theoretically (Kumar et al., 2015; Panda et al., 2015). The longitudinally poled short/continuous piezoelectric fibers in the SPFC/CPFC are oriented along the radial direction within the reference cylindrical coordinate system so as to achieve the improved magnitude of an effective piezoelectric coefficient (e_{11}, 1 for radial direction). First, the geometrical features of the SPFC/CPFC actuator are presented, and the effective electro-elastic properties of the cylindrically orthotropic SPFC/CPFC are estimated by developing an FE procedure. Next, the present FE procedure for estimation of effective electro-elastic properties is verified, and an analysis of effective properties is performed in order to determine the geometrical dimensions of the corresponding representative volume element (RVE) with an objective of the improved magnitude of the major effective piezoelectric coefficient (e_{11}). For effective utilization of the SPFC/CPFC as a material of distributed actuator, an arrangement of surface-electrodes over the top and bottom surfaces of the smart composite lamina is also presented. It may be noted here that the design of a similar SPFC in rectangular coordinates is not yet reported in the literature. So, the constructional features as well as the effective properties of SPFC/CPFC in rectangular coordinates are also presented in parallel to those of the PFCs in cylindrical coordinates.

2.2 Constructional features of SPFC

Figure 2.1 shows a schematic diagram of the present cylindrically orthotropic unidirectional short piezoelectric fiber composite (SPFC). The short piezoelectric fibers have an identical dimension along every axial direction (r,θ,z) in the reference cylindrical coordinate system. Also, the fibers are equally spaced along any of the axial directions (r,θ,z). The fiber and matrix phases are made of monolithic piezoelectric ceramic and epoxy, respectively. The poling direction of the piezoelectric fibers is taken as the radial direction, and the fibers are assumed to be perfectly bonded with the matrix phase.

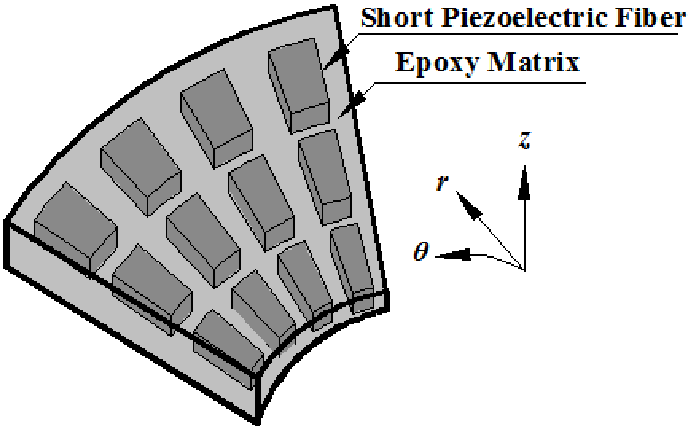

Fig. 2.1 Schematic diagram of short piezoelectric fiber composite (SPFC) in cylindrical coordinates.

For estimation of the effective electro-elastic properties of the SPFC, an RVE is defined as shown in Fig. 2.2. The short piezoelectric fiber is centrally located within the volume of the RVE. The inner/outer radius of the RVE and the corresponding short fiber are denoted by, r_i^c / r_o^c and r_i^f / r_o^f, respectively. So, the symbols l_c and

l_f in Fig. 2.2 stand for the radial lengths of the RVE and the corresponding fiber, respectively. The circumferential span of the RVE/fiber is designated by, θ_c / θ_f, while the thickness of the same is symbolized by, h_c / h_f. The volume fractions of fiber and matrix phases within the volume of RVE are represented by the symbols, v_f and v_m, respectively. Because of the short fiber, the fiber-volume fraction (FVF) can be expressed as, $v_f = (A_r \times L_r)$ $(L_r = l_f / l_c, A_r = \langle \theta_f h_f \rangle / \langle \theta_c h_c \rangle)$. The parameter ($A_r$) is basically the cross-sectional area-ratio (A_f / A_c) between the fiber and the RVE at any radius (r), while the parameter (L_r) signifies the ratio of their radial lengths. The dimensions of the RVE and the corresponding fiber in the θz-plane at any radius are considered to be related by, $(h_f / h_c) = (\theta_f / \theta_c)$. Thus, the area-ratio ($A_r$) may be expressed either by $(\theta_f / \theta_c)^2$ or by $(h_f / h_c)^2$. Alternatively, the dimensions (h_f, θ_f) of the fiber may be expressed in terms of the similar dimensions (h_c, θ_c) of the RVE as, $h_f = h_c \sqrt{A_r}$ and $\theta_f = \theta_c \sqrt{A_r}$.

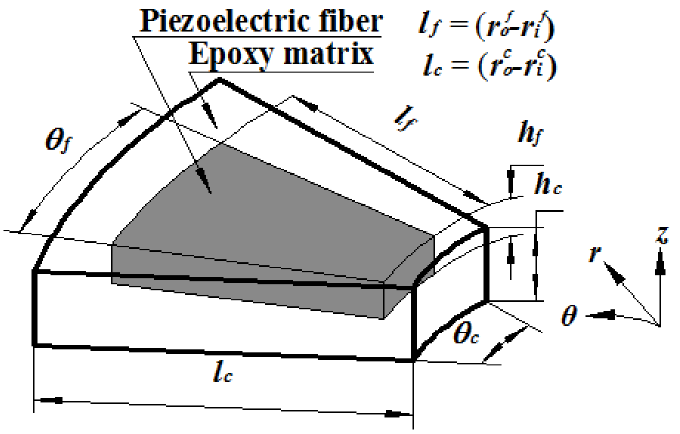

Fig. 2.2 Schematic diagram of RVE of the SPFC in cylindrical coordinates.

According to the aforesaid geometric relations, the dimensions of the RVE can be specified by, L_r, A_r, h_c, θ_c and l_c. A side of the boundary surface of the RVE is denoted by its normal outward direction. So, the six sides of the boundary surface of the RVE are denoted by, $-r$, $+r$, $-\theta$, $+\theta$, $-z$ and $+z$ surfaces. Similar to Fig. 2.1, an SPFC in rectangular coordinates is presented in Fig. 2.3, and the corresponding RVE is shown in Fig. 2.4. The short fiber is centrally located within the volume of the RVE. The length, width and thickness of the RVE

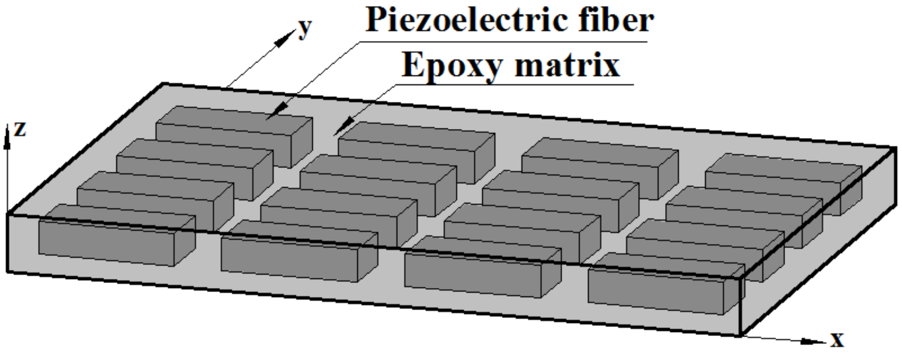

Fig. 2.3 Schematic diagram of a short piezoelectric fiber composite (SPFC) in rectangular coordinates.

(Fig. 2.4) are denoted as, l_c, a_c and b_c, respectively. The same dimensions of the corresponding fiber are symbolized as, l_f, a_f and b_f. The cross-sectional areas of the RVE and the corresponding fiber are denoted by, A_c and A_f, respectively. The six sides of the boundary surface of the RVE are denoted by, $+X$, $-X$, $+Y$, $-Y$, $+Z$ and $-Z$ surfaces.

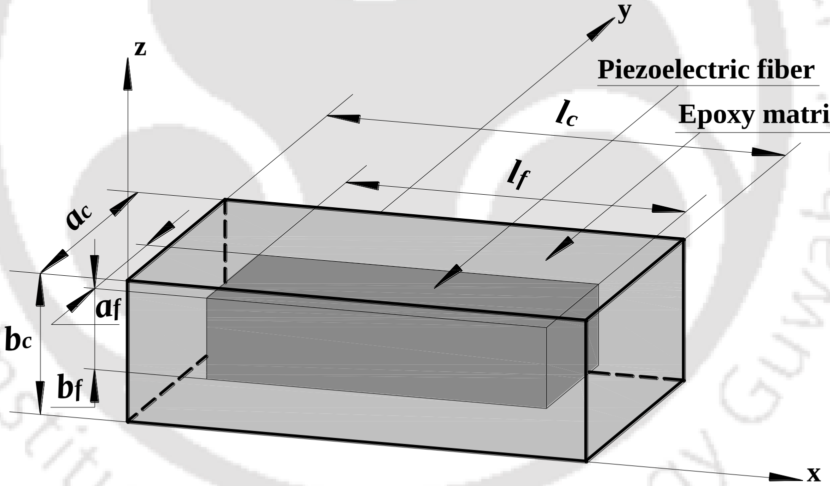

Fig. 2.4 Schematic diagram of RVE of the SPFC in rectangular coordinates.

Although the constructional features of present SPFCs are demonstrated in Figs. 2.1 and 2.3, the same may easily be converted into CPFCs in the respective coordinates through the consideration of continuous fibers instead of the short/discontinuous fibers.

2.3 Effective electro-elastic properties of the smart composite

In the theory of linear piezoelectricity at room temperature, the coupled interaction between the electric and elastic fields is described by four different piezoelectric constitutive formulations (Eq. (1.1)). Among these four different constitutive formulations, the piezoelectric stress formulation is commonly employed when the strain and electric fields are considered as the natural variables. According to this constitutive formulation, the natural variables (strain and electric fields) are related to the stress and electric displacement fields by,

$$\sigma_{ij} = C_{ijkl}\varepsilon_{kl} - e_{sij}E_s \ , \ D_i = e_{ikl}\varepsilon_{kl} + \in_{is} E_s \tag{2.1}$$

where, $i, j, k, l, s = 1,2,3$; C_{ijkl}, e_{sij} and $\in_{is}$ denote the elements of stiffness, piezoelectric and permittivity tensors, respectively; σ_{ij}, ε_{kl}, D_i and E_s are the elements of stress, strain, electric displacement and electric field tensors, respectively. In Eq. (2.1), the mathematical objects are symmetric in i and j, and also in k and l. So, using Voigt notation, ij/kl for $i, j, k, l = 1,2,3$ can be represented as, $11 \to 1$, $22 \to 2$, $33 \to 3$, $23/32 \to 4$, $13/31 \to 5$ and $12/21 \to 6$. Using this notation, Eq. (2.1) can be rewritten as,

$$\sigma_{\xi} = C_{\xi\eta}\varepsilon_{\eta} - e_{\ell\xi}E_{\ell} \ , \ D_{\ell} = e_{\ell\eta}\varepsilon_{\eta} + \in_{\ell\zeta} E_{\zeta} \tag{2.2}$$

where, $\xi, \eta = 1,2,3,4,5,6$ and $\ell, \zeta = 1,2,3$. In Eq. (2.2), the elements of stiffness, piezoelectric and permittivity matrices are defined by (Cady, 1946; Furukawa, 1989),

$$C_{\xi\eta} = \left(\frac{\partial\sigma_{\xi}}{\partial\varepsilon_{\eta}}\right)^{\boldsymbol{E}} , \ e_{\ell\xi} = -\left(\frac{\partial\sigma_{\xi}}{\partial E_{\ell}}\right)^{\boldsymbol{\varepsilon}} \text{ or } e_{\ell\eta} = \left(\frac{\partial D_{\ell}}{\partial\varepsilon_{\eta}}\right)^{\boldsymbol{E}} , \ \in_{\ell\zeta} = \left(\frac{\partial D_{\ell}}{\partial E_{\zeta}}\right)^{\boldsymbol{\varepsilon}} \tag{2.3}$$

The superscript $\boldsymbol{E}$ (Eq. (2.3)) indicates zero or constant electric field and the superscript $\boldsymbol{\varepsilon}$ (Eq. (2.3)) indicates zero or constant strain field. The constitutive relations and material constants in Eqs. (2.2) and (2.3), respectively are given for a homogeneous piezoelectric solid. Analogous to this homogeneous piezoelectric solid, the present piezoelectric composite is considered to be a macroscopically homogeneous piezoelectric solid, and its macroscopic behavior can be defined by the effective constitutive relations according to standard micromechanical theories for composites. These effective constitutive relations are valid only for specially statistically homogeneous fields within the composite, which (fields) can be produced within a heterogeneous body through the imposition of homogeneous boundary conditions over the boundary surfaces of the body (Hasin, 1965; Hasin, 1970). Making use of this analogy, the effective material properties of asymptotically homogeneous composites can be estimated through the application of volume-average strain field and/or electric field by means of the homogeneous kinematic boundary conditions (displacement and/or electric potential) (Aboudi et al., 2013). Following the same, presently the effective material constants of the piezoelectric composite are estimated by applying volume-average strain field and/or electric field over the volume of RVE. The volume-average field quantities over a volume (V_d) are defined by,

$$\bar{\sigma}_\xi = \frac{1}{V_d}\int_{V_d} \sigma_\xi dV_d \ , \ \bar{\varepsilon}_\eta = \frac{1}{V_d}\int_{V_d} \varepsilon_\eta dV_d \ ,$$

$$\bar{E}_\ell = \frac{1}{V_d}\int_{V_d} E_\ell dV_d \ , \ \bar{D}_\zeta = \frac{1}{V}\int_{V} D_\zeta dV \qquad (2.4)$$

where, the over-bar signifies volume-average quantity. The constitutive relations for fiber (f) and matrix (m) phases within the RVE can be written in terms of the volume-average field quantities as,

$$\bar{\sigma}^f_\xi = C^f_{\xi\eta}\bar{\varepsilon}^f_\eta - e^f_{\ell\xi}\bar{E}^f_\ell \qquad (2.5)$$

$$\bar{\sigma}^m_\xi = C^m_{\xi\eta}\bar{\varepsilon}^m_\eta \qquad (2.6)$$

$$\bar{D}^f_\ell = e^f_{\ell\eta}\bar{\varepsilon}^f_\eta + \in^f_{\ell\zeta} \bar{E}^f_\zeta \qquad (2.7)$$

$$\bar{D}^m_\ell = \in^m_{\ell\zeta} \bar{E}^m_\zeta \qquad (2.8)$$

The volume-average field quantities of the RVE can be expressed in terms of the similar quantities of constituents according to the rule of mixtures as,

$$\bar{\sigma}_\xi = (v_f\bar{\sigma}^f_\xi + v_m\bar{\sigma}^m_\xi) \qquad (2.9)$$

$$\bar{D}_\ell = (v_f\bar{D}^f_\ell + v_m\bar{D}^m_\ell) \qquad (2.10)$$

$$\bar{\varepsilon}_\eta = (v_f\bar{\varepsilon}^f_\eta + v_m\bar{\varepsilon}^m_\eta) \qquad (2.11)$$

$$\bar{E}_\zeta = (v_f\bar{E}^f_\zeta + v_m\bar{E}^m_\zeta) \qquad (2.12)$$

Substituting Eqs. (2.5)-(2.6) in Eq. (2.9), and then using Eq. (2.11), the following expression can be obtained,

$$\bar{\sigma}_\xi = C^m_{\xi\alpha}\bar{\varepsilon}_\alpha + v_f(C^f_{\xi\alpha} - C^m_{\xi\alpha})\bar{\varepsilon}^f_\alpha - v_f e^f_{\ell\xi}\bar{E}^f_\ell \qquad (2.13)$$

where, $\alpha = 1,2,3,4,5,6$. Similarly, substituting Eqs. (2.7)-(2.8) in Eq. (2.10), and then using Eq. (2.12), the following expression can be obtained,

$$\bar{D}_\ell = \in^m_{\ell\beta} \bar{E}_\beta + v_f(\in^f_{\ell\beta} - \in^m_{\ell\beta})\bar{E}^f_\beta + v_f e^f_{\ell\eta}\bar{\varepsilon}^f_\eta \tag{2.14}$$

where, $\beta = 1,2,3$. According to the definitions of piezoelectric constants (Eq. (2.3)), the expressions for the effective electro-elastic coefficients of the piezoelectric composite can be obtained as,

$$\bar{C}_{\xi\eta} = C^m_{\xi\eta} + v_f(C^f_{\xi\alpha} - C^m_{\xi\alpha})\left(\frac{\partial\bar{\varepsilon}^f_\alpha}{\partial\bar{\varepsilon}_\eta}\right) - v_f e^f_{\zeta\xi}\left(\frac{\partial \bar{E}^f_\zeta}{\partial\bar{\varepsilon}_\eta}\right) \quad \text{for } \bar{E}_\zeta = 0 \tag{2.15}$$

$$\bar{e}_{\ell\eta} = v_f(\in^f_{\ell\beta} - \in^m_{\ell\beta})\left(\frac{\partial\bar{E}^f_\beta}{\partial\bar{\varepsilon}_\eta}\right) + v_f e^f_{\ell\xi}\left(\frac{\partial\bar{\varepsilon}^f_\xi}{\partial\bar{\varepsilon}_\eta}\right) \quad \text{for } \bar{E}_\zeta = 0 \tag{2.16}$$

$$\bar{\in}_{\ell\zeta} = \in^m_{\ell\zeta} + v_f(\in^f_{\ell\beta} - \in^m_{\ell\beta})\left(\frac{\partial \bar{E}^f_\beta}{\partial \bar{E}_\zeta}\right) + v_f e^f_{\ell\eta}\left(\frac{\partial\bar{\varepsilon}^f_\eta}{\partial\bar{E}_\zeta}\right) \quad \text{for } \bar{\varepsilon}_\eta = 0 \tag{2.17}$$

According to Eqs. (2.15)-(2.17), the effective electro-elastic constants of the composite can be determined by computation of the volume-average field quantities for RVE and fiber phase, and it is presently performed through the imposition of volume-average strain and electric fields over the volume of the RVE by means of applying homogeneous displacement and electric potential boundary conditions. For this computation, an electro-elastic analysis of the RVE is to be carried out, and that is presently done using FE procedure. It may be noted here that the effective properties of the smart composite can be estimated using the standard micromechanics theories like Mori-Tanaka method, Self-consistent method, etc. The same can also be estimated numerically using FE procedure. The FE procedure is very time consuming and expensive procedure. But, it may provide more realistic results in the prediction of electro-elastic constants of piezoelectric composites (Odegard, 2004). So, the FE procedure is utilized at present through the derivation of a three-dimensional FE model of the RVE as presented in the next section. The solutions from FE model of RVE for the applied homogeneous kinematic boundary conditions yield the volume-average field quantities according to the following expressions,

$$\bar{\varepsilon}_\eta = \frac{1}{V_d}\left(\sum_{i=1}^{N_{V_d}} \int_{V_d^i} \varepsilon^i_\eta dV^i_d\right), \quad \bar{E}_\zeta = \frac{1}{V_d}\left(\sum_{i=1}^{N_{V_d}} \int_{V_d^i} E^i_\zeta dV^i_d\right) \tag{2.18}$$

where, N_{V_d} is the number of elements within a volume V_d (RVE/fiber phase/matrix phase); $\varepsilon_\eta^i / E_\zeta^i$ is a component of strain/electric field vector within i^{th} element having the elemental volume of V_d^i. In order to determine the effective coefficients of the composite/RVE, nine sets of homogeneous kinematic boundary conditions are presently applied over the boundary surface of the RVE. The RVE is initially considered as a stress/strain/electric field free solid, and then every set of boundary conditions over its boundary surfaces are applied separately. Every set of boundary conditions yields only one nonzero element of strain ($\bar{\varepsilon}_\eta$ at $\bar{E}_\zeta = 0$) or electric ($\bar{E}_\zeta$ at $\bar{\varepsilon}_\eta = 0$) field vector. Corresponding to this nonzero element (say, $\left\langle \bar{\varepsilon}_\eta = \bar{\varepsilon}_1 \text{ for } \eta = 1;\ \bar{\varepsilon}_\eta = 0 \text{ for } \eta = 2,3,\ldots 6;\ \bar{E}_\zeta = 0 \right\rangle$ or $\left\langle \bar{E}_\zeta = \bar{E}_1 \text{ for } \zeta = 1;\ \bar{E}_\zeta = 0 \text{ for } \zeta = 2,3;\ \bar{\varepsilon}_\eta = 0 \right\rangle$), the derivatives in Eqs. (2.15)-(2.17) can be written as,

$$\frac{\partial \bar{\varepsilon}_\alpha^f}{\partial \bar{\varepsilon}_1} = \frac{\bar{\varepsilon}_\alpha^f}{\bar{\varepsilon}_1} \quad \text{for } \bar{E}_\zeta = 0 \tag{2.19}$$

$$\frac{\partial \bar{E}_\zeta^f}{\partial \bar{\varepsilon}_1} = \frac{\bar{E}_\zeta^f}{\bar{\varepsilon}_1} \quad \text{for } \bar{E}_\zeta = 0 \tag{2.20}$$

$$\frac{\partial \bar{\varepsilon}_\eta^f}{\partial \bar{E}_1} = \frac{\bar{\varepsilon}_\eta^f}{\bar{E}_1} \quad \text{for } \bar{\varepsilon}_\eta = 0 \tag{2.21}$$

$$\frac{\partial \bar{E}_\ell^f}{\partial \bar{E}_1} = \frac{\bar{E}_\ell^f}{\bar{E}_1} \quad \text{for } \bar{\varepsilon}_\eta = 0 \tag{2.22}$$

Introducing these terms in Eqs. (2.15)-(2.17), the effective coefficients, $\bar{C}_{\xi 1}$, $\bar{e}_{\ell 1}$ and $\bar{\in}_{\ell 1}$ can be obtained in terms of the volume-average field quantities over the RVE and the fiber phase. A similar computation can be performed for all the sets of boundary conditions in order to obtain all the effective coefficients of the composite/RVE. The nine sets of kinematic boundary conditions are illustrated in the following points, where the displacements at any point along r, θ and z directions in the cylindrical coordinate system (or x, y and z directions in the rectangular coordinate system) are denoted by u, v and w, respectively. The electric potential at any point within the volume of the RVE is denoted by ϕ.

(a) Effective constants ($\bar{C}_{\xi 1}$, $\bar{e}_{\ell 1}$):

Boundary conditions for RVE in cylindrical coordinates:

$u|_{-r} = 0$, $u|_{+r} = (\varepsilon_1^0 \times l_c)$, $v|_{\pm\theta} = 0$, $w|_{\pm z} = 0$, $\phi|_{\pm r, \pm\theta, \pm z} = 0$.

Boundary conditions for RVE in rectangular coordinates:

$u|_{-X} = 0$, $u|_{+X} = (\varepsilon_1^0 \times l_c)$, $v|_{-Y} = 0$, $v|_{+Y} = 0$, $w|_{-Z} = 0$, $w|_{+Z} = 0$, $\phi|_{\pm X, \pm Y, \pm Z} = 0$.

Elements ($\bar{\varepsilon}_\eta$, $\bar{E}_\zeta$): $\bar{\varepsilon}_1 \approx \varepsilon_1^0$; $\bar{\varepsilon}_\eta = 0$ for $\eta =$ 2,3,4,5,6; $\bar{E}_\zeta = 0$.

Effective material constants:

$$\bar{C}_{\xi 1} = C^m_{\xi 1} + v_f (C^f_{\xi\alpha} - C^m_{\xi\alpha}) \left(\frac{\bar{\varepsilon}^f_\alpha}{\varepsilon^0_1} \right) - v_f e^f_{\zeta\xi} \left(\frac{\bar{E}^f_\zeta}{\varepsilon^0_1} \right)$$

$$\bar{e}_{\ell 1} = v_f (\in^f_{\ell\beta} - \in^m_{\ell\beta}) \left(\frac{\bar{E}^f_\beta}{\varepsilon^0_1} \right) + v_f e^f_{\ell\xi} \left(\frac{\bar{\varepsilon}^f_\xi}{\varepsilon^0_1} \right) \tag{2.23}$$

(b) Effective constants ($\bar{C}_{\xi 2}$, $\bar{e}_{\ell 2}$):

Boundary conditions for RVE in cylindrical coordinates:

$u|_{\pm r} = 0$, $v|_{-\theta} = 0$, $v|_{+\theta} = (\varepsilon_2^0 \times \theta_c)$, $w|_{\pm z} = 0$, $\phi|_{\pm r, \pm\theta, \pm z} = 0$.

Boundary conditions for RVE in rectangular coordinates:

$u|_{-X} = 0$, $u|_{+X} = 0$, $v|_{-Y} = 0$, $v|_{+Y} = (\varepsilon_2^0 \times a_c)$, $w|_{-Z} = 0$, $w|_{+Z} = 0$, $\phi|_{\pm X, \pm Y, \pm Z} = 0$.

Elements ($\bar{\varepsilon}_\eta$, $\bar{E}_\zeta$): $\bar{\varepsilon}_2 \approx \varepsilon_2^0$; $\bar{\varepsilon}_\eta = 0$ for $\eta =$ 1,3,4,5,6 ; $\bar{E}_\zeta = 0$.

Effective material constants:

$$\bar{C}_{\xi 2} = C^m_{\xi 2} + v_f (C^f_{\xi\alpha} - C^m_{\xi\alpha}) \left(\frac{\bar{\varepsilon}^f_\alpha}{\varepsilon^0_2} \right) - v_f e^f_{\zeta\xi} \left(\frac{\bar{E}^f_\zeta}{\varepsilon^0_2} \right)$$

$$\bar{e}_{\ell 2} = v_f (\in^f_{\ell\beta} - \in^m_{\ell\beta}) \left(\frac{\bar{E}^f_\beta}{\varepsilon^0_2} \right) + v_f e^f_{\ell\xi} \left(\frac{\bar{\varepsilon}^f_\xi}{\varepsilon^0_2} \right) \tag{2.24}$$

(c) Effective constants ($\bar{C}_{\xi 3}$, $\bar{e}_{\ell 3}$):

Boundary conditions for RVE in cylindrical coordinates:

$u|_{\pm r} = 0$, $v|_{\pm\theta} = 0$, $w|_{-z} = 0$, $w|_{+z} = (\varepsilon_3^0 \times h_c)$, $\phi|_{\pm r, \pm\theta, \pm z} = 0$.

Boundary conditions for RVE in rectangular coordinates:

$u|_{-X}=0,\ u|_{+X}=0,\ v|_{-Y}=0,\ v|_{+Y}=0,\ w|_{-Z}=0,\ w|_{+Z}=(\varepsilon_3^0\times b_c),\ \phi|_{\pm X,\pm Y,\pm Z}=0$

Elements ($\bar{\varepsilon}_\eta$, $\bar{E}_\zeta$): $\bar{\varepsilon}_3\approx\varepsilon_3^0$; $\bar{\varepsilon}_\eta=0$ for $\eta=$ 1,2,4,5,6; $\bar{E}_\zeta=0$.

Effective material constants:

$$\bar{C}_{\xi 3}=C_{\xi 3}^m+v_f(C_{\xi\alpha}^f-C_{\xi\alpha}^m)\left(\frac{\bar{\varepsilon}_\alpha^f}{\varepsilon_3^0}\right)-v_f e_{\zeta\xi}^f\left(\frac{\bar{E}_\zeta^f}{\varepsilon_3^0}\right)$$

$$\bar{e}_{\ell 3}=v_f(\in_{\ell\beta}^f-\in_{\ell\beta}^m)\left(\frac{\bar{E}_\beta^f}{\varepsilon_3^0}\right)+v_f e_{\ell\xi}^f\left(\frac{\bar{\varepsilon}_\xi^f}{\varepsilon_3^0}\right) \tag{2.25}$$

(d) Effective constants ($\bar{C}_{\xi 4}$, $\bar{e}_{\ell 4}$):

Boundary conditions for RVE in cylindrical coordinates:

$v|_{-z}=0,\ v|_{+z}=(\tfrac{1}{2}\varepsilon_4^0\times h_c),\ w|_{-\theta}=0,\ w|_{+\theta}=(\tfrac{1}{2}\varepsilon_4^0\times\theta_c),\phi|_{\pm r,\pm\theta,\pm z}=0.$

Boundary conditions for RVE in rectangular coordinates:

$v|_{-Z}=0, v|_{+Z}=(\tfrac{1}{2}\varepsilon_4^0\times b_c)$, $w|_{-Y}=0,\ w|_{+Y}=(\tfrac{1}{2}\varepsilon_4^0\times a_c),\ \phi|_{\pm X,\pm Y,\pm Z}=0.$

Elements ($\bar{\varepsilon}_\eta$, $\bar{E}_\zeta$): $\bar{\varepsilon}_4\approx\varepsilon_4^0$; $\bar{\varepsilon}_\eta=0$ for $\eta=$ 1,2,3,5,6; $\bar{E}_\zeta=0$.

Effective material constants:

$$\bar{C}_{\xi 4}=C_{\xi 4}^m+v_f(C_{\xi\alpha}^f-C_{\xi\alpha}^m)\left(\frac{\bar{\varepsilon}_\alpha^f}{\varepsilon_4^0}\right)-v_f e_{\zeta\xi}^f\left(\frac{\bar{E}_\zeta^f}{\varepsilon_4^0}\right)$$

$$\bar{e}_{\ell 4}=v_f(\in_{\ell\beta}^f-\in_{\ell\beta}^m)\left(\frac{\bar{E}_\beta^f}{\varepsilon_4^0}\right)+v_f e_{\ell\xi}^f\left(\frac{\bar{\varepsilon}_\xi^f}{\varepsilon_4^0}\right) \tag{2.26}$$

(e) Effective constants ($\bar{C}_{\xi 5}$, $\bar{e}_{\ell 5}$):

Boundary conditions for RVE in cylindrical coordinates:

$u|_{-z}=0,\ u|_{+z}=(\tfrac{1}{2}\varepsilon_5^0\times h_c),\ w|_{-r}=0,\ w|_{+r}=(\tfrac{1}{2}\varepsilon_5^0\times l_c),\phi|_{\pm r,\pm\theta,\pm z}=0.$

Boundary conditions for RVE in rectangular coordinates:

$u|_{-Z}=0,\ u|_{+Z}=(\tfrac{1}{2}\varepsilon_5^0\times b_c),\ w|_{-X}=0,\ w|_{+X}=(\tfrac{1}{2}\varepsilon_5^0\times l_c),\ \phi|_{\pm X,\pm Y,\pm Z}=0.$

Elements ($\bar{\varepsilon}_\eta$, $\bar{E}_\zeta$): $\bar{\varepsilon}_5\approx\varepsilon_5^0$; $\bar{\varepsilon}_\eta=0$ for $\eta=$ 1,2,3,4,6; $\bar{E}_\zeta=0$.

Effective material constants:

$$\bar{C}_{\xi 5} = C^{m}_{\xi 5} + v_f \left(C^{f}_{\xi\alpha} - C^{m}_{\xi\alpha}\right)\left(\frac{\bar{\varepsilon}^{f}_{\alpha}}{\varepsilon^{0}_{5}}\right) - v_f e^{f}_{\zeta\xi}\left(\frac{\bar{E}^{f}_{\zeta}}{\varepsilon^{0}_{5}}\right)$$

$$\bar{e}_{\ell 5} = v_f \left(\in^{f}_{\ell\beta} - \in^{m}_{\ell\beta}\right)\left(\frac{\bar{E}^{f}_{\beta}}{\varepsilon^{0}_{5}}\right) + v_f e^{f}_{\ell\xi}\left(\frac{\bar{\varepsilon}^{f}_{\xi}}{\varepsilon^{0}_{5}}\right) \qquad (2.27)$$

(f) Effective constants ($\bar{C}_{\xi 6}$, $\bar{e}_{\ell 6}$):

Boundary conditions for RVE in cylindrical coordinates:

$u|_{-\theta} = 0$, $u|_{+\theta} = (\tfrac{1}{2}\varepsilon^{0}_{6} \times \theta_c)$, $v|_{-r} = 0$, $v|_{+r} = (\tfrac{1}{2}\varepsilon^{0}_{6} \times l_c)$, $\phi|_{\pm r, \pm\theta, \pm z} = 0$.

Boundary conditions for RVE in rectangular coordinates:

$u|_{-Y} = 0$, $u|_{+Y} = (\tfrac{1}{2}\varepsilon^{0}_{6} \times a_c)$, $v|_{-X} = 0$, $v|_{+X} = (\tfrac{1}{2}\varepsilon^{0}_{6} \times l_c)$, $\phi|_{\pm X, \pm Y, \pm Z} = 0$.

Elements ($\bar{\varepsilon}_{\eta}$, $\bar{E}_{\zeta}$): $\bar{\varepsilon}_{6} \approx \varepsilon^{0}_{6}$; $\bar{\varepsilon}_{\eta} = 0$ for $\eta =$ 1,2,3,4,5; $\bar{E}_{\zeta} = 0$.

Effective material constants:

$$\bar{C}_{\xi 6} = C^{m}_{\xi 6} + v_f \left(C^{f}_{\xi\alpha} - C^{m}_{\xi\alpha}\right)\left(\frac{\bar{\varepsilon}^{f}_{\alpha}}{\varepsilon^{0}_{6}}\right) - v_f e^{f}_{\zeta\xi}\left(\frac{\bar{E}^{f}_{\zeta}}{\varepsilon^{0}_{6}}\right)$$

$$\bar{e}_{\ell 6} = v_f \left(\in^{f}_{\ell\beta} - \in^{m}_{\ell\beta}\right)\left(\frac{\bar{E}^{f}_{\beta}}{\varepsilon^{0}_{6}}\right) + v_f e^{f}_{\ell\xi}\left(\frac{\bar{\varepsilon}^{f}_{\xi}}{\varepsilon^{0}_{6}}\right) \qquad (2.28)$$

(g) Effective constant ($\bar{\in}_{\ell 1}$):

Boundary conditions for RVE in cylindrical coordinates:

$\phi|_{\pm z} = 0$, $\phi|_{\pm\theta} = 0$, $\phi|_{-r} = 0$, $\phi|_{+r} = -(E^{0}_{1} \times l_c)$, $u|_{\pm r} = 0$, $v|_{\pm\theta} = 0$, $w|_{\pm z} = 0$.

Boundary conditions for RVE in rectangular coordinates:

$\phi|_{\pm Z} = 0$, $\phi|_{\pm Y} = 0$, $\phi|_{-R} = 0$, $\phi|_{+R} = -(E^{0}_{1} \times l_c)$, $u|_{\pm X} = 0$, $v|_{\pm Y} = 0$, $w|_{\pm Z} = 0$.

Elements ($\bar{\varepsilon}_{\eta}$, $\bar{E}_{\zeta}$): $\bar{E}_{1} \approx E^{0}_{1}$; $\bar{E}_{\zeta} = 0$ for $\zeta =$ 2,3; $\bar{\varepsilon}_{\eta} = 0$.

Effective material constants:

$$\bar{\in}_{\ell 1} = \in^{m}_{\ell 1} + v_f \left(\in^{f}_{\ell\beta} - \in^{m}_{\ell\beta}\right)\left(\frac{\bar{E}^{f}_{\beta}}{E^{0}_{1}}\right) + v_f e^{f}_{\ell\eta}\left(\frac{\bar{\varepsilon}^{f}_{\eta}}{E^{0}_{1}}\right) \qquad (2.29)$$

(h) Effective constant $(\overline{\in}_{\ell 2})$:

Boundary conditions for RVE in cylindrical coordinates:

$\phi|_{\pm r}=0$, $\phi|_{\pm z}=0$, $\phi|_{-\theta}=0$, $\phi|_{+\theta}=-(E_2^0\times\theta_c)$, $u|_{\pm r}=0$, $v|_{\pm\theta}=0$, $w|_{\pm z}=0$.

Boundary conditions for RVE in rectangular coordinates:

$\phi|_{\pm X}=0$, $\phi|_{\pm Z}=0$, $\phi|_{-Y}=0$, $\phi|_{+Y}=-(E_2^0\times a_c)$, $u|_{\pm X}=0$, $v|_{\pm Y}=0$, $w|_{\pm Z}=0$.

Elements ($\bar{\varepsilon}_\eta$, $\bar{E}_\zeta$): $\bar{E}_2\approx E_2^0$; $\bar{E}_\zeta=0$ for $\zeta=$ 1,3; $\bar{\varepsilon}_\eta=0$.

Effective material constants:

$$\overline{\in}_{\ell 2}=\in_{\ell 2}^{m}+v_f(\in_{\ell\beta}^{f}-\in_{\ell\beta}^{m})\left(\frac{\bar{E}_\beta^f}{E_2^0}\right)+v_f e_{\ell\eta}^{f}\left(\frac{\bar{\varepsilon}_\eta^f}{E_2^0}\right) \tag{2.30}$$

(i) Effective constant $(\overline{\in}_{\ell 3})$:

Boundary conditions for RVE in cylindrical coordinates:

$\phi|_{\pm r}=0$, $\phi|_{\pm\theta}=0$, $\phi|_{-z}=0$, $\phi|_{+z}=-(E_3^0\times h_c)$, $u|_{\pm r}=0$, $v|_{\pm\theta}=0$, $w|_{\pm z}=0$.

Boundary conditions for RVE in rectangular coordinates:

$\phi|_{\pm R}=0$, $\phi|_{\pm Y}=0$, $\phi|_{-X}=0$, $\phi|_{+X}=-(E_3^0\times b_c)$, $u|_{\pm X}=0$, $v|_{\pm Y}=0$, $w|_{\pm Z}=0$.

Elements ($\bar{\varepsilon}_\eta$, $\bar{E}_\zeta$): $\bar{E}_3\approx E_3^0$; $\bar{E}_\zeta=0$ for $\zeta=$ 1,2; $\bar{\varepsilon}_\eta=0$.

Effective material constants:

$$\overline{\in}_{\ell 3}=\in_{\ell 3}^{m}+v_f(\in_{\ell\beta}^{f}-\in_{\ell\beta}^{m})\left(\frac{\bar{E}_\beta^f}{E_3^0}\right)+v_f e_{\ell\eta}^{f}\left(\frac{\bar{\varepsilon}_\eta^f}{E_3^0}\right) \tag{2.31}$$

2.4 FE model of RVE

The constitutive relations for fiber and matrix phases within the RVE can be expressed as,

$$\begin{Bmatrix}\boldsymbol{\sigma}^q\\ \boldsymbol{D}^q\end{Bmatrix}=C^q\begin{Bmatrix}+\boldsymbol{\varepsilon}\\ -\boldsymbol{E}\end{Bmatrix} \tag{2.32}$$

The superscript q in Eq. (2.32) denotes the quantities within the fiber or the matrix phases according to its value as 1 or 2, respectively. The different matrix and vector quantities in Eq. (2.32) are as follows,

$$\begin{Bmatrix} +\boldsymbol{\varepsilon} \\ -\boldsymbol{E} \end{Bmatrix} = \{\varepsilon_1 \quad \varepsilon_2 \quad \varepsilon_3 \quad \varepsilon_4 \quad \varepsilon_5 \quad \varepsilon_6 \quad -E_1 \quad -E_2 \quad -E_3\}^{\mathrm{T}}$$

$$\begin{Bmatrix} \boldsymbol{\sigma} \\ \boldsymbol{D} \end{Bmatrix} = \{\sigma_1 \quad \sigma_2 \quad \sigma_3 \quad \sigma_4 \quad \sigma_5 \quad \sigma_6 \quad D_1 \quad D_2 \quad D_3\}^{\mathrm{T}}$$

$$\boldsymbol{C}^1 = \begin{bmatrix} \boldsymbol{C}_f & \boldsymbol{e}_f^{\mathrm{T}} \\ \boldsymbol{e}_f & -\boldsymbol{\epsilon}_f \end{bmatrix}, \quad \boldsymbol{C}^2 = \begin{bmatrix} \boldsymbol{C}_m & \boldsymbol{0} \\ \boldsymbol{0} & -\boldsymbol{\epsilon}_m \end{bmatrix} \tag{2.33a}$$

where, $\boldsymbol{C}_f / \boldsymbol{C}_m$ is the stiffness matrix for fiber/matrix phase; $\boldsymbol{\epsilon}_f / \boldsymbol{\epsilon}_m$ is the permittivity matrix of fiber/matrix phase; $\boldsymbol{e}_f$ is the piezoelectric matrix of the fiber phase. The form of these property matrices are as follows,

$$\boldsymbol{\epsilon}_f = \begin{bmatrix} \epsilon_{11}^f & 0 & 0 \\ 0 & \epsilon_{22}^f & 0 \\ 0 & 0 & \epsilon_{33}^f \end{bmatrix}, \quad \boldsymbol{\epsilon}_m = \begin{bmatrix} \epsilon_{11}^m & 0 & 0 \\ 0 & \epsilon_{22}^m & 0 \\ 0 & 0 & \epsilon_{33}^m \end{bmatrix}, \quad \boldsymbol{e}_f = \begin{bmatrix} e_{11} & e_{12} & e_{13} & 0 & 0 & 0 \\ 0 & 0 & 0 & 0 & 0 & e_{26} \\ 0 & 0 & 0 & 0 & e_{35} & 0 \end{bmatrix}$$

$$\boldsymbol{C}_f = \begin{bmatrix} C_{11}^f & C_{12}^f & C_{13}^f & 0 & 0 & 0 \\ C_{21}^f & C_{22}^f & C_{23}^f & 0 & 0 & 0 \\ C_{31}^f & C_{32}^f & C_{33}^f & 0 & 0 & 0 \\ 0 & 0 & 0 & C_{44}^f & 0 & 0 \\ 0 & 0 & 0 & 0 & C_{55}^f & 0 \\ 0 & 0 & 0 & 0 & 0 & C_{66}^f \end{bmatrix}, \quad \boldsymbol{C}_m = \begin{bmatrix} C_{11}^m & C_{12}^m & C_{13}^m & 0 & 0 & 0 \\ C_{21}^m & C_{22}^m & C_{23}^m & 0 & 0 & 0 \\ C_{31}^m & C_{32}^m & C_{33}^m & 0 & 0 & 0 \\ 0 & 0 & 0 & C_{44}^m & 0 & 0 \\ 0 & 0 & 0 & 0 & C_{55}^m & 0 \\ 0 & 0 & 0 & 0 & 0 & C_{66}^m \end{bmatrix} \tag{2.33b}$$

It should be noted here that Eq. (2.33b) represents the material properties for longitudinally (1 direction) poled piezoelectric fibers. The electro-elastic state at any point within the RVE can be defined by an electro-elastic state vector ($\boldsymbol{d}$) as,

$$\boldsymbol{d} = [u \quad v \quad w \quad \phi]^{\mathrm{T}} \tag{2.34}$$

Using this electro-elastic state vector ($\boldsymbol{d}$), the strain ($\boldsymbol{\varepsilon}$) and electric field ($\boldsymbol{E}$) vectors at any point within the RVE can be expressed in terms of an operator matrix ($\boldsymbol{L}$) as,

$$\begin{Bmatrix} +\boldsymbol{\varepsilon} \\ -\boldsymbol{E} \end{Bmatrix} = \boldsymbol{L}\boldsymbol{d} \tag{2.35a}$$

In Eq. (2.35a), the form of the operator matrix ($\boldsymbol{L}$) for the RVE in cylindrical coordinates ($\boldsymbol{L}_{cylindrical}$) or for the RVE in rectangular coordinates ($\boldsymbol{L}_{\mathrm{rectangular}}$) is as follows,

$$\boldsymbol{L}_{cylindrical}=\begin{bmatrix} \frac{\partial}{\partial r} & \frac{1}{r} & 0 & 0 & \frac{\partial}{\partial z} & \frac{1}{r}\frac{\partial}{\partial\theta} & 0 & 0 & 0 \\ 0 & \frac{1}{r}\frac{\partial}{\partial\theta} & 0 & \frac{\partial}{\partial z} & 0 & \frac{\partial}{\partial r}-\frac{1}{r} & 0 & 0 & 0 \\ 0 & 0 & \frac{\partial}{\partial z} & \frac{1}{r}\frac{\partial}{\partial\theta} & \frac{\partial}{\partial r} & 0 & 0 & 0 & 0 \\ 0 & 0 & 0 & 0 & 0 & 0 & \frac{\partial}{\partial r} & \frac{1}{r}\frac{\partial}{\partial\theta} & \frac{\partial}{\partial z} \end{bmatrix}^{\mathrm{T}}$$

$$\boldsymbol{L}_{\mathrm{rectangular}}=\begin{bmatrix} \frac{\partial}{\partial x} & 0 & 0 & 0 & \frac{\partial}{\partial z} & \frac{\partial}{\partial y} & 0 & 0 & 0 \\ 0 & \frac{\partial}{\partial y} & 0 & \frac{\partial}{\partial z} & 0 & \frac{\partial}{\partial x} & 0 & 0 & 0 \\ 0 & 0 & \frac{\partial}{\partial z} & \frac{\partial}{\partial y} & \frac{\partial}{\partial x} & 0 & 0 & 0 & 0 \\ 0 & 0 & 0 & 0 & 0 & 0 & \frac{\partial}{\partial x} & \frac{\partial}{\partial y} & \frac{\partial}{\partial z} \end{bmatrix}^{\mathrm{T}} \tag{2.35b}$$

Using Eq. (2.32), the first variation of electro-elastic internal energy of RVE can be written as (Tiersten, 1969),

$$\delta U=\sum_{q=1}^{2}\left(\int_{V^q}\left\langle\{\delta\boldsymbol{\varepsilon}\quad-\delta\boldsymbol{E}\}\boldsymbol{C}^q\begin{Bmatrix}+\boldsymbol{\varepsilon}\\-\boldsymbol{E}\end{Bmatrix}\right\rangle dV^q\right) \tag{2.36}$$

where, δ is an operator for first variation; V^q is the volume of fiber phase ($q=1$) or matrix phase ($q=2$). Introducing Eq. (2.35a) in Eq. (2.36), the following form of δU can be obtained,

$$\delta U=\sum_{q=1}^{2}\left(\int_{V^q}\left\langle\delta\boldsymbol{d}^{\mathrm{T}}\boldsymbol{L}^{\mathrm{T}}\boldsymbol{C}^q\boldsymbol{L}\boldsymbol{d}\right\rangle dV^q\right) \tag{2.37}$$

For deriving the FE model, the volume of RVE is discretized by 27-node isoparametric element as shown in Fig. 2.5(a). The edges of every element are in parallel to the axis of the reference cylindrical coordinate system, while an element is made of either fiber or matrix material. At any point within a typical element, the electro-elastic state vector ($\boldsymbol{d}$) can be written as,

$$\boldsymbol{d} = \boldsymbol{N}\boldsymbol{d}^{e} \tag{2.38}$$

where, $\boldsymbol{N}$ is the shape function matrix and $\boldsymbol{d}^{e}$ is the elemental nodal electro-elastic state vector. Introducing Eq. (2.38) in Eq. (2.37), the simplified expression for the first variation of electro-elastic internal energy (δU^{e}) of a typical element can be obtained as,

$$\delta U^{e} = (\delta \boldsymbol{d}^{e})^{\mathrm{T}} \left\langle \boldsymbol{K}^{e} \boldsymbol{d}^{e} \right\rangle, \ \boldsymbol{K}^{e} = \int_{V_e^q} \left(\boldsymbol{N}^{\mathrm{T}} \ \boldsymbol{L}^{\mathrm{T}} \ \boldsymbol{C}^{q} \ \boldsymbol{L} \ \boldsymbol{N} \right) dV_e^q \tag{2.39}$$

where, V_e^q is the elemental volume within fiber phase ($q = 1$) or matrix phase ($q = 2$). Assembling the elemental equations (Eq. (2.39)) in the global space, the global expression for internal energy of RVE can be obtained as,

$$\delta U = (\delta \boldsymbol{X})^{\mathrm{T}} \left\langle \boldsymbol{K} \, \boldsymbol{X} \right\rangle \tag{2.40}$$

where, $\boldsymbol{K}$ is the global electro-elastic coefficient matrix; $\boldsymbol{X}$ is the global nodal electro-elastic state vector.

The electro-elastic analysis of the RVE is carried out by applying the kinematic boundary conditions (Eqs. (2.23)-(2.31)) over its (RVE) boundary surface. If these boundary conditions are directly applied to the boundary surface of RVE, then it results in over-constrained RVE edges (Odegard, 2004). This kind of over-constrained deformation of RVE can be avoided by applying the kinematic boundary conditions over the full FE model of RVE instead of applying the same boundary conditions directly to its (RVE) boundary surface (Odegard, 2004). So, the kinematic boundary conditions (Eqs. (2.23)-(2.31)) are presently applied over the FE model of RVE (Eq. (2.40)) following a procedure described in (Cook et al., 2001). For a specified nodal electric potential or displacement over the boundary surface, the first variation of the corresponding element of $\boldsymbol{X}$ (say, X_i) is zero ($\delta X_i = 0$). Thus, the corresponding (i^{th}) row of $\boldsymbol{K}$ is to be deleted while a column ($\boldsymbol{P}_i$) of $\boldsymbol{K}$ with the same index (i) is to be removed for formation of electric potential or displacement load vector as,

$$\delta U = (\delta \boldsymbol{X}_r)^{\mathrm{T}} \left\langle \boldsymbol{K}_r \, \boldsymbol{X}_r + \boldsymbol{P}_i X_i \right\rangle \tag{2.41}$$

where, $\boldsymbol{K}_r$ and $\boldsymbol{X}_r$ are the reduced electro-elastic coefficient matrix and nodal electro-elastic state vector, respectively, after the implementation of boundary condition. For a number (N_b) of specified nodal degrees of freedom over the boundary surface of RVE, Eq. (2.41) can be written in general form as,

$$\delta U = (\delta \boldsymbol{X}_r)^{\mathrm{T}} \left\langle \boldsymbol{K}_r \, \boldsymbol{X}_r + \sum_{i=1}^{N_b} \boldsymbol{P}_i X_i \right\rangle \tag{2.42}$$

Employing the principle of minimum potential energy, Eq. (2.42) can be written as,

$$\boldsymbol{K}_r \, \boldsymbol{X}_r = -\sum_{i=1}^{N_b} \boldsymbol{P}_i X_i \tag{2.43}$$

Equation (2.43) represents the electro-elastic FE model of RVE under the specified nodal electric potentials and/or displacements. Using Eq. (2.43), the nodal solutions for electric potential and displacement fields within the RVE corresponding to every set of boundary conditions (Eqs. (2.23)-(2.31)) can be obtained. Subsequently, the volume-average (RVE/phase) strain and electric fields can be computed according to Eq. (2.18) using these nodal solutions.

2.5 Arrangement of electrodes

According to the geometrical features and poling direction of present smart composite (Figs. 2.2 and 2.4), the magnitude of one effective piezoelectric coefficient (e_{11}, 1 for the longitudinal direction of fibers) is significantly larger than the magnitudes of other effective piezoelectric coefficients. Thus, for the utilization of this smart composite as a material of distributed actuator based on the effective coefficient (e_{11}), the electric field is to be applied along the longitudinal direction (poling direction) of fibers. It can be achieved through an arrangement of electrodes over the top and bottom surfaces of the composite lamina as illustrated in Fig. 2.5(b) for the SPFC in cylindrical coordinates.

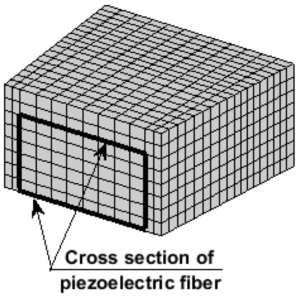

Fig. 2.5(a) FE model of typical sub-volume/RVE.

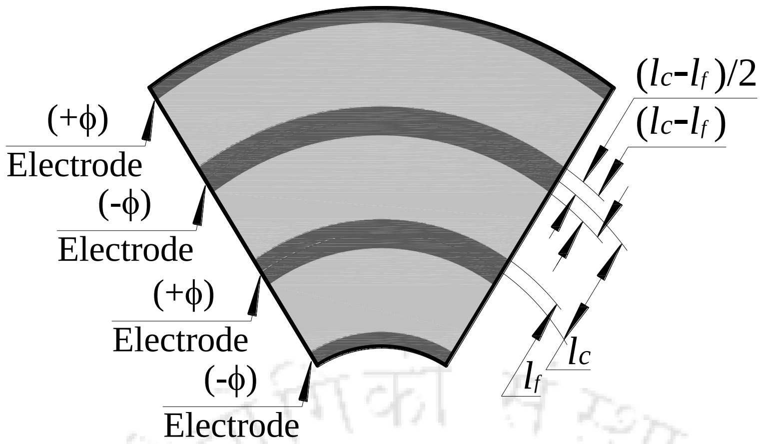

Fig. 2.5(b) Top/bottom surface of the SPFC in cylindrical coordinates with electrodes.

Figure 2.5(b) shows the top/bottom surface of the SPFC lamina (Fig. 2.1) over which the surface-electrodes are provided at the radial gap of any two consecutive short fibers. The uniform polarity of the external voltage is considered for the top and bottom surface-electrodes lying on the same radial location, while any two consecutive electrodes along the radial direction are of opposite polarity. Any two consecutive electrodes of opposite polarity are denoted as a pair of electrodes.

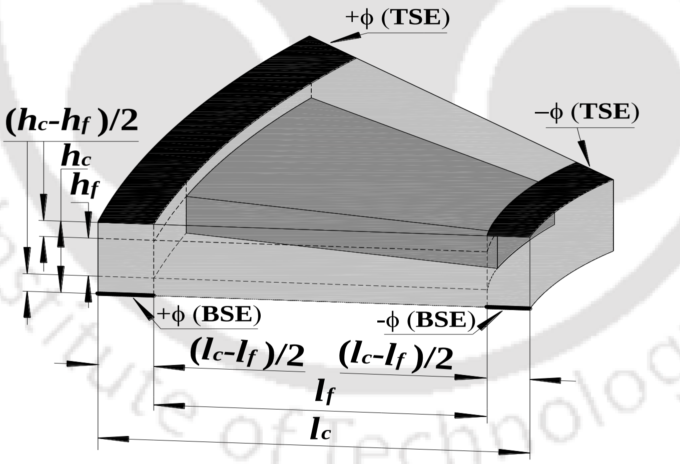

TSE: Top surface electrode, BSE: Bottom surface electrode

Fig. 2.6 RVE of SPFC in cylindrical coordinates with surface-electrodes.

Across all the pairs of electrodes, uniform applied voltage is considered, and it yields uniform magnitude of the electric field within all such pairs. But, the radial component of the electric field within a pair of electrodes is in the opposite direction to that of the same within the consecutive pairs of electrodes. For obtaining the electrically induced actuation force in the same direction from all pairs of electrodes, the corresponding piezoelectric fibers are poled along the radial direction in an alternate manner. According to this arrangement of surface-electrodes, the macroscopic behaviour of the SPFC actuator can be estimated by defining an elemental volume as illustrated in Fig. 2.6.

The volume in Fig. 2.6 is basically a volume of RVE (Fig. 2.2) with surface-electrodes. Similar to Figs. 2.5(b) and 2.6, the arrangement of electrodes for the SPFC in rectangular coordinates is illustrated in Figs. 2.7(a) and 2.7(b). In this arrangement of electrodes, it seems too small in-plane gap between any two consecutive surface-electrodes. But it facilitates to achieve a significant magnitude of the externally induced electric field in effect of the small applied voltage across the pairs of surface-electrodes. The difficulty may arise in the fabrication of the SPFC actuator because of the small in-plane gap between any two consecutive surface-electrodes. But this gap can be increased by increasing the length of fibers or fiber aspect ratio. The fiber aspect ratio does not have much effect on the magnitude of effective magnitude of induced electric field or driving electric field for an applied voltage across the pairs of electrodes in the use of the SPFC as an actuator. In this evaluation of driving electric field, the difficulty arises due to the material heterogeneity.

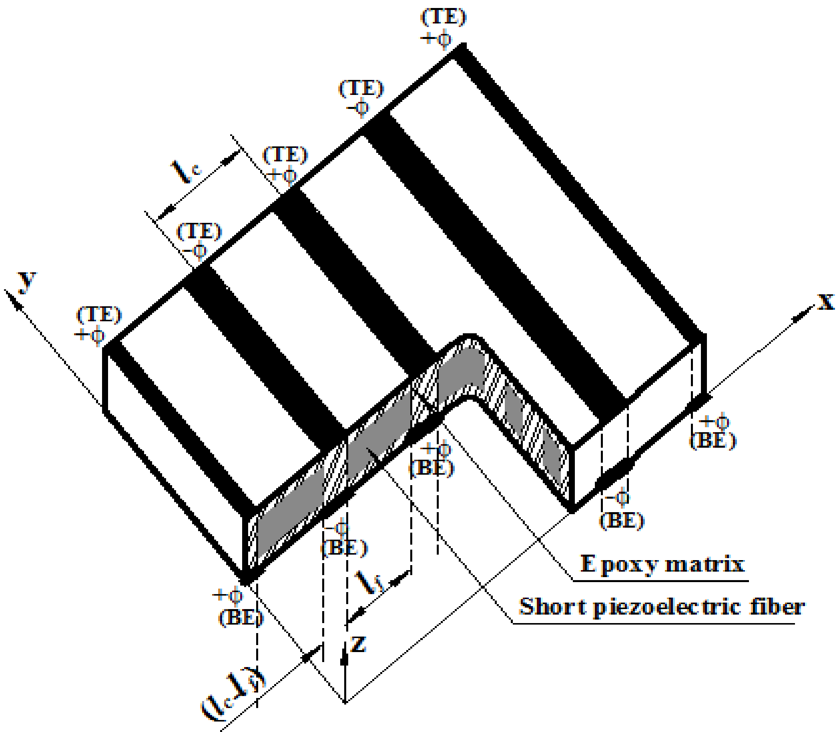

TE: Top electrode, BE: Bottom electrode

(a)

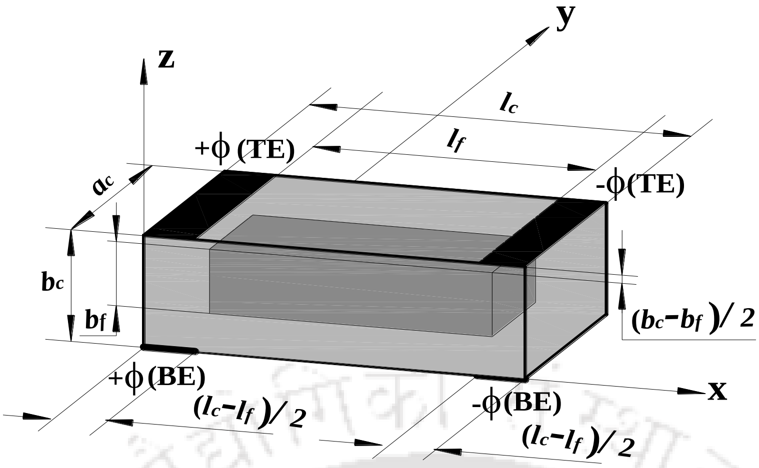

(b)

Fig. 2.7(a) Arrangement of electrodes over the top and bottom surfaces of SPFC in rectangular coordinates, (b) the corresponding RVE with electrodes.

The effective properties or constitutive behaviour of the smart composite is valid only for specially statistically homogeneous fields which can be produced by means of homogeneous kinematic/kinetic boundary conditions over the surface of large composite (Hasin, 1970). The present applied electric potentials over the surface-electrodes do not satisfy the conditions for homogeneous kinematic boundary conditions. So, in a strict sense, the corresponding statistically homogeneous electric field would not be adequate to the effective constitutive relation. As a consequence, for a situation where the aforesaid specially statistically homogeneous fields do not arise or cannot be produced, an assumption of local averages of fields over the volume of RVE may be made to salvage the analysis (Hasin, 1970). Following this assumption in the present analysis, the local electric field within the elemental volume (RVE) with surface-electrodes (Fig. 2.6 or Fig. 2.7(b)) is considered as the local volume-average electric field over the same volume (RVE). Without this assumption, it is difficult to model the induced electric field within a local heterogeneous volume of the large smart composite actuator. However, as per this consideration, the induced electric field due to an external voltage can be taken as its volume-average quantity over the volume of RVE according to Eq. (2.12). Now, for structural applications of the smart actuator under the assumption of small strain, the induced electric field due to the strain of overall structure is of very small magnitude as compared to the large magnitude of the applied electric field by means of external voltage through electrodes. So, the magnitude of volume-average electric field ($\bar{E}$) over the volume of RVE may be considered as a function of applied voltage (V) only. Since one value of applied voltage yields one magnitude of $\bar{\boldsymbol{E}}$ within the actuator, $\bar{\boldsymbol{E}}$ is a single-valued function of applied voltage (V). This functional relation for the SPFC/CPFC in cylindrical coordinates may be represented by the following expressions (Eq. (2.44a)), where $G_r(V)$, $G_\theta(V)$ and $G_z(V)$ are the functions of applied voltage (V) corresponding to the components of volume-average electric field ($\bar{E}_r$, $\bar{E}_\theta$, $\bar{E}_z$).

$$\bar{E}_r = G_r(V)V\,,\ \bar{E}_\theta = G_\theta(V)V\,,\ \bar{E}_z = G_z(V)V \tag{2.44a}$$

Similar expressions may also be written for the SPFC/CPFC in rectangular coordinates as given in Eq. (2.44b).

$$\bar{E}_x = G_x(V)V\,,\ \bar{E}_y = G_y(V)V\,,\ \bar{E}_z = G_z(V)V \tag{2.44b}$$

It may be noted here that the same arrangement of surface-electrodes may be considered for the consideration of the continuous fibers instead of the short fibers, and also the same procedure as considered for SPFC actuator may be followed for CPFC actuator for its mathematical modelling. The foregoing demonstration is for a lamina of present SPFC/CPFC actuator. For achieving greater actuation force in an application, several SPFC/CPFC laminas can be used in the form of a laminate with the proper alignment of surface-electrodes as illustrated in Fig. 2.8 or Fig. 2.9 for the SPFC/CPFC in cylindrical or rectangular coordinates, respectively.

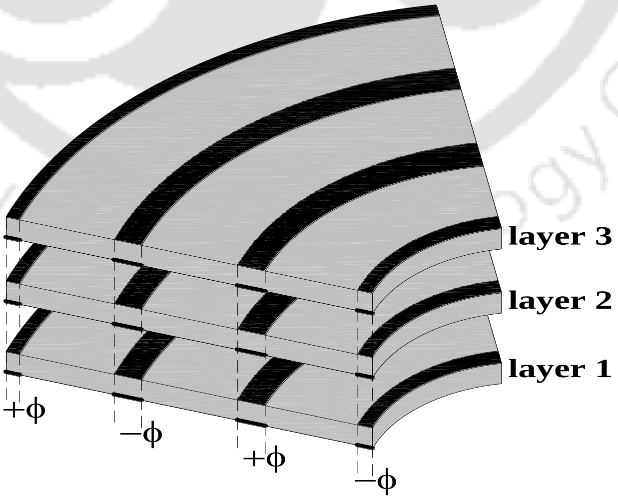

Fig. 2.8 Schematic diagram for the alignment of electrodes in forming a laminate of several layers of SPFC in cylindrical coordinates.

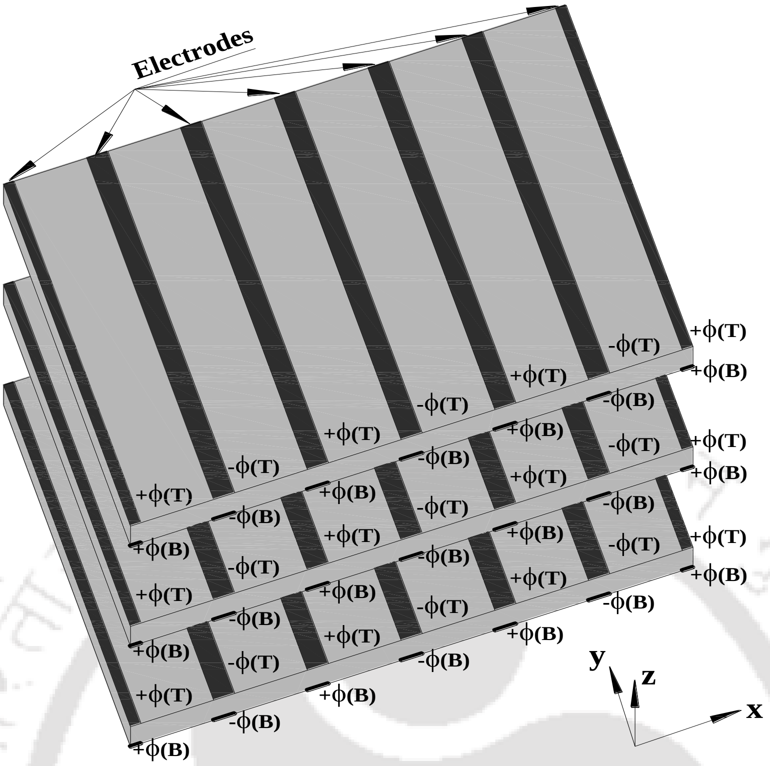

T: Top electrode, B: Bottom electrode

Fig. 2.9 Schematic diagram for the alignment of electrodes in forming a laminate of several layers of SPFC in rectangular coordinates.

2.6 Results and discussions

In this section, first, the present numerical procedure in estimating the effective properties of the smart composite is verified. Subsequently, the magnitudes of the effective coefficients are evaluated, and the geometrical properties of the RVE are decided with an objective of the improved magnitude of the major effective piezoelectric coefficient (e_{11}).

Since a similar SPFC is not available in the literature, the present FE procedure is verified considering the continuous piezoelectric fibers of the smart composite in rectangular coordinates. The poling direction of the continuous piezoelectric fibers is considered as the thickness direction, and the effective electro-elastic coefficients are computed using the present FE procedure. These results are illustrated in Table 2.1 together with the similar analytical results available in (Ray, 2006a). It may be observed from this table that the present results are in good agreement with the available analytical results, and thus this comparison verifies the accuracy of the present FE procedure.

Table 2.1 Verification of present FE formulation for estimation of effective electro-elastic constants of piezoelectric composites.

$^{*}R_{31} = ((e_{31})_{composite} / (e_{31})_{piezoelectricfiber})$

v_f	Source	$^{*}R_{31}$	C_{11}(GPa)	C_{12}(GPa)	C_{22}(GPa)
0.2	Present	0.6654	18.71	3.396	5.27
	Ray (2006a)	0.6859	17.93	3.191	4.794
0.4	Present	1.3334	34.55	4.752	6.62
	Ray (2006a)	1.3563	32.35	4.207	6.325
0.6	Present	1.9837	49.06	6.795	10.10
	Ray (2006a)	1.9902	47.63	6.177	9.293

Next, the poling direction of the continuous fibers is taken as their longitudinal direction, and the effective coefficients of the smart composite are computed according to the present FE procedure. These results are illustrated in Fig. 2.10 along with the similar analytical and experimental results available in (Aboudi et al., 2013; Chan and Unsworth, 1989). It may be observed from Fig. 2.10 that the present results are very close to the analytical/experimental results available in (Aboudi et al., 2013; Chan and Unsworth, 1989). This comparison verifies the accuracy of the present FE procedure in estimating the properties of PFCs comprised of longitudinally poled piezoelectric fibers.

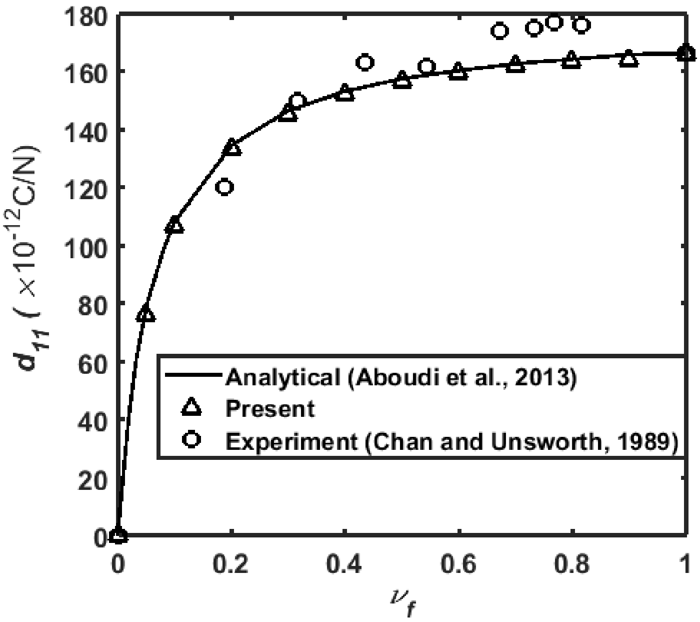

Fig. 2.10 Verification of present FE procedure for computation of effective properties of PFCs.

2.6.1 Effective coefficients of SPFC/CPFC

The materials for fiber and matrix phases of the SPFC are considered as PZT-5H and Epoxy, respectively. Table 2.2 presents the material properties of these constituent materials. For the specified constituent materials, the electro-elastic properties of SPFC are mainly dependent on the area-ratio (A_r) and length-ratio (L_r) through the relation, $v_f = (A_r \times L_r)$. Further, since the SPFC acts as a material of distributed actuator by the application of electric field along the poling direction of fibers, the important effective piezoelectric coefficients are, e_{11}, e_{12} and e_{13}. So, the present analysis is carried out mainly for investigating the effects of these parameters (A_r, L_r) on the magnitudes of effective coefficients, e_{11}, e_{12} and e_{13}.

Figure 2.11 represents the variations of the effective piezoelectric coefficients with the area-ratio (A_r) for continuous piezoelectric fibers ($L_r = 1$). For the variation of the area-ratio (A_r) without altering the thickness (h_c) and circumferential span (θ_c) of RVE, the fiber dimensions (h_f , θ_f) are varied following the relations, $h_f = h_c\sqrt{A_r}$ and $\theta_f = \theta_c\sqrt{A_r}$. It may be observed from Fig. 2.11 that the magnitude of the effective coefficient (e_{11}) significantly increases with the increasing area-ratio. But, the magnitude of other coefficient (e_{12}/e_{13}) varies insignificantly. The magnitude of e_{12}/e_{13} is also indicatively lesser than that of e_{11}. This result infers that the use of the smart composite as a material of distributed actuator would be based on the coefficient (e_{11}), and its (e_{11}) magnitude can be increased by increasing the area-ratio.

Table 2.2 Material properties of constituent materials (Ray, 2006a).

Fiber/Matrix	C_{11} (GPa)	C_{12} (GPa)	C_{23} (GPa)	C_{22} (GPa)	C_{44} (GPa)
Epoxy	3.86	2.57	2.57	3.86	0.64
PZT-5H	124	96	98	151	26.5

Fiber/Matrix	e_{11} (C/m^2)	e_{12}/e_{13} (C/m^2)	e_{26}/e_{35} (C/m^2)	$\in_{11}$ (C/Vm) ($\times 10^{-09}$)	$\in_{22}/\in_{33}$ (C/Vm) ($\times 10^{-09}$)
Epoxy	0	0	0	0.079	0.079
PZT-5H	27	-5.1	17	13.27	13.4

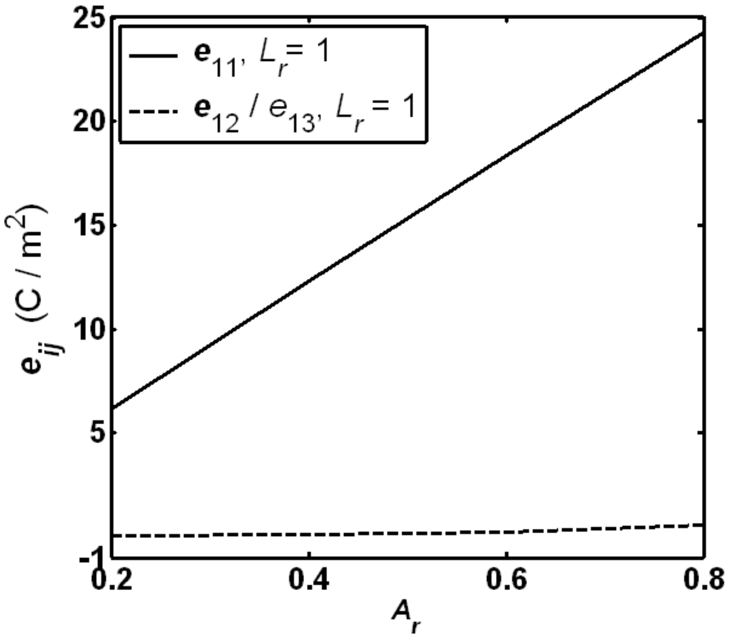

Fig. 2.11 Variations of effective piezoelectric coefficients (e_{11}, e_{12}, e_{13}) with the area ratio (A_r).

For the use of short piezoelectric fibers ($L_r < 1$), the variations of the same coefficients (e_{11}, e_{12}, e_{13}) with the length-ratio (L_r) are illustrated in Fig. 2.12 for different values of area-ratio (A_r). In this computation, the fiber-length is varied keeping the constant values of other geometrical parameters in such a manner that the central location of short fiber within the RVE does not alter.

For any value of the area-ratio (A_r), it may be observed from Fig. 2.12 that the magnitude of coefficient e_{11} increases significantly with the increasing length-ratio (L_r) and reaches to its (e_{11}) maximum value for, $L_r = 1$ (continuous fiber). The other coefficient (e_{12} / e_{13}) also increases with the increasing length ratio (L_r). But, after a certain value of, L_r, its (e_{12} / e_{13}) magnitude decreases to the minimum value for continuous fiber ($L_r = 1$). Similar to the case of continuous fibers ($L_r = 1$, Fig. 2.11), the magnitude of e_{12} / e_{13} is much lesser than that of e_{11} (Fig. 2.12). Thus, for both the forms (short and continuous) of piezoelectric fibers within the present smart composite, the coefficient e_{11} would be chosen as the major piezoelectric coefficient in its (SPFC/CPFC) use as a distributed actuator. In case of SPFC, Fig. 2.12 shows a higher value of L_r (close to 1) for the improved magnitude of e_{11}. The same figure (Fig. 2.12) also indicates significant effect of area-ratio on the magni-

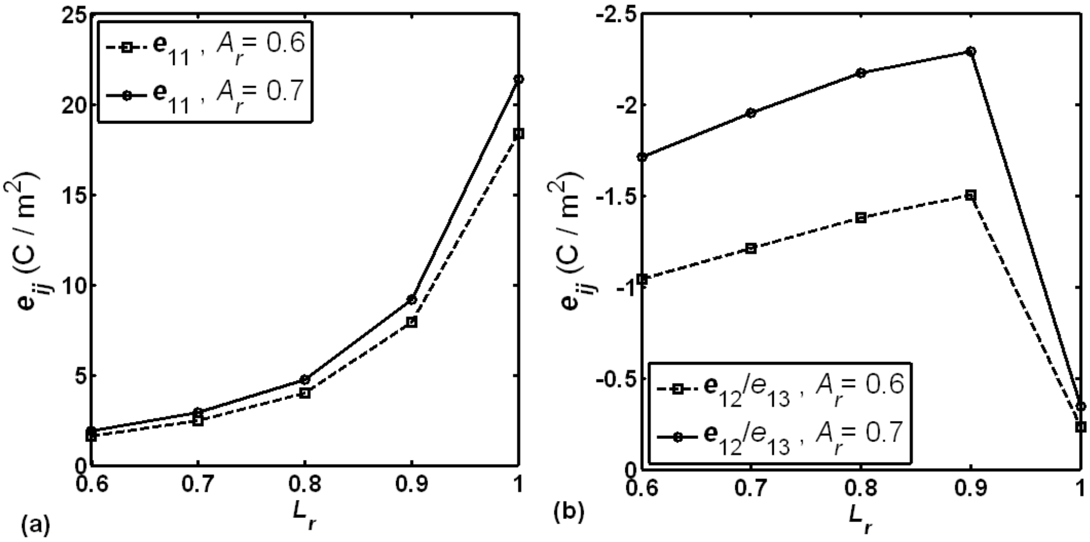

Fig. 2.12 Variations of the effective piezoelectric coefficients (e_{11}, e_{12}, e_{13}) with the length-ratio (L_r) for different values of the area-ratio (A_r).

-tude of e_{11} for a higher value of length-ratio. So, for SPFC, higher values of both the area-ratio and length-ratio are to be considered for the improved magnitude of e_{11}. On the basis of these results, a higher value of area-ratio is chosen at present as 0.6 for both the SPFC and CPFC, while a higher value of length-ratio for SPFC is chosen as 0.95. Basically, the CPFC is modified into an SPFC by reducing the value of length-ratio from 1 to 0.95. This modification causes a little decrease in the magnitude of e_{11} (Fig. 2.12(a)) from its maximum possible magnitude (at $L_r = 1$). But, an advantage of greater flexibility and conformability of the smart composite can be achieved, and that is useful in its structural applications.

Like area-ratio and length-ratio, the dimensions like l_c, h_c and θ_c are also to be mentioned for complete geometrical properties of RVE. These dimensions (l_c, h_c, θ_c) of RVE are directly related to the similar dimensions (l_f, h_f, θ_f) of corresponding fiber by the relations, $l_f = L_r l_c$, $h_f = h_c\sqrt{A_r}$ and $h_f = h_c\sqrt{A_r}$. So, the dimensions of fiber can also be specified instead of those of RVE. For the aforesaid selected values of area-ratio and length-ratio ($A_r = 0.6$, $L_r = 0.95$), the cross-sectional dimensions (h_f, θ_f) are considered to have small values as compared to the value of longitudinal dimension (l_f). This consideration results in negligibly small effects of variations of these parameters (h_f, θ_f) on the magnitudes of effective coefficients (e_{11}, e_{12}, e_{13}) when other geometrical parameters remain with their constant values. So, for simplicity, these dimensions (h_f, θ_f) can be represented by a single parameter, A_f ($A_f = h_f \theta_f$). Now, for specified values of A_r and L_r, the values of A_f and l_f may be assigned arbitrarily. But, this arbitrary assignment may have an effect on the magnitudes of the effective coefficients (e_{11}, e_{12}, e_{13}), and that implies a relation among these parameters (A_f, l_f) for the improved magnitude of, e_{11}. This relation is estimated at present by defining a parameter as fiber aspect ratio ($S_f = l_f / A_f$). Presently, two values of A_r are considered by varying A_f with a constant value of A_c ($A_c = h_c \theta_c$, $A_r = A_f / A_c$). For every value of A_r or A_f, S_f is varied through the variation of l_f. It should be noted here that the value of l_c would vary with l_f for the constant value of, L_r.

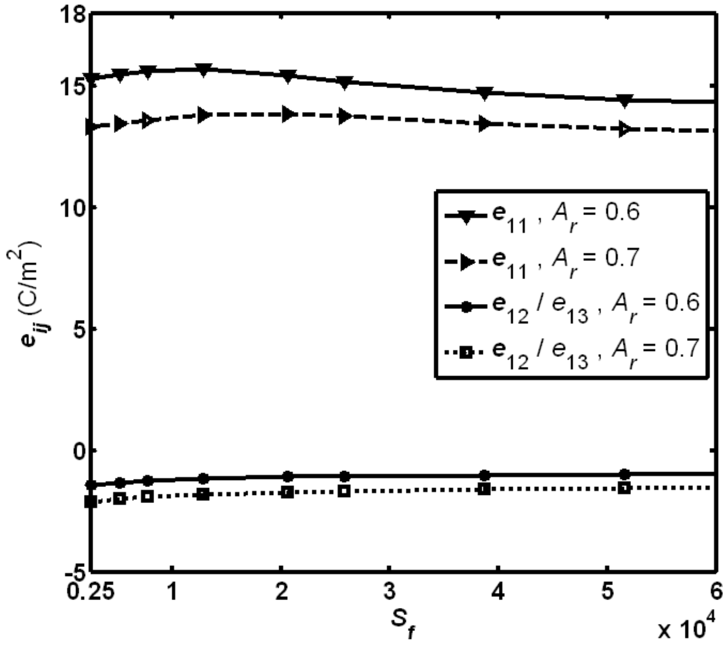

Fig. 2.13 Variations of effective piezoelectric coefficients (e_{11}, e_{12}, e_{13}) with the fiber aspect ratio (S_f) ($L_r = 0.95$).

Figure 2.13 illustrates the variations of coefficients (e_{11}, e_{12}, e_{13}) with the fiber aspect ratio (S_f) for different values of area-ratio (A_r). It may be observed from Fig. 2.13 that there is a little variation of every coefficient ($e_{11} / e_{12} / e_{13}$) with the piezoelectric fiber aspect ratio (S_f) for any value of A_r or A_f. Also, the nature of variation of any of the coefficients (e_{11}, e_{12}, e_{13}) does not alter for different values of area-ratio. Thus, for specified values of area-ratio and length-ratio, the value of S_f can be chosen from this result (Fig. 2.13), and that is taken at present as 1.2×10^4 for an improved magnitude of, e_{11}. According to the present geometrical properties (SPFC, $L_r = 0.95$, $A_r = 0.6$, $S_f = 1.2 \times 10^4$) of RVE, the effective electro-elastic properties are illustrated in Table 2.3. The same table also illustrates similar properties when the continuous piezoelectric fiber of RVE is considered (CPFC, $L_r = 1$, $A_r = 0.6$). It may be observed from Table 2.3 that the magnitude of the major effective piezoelectric coefficient (e_{11}) decreases for the use of short piezoelectric fibers ($L_r = 0.95$) instead of continuous fibers ($L_r = 1$). This decrease in the magnitude of e_{11} is an important concern when one intends to use SPFC actuator instead of CPFC actuator. The corresponding change in the actuation capability is studied in the next chapter considering the aforesaid arrangement of surface-electrodes.

Table 2.3 Effective electro-elastic properties of SPFC/CPFC in cylindrical coordinates.

Smart Composite	e_{11} (C/m^2)	e_{12} / e_{13} (C/m^2)	e_{26} / e_{35} (C/m^2)	$\in_{11}$ (C/Vm) ($\times 10^{-09}$)	$\in_{22} / \in_{33}$ (C/Vm) ($\times 10^{-09}$)
SPFC	13.818	-1.158	1.220	0.95	0.302
CPFC	18.379	-0.231	1.429	8.75	0.28

Smart Composite	C_{11} (GPa)	C_{12} (GPa)	C_{23} (GPa)	C_{22} (GPa)	C_{44} (GPa)	C_{55} (GPa)
SPFC	31.635	4.734	4.201	12.623	1.628	2.229
CPFC	36.019	6.794	4.34	13.056	1.649	2.503

The foregoing results are evaluated for the SPFC/CPFC in cylindrical coordinates. Similar results are also evaluated for the SPFC/CPFC in rectangular coordinates, and the same characteristics in the electromechanical behaviour are obtained. This may be due to the fact that the geometrical and material properties of the SPFC/CPFC remain the same for its construction in both the coordinate systems.

The values of the length-ratio (L_r), area-ratio (A_r) and fiber aspect ratio (S_f) for the SPFC/CPFC in cylindrical coordinates are not altered for the SPFC/CPFC in rectangular coordinates. The corresponding properties of the SPFC/CPFC in rectangular coordinates are furnished in Table 2.4. In comparison to Table 2.3, Table 2.4 shows negligibly small change in the magnitudes of the effective coefficients due to the alteration of the coordinate system.

Table 2.4 Effective coefficients of SPFC/CPFC in rectangular coordinates.

Smart Composite	e_{11} (C/m^2)	e_{21} / e_{31} (C/m^2)	e_{62} / e_{53} (C/m^2)	$\in_{11}$ (C/Vm) (×10^{-09})	$\in_{22}$ / $\in_{33}$ (C/Vm) (×10^{-09})	
SPFC	13.486	-1.032	1.222	0.534	0.295	
CPFC	18.380	-0.230	1.394	8.113	0.200	
Smart composite	C_{11} (GPa)	C_{12} (GPa)	C_{23} (GPa)	C_{22} (GPa)	C_{44} (GPa)	C_{55} (GPa)
SPFC	29.979	5.008	4.150	12.533	1.607	2.224
CPFC	36.014	6.793	4.325	13.070	1.637	2.458

2.6.2 Electric field for present arrangement of surface-electrodes

The foregoing results show a significant magnitude of e_{11} for the present SPFC/CPFC. In order to exploit this piezoelectric coefficient in the use of SPFC/CPFC as a material of distributed actuator, an arrangement of surface-electrodes is shown in Figs. 2.5(b) and 2.7(a). The corresponding volume-average electric field over the volume of RVE is expressed as a function of applied voltage (V) according to Eq. (2.44). This functional relation is evaluated numerically, and the same is presented in this section.

For the RVE of SPFC/CPFC in rectangular coordinates, Fig. 2.14 illustrates the variations of the volume-average electric field components ($\bar{E}_x, \bar{E}_y, \bar{E}_z$) with the applied voltage (V) across the pairs of surface-electrodes. The physical dimensions of the RVE (Fig. 2.7(b)) are considered as $a_c =$ 50 μm, $b_c = 50$ μm. For both the SPFC and CPFC, $A_r =$ 0.6 ($A_r = a_f b_f / a_c b_c, a_f = b_f$, $a_c = b_c$), $S_f = l_f / a_f = 6$. For SPFC, $L_r = l_f / l_c =$ 0.95 while the same parameter for CPFC is equal to 1. The longitudinal gap between any consecutive electrodes for SPFC is taken as, $(l_c - l_f)$ and the same gap is also considered for CPFC. It may be observed from Fig. 2.14 that all components of volume-average electric field linearly vary with the applied voltage (V). Also, the magnitude of the longitudinal component ($\bar{E}_x$) of the volume-average electric field ($\bar{\boldsymbol{E}}$) is significantly higher than that for any of its ($\bar{\boldsymbol{E}}$) other components ($\bar{E}_y, \bar{E}_z$). So, the present arrangement of surface-electrodes facilitates to achieve a higher value of $\bar{E}_x$, and it is useful for achieving sufficient actuation force through the piezoelectric coefficient (e_{11}). For any value of the applied voltage, it may also be observed from Fig. 2.14(a) that the magnitude of $\bar{E}_x$ in SPFC is more than that in CPFC. Although a higher magnitude of $\bar{E}_x$ is obtained for SPFC, but the corresponding magnitude of e_{11} is lesser than that of the CPFC. So, the change in the actuation capability of the PFC due to the use of the short fibers (SPFC) instead of the continuous fibers (CPFC) is difficult to presume without a study on their (SPFC and CPFC) actuation capabilities in an application. This study in performed in the next chapter. However, it is important to mention here that the magnitudes of the gradients (G_x, G_y, G_z, Eq. 2.44) are dependent on the materials for the constituents as well as the geometric dimensions of the RVE. For the present constituents and geometric dimensions of RVE in rectangular coordinates, the magnitudes of G_x for SPFC and CPFC are obtained as 889.18 m^{-1} and 616.38 m^{-1}, respectively, according to the results in Fig. 2.14(a).

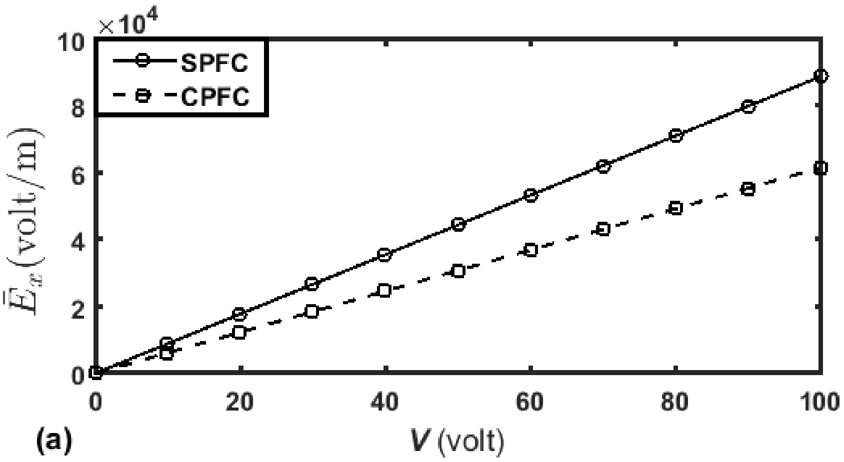

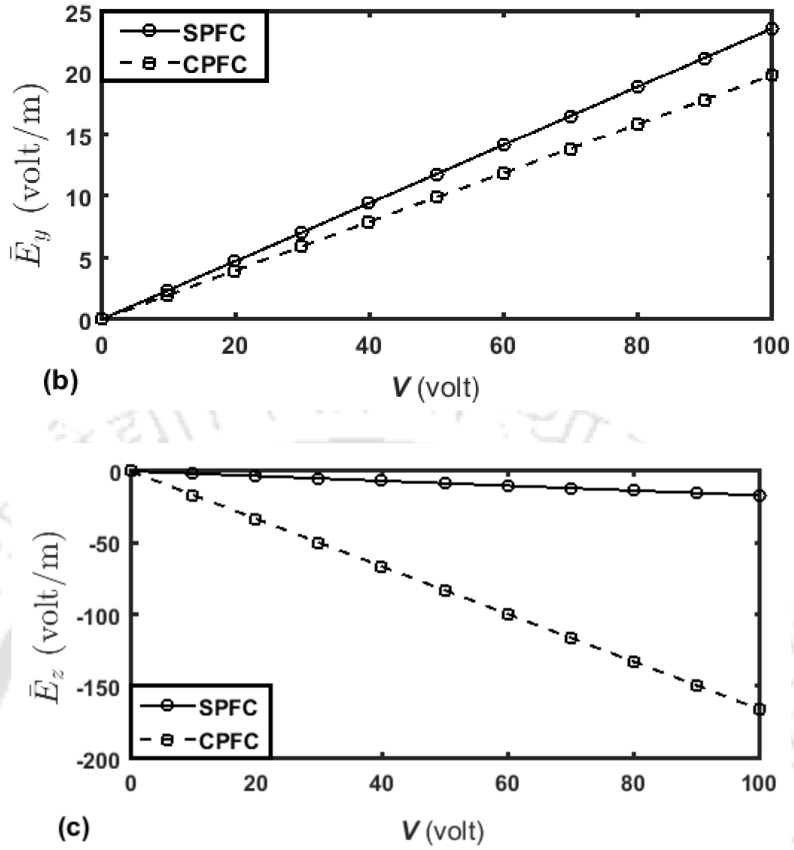

Fig. 2.14 Variations of the volume-average electric field components ($\bar{E}_x$, $\bar{E}_y$, $\bar{E}_z$) with the applied voltage (V).

Since the other similar parameters (G_y, G_z) have negligibly small magnitudes in comparison to the magnitude of G_x, these parameters (G_y, G_z) are presently assumed as $G_y = 0$, $G_z = 0$. Similar to the results in Fig. 2.14, the variations of the volume-average electric field components ($\bar{E}_r$, $\bar{E}_\theta$, $\bar{E}_z$) for the SPFC/CPFC in cylindrical coordinates are also evaluated. The geometrical properties of RVE for SPFC are considered as, $r_i = 100$ mm, $\theta_c = 0.001$ rad, $h_c = 0.1$ mm, $S_f = l_f/(\theta_f h_f)$ = 6.4549×10^{3}, $A_r = 0.6$ ($A_r = \theta_f h_f/\theta_c h_c$, $(\theta_f/\theta_c) = (h_f/h_c)$) and $L_r = 0.95$. The same dimensions for the RVE of CPFC ($L_r = 1$) are also considered. These results exhibit the same characteristics of the volume-average electric field components ($\bar{E}_r$, $\bar{E}_\theta$, $\bar{E}_z$) as those are obtained for the similar parameters ($\bar{E}_x$, $\bar{E}_y$, $\bar{E}_z$) in the previous results (Fig. 2.14). So, the radial component ($\bar{E}_r$) of the volume-average electric field is considered only, and its variation is illustrated in Fig. 2.15. The corresponding magnitudes of G_r for SPFC and CPFC in cylindrical coordinates are obtained as, 540.65 m^{-1} and 369.55 m^{-1}, respectively, according to the aforesaid geometric dimensions of their (SPFC/CPFC) RVEs.

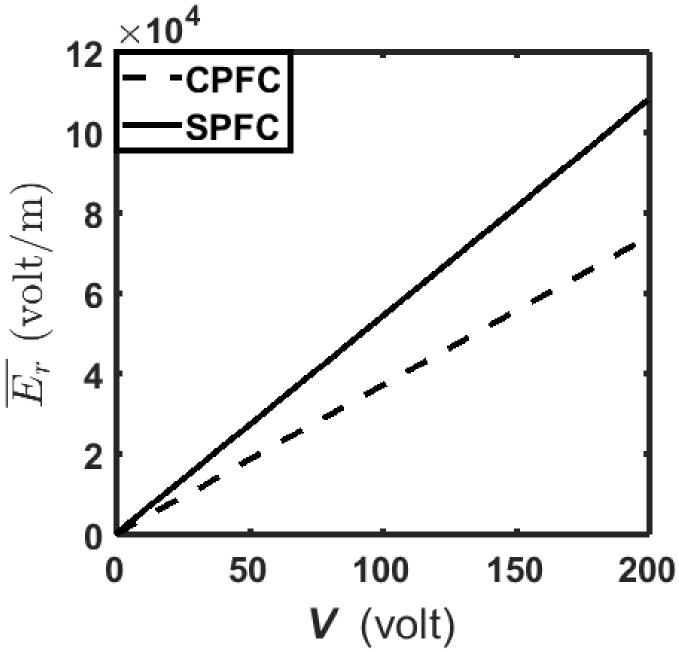

Fig. 2.15 Variations of radial component ($\bar{E}_r$) of volume-average electric field ($\bar{E}$) with the applied voltage (V).

2.7 Conclusions

In this chapter, an SPFC is designed in cylindrical/rectangular coordinates. The SPFC is comprised of unidirectional short piezoelectric fibers embedded in the epoxy matrix. The poling direction of the unidirectional fibers is considered as their longitudinal direction. The effective electro-elastic coefficients of this SPFC are evaluated using FE procedure, and it is also extended for the continuous form (CPFC) of fibers instead of their (fibers) discontinuous form (SPFC). These results reveal an indicative magnitude of an effective piezoelectric coefficient (e_{11}) while the other similar piezoelectric coefficients appear with very small magnitude. So, further study is performed to study the effects of different geometric parameters of the RVE on the effective coefficient (e_{11}), and the appropriate geometrical properties of the corresponding microstructure (RVE) are determined with an objective of the maximum magnitude of the effective coefficient (e_{11}). For the utilization of this SPFC/CPFC as a material of distributed actuator based on its effective coefficient (

e_{11}), an arrangement of surface-electrodes over its top and bottom surfaces is proposed, and the corresponding driving electric field for applied voltage through the surface-electrodes is determined. It is found that the driving electric field increases as the continuous fibers are replaced by short/discontinuous ones, while the magnitude of the coefficient (e_{11}) decreases. So, the actuation capability of the smart composite may improve or degrade due to the use of the unidirectional short/discontinuous fibers instead of the continuous ones, and it is investigated in the next chapter.

CHAPTER
3
Control capability of an extension mode short piezoelectric fiber composite (SPFC) actuator in cylindrical/rectangular coordinates

3.1 Introduction

A short piezoelectric fiber composite (SPFC) is designed in the previous chapter. For its utilization as a material of distributed actuator in control of structural vibration, an arrangement of the surface-electrodes has also been introduced. In this chapter, the control capability of this SPFC actuator is investigated considering its configurations in the cylindrical and rectangular coordinates separately (Kumar et al., 2015; Panda et al., 2015). First, the SPFC in rectangular coordinates is considered, and its actuation capability in counteraction of bending deformation of a simply-supported beam is investigated. Next, the actuation capability of the SPFC in cylindrical coordinates is investigated for controlling the vibration of an annular substrate plate. In both the cases of the present study, the control performance of SPFC actuator is compared with that of CPFC actuator in order to understand the advantages and disadvantages in the use of short/discontinuous fibers instead of continuous fibers within the piezoelectric fiber composite (PFC).

3.2 Analysis of a simply-supported beam integrated with SPFC/CPFC layer

In order to investigate the actuation-capability of presently designed SPFC actuator in rectangular coordinates, a bending analysis of a simply-supported thin beam integrated with a layer of the same actuator (Fig. 3.1) is performed. Usually, the piezoelectric actuators are used in control of deformations of flexible structures which are also susceptible to undergo large/nonlinear deflection under the mechanical loads. So, a thin substrate beam is considered, and a geometrically nonlinear analysis of the overall smart beam is carried out.

An electro-elastic nonlinear semi-analytical model of the overall smart beam is derived in this section considering small strain and large deflection. The length, width and thickness of the substrate isotropic beam are denoted as, l, b and h, respectively. The thickness of the SPFC/CPFC layer is represented by the symbol, h_p. The middle plane of the substrate beam is considered as the reference plane, and the middle point of one of the edges of the reference plane is located as the origin of the reference coordinate system (Fig. 3.1). The piezoelectric fibers in the SPFC/CPFC actuator layer are oriented along the longitudinal direction (x-axis).

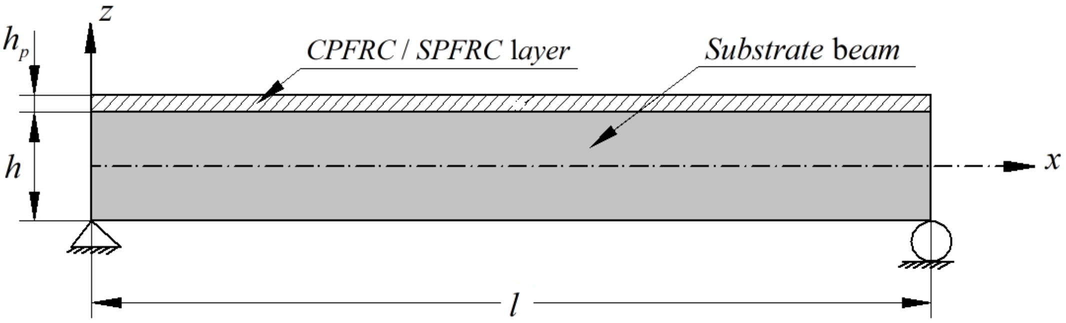

Fig. 3.1 Schematic diagram of a simply-supported beam integrated with a layer of SPFC/CPFC actuator.

3.2.1 Variational formulation for smart beam

According to the first order shear deformation theory (FSDT), the displacement components u and w at any point within the smart beam along the x and z directions, respectively can be written as,

$$u(x,z) = u_0(x) + z\phi_x(x)\,,\ \ w(x,z) = w_0(x) \tag{3.1}$$

where, u_0 and w_0 are the translational displacements along the x and z directions, respectively, at any point on the reference plane; ϕ_x is the rotation of the normal to the reference plane. The state of strain and the state of stress at any point in the smart beam can be written as,

$$\boldsymbol{\varepsilon} = \{\varepsilon_x \quad \varepsilon_z \quad \gamma_{xz}\}^{\mathrm{T}},\ \boldsymbol{\sigma} = \{\sigma_x \quad \sigma_z \quad \tau_{xz}\}^{\mathrm{T}} \tag{3.2}$$

where, ε_x and ε_z are the normal strains along the x and z directions, respectively; γ_{xz} is the shear stain in the xz-plane; σ_x and σ_z are the normal stresses along the x and z directions, respectively; τ_{xz} is the transverse shear stress in the xz-plane. According to the displacement field (Eq. (3.1)), the von Karman nonlinear strain-displacement relations can be written as,

$$\varepsilon_x = \frac{\partial u_0}{\partial x} + \frac{1}{2}\left(\frac{\partial w_0}{\partial x}\right)^2 + z\frac{\partial \phi_x}{\partial x},\ \varepsilon_z = 0,\ \gamma_{xz} = \frac{\partial w_0}{\partial x} + \phi_x \qquad (3.3)$$

According to Eq. (3.3), the strain and stress vectors (Eq. (3.2)) can be reduced as follows,

$$\boldsymbol{\varepsilon} = \{\varepsilon_x \quad \gamma_{xz}\}^{\mathrm{T}},\ \boldsymbol{\sigma} = \{\sigma_x \quad \tau_{xz}\}^{\mathrm{T}} \qquad (3.4)$$

The constitutive relations for the isotropic substrate beam and the SPFC/CPFC layer can be written as,

$$\boldsymbol{\sigma}^k = \boldsymbol{C}^k \boldsymbol{\varepsilon}^k,\ k = 1$$

$$\boldsymbol{\sigma}^k = \boldsymbol{C}^k \boldsymbol{\varepsilon}^k - \boldsymbol{e}^k \boldsymbol{E}^k,\ \boldsymbol{D}^k = (\boldsymbol{e}^k)^{\mathrm{T}} \boldsymbol{\varepsilon}^k + \in^k \boldsymbol{E}^k,\ k = 2 \qquad (3.5)$$

where, the superscript k denotes the substrate beam or the actuator layer according to its value as 1 or 2, respectively. The forms of stiffness matrix ($\boldsymbol{C}^k$), piezoelectric matrix ($\boldsymbol{e}^k$), permittivity matrix ($\in^k$), electric field vector ($\boldsymbol{E}^k$) and electric displacement vector ($\boldsymbol{D}^k$) are as follows,

$$\boldsymbol{C}^k = \begin{bmatrix} C_{11}^k & 0 \\ 0 & C_{55}^k \end{bmatrix},\ \boldsymbol{e}^k = \begin{bmatrix} e_{11}^k & 0 \\ 0 & e_{53}^k \end{bmatrix},\ \in^k = \begin{bmatrix} \in_{11}^k & 0 \\ 0 & \in_{33}^k \end{bmatrix}$$

$$\boldsymbol{E}^k = \begin{bmatrix} E_x^k & E_z^k \end{bmatrix}^{\mathrm{T}},\ \boldsymbol{D}^k = \begin{bmatrix} D_x^k & D_z^k \end{bmatrix}^{\mathrm{T}} \qquad (3.6)$$

where, C_{ij}^k are the stiffness coefficients; e_{ij}^k are the piezoelectric coefficients; $\in_{ij}^k$ are the elements of permittivity matrix; E_x^k and E_z^k are the electric field components along the x and z directions, respectively; D_x^k and D_z^k are the components of electric displacement along the x and z directions, respectively. The overall beam is considered to be subjected to the uniformly distributed transverse load of intensity, p, and thus the first variation of its (overall beam) total potential energy (δT_p) can be written as (Tiersten, 1969),

$$\delta T_p = \int_0^l \left[\left(\sum_{k=1}^{2} \int_{h_k}^{h_{k+1}} (\delta \boldsymbol{\varepsilon}^k)^{\mathrm{T}} \boldsymbol{\sigma}^k \mathrm{d}z \right) - \int_{h_k}^{h_{k+1}} \left\langle (\delta \boldsymbol{E}^k)^{\mathrm{T}} \boldsymbol{D}^k \right\rangle_{k=2} dz - (\delta w)\, p \right] dx \qquad (3.7)$$

Since the present analysis of the overall smart beam is carried out considering its small strain, the contribution of the strain to the induced electric field in the actuator layer is very small in comparison to that of the externally applied voltage across the pairs of surface-electrodes (Fig. 2.7(a)). So, it is reasonable to assume that the electric field within the actuator layer appears for the externally applied voltage only. It may be recalled from the previous chapter (Chapter 2) that the electric field within the SPFC/CPFC actuator is assumed as the average field over the volume of RVE in the view of RVE-based arrangement of surface-electrodes and uniformly applied voltage across all pairs of surface-electrodes. Since this volume-average electric field is the function of applied voltage (V) only for the small strain-based analysis (Eq. 2.44(b)), the field quantity $\boldsymbol{E}^k$ ($k=2$) in Eqs. (3.5)-(3.7) may be expressed as, $\bar{\boldsymbol{E}}^k(V)$ (or $\left[\bar{E}_x^k(V) \quad \bar{E}_z^k(V)\right]^{\mathrm{T}}$), $k=2$) where the over-bar denotes the volume-average quantity. Now, $\bar{\boldsymbol{E}}^k(V)$ has a fixed value corresponding to a specified/applied voltage (V) across the pairs of surface-electrodes, and this yields, $\delta\bar{\boldsymbol{E}}^{\boldsymbol{k}}(V)=\mathbf{0}$. Introducing this relation ($\delta\bar{\boldsymbol{E}}^{\boldsymbol{k}}(V)=\mathbf{0}$) along with Eqs. (3.3) and (3.6) in Eq. (3.7), and then employing the principle of minimum potential energy ($\delta T_p=0$), the following variational expressions associated with the homogeneous form of essential boundary conditions can be obtained,

$$\int_0^l (L_1\delta u_0 + L_2\delta w_0 + L_3\delta\phi_x)dx - N_x\delta u_0 \big|_0^l - M_x\delta\phi_x \big|_0^l = 0$$

$$L_1 = \frac{\partial N_x}{\partial x},\; L_2 = \frac{\partial Q_x}{\partial x} + N_x\frac{\partial^2 w_0}{\partial x^2} + \frac{\partial N_x}{\partial x}\frac{\partial w_0}{\partial x} + p \;,\; L_3 = \frac{\partial M_x}{\partial x} - Q_x \qquad (3.8a)$$

$$w_0 = 0 \quad \text{at} \;\; x = 0,\, l \qquad (3.8b)$$

The stress (N_x, Q_x) and moment (M_x) resultants appearing in Eq. (3.8a) are,

$$N_x = \sum_{k=1}^{2}\int_{h_k}^{h_{k+1}} \sigma_x dz,\; M_x = \sum_{k=1}^{2}\int_{h_k}^{h_{k+1}} \sigma_x z dz,\; Q_x = \sum_{k=1}^{2}\int_{h_k}^{h_{k+1}} \tau_{xz} dz \qquad (3.9)$$

Satisfying the essential boundary conditions (Eq. (3.8b), a displacement field for a particular mode of deformation of the overall beam is assumed as (Chia, 1980),

$$u_0 = U\cos(\alpha x) - \langle \pi/(4l)\rangle \Gamma^2 \sin(2\alpha x),\ w_0 = \Gamma\sin(\alpha x),$$
$$\phi_x = R\cos(\alpha x) \tag{3.10}$$

where, $\alpha = (m\pi/l)$; m is a mode number; U, Γ and R are the unknown constants. Substituting the displacement functions (Eq. (3.10)) in the variational statement (Eq. (3.8a)), the Galerkin governing equations can be obtained as,

$$\int_0^l \langle L_1 \cos(\alpha x)\rangle dx - \langle N_x \cos(\alpha x)\rangle_0^l = 0 \tag{3.11a}$$

$$\int_0^l \langle L_2 \sin(\alpha x) - (1/2)\alpha\Gamma L_1 \sin(2\alpha x)\rangle dx = 0 \tag{3.11b}$$

$$\int_0^l \langle L_3 \cos(\alpha x)\rangle dx - \langle M_x \cos(\alpha x)\rangle_0^l = 0 \tag{3.11c}$$

Substituting the displacement fields (Eq. (3.10)) in Eq. (3.11) and then simplifying the resulting expressions, the following nonlinear algebraic equations can be obtained,

$$H_1U + H_2\Gamma^2 + H_3R + H_4 = 0 \tag{3.12a}$$

$$H_5U\Gamma + H_6\Gamma^3 + H_7\Gamma R + H_8\Gamma + H_9R - H_{10}p = 0 \tag{3.12b}$$

$$H_{11}U + H_{12}\Gamma^2 + H_{13}\Gamma + H_{14}R + H_{15} = 0 \tag{3.12c}$$

In Eq. (3.12), the various coefficients are as follows,

$$\begin{gathered}
H_1 = (l/2)A_{11}\alpha^2,\ H_2 = -(2/3)A_{11}\alpha^2,\ H_3 = (l/2)B_{11}\alpha^2\ , \\
H_4 = 2e_{11}\left\langle \bar{E}_x^k(V)\right\rangle_{k=2} h_p\ , \\
H_5 = -(4/3)A_{11}\alpha^2\ ,\ H_6 = (3l/16)A_{11}\alpha^4\ ,\ H_7 = -(4/3)B_{11}\alpha^2\ , \\
H_8 = (l/2)A_{55}\alpha^2 - (l/2)e_{11}\left\langle \bar{E}_x^k(V)\right\rangle_{k=2} h_p\alpha^2\ , \\
H_9 = (l/2)A_{55}\alpha\ ,\ H_{10} = 2/\alpha\ ,\ H_{11} = (l/2)B_{11}\alpha^2\ , \\
H_{12} = -(2/3)B_{11}\alpha^2\ ,\ H_{13} = (l/2)A_{55}\alpha\ , \\
H_{14} = (l/2)\left\langle D_{11}\alpha^2 + A_{55}\right\rangle,\ H_{15} = e_{11}\left\langle \bar{E}_x^k(V)\right\rangle_{k=2}(h_p^2 + hh_p)
\end{gathered} \tag{3.13}$$

In Eq. (3.13), the different rigidity elements (A_{ij}, B_{ij}, D_{ij}) are as follows,

$$A_{11} = \sum_{k=1}^{2}\left(\int_{h_k}^{h_{k+1}} C_{11}^k dz\right),\ A_{55} = \sum_{k=1}^{2}\left(\int_{h_k}^{h_{k+1}} C_{55}^k dz\right),$$

$$B_{11}=\sum_{k=1}^{2}\left(\int_{h_k}^{h_{k+1}} C_{11}^{k} z dz\right)\ ,\ D_{11}=\sum_{k=1}^{2}\left(\int_{h_k}^{h_{k+1}} z^2 C_{11}^{k} dz\right) \qquad (3.14)$$

Equations (3.12a-3.12c) are the equilibrium equations corresponding to the geometrically nonlinear electro-elastic bending of a simply-supported beam integrated with a layer of SPFC/CPFC actuator. For numerical evaluation of the bending responses of the overall smart beam, these simultaneous nonlinear algebraic equations are solved using direct iteration method.

3.2.2 Numerical results for the analysis of smart beam

In this section, first, the variational formulation for the bending analysis of the smart beam is verified. Next, the numerical results for the nonlinear bending of the simply-supported smart beam are presented for investigating the actuation capabilities of the SPFC and CPFC actuators. The geometrical properties of the smart beam are considered as, $l=1$ m, $h=10$ mm, $h_p=250$ μm (Fig. 3.1). The material of the substrate beam is considered as Aluminum ($E=$ 70 GPa, ν = 0.3) (E and ν are Young's modulus and Poisson's ratio, respectively). The material properties of the actuator layer made of SPFC/CPFC in rectangular coordinates are given in Table 2.4. The gradients (G_x for SPFC and CPFC actuators) for computation of $\bar{E}_x^k(V)_{k=2}$ (Eq. (3.13)) are given in section 2.6.2. For presenting the numerical results, the following dimensionless parameters are considered,

$$W=(w_{x=l/2}/h)\ ,\ Q=(ps^4)/E\ ,\ S=(l/h) \qquad (3.15)$$

In order to verify the present variational formulation for the analysis of the simply-supported smart beam, first a negligibly small thickness ($h_p \approx 0$) of the deactivated ($V=0$) actuator layer is considered, and the deformed shape of the overall beam for a transversely applied mechanical load is plotted in Fig. 3.2 together with the similar result available in the literature (Fallah and Ebrahaminejad, 2014). It may be observed from Fig. 3.2 that the present results are in excellent agreement with similar results for an identical beam analyzed by (Fallah and Ebrahaminejad, 2014). Next, to verify the present variational formulation for handling the electro-elastic coupling, the overall beam is considered as a simply-supported piezoelectric beam ($h\approx 0$, $h_p=0.002$ m, $l=0.2$

m), and its electro-elastic deflections corresponding to different values of the applied electric field ($\bar{E}_x$) are computed. These results are illustrated in Table 3.1 along with the similar results obtained by developing an FE model of the same piezoelectric beam in ANSYS software. It may be observed from Table 3.1 that the present analytical results are in good agreement with the similar results obtained from the model developed in ANSYS software. These comparisons (Fig. 3.2 and Table 3.1) verify the accuracy of the present electro-elastic variational formulation for analyzing the electro-elastic bending of a smart beam.

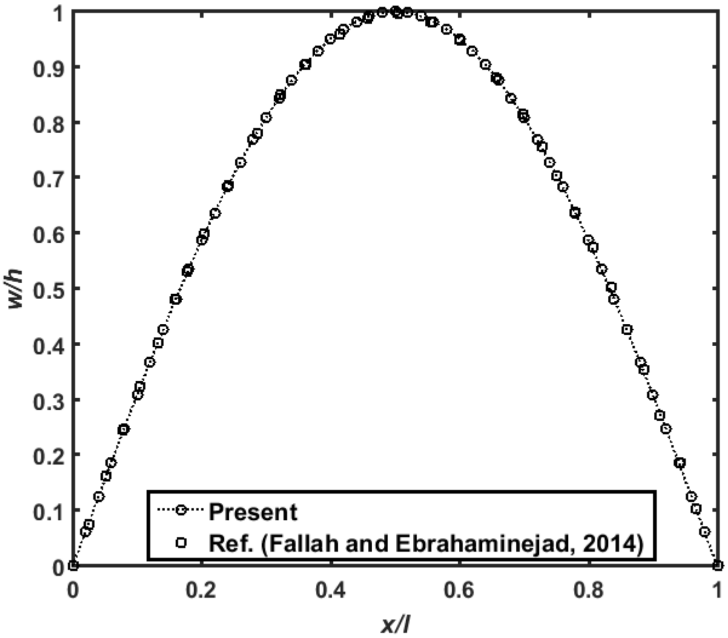

Fig. 3.2 Comparison of deformed shape of the overall simply-supported beam ($h_p \approx 0$, $V = 0$) with that of an identical beam analyzed in (Fallah and Ebrahaminejad, 2014).

Table 3.1 Transverse deflection ($w|_{x=l/2}$) of the simply-supported smart beam ($h \approx 0$, $h_p = 0.002$ m, $l = 0.2$ m) due to the applied electric field ($\bar{E}_x$).

$\bar{E}_x$ (×10³ volt/m)	$w\vert_{x=l/2}$ (×10⁻⁷ m)	
	ANSYS	Present
88.92	0.3938	0.4025
177.84	0.7876	0.8049
266.75	1.1814	1.2074
355.67	1.5752	1.6098
444.60	1.9690	2.0123

The magnitude of actuation (M_a) by the smart actuator layer at a particular applied load (Q) is measured in terms of the change in transverse deflection (W) due to an applied voltage ($M_a = \left|(W)_{V\neq 0} - (W)_{V=0}\right|$). For the linear bending deformation of the overall smart structure as well as linear piezoelectric actuator, it is well known that the magnitude of actuation by the actuator remains constant for any value of applied load (Q). The variation in the actuation-capability of the linear piezoelectric actuator with the load (Q) appears when the overall structure starts to deform nonlinearly. So, the boundary value of load (Q) between the linear and nonlinear deformations of the smart beam is first identified to study the performance of SPFC actuator layer for controlling both the linear and nonlinear deformations.

Figure 3.3 illustrates the variation of the dimensionless transverse deflection (W) of the simply-supported smart beam with the mechanical load (Q) in the absence of the external voltage. It may be observed from this figure that the overall beam undergoes nonlinear deformation as the applied load (Q) exceeds its value of 4. It may also be observed from the same figure that the deflection of the overall beam at any applied load (Q) does not change indicatively if the deactivated SPFC

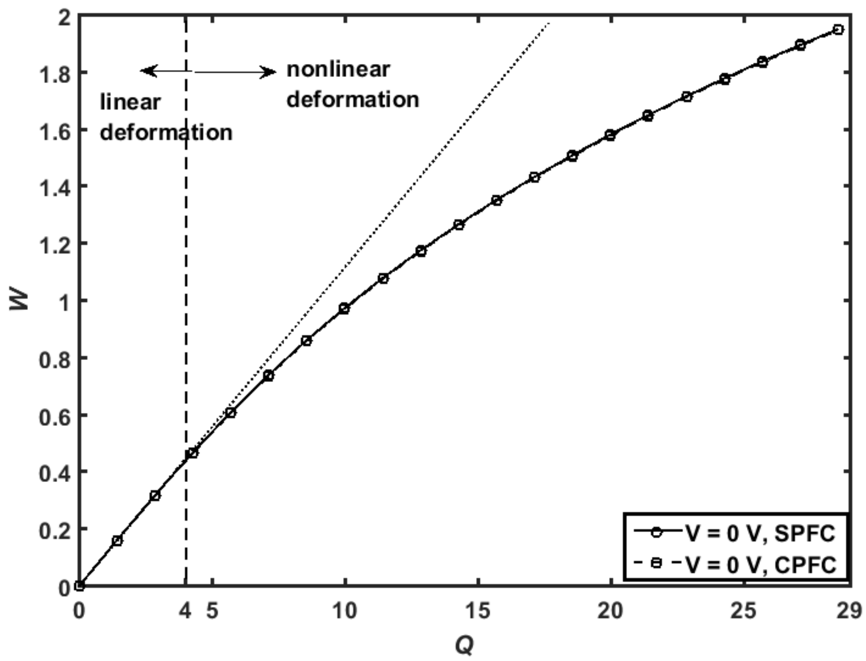

Fig. 3.3 Variation of dimensionless transverse deflections (W) at the middle point of the overall smart beam with the mechanical load (Q).

layer ($V = 0$) is replaced by the deactivated CPFC layer ($V = 0$). Thus, for both the smart composite actuators, this value ($Q = 4$) of the applied load can be referred to study the linear and nonlinear deformation characteristics of the smart beam. Figure 3.4 illustrates the variation of the magnitude of actuation (M_a) caused by SPFC/CPFC layer with the applied mechanical load (Q). For an applied voltage ($V =$ 300 volt or 500 volt), it may be observed from this figure that the magnitude of actuation caused by any of the actuators decreases with the increased mechanical load. This may be due to the fact that the rate of change of electrically induced actuation-force is lesser than that of the overall nonlinear stiffness of the smart beam even though both the parameters increase with the increasing mechanical load. For a higher value of the applied voltage, the same figure shows a greater rate of decrease of the magnitude of actuation with the increasing load (Q). So, an insignificant change in the magnitude of actuation corresponding to an increase of the applied voltage (V) can be observed at a higher mechanical load (Q). Therefore, any of the actuators (SPFC or CPFC) can be used for controlling small or moderate deflection of the overall smart beam.

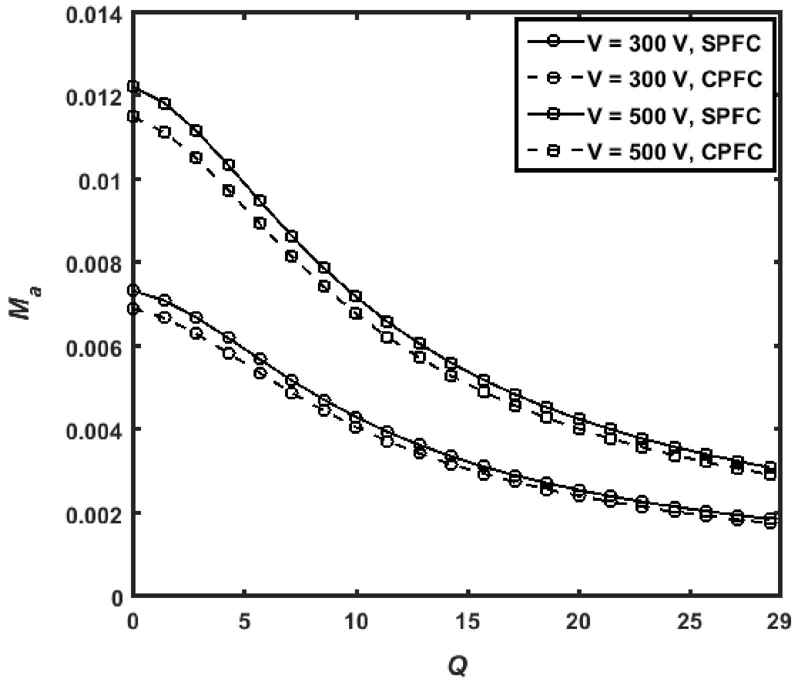

Fig. 3.4 Variations of the magnitude of actuation (M_a) by the SPFC/CPFC actuator with the applied mechanical load (Q) for different values of applied voltage (V).

It is interesting to observe from the same figure (Fig. 3.4) that the magnitude of actuation caused by SPFC actuator is more than that caused by CPFC actuator for any value of the applied voltage (V). Although a small increase of M_a occurs due to the use of the SPFC actuator instead of the CPFC actuator, but this observation is important for the usefulness of the SPFC in comparison to that of the CPFC. As discussed in the previous chapters (Chapter 1 and Chapter 2), the present SPFC actuator is designed mainly to have a flexible smart composite actuator over the CPFC actuator. Along with this advantage, the analysis shows an additional advantage of greater actuation capability in the use of SPFC actuator.

Figure 3.5 demonstrates the variations of the magnitude of actuation caused by SPFC/CPFC actuator with the applied voltage (V) for linear ($Q = 1$) and nonlinear ($Q = 20$) deformations of the overall beam. It may be observed from this figure that the magnitude of actuation linearly increases with the increasing applied voltage (V) for both the linear and nonlinear deformations of the overall beam. Similar to the previous results (Fig. 3.4), Fig. 3.5 also shows greater actuation capability of SPFC actuator as compared to that of CPFC actuator although it is a small difference in the quantitative measure.

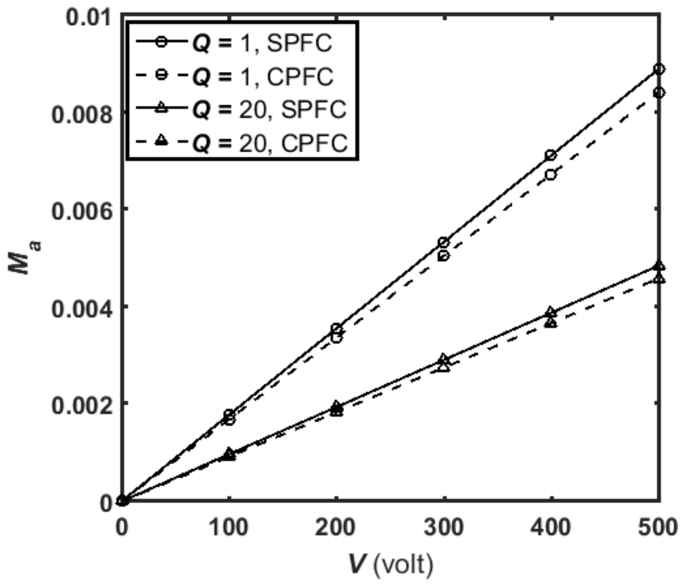

Fig. 3.5 Variations of the magnitude of actuation (M_a) by the SPFC/CPFC actuator with the applied voltages (V) for linear ($Q = 1$) and nonlinear ($Q = 20$) deformations of the overall beam.

3.3 Vibration analysis of a host annular plate integrated with the SPFC/CPFC layer

The present SPFC actuator is designed in cylindrical coordinates mainly for controlling the vibration of plane structures of revolution. In order to substantiate the corresponding control capability of the actuator, a vibration analysis of an annular plate integrated with the patches of the SPFC actuator is performed by deriving an FE model of the overall smart annular plate. The CPFC actuator is also considered instead of the SPFC actuator for a comparison study of their control capabilities.

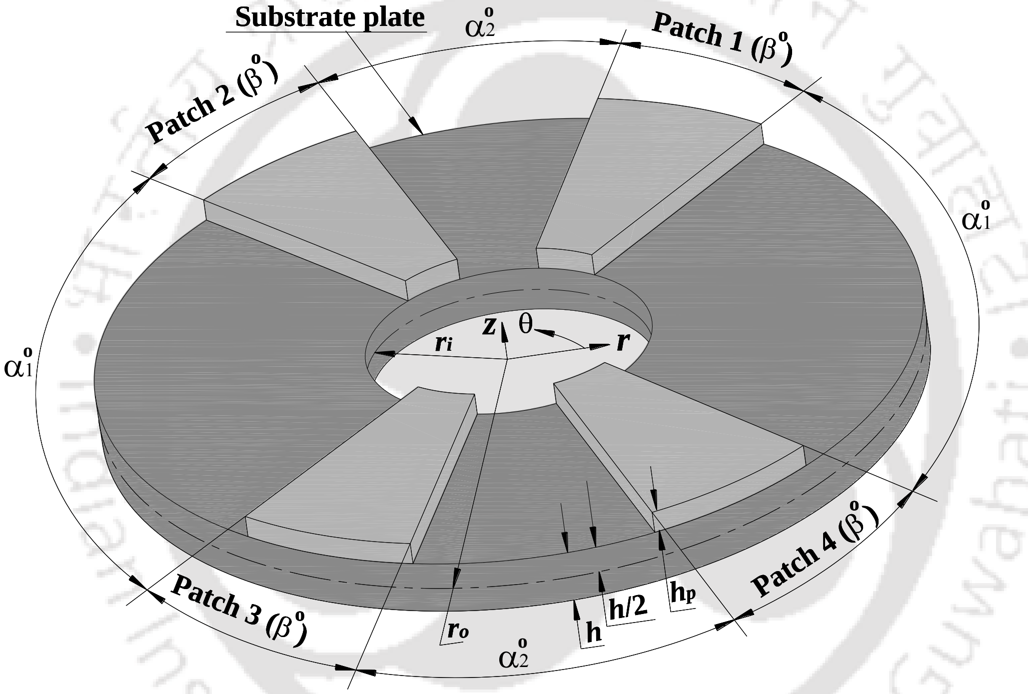

Fig. 3.6 Schematic diagram of annular plate integrated with the patches of SPFC/CPFC actuator.

Figure 3.6 shows an annular substrate plate integrated with four identical patches of SPFC/CPFC actuator. The middle plane of the annular substrate plate is considered as the reference plane, and the origin of the reference cylindrical coordinate system (r,θ,z) is located at the centre of this reference annular plane. The inner and outer radii of the overall annular plate are denoted by, r_i and r_o , respectively. The thickness of the substrate plate and the actuator-patches are symbolized by, h and h_p , respectively. The circumferential span of every patch is denoted by the angle, β^{o}, and their locations on the top surface of the substrate plate are indicated by the angles, α_1^{o} and α_2^{o} (Fig. 3.6). The radial length of patches is identical to that of the annular substrate plate, and the patches are considered to be located symmetrically ($\alpha_1^{\text{o}} = \alpha_1^{\text{o}} = \alpha^{\text{o}}$).

3.3.1 FE model of smart annular plate

A thin smart annular plate (Fig. 3.6) is considered in the present study. So, the state of stress and the state of strain at any point in the overall annular plate can be written as,

$$\boldsymbol{\sigma}_b = \{\sigma_r \;\; \sigma_\theta \;\; \tau_{r\theta}\}^{\mathrm{T}}, \quad \boldsymbol{\sigma}_s = \{\tau_{rz} \;\; \tau_{\theta z}\}^{\mathrm{T}} \tag{3.16}$$

$$\boldsymbol{\varepsilon}_b = \{\varepsilon_r \;\; \varepsilon_\theta \;\; \varepsilon_{r\theta}\}^{\mathrm{T}}, \quad \boldsymbol{\varepsilon}_s = \{\varepsilon_{rz} \;\; \varepsilon_{\theta z}\}^{\mathrm{T}} \tag{3.17}$$

The kinematics of deformation of the thin smart annular plate is defined according to the first-order shear deformation theory (FSDT) as,

$$u_p(r,\theta,z,t) = u_0(r,\theta,t) + z\phi_r(r,\theta,t) \tag{3.18a}$$

$$v_p(r,\theta,z,t) = v_0(r,\theta,t) + z\phi_\theta(r,\theta,t) \tag{3.18b}$$

$$w_p(r,\theta,z,t) = w_0(r,\theta,t) \tag{3.18c}$$

where, u_p, v_p and w_p are the displacements at any point within the plate along the r, θ and z directions, respectively; u_0, v_0 and w_0 are the displacements at any point on the reference plane along the r, θ and z directions, respectively; ϕ_r and ϕ_θ are the rotations of the normal to the reference plane with respect to the θ and r axes, respectively. The generalized displacements in Eq. (3.18) can be represented by a displacement vector ($\boldsymbol{d}_p$) as,

$$\boldsymbol{d}_p = \{u_o \quad v_o \quad w_o \quad \phi_r \quad \phi_\theta\}^{\mathrm{T}} \tag{3.19}$$

According to the displacement field (Eq. (3.18)), the strain-displacement relations at any point of the overall annular plate can be written as,

$$\varepsilon_b = (\boldsymbol{L}_{bt} + z\boldsymbol{L}_{br})\boldsymbol{d}_p, \; \varepsilon_s = \boldsymbol{L}_s\boldsymbol{d}_p \tag{3.20}$$

In Eq. (3.20), the operator matrices ($\boldsymbol{L}_{bt}$, $\boldsymbol{L}_{br}$, $\boldsymbol{L}_s$) are as follows,

$$\boldsymbol{L}_{bt}=\begin{bmatrix} \partial/\partial r & 0 & 0 & 0 & 0 \\ 1/r & (1/r)(\partial/\partial\theta) & 0 & 0 & 0 \\ (1/r)(\partial/\partial\theta) & (\partial/\partial r)-(1/r) & 0 & 0 & 0 \end{bmatrix}$$

$$\boldsymbol{L}_{br}=\begin{bmatrix} 0 & 0 & 0 & \partial/\partial r & 0 \\ 0 & 0 & 0 & 1/r & (1/r)(\partial/\partial\theta) \\ 0 & 0 & 0 & (1/r)(\partial/\partial\theta) & (\partial/\partial r)-(1/r) \end{bmatrix}$$

$$\boldsymbol{L}_{s}=\begin{bmatrix} 0 & 0 & \partial/\partial r & 1 & 0 \\ 0 & 0 & (1/r)(\partial/\partial\theta) & 0 & 1 \end{bmatrix} \tag{3.21}$$

The constitutive relations for the substrate isotropic annular plate can be written as follows,

$$\boldsymbol{\sigma}_b^k=\boldsymbol{C}_b^k\boldsymbol{\varepsilon}_b \ , \ \boldsymbol{\sigma}_s^k=\boldsymbol{C}_s^k\boldsymbol{\varepsilon}_s \ , \ k=1 \tag{3.22}$$

where, $\boldsymbol{C}_b^k$ and $\boldsymbol{C}_s^k$ $(k=1)$ are the stiffness matrices for the isotropic material of substrate plate, and the corresponding forms are as follows,

$$\boldsymbol{C}_b^k=\frac{E}{1-\nu^2}\begin{bmatrix} 1 & \nu & 0 \\ \nu & 1 & 0 \\ 0 & 0 & \frac{1-\nu}{2} \end{bmatrix}, \ \boldsymbol{C}_s^k=\frac{E}{1+\nu}\begin{bmatrix} 1/2 & 0 \\ 0 & 1/2 \end{bmatrix}, \ k=1 \tag{3.23}$$

In Eq. (3.23), E and ν stand for Young's modulus and Poisson's ratio, respectively. The constitutive relations for the SPFC/CPFC actuator can be written as follows,

$$\boldsymbol{\sigma}_b^k=\boldsymbol{C}_b^k\boldsymbol{\varepsilon}_b-\boldsymbol{e}_b\boldsymbol{E} \ , \ \boldsymbol{\sigma}_s^k=\boldsymbol{C}_s^k\boldsymbol{\varepsilon}_s-\boldsymbol{e}_s\boldsymbol{E} \ , \ \boldsymbol{D}=\boldsymbol{e}_b{}^{\mathrm{T}}\boldsymbol{\varepsilon}_b+\boldsymbol{e}_s{}^{\mathrm{T}}\boldsymbol{\varepsilon}_s+\boldsymbol{\epsilon}\,\boldsymbol{E} \ , \ k=2 \tag{3.24}$$

In Eqs. (3.23) and (3.24), the superscript k denotes the substrate plate or the actuator-patch according to its value as 1 or 2, respectively. The forms of the elastic matrices $(\boldsymbol{C}_b^k, \boldsymbol{C}_s^k, k=2)$, piezoelectric matrices $(\boldsymbol{e}_b, \boldsymbol{e}_s)$ and permittivity matrix $(\boldsymbol{\epsilon})$ appearing in Eq. (3.24) are given by,

$$\boldsymbol{C}_b^k=\begin{bmatrix} C_{11}^k & C_{12}^k & 0 \\ C_{12}^k & C_{22}^k & 0 \\ 0 & 0 & C_{66}^k \end{bmatrix}, \ \boldsymbol{C}_s^k=\begin{bmatrix} C_{55}^k & 0 \\ 0 & C_{44}^k \end{bmatrix}, \ k=2$$

$$\boldsymbol{e}_b^{\mathrm{T}} = \begin{bmatrix} e_{11} & 0 & 0 \\ e_{12} & 0 & 0 \\ 0 & e_{26} & 0 \end{bmatrix},\ \boldsymbol{e}_s^{\mathrm{T}} = \begin{bmatrix} 0 & 0 & e_{35} \\ 0 & 0 & 0 \end{bmatrix},\ \boldsymbol{\in} = \begin{bmatrix} \in_{11} & 0 & 0 \\ 0 & \in_{22} & 0 \\ 0 & 0 & \in_{33} \end{bmatrix} \tag{3.25}$$

The present analysis deals with the small amplitude vibration of the smart annular plate with an assumption of small strain. Under the small strain of the smart annular plate and uniform value of applied voltage (V) across all pairs of surface-electrodes, the components (E_r, E_θ, E_z) of volume-average electric field ($\boldsymbol{E}$) within the actuator-patch may be assumed as the functions of applied voltage (V) only as it is discussed in the previous analysis of a smart beam. The electric field ($\boldsymbol{E}$) then can be written following Eq. (2.44a) as,

$$\boldsymbol{E} = \left[G_r(V) \quad G_\theta(V) \quad G_z(V)\right]^{\mathrm{T}} V \tag{3.26}$$

The overall annular plate is considered to be subjected to a transversely distributed harmonic load ($p(r,\theta,t)$). Thus, the first variations of total potential energy (δT_p) and total kinetic energy (δT_k) of the smart annular plate at an instant of time (t) can be written as,

$$\begin{gathered} \delta T_p = \int_{r_i}^{r_o}\int_0^{2\pi}\left[\sum_{k=1}^{2}\int_{h_k}^{h_{k+1}}\left(\delta\boldsymbol{\varepsilon}_b^{\mathrm{T}}\boldsymbol{\sigma}_b^k + \delta\boldsymbol{\varepsilon}_s^{\mathrm{T}}\boldsymbol{\sigma}_s^k\right)dz - \int_{h_k}^{h_{k+1}}(\delta\boldsymbol{E}^{\mathrm{T}}\mathbf{D})_{k=2}\,dz - Q_p\right] r d\theta dr \\ Q_p = \left\langle(\delta w_p)p\right\rangle_{z=-h/2} \end{gathered} \tag{3.27}$$

$$\delta T_k = \int_{r_i}^{r_o}\int_0^{2\pi}\left(\sum_{k=1}^{2}\int_{h_k}^{h_{k+1}}\left(\left\{\delta\dot{u}_p \quad \delta\dot{v}_p \quad \delta\dot{w}_p\right\}\rho^k\left\{\dot{u}_p \quad \dot{v}_p \quad \dot{w}_p\right\}^{\mathrm{T}}\right)dz\right) r d\theta dr \tag{3.28}$$

where, ρ^k is the mass density of the substrate plate ($k=1$) or actuator-patch ($k=2$). For deriving FE model of the overall annular plate, the plane of the plate is discretized into ($n_1 \times m_1$) number of 9-node isoparametric elements. The equally spaced circumferential lines divide the radial length ($r_0 - r_i$) into n_1 number of equal divisions, while the equally spaced radial lines divide the circumference (2π) into m_1 number of equal divisions. The inner/outer boundaries of a typical element along radial and circumferential directions are denoted by, r_i^e / r_o^e and θ_i^e / θ_o^e, respectively. The generalized displacement vector (Eq. (3.19)) at any point within an element can be written as,

$$\boldsymbol{d}_p = \boldsymbol{N}_p \boldsymbol{d}_p^e \tag{3.29}$$

where, $\boldsymbol{N}_p$ is the shape function matrix and $\boldsymbol{d}_p^e$ is the elemental nodal displacement vector. Substituting Eqs. (3.20), (3.22), (3.24) and (3.26) in Eqs. (3.27)-(3.28), the first variations of the total potential energy (δT_p^e) and total kinetic energy (δT_k^e) for an element can be obtained as,

$$\delta T_p^e = \int_{r_i^e}^{r_o^e}\int_{\theta_i^e}^{\theta_o^e} \delta \boldsymbol{d}_p{}^{\mathrm{T}} \begin{bmatrix} \left\langle \begin{matrix} \boldsymbol{L}_{bt}{}^{\mathrm{T}}\boldsymbol{A}_b\boldsymbol{L}_{bt} + \boldsymbol{L}_{bt}{}^{\mathrm{T}}\boldsymbol{B}_b\boldsymbol{L}_{br} + \boldsymbol{L}_{br}{}^{\mathrm{T}}\boldsymbol{B}_b\boldsymbol{L}_{bt} \\ +\boldsymbol{L}_{br}{}^{\mathrm{T}}\boldsymbol{D}_b\boldsymbol{L}_{br} + \boldsymbol{L}_s{}^{\mathrm{T}}\boldsymbol{A}_s\boldsymbol{L}_s \end{matrix} \right\rangle \boldsymbol{d}_p \\ -\left\langle \boldsymbol{L}_{bt}{}^{\mathrm{T}}\boldsymbol{A}_{be}(V) + \boldsymbol{L}_{br}{}^{\mathrm{T}}\boldsymbol{B}_e(V) + \boldsymbol{L}_s{}^{\mathrm{T}}A_{se}(V)\right\rangle V \\ -\boldsymbol{P}_{cm}(t) \end{bmatrix} r d\theta dr \tag{3.30}$$

$$\delta T_k^e = \int_{r_i^e}^{r_o^e}\int_{\theta_i^e}^{\theta_o^e} \left(\delta \dot{\boldsymbol{d}}_p{}^{\mathrm{T}} \bar{\boldsymbol{m}} \dot{\boldsymbol{d}}_p\right) r d\theta dr \tag{3.31}$$

In Eqs. (3.30)-(3.31), the rigidity matrices ($\boldsymbol{A}_b$, $\boldsymbol{A}_s$, $\boldsymbol{B}_b$, $\boldsymbol{D}_b$), electro-elastic coupling vectors ($\boldsymbol{A}_{be}(V)$, $\boldsymbol{A}_{se}(V)$, $\boldsymbol{B}_e(V)$), mass matrix per unit area ($\bar{\boldsymbol{m}}$) and load vector ($\boldsymbol{P}_{cm}(t)$) are given by,

$$\boldsymbol{A}_b = \sum_{k=1}^{2}\int_{h_k}^{h_{k+1}} \boldsymbol{C}_b^k dz, \quad \boldsymbol{A}_s = \sum_{k=1}^{2}\int_{h_k}^{h_{k+1}} \boldsymbol{C}_s^k dz,$$

$$\boldsymbol{B}_b = \sum_{k=1}^{2}\int_{h_k}^{h_{k+1}} \boldsymbol{C}_b^k z dz, \quad \boldsymbol{D}_b = \sum_{k=1}^{2}\int_{h_k}^{h_{k+1}} \boldsymbol{C}_b^k z^2 dz$$

$$\boldsymbol{A}_{be}(V) = \int_{h_k}^{h_{k+1}} \boldsymbol{e}_b \left\{G_r(V)\ G_\theta(V)\ G_z(V)\right\}^{\mathrm{T}}\Big|_{k=2} dz,$$

$$\boldsymbol{A}_{se}(V) = \int_{h_k}^{h_{k+1}} \boldsymbol{e}_s \left\{G_r(V)\ G_\theta(V)\ G_z(V)\right\}^{\mathrm{T}}\Big|_{k=2} dz,$$

$$\boldsymbol{B}_e(V) = \int_{h_k}^{h_{k+1}} \boldsymbol{e}_b \left\{G_r(V)\ G_\theta(V)\ G_z(V)\right\}^{\mathrm{T}}\Big|_{k=2} zdz,$$

$$\boldsymbol{P}_{cm}(t) = \{0 \quad 0 \quad p(r,\theta,t) \quad 0 \quad 0\}^{\mathrm{T}},$$

$$\bar{\boldsymbol{m}} = \sum_{k=1}^{2}\int_{h_k}^{h_{k+1}} (\boldsymbol{Z}_t{}^{\mathrm{T}}\rho^k\boldsymbol{Z}_t + \boldsymbol{Z}_t{}^{\mathrm{T}}\rho^k\boldsymbol{Z}_r + \boldsymbol{Z}_r{}^{\mathrm{T}}\rho^k\boldsymbol{Z}_t + \boldsymbol{Z}_r{}^{\mathrm{T}}\rho^k\boldsymbol{Z}_r) dz,$$

$$\boldsymbol{Z}_t = \begin{bmatrix} 1 & 0 & 0 & 0 & 0 \\ 0 & 1 & 0 & 0 & 0 \\ 0 & 0 & 1 & 0 & 0 \end{bmatrix}, \quad \boldsymbol{Z}_r = \begin{bmatrix} 0 & 0 & 0 & z & 0 \\ 0 & 0 & 0 & 0 & z \\ 0 & 0 & 0 & 0 & 0 \end{bmatrix} \tag{3.32}$$

For an element without actuator-patch, the electro-elastic coupling vectors ($\boldsymbol{A}_{be}(V)$, $\boldsymbol{A}_{se}(V)$, $\boldsymbol{B}_{e}(V)$) are null vectors. Also, the rigidity matrices ($\boldsymbol{A}_b$, $\boldsymbol{A}_s$, $\boldsymbol{B}_b$, $\boldsymbol{D}_b$) and mass matrix ($\bar{\boldsymbol{m}}$) are only for the substrate plate ($k=1$). Using Eq. (3.29), the total strain energy and the total kinetic energy for a typical element can be expressed as,

$$\delta T_p^e = (\delta \boldsymbol{d}_p^e)^{\mathrm{T}} \left\langle (\boldsymbol{K}_b^e + \boldsymbol{K}_s^e)\boldsymbol{d}_p^e - \boldsymbol{P}_E^e(V)V - \boldsymbol{P}_M^e(t) \right\rangle \tag{3.33}$$

$$\delta T_k^e = (\delta \dot{\boldsymbol{d}}_p^e)^{\mathrm{T}} \boldsymbol{M}^e \dot{\boldsymbol{d}}_p^e \tag{3.34}$$

In Eqs. (3.33)-(3.34), the different matrix quantities are as follows,

$$\boldsymbol{K}_b^e = \int_{r_i^e}^{r_o^e} \int_{\theta_i^e}^{\theta_o^e} \left[\boldsymbol{N}_p{}^{\mathrm{T}} (\boldsymbol{L}_{bt}{}^{\mathrm{T}} \boldsymbol{A}_b \boldsymbol{L}_{bt} + \boldsymbol{L}_{bt}{}^{\mathrm{T}} \boldsymbol{B}_b \boldsymbol{L}_{br} + \boldsymbol{L}_{br}{}^{\mathrm{T}} \boldsymbol{B}_b \boldsymbol{L}_{bt} + \boldsymbol{L}_{br}{}^{\mathrm{T}} \boldsymbol{D}_b \boldsymbol{L}_{br}) \boldsymbol{N}_p \right] r d\theta dr$$

$$,$$

$$\boldsymbol{K}_s^e = \int_{r_i^e}^{r_o^e} \int_{\theta_i^e}^{\theta_o^e} \left[\boldsymbol{N}_p{}^{\mathrm{T}} (\boldsymbol{L}_s{}^{\mathrm{T}} \boldsymbol{A}_s \boldsymbol{L}_s) \boldsymbol{N}_p \right] r d\theta dr ,$$

$$\boldsymbol{P}_E^e(V) = \int_{r_i^e}^{r_o^e} \int_{\theta_i^e}^{\theta_o^e} \left[\boldsymbol{N}_p{}^{\mathrm{T}} \left\langle \boldsymbol{L}_{bt}{}^{\mathrm{T}} \boldsymbol{A}_{be}(V) + \boldsymbol{L}_{br}{}^{\mathrm{T}} \boldsymbol{B}_e(V) + \boldsymbol{L}_s{}^{\mathrm{T}} \boldsymbol{A}_{se}(V) \right\rangle \right] r d\theta dr ,$$

$$\boldsymbol{P}_M^e(t) = \int_{r_i^e}^{r_o^e} \int_{\theta_i^e}^{\theta_o^e} \left[\boldsymbol{N}_p{}^{\mathrm{T}} \boldsymbol{P}_{cm}(t) \right] r d\theta dr , \;\; \boldsymbol{M}^e = \int_{r_i^e}^{r_o^e} \int_{\theta_i^e}^{\theta_o^e} \left[\boldsymbol{N}_p{}^{\mathrm{T}} \bar{\boldsymbol{m}} \boldsymbol{N}_p \right] r d\theta dr \tag{3.35}$$

In Eq. (3.33), the bending and shear counterparts of the total stiffness matrix are separately formulated for implementing the selective integration in a straight forward manner. The governing equations of motion of the smart annular plate are derived employing the Hamilton's principle as,

$$\int_{t_1}^{t_2} \left(\delta T_k^e - \delta T_p^e \right) dt = 0 \tag{3.36}$$

Introducing the expressions of δT_p^e and δT_k^e (Eqs. (3.33) and (3.34)) in Eq. (3.36), the following governing equations of motion for a typical element of the smart annular plate can be obtained,

$$\boldsymbol{M}^e \ddot{\boldsymbol{d}}_p^e + (\boldsymbol{K}_b^e + \boldsymbol{K}_s^e)\boldsymbol{d}_p^e = \boldsymbol{P}_E^e(V)V + \boldsymbol{P}_M^e(t) \tag{3.37}$$

Assembling the elemental governing equations of motion (Eq. (3.37)) into the global space, the following global equations of motion of the smart annular plate can be obtained,

$$\boldsymbol{M}\ddot{\boldsymbol{X}}_p + (\boldsymbol{K}_b + \boldsymbol{K}_s)\boldsymbol{X}_p = \sum_{q=1}^{4} \boldsymbol{P}_E^q(V^q)V^q + \boldsymbol{P}_M(t) \tag{3.38}$$

In Eq. (3.38), $\boldsymbol{M}$ is the global mass matrix; $\boldsymbol{K}_b$ and $\boldsymbol{K}_s$ are bending and shear counterparts of global stiffness matrix; $\boldsymbol{P}_M(t)$ is the global mechanical load vector; $\boldsymbol{X}_p$ is the global nodal displacement vector; $\boldsymbol{P}_E^q$ is the coefficient vector of global electrical load for q^{th} actuator-patch and V^q is the applied voltage corresponding to the q^{th} actuator-patch.

3.3.2 Smart damping

The external voltage to the actuator-patches is supplied according to the negative velocity feedback control strategy. Every actuator-patch is equipped with a velocity sensor at its middle point to sense the transverse velocity ($\dot{w}^q$) at that point, and this velocity is fed back to the corresponding actuator-patch in the form of a control voltage (V^q) with a control gain (k_d^q) as,

$$V^q = -k_d^q \dot{w}^q \tag{3.39}$$

The sensing-point velocity ($\dot{w}^q$) can also be expressed in terms of the global nodal velocity vector ($\dot{\boldsymbol{X}}_p$) by introducing a transformation vector ($\boldsymbol{N}_T^q$) as,

$$\dot{w}^q = \boldsymbol{N}_T^q \dot{\boldsymbol{X}}_p \tag{3.40}$$

Using Eqs. (3.39)-(3.40), Eq. (3.38) can be expressed as,

$$\begin{gathered} \boldsymbol{M}\ddot{\boldsymbol{X}}_p + (\boldsymbol{K}_b + \boldsymbol{K}_s)\boldsymbol{X}_p = \left(-\sum_{q=1}^{4} \boldsymbol{C}^q(\dot{w}^q) \right) \dot{\boldsymbol{X}}_p + \boldsymbol{P}_M(t), \\ \boldsymbol{C}^q(\dot{w}^q) = \left\langle \boldsymbol{P}_{Ec}^q(\dot{w}^q) k_d^q \boldsymbol{N}_T^q \right\rangle \end{gathered} \tag{3.41}$$

In Eq. (3.41), $\boldsymbol{P}_{Ec}^q(\dot{w}^q)$ can be obtained by introducing Eq. (3.39) in the expression of $\boldsymbol{P}_E^q(V^q)$. Equation (3.41) can also be written in a simplified form as,

$$\boldsymbol{M}\ddot{\boldsymbol{X}}_p + \boldsymbol{C}_t \dot{\boldsymbol{X}}_p + \boldsymbol{K}_t \boldsymbol{X}_p = \boldsymbol{P}_M(t), \; \boldsymbol{C}_t = \sum_{q=1}^{4} \boldsymbol{C}^q(\dot{w}^q), \; \boldsymbol{K}_t = (\boldsymbol{K}_b + \boldsymbol{K}_s) \tag{3.42}$$

The damping matrix ($\boldsymbol{C}_t$) in Eq. (3.42) signifies an electrically induced smart damping in the overall plate. For the linear relation between the electric field ($\boldsymbol{E}$) and applied voltage (V) or for constant values of G_r, G_θ and G_z, the damping coefficient matrix (C_t) is independent of sensing-point velocities ($\dot{w}^q$). Otherwise, it (C_t) would vary according to the velocities of sensing-points.

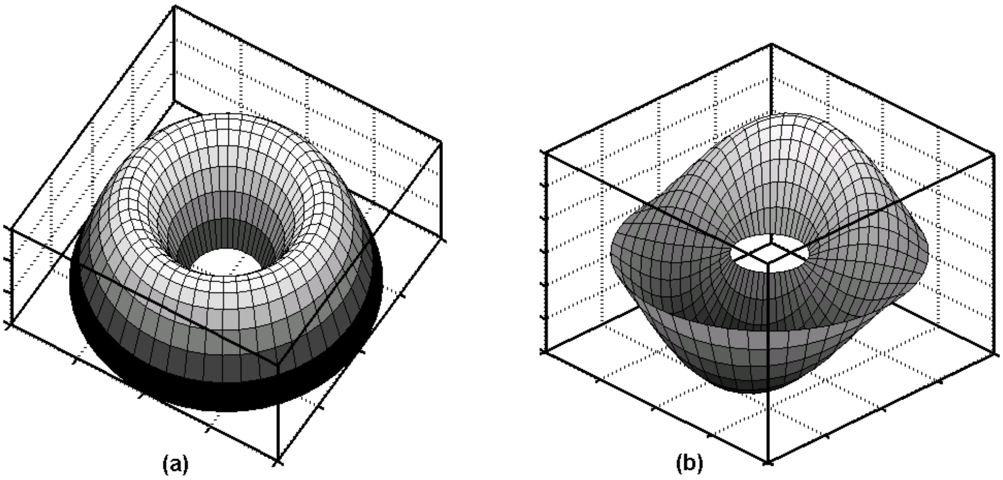

Fig. 3.7(a) First and (b) second bending mode-shapes of the simply-supported overall annular plate.

In the present analysis, the control capability of the patches of SPFC/CPFC actuator is assessed within a specified range of driving frequency. Within that range of frequency, the simply-supported ($v_o = 0$, $w_o = 0$, $\phi_\theta = 0$ at $r = r_i$ and r_o) overall annular plate can vibrate in a shape of its first or second bending mode as shown in Fig. 3.7. Since the actuator-patches are attached to the top-surface of the substrate plate, they act mainly against the mechanically induced radial stress (σ_r) on the same substrate-surface for every mode of vibration. Now, for both modes (Fig. 3.7), the radial stress (σ_r) at the top substrate-surface may not be distributed in a uniform manner along the circumferential direction. So, for effective control of both the modes of vibration, the voltage to the actuator-patches is to be supplied in an adequate manner so that every actuator-patch can act against the mechanically induced radial stress (σ_r) around its location. In order to conform this in the present use of velocity feedback control strategy, every actuator-patch is equipped with a velocity-sensor and activated according to the corresponding local velocity. As a consequence, one configuration (locations) of actuator-patches may not be sufficient for effective control of all modes of vibration within a given range of driving frequency. But, it (configuration) is to be utilized for the same purpose because of the physical infeasibility in shifting the patch-configuration during operation of the overall plate within a range of driving frequency. On this ground, the activation of actuator-patches according to their local velocity facilitates to control several modes of vibration of the overall plate even though the patch-configuration remains the same.

3.3.3 Numerical results for the analysis of vibration of the smart annular plate

In this section, first the FE formulation for the smart annular plate is verified. Next, the control capability of the SPFC/CPFC actuator is substantiated through the numerical evaluation of frequency responses of the simply-supported smart annular plate. The geometrical properties of the overall annular plate are considered as, $r_i = 0.25$ m, $r_o = 1$ m, $h = 4$ mm, $h_p = 250$ μm, $\beta = 60^{\circ}$ and $\alpha = 30^{\circ}$. The substrate annular plate is considered to be made of Aluminum (E = 70 GPa, ν = 0.3, ρ = 2700 kg/m^3) while the material properties of the smart actuator patches are given in Table 2.3. The density of actuator patches is taken according to the rule of mixture ($\rho_c = 3666$ kg/m^3). For the linear relation between the electric field ($\boldsymbol{E}$) and the applied voltage (V) (Fig. 2.15), the parameters G_r, G_θ and G_z have constant values which are taken from section 2.6.2. For the constant values of these parameters, the damping coefficient matrix ($\boldsymbol{C}_t$) is independent of the velocities ($\dot{w}^q$) at sensing-points, and it yields linear governing equations of motion (Eq. (3.42)) of the overall smart annular plate. In order to excite first two bending modes (Fig. 3.7) of the overall annular plate, the transversely distributed harmonic mechanical load is considered as,

$$p(r,\theta,t) = p\langle 1+\cos(\theta)\rangle e^{j\omega t}, \quad j=\sqrt{-1} \tag{3.43}$$

where, p indicates the intensity of the transversely distributed load and ω is the driving frequency. For the steady-state linear vibration of the overall plate under this mechanical excitation (Eq. (3.43)), the nodal displacement vector ($\boldsymbol{X}_p$) can be written as (Meirovitch, 2007),

$$\boldsymbol{X}_p = \bar{\boldsymbol{X}} e^{j\omega t}, \quad \bar{\boldsymbol{X}} = (\boldsymbol{X}_R + j\boldsymbol{X}_I) \tag{3.44}$$

where, $\bar{\boldsymbol{X}}$ is a complex nodal displacement vector and $\boldsymbol{X}_R / \boldsymbol{X}_I$ is its real/imaginary counterpart. Substituting Eq. (3.44) in the linear form of governing equations of motion (Eq. (3.42)), the following algebraic equations can be obtained,

$$\left(-\omega^2\boldsymbol{M}+j\omega\boldsymbol{C}_t+\boldsymbol{K}_t\right)\bar{\boldsymbol{X}}=\boldsymbol{P}_M^0 \tag{3.45}$$

The complex nodal displacement vector ($\bar{X}$) can be obtained by solving Eq. (3.45), and the absolute value of the same ($\bar{X}$) is the nodal displacement-amplitude vector for the linear steady-state vibration of the smart annular plate.

Table 3.2 Comparison of the first two dimensionless natural frequencies ($\Omega_0=\omega_0 r_0\sqrt{\rho h/D}$, $\Omega_1=\omega_1 r_0\sqrt{\rho h/D}$) of the simply-supported annular plate ($h_p\approx 0$) with the similar results given in (Chakraverty et al., 2001)

(ν = 1/3, r_i/r_0 = 0.4, h/r_0 = 0.001), $D=Eh^3/12(1-\nu^2)$).

Source	Ω_0	Ω_1
Chakraverty et al., 2001	28.08	30.09
Present FE results	28.35	30.43

In order to verify the present FE model of the smart annular plate, the dimensionless natural frequencies (Ω_0, Ω_1) for first two bending modes of vibration of the simply-supported annular plate ($h_p\approx 0$) are computed and compared with the similar results available in the literature (Chakraverty et al., 2001). This comparison is illustrated in Table 3.2. Table 3.2 shows a good agreement of present results with similar results reported in an earlier study (Chakraverty et al., 2001). This comparison verifies the accuracy of the present FE model for the annular plate. Next, the modelling of electro-elastic coupling is verified. Since similar smart composite actuator is not available in the literature, this verification is carried out considering a circular substrate plate integrated with a vertically poled monolithic piezoelectric layer. A negligibly small thickness ($h\approx 0$) of substrate plate is considered, and the transverse deflections at different radial locations of the simply-supported overall smart circular plate are computed for an applied electric field across the top and bottom electrode-surfaces of the piezoelectric layer. These results are then compared with those for a similar smart circular plate studied by Dong et al. (Dong et al., 2007). Figure 3.8 illustrates this comparison, and it shows an excellent agreement of present results with the similar published results (Dong et al., 2007). Thus, the present FE formulation is verified for handling the electro-elastic coupling in piezoelectric actuator.

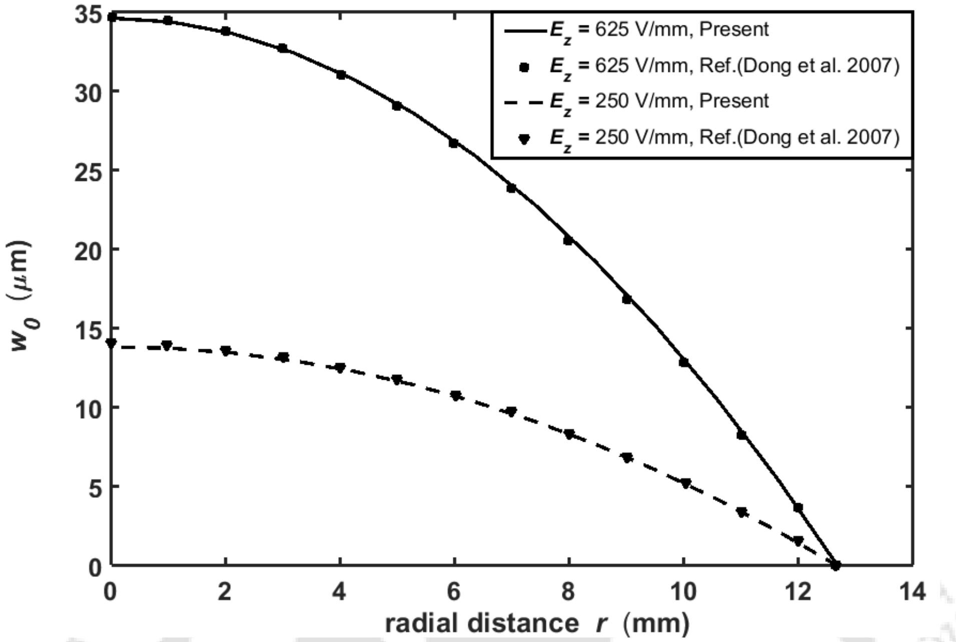

Fig. 3.8 Verification of FE formulation for handling electro-elastic coupling in piezoelectric actuator.

In order to present the frequency responses of the overall annular plate, the transverse displacement-amplitude (A_w) of flexural vibration at a point ($(r_o - r_i)/2, \pi/4, 0$) on the plate is computed at every frequency and represented by, $W = (A_w / h)$. The present SFC/CPFC actuators are utilized to reduce the amplitude of vibration of the overall annular plate by inducing smart damping within it (overall plate). The maximum reduction of amplitude due to smart damping occurs at the resonant frequency for any mode of vibration. So, for every mode of vibration, the efficiency of actuators (SPFC and CPFC) in inducing smart damping within the overall plate is measured in terms of the change of transverse displacement-amplitude (W_{peak}) at the resonant frequency. All actuator-patches are considered to be activated by a uniform value of the control gain ($k_d^q = k_d$, $q =$ 1, 2, 3, 4). But, the velocity-amplitudes corresponding to the locations of velocity-sensors may be of different values. So, the control-voltages for four actuator-patches are computed separately at any frequency of vibration, and the maximum one (V^m) is taken at that frequency for presenting the numerical results. Figure 3.9(a) demonstrates the frequency responses of the smart annular plate when the actuator-patches are either made of SPFC or made of CPFC. The corresponding variations of control-voltage (V^m) are also illustrated in Fig. 3.9(b).

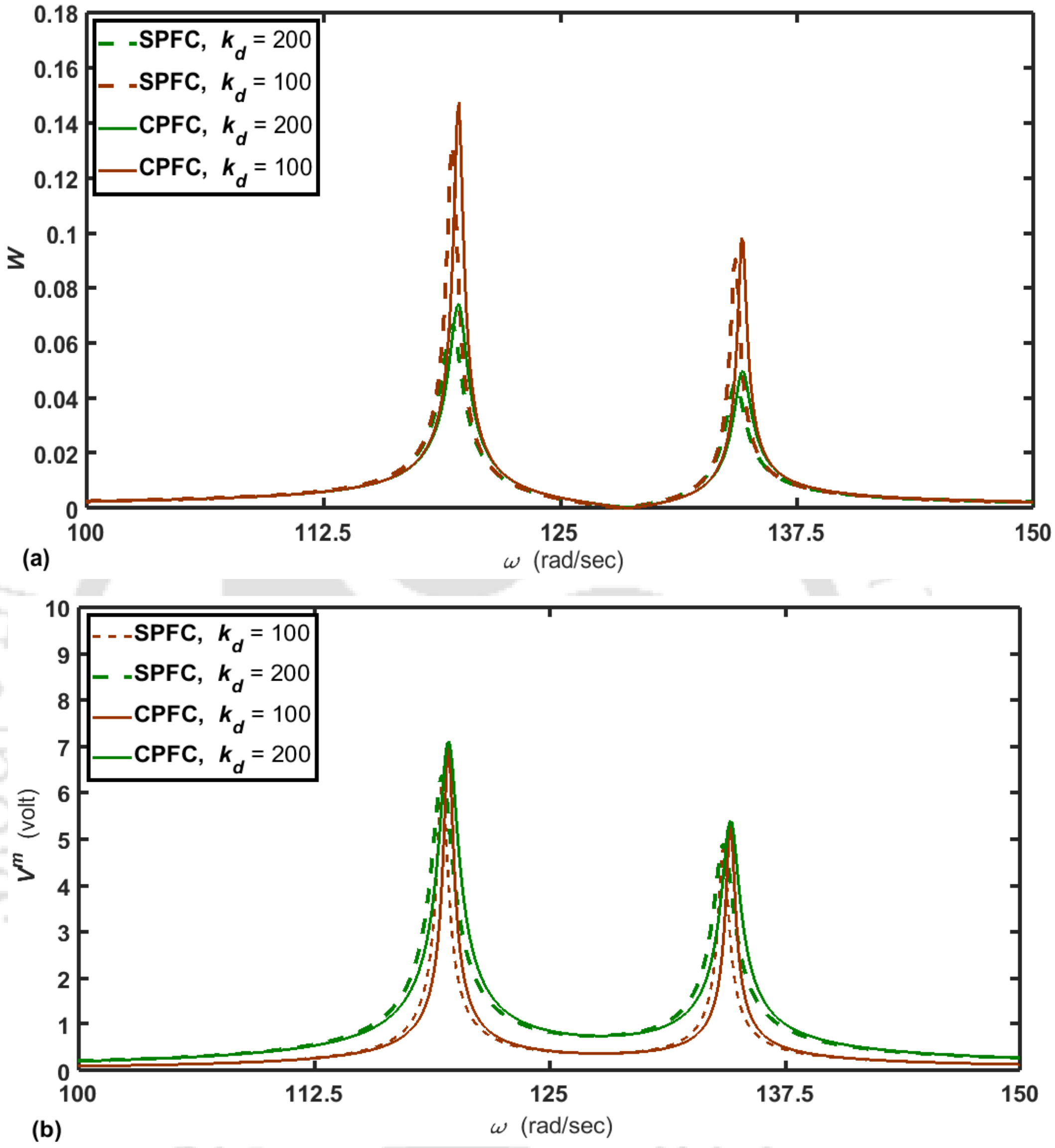

Fig. 3.9(a) Controlled frequency responses of the annular plate integrated with the patches of SPFC/CPFC actuator, (b) variations of corresponding control voltage (p = 0.3 N/m², k_d = 100, 200).

It may be observed from Fig. 3.9 that the SPFC/CPFC induces significant damping within the overall annular plate in the expense of reasonable control voltage. The smart damping in the overall plate can also be increased by increasing the value of the control-gain (k_d). But, the corresponding required control-voltage (V^m, Fig. 3.9(b)) remains almost the same because of the constant value of load-parameter (p). For a particular value of the control-gain (k_d), Fig. 3.9 illustrates an important observation that the induced damping in the overall plate by CPFC actuator is a little lesser than that by SPFC actuator in the expense of more control-voltage (V^m). In order to exemplify this difference for every mode (first and second modes) of vibration, the variations of peak amplitude (W_{peak}) either with the load parameter (p , a constant value of k_d) or with the control gain (k_d , a constant value of p) are presented in Figs. 3.10 and 3.11.

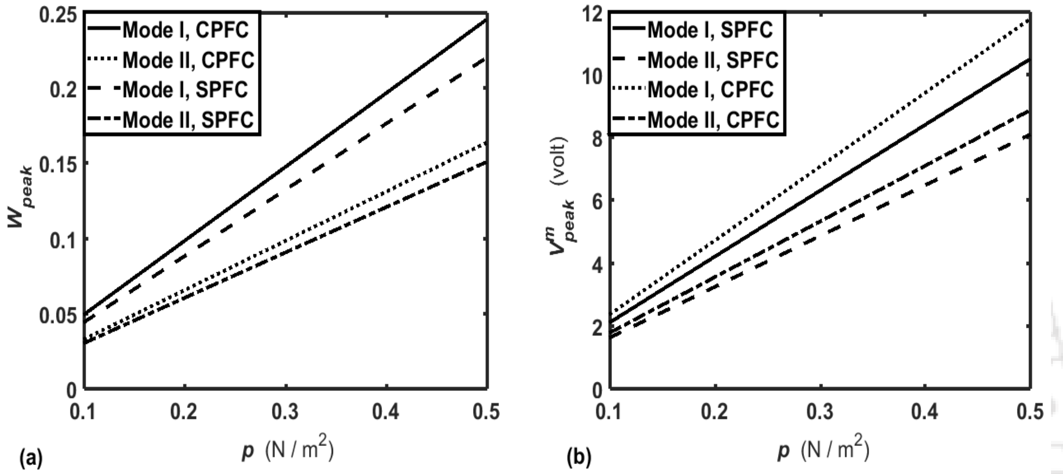

Fig. 3.10 Variations of (a) the peak-amplitude (W_{peak}) and (b) the corresponding control voltage (V^m_{peak}) with the load-parameter (p) for first two bending modes of vibration of the overall annular plate ($k_d = 100$).

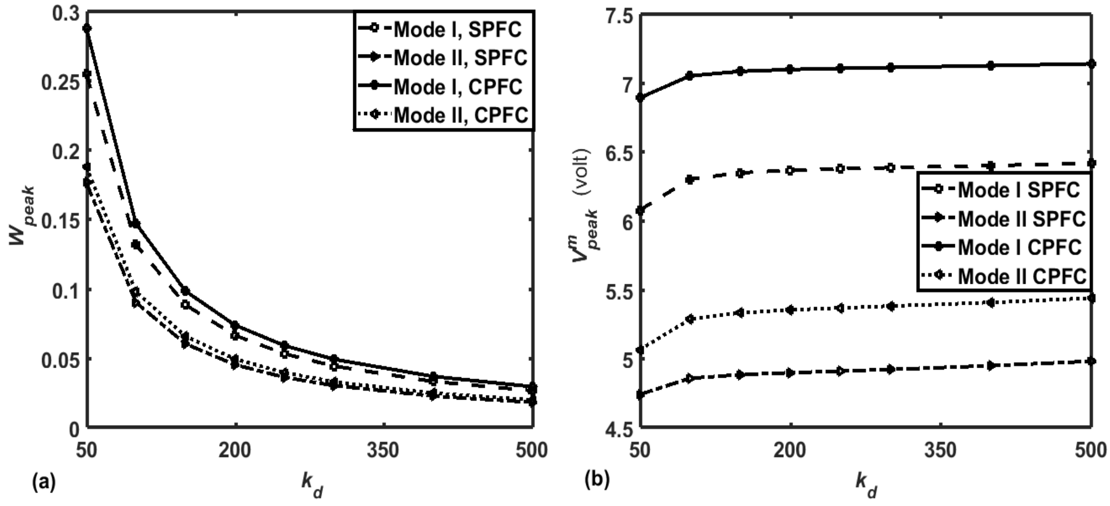

Fig. 3.11 Variations of (a) the peak-amplitude (W_{peak}) and (b) the corresponding control voltage (V^m_{peak}) with control gain k_d for first two bending modes of vibration of the overall annular plate (p = 0.3 *N/m²*).

Figure 3.10 illustrates the variations of peak amplitude (W_{peak}) and the corresponding control voltage (V_{peak}^{m}) with the load-parameter (p) for a constant value of the control gain ($k_d = 100$). Figure 3.11 demonstrates the variations of the same parameters (W_{peak}, V_{peak}^{m}) with the control gain (k_d) for a constant value of the load-parameter ($p = 0.3$ N/m^2). In comparison to CPFC actuator, it may be observed from Figs. 3.10 and 3.11 that the SPFC actuator induces more damping in the expense of lesser control-voltage. This difference also increases as the value of W_{peak} increases either by increasing the value of load-parameter (p, a constant value of k_d) or by reducing the value of control gain (k_d, a constant value of p). However, from these observations (Figs. 3.9-3.11), it may be concluded that the control capability of PFC actuator with the cylindrical principal material system can be improved by the use of short/discontinuous piezoelectric fibers instead of the similar fibers in continuous form. The use of the short/discontinuous fibers instead of the continuous fibers also facilitates to have greater flexibility and conformability of the smart actuator.

For constant values of load-parameter (p) and control gain (k_d), Fig. 3.12 illustrates the variations of peak-amplitude (W_{peak}) and the corresponding control voltage (V_{peak}^{m}) with the thickness (h_p) of the actuator-patches for first bending mode of vibration of the overall annular plate. For every value of h_p, W_{peak} is computed at the corresponding resonant frequency (for the first mode). The variation of W_{peak} at a resonant frequency infers the change of damping within the overall annular plate. So, Figs. 3.12(a) and 3.12(b) indicate that a significant damping within the overall annular plate in the expense of a low value of control voltage can be achieved by increasing the thickness of the SPFC/CPFC actuator-patches. But, for constant values of k_d and p, this increase of damping continues up to the certain value of increasing h_p. Beyond that value of h_p, the negligibly small rate of decrease of W_{peak} with increasing h_p (Fig. 3.12(a)) appears, and it indicates insignificant effect of h_p on the smart damping within the overall plate.

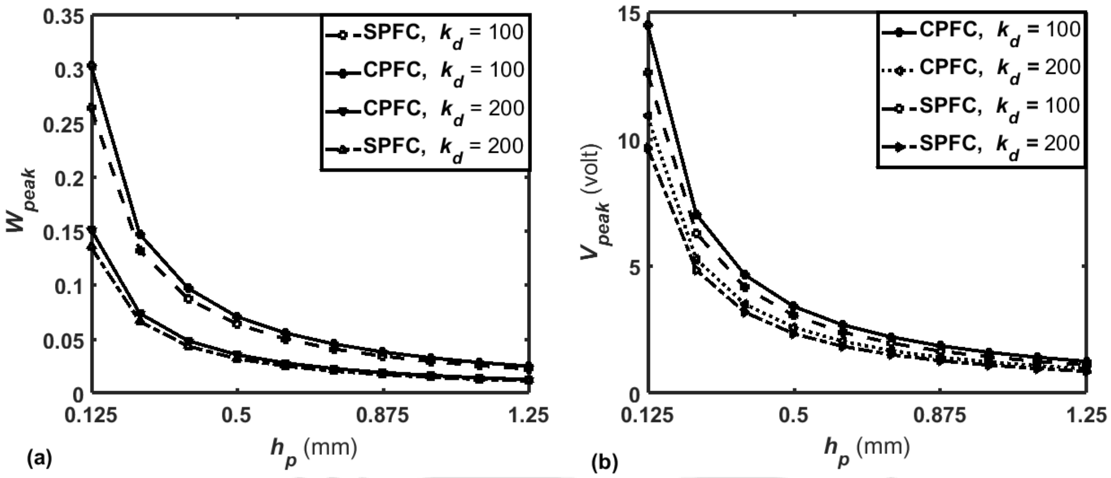

Fig. 3.12 Variations of (a) the peak-amplitude (W_{peak}) and (b) the corresponding control voltage (V^m_{peak}) with the thickness of (h_p) actuator-patches ($p = 0.3$ *N/m²*, $k_d = 100$ or 200) for first bending mode of vibration of the smart annular plate.

3.4 Conclusions

In this chapter, the actuation capability of the SPFC actuator in counteraction/control of structural deformation/vibration is investigated by taking the host structures of a simply-supported beam and annular plate. The SPFC is a modified form of CPFC, and thus the actuation capability of the SPFC is investigated with reference to the same of the CPFC. First, the actuation capability of the SPFC/CPFC in rectangular coordinates is investigated by means of utilizing it for counteraction of moderate bending deflection of a simply-supported beam. A layer of SPFC/CPFC actuator is attached to the top surface of the host beam, and the bending deformation characteristics of the smart beam are studied by deriving a semi-analytical model based on the first-order shear deformation theory and von Karman nonlinear strain-displacement relations. The semi-analytical model is first verified, and then the numerical results for bending deformations of the smart beam are evaluated with and without applying the external voltage. These results reveal significant actuation capability of the SPFC actuator for counteraction of small and moderate bending deflections of beams. The results also reveal that the actuation capability of the PFC actuator increases when short fibers (SPFC) are used instead of continuous fibers (CPFC) retaining the same applied voltage and arrangement of surface-electrodes.

Next, the actuation capability of the SPFC/CPFC in cylindrical coordinates is investigated by utilizing it for control of transverse vibration of an annular substrate plate. The SPFC/CPFC actuator is used in the form of patches which are attached to the top surface of the simply-supported annular plate. The overall smart annular plate is considered to operate within a frequency range that includes its (overall plate) first two natural bending modes. For efficient control of both the modes of vibration of the overall plate, the actuator-patches are activated by means of the feedback of their local transverse velocities. Based on this control strategy and the first-order shear deformation theory, an FE model of the smart annular plate is developed, and its frequency responses corresponding to its first two bending modes of vibration are evaluated. These results exhibit significant performance of both the actuators (SPFC/CPFC) in inducing smart damping within the overall annular plate. It is observed that the SPFC possesses a little more control power than that of the CPFC even though the magnitude of the concerned coefficient (e_{11}) for SPFC (Table 2.3) is lesser than that for CPFC. The overall analysis suggests short piezoelectric fibers instead of continuous fibers along with a special arrangement of surface-electrodes for achieving better actuation capability, greater flexibility and good conformability of the PFC actuator.

CHAPTER 4

A comparative study on the smart damping capabilities of cylindrically orthotropic piezoelectric fiber composite actuators in vibration control of annular plates

4.1 Introduction

The literature review in Chapter 1 shows a good number of studies on the actuation capabilities of horizontally and vertically reinforced 1-3 PFC actuators (Mallik and Ray, 2003; Smith and Auld, 1991). Of these 1-3 PFCs, the horizontally reinforced 1-3 PFC can provide in-plane actuation force, and thus it is mostly utilized for counteraction of the bending mode of deformation of thin-walled and flexible structures. This 1-3 PFC is presently utilized for control of bending deformation of thin annular/circular plates. For efficient utilization of this 1-3 PFC (Mallik and Ray, 2003), its construction is converted from rectangular to cylindrical coordinates, and the laminate is made in the cylindrical coordinate frame as shown in Fig. 4.1(a). Every layer of this laminate is a cylindrically orthotropic 1-3 PFC lamina that is comprised of transversely poled piezoelectric fibers. For control activity of every 1-3 PFC layer, the external electric field would act in the transverse direction, and it is achieved by means of supplying external voltage across the top and bottom fully electrode-surfaces (Fig. 4.1(a)). The poling direction (p) of a 1-3 PFC layer within the laminate is in opposite to that of its consecutive layers so that the major electrically induced actuation forces from all the layers appear in the same (positive/negative) radial direction. For achieving the major in-plane actuation force along the circumferential direction, a similar laminate can also be formed by altering the orientation of the fibers in every layer from radial to the circumferential direction. This laminate is also shown in Fig. 4.1(b). The actuation capabilities of these PFC laminates (Figs. 4.1(a) and 4.1(b)) are quantified by the piezoelectric coefficient (e_{31}) of the fibers. As the piezoelectric coefficient (e_{33}) of the fibers has a greater magnitude than that of the coefficient (e_{31}) of the same fibers, the 1-3 PFC based on the piezoelectric coefficient (e_{33}) may possess greater actuation capability. So, it was implemented in the design of 2-2 PFC (AFC/MFC), and presently the same has been performed for the design of CPFC or 1-3 PFC in cylindrical coordinates (Chapter 2) particularly for having the in-plane actuation force based on the piezoelectric coefficient of maximum magnitude. The present SPFC (Chapter 2) is a modification of the CPFC mainly for having greater flexibility and conformability. However, similar to the laminates in Figs. 4.1(a)

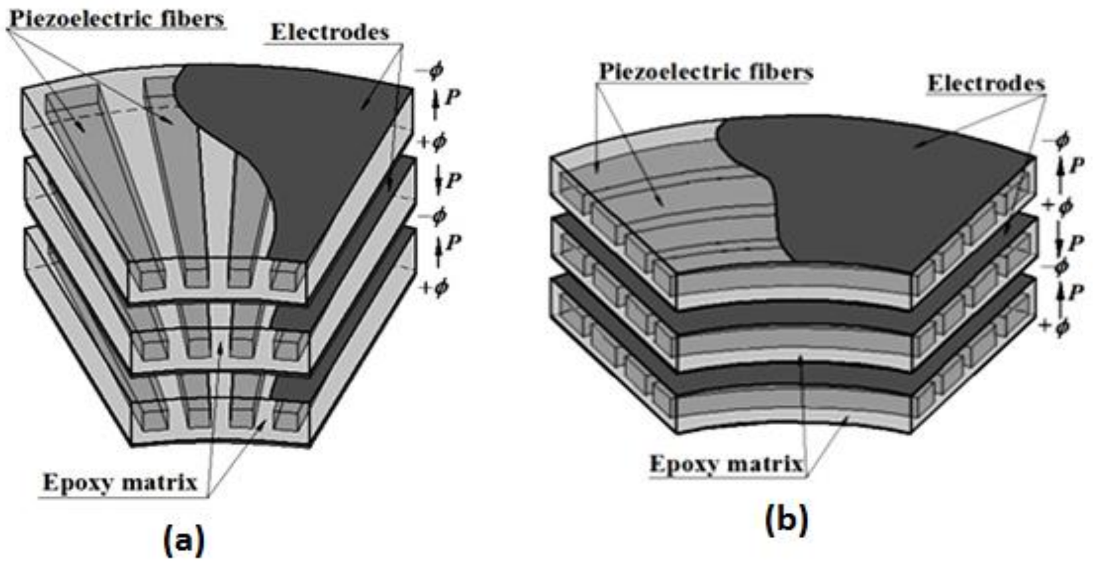

Fig. 4.1 Schematic diagrams of cylindrically orthotropic PFC laminates with (a) radially or (b) circumferentially reinforced fibers with transverse poling direction (ϕ: electric potential, p: poling direction of fibers).

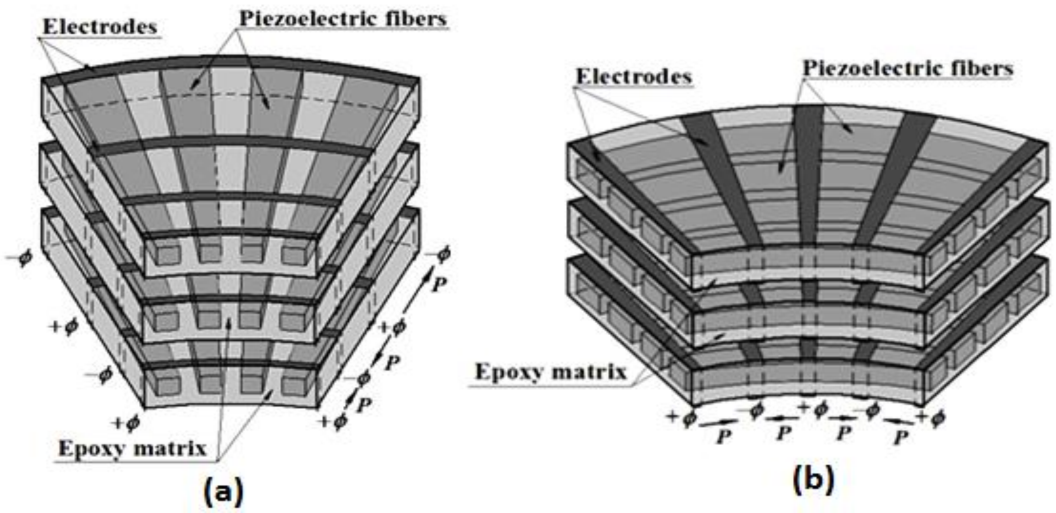

Fig. 4.2 Schematic diagrams of cylindrically orthotropic PFC laminates with (a) radially or (b) circumferentially reinforced fibers with longitudinal poling direction (ϕ: electric potential, p: poling direction of fibers).

and 4.1(b), the laminates of present SPFC/CPFC (Fig. 2.8) can also be formed for achieving the in-plane actuation force either in radial or in the circumferential direction as shown in Figs. 4.2(a) or 4.2(b), respectively. These PFC laminates act as the extension mode PFC actuators.

Generally, an extension mode piezoelectric actuator in cylindrical coordinates is attached to the top/bottom surface of an annular or a circular plate. The actuator provides the in-plane actuation forces along both the radial and circumferential directions against the mechanically induced in-plane normal stresses in the overall plate due to its bending mode of deformation. As the requirement of actuation force usually appears in both the radial and circumferential directions in control of flexural vibration of an annular/a circular plate, any of the aforesaid PFC laminates (Figs. 4.1 and 4.2) can be utilized. But, it is not possible to achieve identical control-performance of all the PFC laminates as per their electro-elastic properties. So, a quantitative assessment of their (PFC laminates in Figs. 4.1 and 4.2) control-capabilities or a quantitative comparative study on their (PFC laminates) control-capabilities is needed to identify appropriate one for efficient control of vibration of an annular or a circular plate. It is carried out in this chapter to address appropriate one among the available 1-3 PFCs (Figs. 4.1 and 4.2) for efficient control of an annular plate (Kumar et al., 2017). It should be noted here that this comparison study is performed considering the PFC laminates with continuous piezoelectric fibers. Every PFC actuator/laminate is presently utilized in the form of patches which are optimally configured over the host plate-surface through the proposition of a new numerical methodology. With the aid of these optimal configurations of the PFC actuators, they are considered to act in the form of smart dampers, and their actuation/damping capabilities are quantified for a study on their relative control-capabilities. The overall study is presented in the following manner.

First, a configuration of an annular plate integrated with PFC actuator-patches is presented for effective utilization of the actuator-patches by means of the feedback of their local velocities. Next, the geometrical and material properties of the PFC actuators (Figs. 4.1 and 4.2) are outlined for handling all these actuators in a uniform manner especially for a comparative study on their control-capabilities. On the basis of these properties of PFC actuators, the functional relations between the driving electric field and applied voltage are evaluated for all the actuators. These relations are subsequently utilized in the derivation of an FE model of the smart annular plate. With the aid of this FE model, a new numerical methodology in deciding the optimal configuration of actuator-patches corresponding to a mode of vibration of the smart annular plate is presented. Through this numerical methodology, the optimal configurations of the smart annular plate for different PFC actuators are decided for each of its (plate) fundamental symmetric and asymmetric modes of vibration. Based on these optimal configurations of the smart annular plate, the modal damping-capabilities of the PFC actuators are evaluated. These evaluated results for each of the fundamental symmetric and asymmetric modes of vibration are then analyzed for the study on their (PFC actuators) relative damping-capabilities. The numerical results not only address the control/damping-capabilities of the actuators in a common reference frame of the annular plate but also recommend the potential one among the aforesaid PFC actuators in control of similar plane structures.

4.2 Configuration of smart annular plate

A smart annular plate is shown in Fig. 4.3 considering two patches of PFC actuator over the top surface of the host annular plate. The middle plane of the host annular plate is considered as the reference plane, and the centre of this reference annular plane is taken as the origin of the reference cylindrical coordinate system ($r\theta z$) (Fig. 4.3). The inner and outer radii of the host annular plate/annular patches are denoted by, r_i / r_i^p and r_o / r_o^p, respectively. The inner/outer circumferential boundary of the annular patches is denoted by, $\theta_{iq}^p / \theta_{oq}^p$ where q indicates a patch among the N_p number of patches. The thickness of the host plate/patches is denoted by, h / h_p. The number (N_p), size and locations ($r_i^p, r_o^p, \theta_{iq}^p, \theta_{oq}^p$) of the actuator-patches vary in the subsequent analysis of the overall plate. For effective utilization of all the actuator-patches in control of a bending mode of vibration of the overall plate, every actuator-patch would act against the time-varying mechanical stresses around its location. In order to achieve this control-activity of the actuator-patches, presently the velocity feedback control strategy is utilized by means of locating velocity sensors at the middle points of the patches. Every actuator-patch then acts against the local mechanical stresses as per its own velocity sensed by the associated velocity sensor. According to this control strategy, the electrically induced actuation forces in the actuator-patches appear in the form of damping forces within the overall plate. So, the active control capability of an actuator is achieved as its active damping-capability that is presently quantified by means of the modal loss factor for the individual mode of vibration of the overall plate.

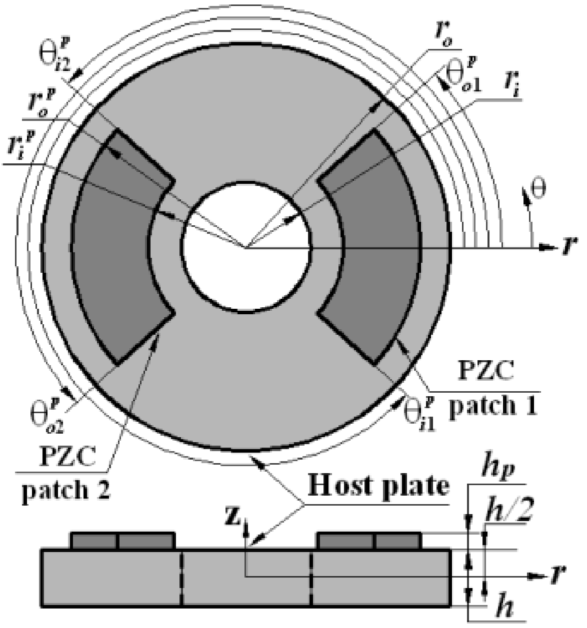

Fig. 4.3 Schematic diagram of an annular plate integrated with PFC actuator-patches.

For the sake of simplicity in the presentation, the four types of PFCs (Figs. 4.1 and 4.2) are denoted in abbreviated forms as, TCR (Fig. 4.1(a)), TCC (Fig. 4.1(b)), LCR (Fig. 4.2(a)) and LCC (Fig. 4.2(b)). The first letter of the abbreviated forms denotes the poling direction of piezoelectric fibers (L/T is for longitudinal/transverse direction). The second letter of the same signifies continuous fibers. The third letter denotes the direction of reinforcement of fibers (R/C is for the radial/circumferential reinforcement).

The PFC actuators (Figs. 4.1 and 4.2) are separately utilized for the material of actuator-patches, and their active damping-capabilities in control of a bending mode of vibration of the overall annular plate are evaluated under the following circumstances especially for the aforesaid comparison study.

(a) Uniform material and geometrical properties of the host annular plate for all the PFCs.

(b) Uniform boundary conditions over the boundary edges of the smart annular plate for all the PFCs.
(c) Uniform mode of vibration of the smart annular plate for all the PFCs.
(d) Uniform value of control-gain for all the PFCs.
(e) Uniform value of layer-thickness and equal number of layers in all the PFCs.
(f) Uniform constituent materials and fiber volume fraction of all the PFCs.

Under these circumstances, the comparison study on the control-capabilities of the PFC actuators is performed on the basis of best damping-capability of every PFC actuator corresponding to a bending mode of vibration of the overall plate. In order to achieve it, it is generally recommended to configure the actuator-patches in an optimal manner for the bending mode of vibration under study. So, the active damping-capability of every PFC actuator at a particular mode of vibration is presently evaluated after configuring its patches optimally over the top surface of the host annular plate.

Table 4.1 Material properties of PZT-5H and epoxy (Ray, 2006a) (C_{ij}, e_{ij} and $\in_{ij}$ are in GPa, C/m² and C/Vm×10⁻⁰⁹, respectively; PZT-5H is poled in the transverse (z /3) direction).

Fiber/Matrix	C_{11}	C_{12}	C_{23}	C_{33}	C_{44}
Epoxy	3.86	2.57	2.57	3.86	0.64
PZT-5H	151	98	96	124	23

Fiber/Matrix	e_{31}	e_{33}	e_{24}	$\in_{11}$	$\in_{33}$
Epoxy	0	0	0	0.079	0.079
PZT-5H	-5.1	27	17	13.27	13.4

The PFC actuators (Figs. 4.1 and 4.2) are constructed in different ways. The common aspects in their constructional features are the constituent materials, fiber-volume fraction, thickness of the layers and number of layers within the actuator-laminate. These parameters are chosen to be uniform parameters in all the PFC actuators for the comparison of their active damping-capabilities. The thickness (h_p^l) of every layer in any PFC laminate is taken as 100 μm, while it (laminate) is comprised of three layers. The materials for the fiber and matrix phases in all the PFCs are taken as PZT-5H and epoxy (Table 4.1), respectively, and the fiber volume fraction is taken as 40%. According to these constituent materials and fiber-volume fraction, the effective electro-elastic properties of LCR/LCC are computed following the same procedure as given in Chapter 2 (Kumar et al., 2015). These properties are illustrated in Table 4.2. The effective properties of TCR for the same constituents and fiber volume fraction are obtained from (Ray, 2006a), and illustrated in the same table (Table 4.2). The properties of TCC (Table 4.2) are obtained by the transformation of the properties of TCR for the change in orientation of continuous fibers from radial to the circumferential direction.

Table 4.2 Material properties of the cylindrically orthotropic PFC actuators (LCR, LCC, TCR, TCC) (C_{ij} and e_{ij} are in GPa and C/m², respectively).

PFC	C_{11}	C_{12}	C_{22}	C_{44}	C_{55}	e_{11}	e_{12}
LCR	24.62	4.512	7.902	1.129	1.519	12.290	-0.106

PFC	C_{11}	C_{12}	C_{22}	C_{44}	C_{55}	e_{21}	e_{22}
LCC	7.902	4.512	24.62	1.519	1.129	-0.106	12.290

PFC	C_{11}	C_{12}	C_{22}	C_{44}	C_{55}/C_{66}	e_{31}	e_{32}
TCR	32.34	4.207	6.325	1.05	1.29	-6.917	-0.05

PFC	C_{11}	C_{12}	C_{22}	C_{44}/C_{66}	C_{55}	e_{31}	e_{32}
TCC	6.325	4.207	32.34	1.29	1.05	-0.05	-6.917

4.3 Electric field vs. applied voltage for the PFC actuators

For the LCR actuator (Fig. 4.2(a)), the radial distance between a pair of electrodes ($+\phi$ and $-\phi$) is considered as 10 mm, while the radial width of the surface-electrodes is 100 µm. The corresponding variation of the volume-average electric field component ($\bar{E}_r$) with the applied voltage (V) across the pairs of surface-electrodes is illustrated in Fig. 4.4. This result shows a linear relation between $\bar{E}_r$ and applied voltage (V) that can be expressed as, $\bar{E}_r = G_r V$ following Eq. (2.44a) where the value of the gradient G_r is 96.865 m^{-1}.

In case of LCC actuator (Fig. 4.2(b)), the volume-average electric field component ($\bar{E}_\theta$) in the circumferential direction is the main applied field for its control activity. The characteristics of this applied electric field ($\bar{E}_\theta$) are observed as similar to those of $\bar{E}_r$ in the previous case (LCR) since the LCC actuator is constructed in the same way by taking the fibers and surface-electrodes in the circumferential direction (Figs. 4.2(a) and 4.2(b)). So, the same value of the gradient (G_θ) for the linear relation ($\bar{E}_\theta = G_\theta V$) between the electric field ($\bar{E}_\theta$) and applied voltage (V) is considered in the use of LCC actuator.

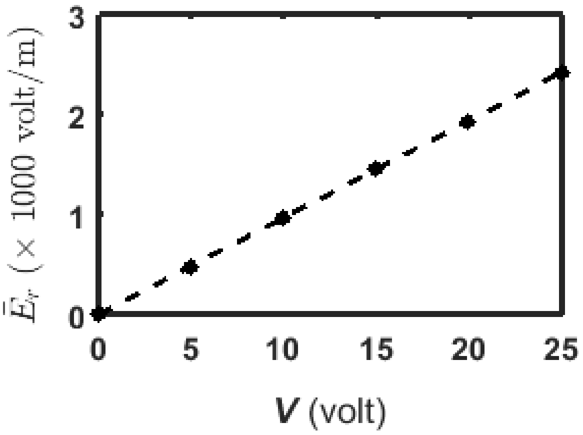

Fig. 4.4 Variation of electric field ($\bar{E}_r$) with the applied voltage (V) across the pairs of surface-electrodes of LCR (Fig. 4.2(a)).

For the TCR and TCC actuators (Figs. 4.1(a) and 4.1(b)), the applied electric field would act in the transverse direction, and it is generally achieved by supplying the external voltage (V) across their top and bottom fully electrode-surfaces (Ray and Mallik, 2004a). Presently, the top and bottom surfaces of every layer of TCR/TCC actuator are considered to be fully electrode-surfaces, and the electric field ($\bar{E}_z$) is applied across these surface-electrodes. It may be noted here that the surface-electrodes can also be placed only over the top and bottom surfaces of the whole TCR/TCC laminate. But, this arrangement of surface-electrodes requires more control-voltage for the control activity of the actuator than that (required voltage) in case of layer-wise arrangement of surface-electrodes. However, as the layers are very thin (layer thickness, h_p^l = 100 μm), the electric field components for an applied voltage (V) across the electrodes can be assumed as, $\bar{E}_r \approx 0$, $\bar{E}_\theta \approx 0$, $\bar{E}_z = (-1/h_p^l)V$. It can also be expressed in the form as, $\bar{E}_z = G_z V$ where the value of the gradient (G_z) is -10000 m^{-1}.

A common issue in the uses of these actuators is that the induced electric field within a PFC actuator appears due to the applied electric potential/electric field as well as the mechanical strain of the overall structure. Generally, the magnitude of the induced electric field due to the mechanical strain only is very small as compared to the magnitude of the induced field due to a large applied electric field. So, the induced electric field in a PFC may be assumed as a result of the applied electric field only especially in its (PFC) utilization as an actuator. Based on this assumption, the above relations ($\bar{E}_r = G_r V$, $\bar{E}_\theta = G_\theta V$, $\bar{E}_z = G_z V$) between the induced electric field ($\bar{E}_r$ / $\bar{E}_\theta$ / $\bar{E}_z$) and applied voltage (V) may be utilized for mathematical modelling of the PFC actuators. In order to assess the relative control-capabilities of the PFC actuators, it is required to activate all these PFCs with uniform input/applied electric field. This requirement can be achieved by supplying voltage (V_{PFC}) to the PFC actuators in different magnitudes as, $V_{PFC} = \alpha_v V$, where V is a reference voltage and the constant (α_v) for TCR, TCC, LCR and LCC actuators appears with the values of 1, 1, (G_z / G_r) and (G_z / G_θ), respectively.

4.4 FE model of smart annular plate

An FE model of the smart annular plate (Fig. 4.3) is derived in this section according to the aforesaid control strategy. The state of stress and the state of strain at any point within the overall annular plate can be written following Eqs. (3.16) and (3.17).

$$\boldsymbol{\sigma}_b = \{\sigma_r \quad \sigma_\theta \quad \tau_{r\theta}\}^{\mathrm{T}}, \quad \boldsymbol{\sigma}_s = \{\tau_{rz} \quad \tau_{\theta z}\}^{\mathrm{T}} \tag{3.16}$$

$$\boldsymbol{\varepsilon}_b = \{\varepsilon_r \quad \varepsilon_\theta \quad \varepsilon_{r\theta}\}^{\mathrm{T}}, \quad \boldsymbol{\varepsilon}_s = \{\varepsilon_{rz} \quad \varepsilon_{\theta z}\}^{\mathrm{T}} \tag{3.17}$$

Since a thin smart annular plate is considered in the present study, its kinematics of deformation is defined according to the first-order shear deformation theory (FSDT) as given in Eqs. (3.18a)-(3.18c).

$$u_p(r,\theta,z,t) = u_0(r,\theta,t) + z\phi_r(r,\theta,t) \tag{3.18a}$$

$$v_p(r,\theta,z,t) = v_0(r,\theta,t) + z\phi_\theta(r,\theta,t) \tag{3.18b}$$

$$w_p(r,\theta,z,t) = w_0(r,\theta,t) \tag{3.18c}$$

The generalized displacements (u_0, v_0, w_0, ϕ_r, ϕ_θ) in the displacement field (Eqs. (3.18a)-(3.18c)) can be expressed in terms of the generalized displacement vector ($\boldsymbol{d}$) as,

$$\boldsymbol{d} = \{u_0 \quad v_0 \quad w_0 \quad \phi_r \quad \phi_\theta\}^{\mathrm{T}} \tag{4.1}$$

According to the displacement field (Eqs. (3.18a)-(3.18c)), the strain-displacement relations are given in Eqs. (3.20)-(3.21). The same relations can also be written as follows,

$$\boldsymbol{\varepsilon}_b = \boldsymbol{\varepsilon}_b^{\mathrm{o}} + z\boldsymbol{\kappa}_b,\ \boldsymbol{\varepsilon}_s = \left\{ \left(\phi_r + \frac{\partial w_0}{\partial r} \right) \quad \left(\phi_\theta + \frac{1}{r}\frac{\partial w_0}{\partial \theta} \right) \right\}^{\mathrm{T}}$$

$$\boldsymbol{\varepsilon}_b^{\mathrm{o}} = \left\{ \frac{\partial u_0}{\partial r} \quad \left(\frac{1}{r}\frac{\partial v}{\partial \theta} + \frac{u}{r} \right) \quad \left(\frac{\partial v}{\partial r} + \frac{1}{r}\frac{\partial u}{\partial \theta} - \frac{v}{r} \right) \right\}^{\mathrm{T}},$$

$$\boldsymbol{\kappa}_b = \left\{ \frac{\partial \phi_r}{\partial r} \quad \left(\frac{1}{r}\frac{\partial \phi_\theta}{\partial \theta} + \frac{\phi_r}{r} \right) \quad \left(\frac{\partial \phi_\theta}{\partial r} + \frac{1}{r}\frac{\partial \phi_r}{\partial \theta} - \frac{\phi_\theta}{r} \right) \right\}^{\mathrm{T}} \tag{4.2}$$

The constitutive relations for the substrate isotropic plate or the actuator-patches are given in Eqs. (3.22) and (3.24). These constitutive relations can also be expressed in common expressions for both the layers as follows,

$$\boldsymbol{\sigma}_b^k = \boldsymbol{C}_b^k \boldsymbol{\varepsilon}_b - \boldsymbol{e}_b^k \boldsymbol{E},\ \boldsymbol{\sigma}_s^k = \boldsymbol{C}_s^k \boldsymbol{\varepsilon}_s - \boldsymbol{e}_s^k \boldsymbol{E} \tag{4.3}$$

$$\boldsymbol{D}^k = (\boldsymbol{e}_b^k)^{\mathrm{T}} \boldsymbol{\varepsilon}_b + (\boldsymbol{e}_s^k)^{\mathrm{T}} \boldsymbol{\varepsilon}_s + \boldsymbol{\epsilon}^k\ \boldsymbol{E},\ k = 1,2 \tag{4.4}$$

where, the superscript k denotes substrate plate or actuator-patch according to its value as 1 or 2, respectively. As the substrate plate is made of an isotropic material, the piezoelectric matrices ($\boldsymbol{e}_b^k$ and $\boldsymbol{e}_s^k$) are the null matrices for the substrate plate ($k = 1$). The forms of the stiffness matrices ($\boldsymbol{C}_b^k$, $\boldsymbol{C}_s^k$) of the substrate plate ($k = 1$) are given in Eq. (3.23). For the PFC actuator-patches (k = 2), the forms of various property matrices can be written as,

$$\boldsymbol{C}_b^2 = \begin{bmatrix} C_{11}^2 & C_{12}^2 & 0 \\ C_{21}^2 & C_{22}^2 & 0 \\ 0 & 0 & C_{66}^2 \end{bmatrix},\ \boldsymbol{C}_s^2 = \begin{bmatrix} C_{55}^2 & 0 \\ 0 & C_{44}^2 \end{bmatrix},\ {}^r\boldsymbol{e}_b^2 = \begin{bmatrix} e_{11}^2 & 0 & 0 \\ e_{12}^2 & 0 & 0 \\ 0 & e_{26}^2 & 0 \end{bmatrix},$$

$${}^r\boldsymbol{e}_s^2 = \begin{bmatrix} 0 & 0 & e_{35}^2 \\ 0 & 0 & 0 \end{bmatrix},\ {}^\theta\boldsymbol{e}_b^2 = \begin{bmatrix} 0 & e_{21}^2 & 0 \\ 0 & e_{22}^2 & 0 \\ e_{16}^2 & 0 & 0 \end{bmatrix},\ {}^\theta\boldsymbol{e}_s^2 = \begin{bmatrix} 0 & 0 & 0 \\ 0 & 0 & e_{34}^2 \end{bmatrix},$$

$${}^z\boldsymbol{e}_b^2 = \begin{bmatrix} 0 & 0 & e_{31}^2 \\ 0 & 0 & e_{32}^2 \\ 0 & 0 & 0 \end{bmatrix},\ {}^z\boldsymbol{e}_s^2 = \begin{bmatrix} e_{15}^2 & 0 & 0 \\ 0 & e_{24}^2 & 0 \end{bmatrix} \tag{4.5}$$

For radially/circumferentially/transversely poled fibers, the corresponding forms of the matrices ($\boldsymbol{e}_b^k$, $\boldsymbol{e}_s^k$) in Eq. (4.5) are denoted by the superscript $r\,/\,\theta\,/\,z$.

The overall plate is considered to operate under a transversely distributed harmonic mechanical load of, $p(r,\theta)e^{j\omega t}$ ($j=\sqrt{-1}$) where ω is the operating frequency and $p(r,\theta)$ is the intensity of the distributed load over the plane ($r\theta$) of the plate. For the vibration of the overall plate under this dynamic load, the first variations of total potential energy (δT_p) and total kinetic energy (δT_k) of the overall plate at an instant of time (t) can be written according to Eq. (3.27) and (3.28).

$$\delta T_p = \int_{r_i}^{r_o}\int_0^{2\pi}\left[\sum_{k=1}^{2}\int_{h_k}^{h_{k+1}}\left(\delta\boldsymbol{\varepsilon}_b^{\mathrm{T}}\,\boldsymbol{\sigma}_b^k + \delta\boldsymbol{\varepsilon}_s^{\mathrm{T}}\boldsymbol{\sigma}_s^k\right)dz - \int_{h_k}^{h_{k+1}}(\delta\boldsymbol{E}^{\mathrm{T}}\boldsymbol{D})_{k=2}\,dz - Q_p\right] rd\theta dr \tag{3.27}$$

$$\delta T_k = \int_{r_i}^{r_o}\int_0^{2\pi}\left(\sum_{k=1}^{2}\int_{h_k}^{h_{k+1}}\left(\left\{\delta\ddot{u}_p \quad \delta\dot{v}_p \quad \delta\dot{w}_p\right\}\rho^k\left\{\ddot{u}_p \quad \dot{v}_p \quad \dot{w}_p\right\}^{\mathrm{T}}\right)dz\right) rd\theta dr \tag{3.28}$$

In Eq. (3.27), the term (Q_p) for the mechanical load has the following form for the transversely distributed harmonic load,

$$\mathrm{Q}_p = (\delta w)pe^{j\omega t} \tag{4.6}$$

Using Eqs. (4.1), (4.2), (4.3) and (4.4) along with the linear relations between electric field components ($E_r\,/\,E_\theta\,/\,E_z$) and applied voltage (V), Eqs. (3.27)-(3.28) can be expressed as,

$$\delta T_p = \int_{r_i}^{r_o}\int_0^{2\pi}\begin{pmatrix} \delta\boldsymbol{\varepsilon}_b^{\mathrm{oT}}\left\langle \boldsymbol{A}_b\boldsymbol{\varepsilon}_b^{\mathrm{o}} + \boldsymbol{B}_b\boldsymbol{\kappa}_b\right\rangle + \delta\boldsymbol{\kappa}_b{}^{\mathrm{T}}\left\langle \boldsymbol{B}_b\boldsymbol{\varepsilon}_b^{\mathrm{o}} + \boldsymbol{D}_b\boldsymbol{\kappa}_b\right\rangle \\ +\delta\boldsymbol{\varepsilon}_s{}^{\mathrm{T}}\boldsymbol{A}_s\boldsymbol{\varepsilon}_s - \left\langle \delta\boldsymbol{\varepsilon}_b^{\mathrm{oT}}\boldsymbol{A}_{be} + \delta\boldsymbol{\kappa}_b{}^{\mathrm{T}}\boldsymbol{B}_{be} + \delta\boldsymbol{\varepsilon}_s{}^{\mathrm{T}}\boldsymbol{A}_{se}\right\rangle V \\ -(\delta w_0)pe^{j\omega t} \end{pmatrix} rd\theta dr \tag{4.7}$$

$$\delta T_k^e = \int_{r_i^e}^{r_o^e}\int_{\theta_i^e}^{\theta_o^e}\left(\delta\dot{\boldsymbol{d}}^{\mathrm{T}}\bar{\boldsymbol{m}}\dot{\boldsymbol{d}}\right) rd\theta dr \tag{4.8}$$

In Eqs. (4.7) and (4.8), the expressions for rigidity matrices ($\boldsymbol{A}_b$, $\boldsymbol{A}_s$, $\boldsymbol{B}_b$, $\boldsymbol{D}_b$) and mass matrix per unit area ($\bar{\boldsymbol{m}}$) are given in Eq. (3.32), and the electro-elastic coupling vectors ($\boldsymbol{A}_{be}$, $\boldsymbol{A}_{se}$, $\boldsymbol{B}_e$) are as follows,

$$\boldsymbol{A}_{be} = \int_{h_k}^{h_{k+1}}\boldsymbol{e}_b^k\boldsymbol{G}\alpha_v\,dz\Big|_{k=2},\quad \boldsymbol{A}_{se} = \int_{h_k}^{h_{k+1}}\boldsymbol{e}_s^k\boldsymbol{G}\alpha_v\,dz\Big|_{k=2},$$
$$\boldsymbol{B}_{be} = \int_{h_k}^{h_{k+1}}\boldsymbol{e}_b^k\boldsymbol{G}\alpha_v\,zdz\Big|_{k=2}, \tag{4.9}$$

where, the gradient vector ($\boldsymbol{G}$) for different PFC actuators are as follows,

$$\begin{gathered}\boldsymbol{G}=\{G_r \quad 0 \quad 0\}^{\mathrm{T}} \text{ for LCR actuator} \\ \boldsymbol{G}=\{0 \quad G_\theta \quad 0\}^{\mathrm{T}} \text{ for LCC actuator} \\ \boldsymbol{G}=\{0 \quad 0 \quad G_z\}^{\mathrm{T}} \text{ for TCR/TCC actuator}\end{gathered} \tag{4.10}$$

In order to derive FE model of the smart plate, the plane of the annular plate is discretized using nine-node quadrilateral isoparametric elements. The FE mesh is generated by dividing the radial and circumferential spans in such a manner that the edges of every element are in parallel to the radial and circumferential directions. Since the PFC actuators are used in the patch form, the FE mesh is comprised of two kinds of elements having different stacking sequences. One element is only for the substrate plate, and the other one has the actuator layer over the substrate layer. At any point within an element, the generalized displacement vector ($\boldsymbol{d}$) and strain vectors ($\boldsymbol{\varepsilon}_b^0, \boldsymbol{\varepsilon}_s, \boldsymbol{\kappa}_b$) can be written in terms of the shape function matrix ($\boldsymbol{N}$) and the elemental nodal displacement vector ($\boldsymbol{d}^e$) as follows,

$$\begin{gathered}\boldsymbol{d}=\boldsymbol{N}\boldsymbol{d}^e \\ \boldsymbol{\varepsilon}_b^0=\boldsymbol{B}_b^0\boldsymbol{d}^e, \;\; \boldsymbol{\varepsilon}_s=\boldsymbol{B}_s\boldsymbol{d}^e, \;\; \boldsymbol{\kappa}_b=\boldsymbol{B}_\kappa\boldsymbol{d}^e, \\ \boldsymbol{B}_b^0=\boldsymbol{L}_{bt}\boldsymbol{N}, \;\; \boldsymbol{B}_s=\boldsymbol{L}_{br}\boldsymbol{N}, \;\; \boldsymbol{B}_\kappa=\boldsymbol{L}_s\boldsymbol{N}\end{gathered} \tag{4.11}$$

The different operator matrices ($\boldsymbol{L}_{bt}, \boldsymbol{L}_{br}, \boldsymbol{L}_s$) appearing in Eq. (4.11) are given in Eq. (3.21). Using Eq. (4.11), a procedure as given in Section 3.3.1 in Chapter 3 is followed to derive the global equations of motion for the vibration of the overall plate in the form of Eq. (3.38).

$$\boldsymbol{M}\ddot{\boldsymbol{X}}_p+(\boldsymbol{K}_b+\boldsymbol{K}_s)\boldsymbol{X}_p=\sum_{q=1}^{4}\boldsymbol{P}_E^q(V^q)V^q+\boldsymbol{P}_M(t) \tag{3.38}$$

In Eq. (3.38), the electro-elastic coupling vector ($\boldsymbol{P}_E^e(V)$) is independent of the applied voltage (V) for the linear relations between the electric field components ($E_r / E_\theta / E_z$) and voltage (V). Also, for the consideration of a number (N_p) of actuator-patches and the transversely distributed harmonic load ($p(r,\theta)e^{j\omega t}$), Eq. (3.38) can be rewritten as,

$$\boldsymbol{M}\ddot{\boldsymbol{X}} + (\boldsymbol{K}_b + \boldsymbol{K}_s)\boldsymbol{X} = \sum_{q=1}^{N_p} \boldsymbol{F}_E^q V^q + \boldsymbol{F}_M e^{j\omega t} \tag{4.12}$$

In Eq. (4.12), $\boldsymbol{X}$ is the global nodal displacement vector; $\boldsymbol{F}_M$ is the global nodal mechanical load-amplitude vector; $\boldsymbol{F}_E^q$ is the global nodal electro-elastic coefficient vector for q^{th} actuator-patch among the N_p number of actuator-patches; V^q is the applied voltage across the pairs of surface-electrodes of q^{th} actuator-patch.

Every actuator-patch is equipped with a velocity-sensor at its middle point. The transverse velocity ($\dot{w}^q$) at this middle point is sensed and fed back in the form of voltage (V_q) across the pairs of surface-electrodes of the corresponding (q^{th}) actuator-patch following the negative velocity feedback control strategy as given in Eq. (3.39).

$$V_q = -k_d^q \dot{w}^q \tag{3.39}$$

The velocity ($\dot{w}^q$) at the middle point of q^{th} patch can be expressed in terms of the global nodal velocity vector as given in Eq. (3.40).

$$\dot{w}^q = \boldsymbol{N}_T^q \dot{\boldsymbol{X}}_p \tag{3.40}$$

Using Eqs. (3.39) by expressing the local velocity ($\dot{w}^q$) in terms of the global nodal velocity vector ($\dot{\boldsymbol{X}}$) through Eq. (3.40), Eq. (4.12) can be written as,

$$\boldsymbol{M}\ddot{\boldsymbol{X}} + (\boldsymbol{K}_b + \boldsymbol{K}_s)\boldsymbol{X} = -\left\langle \sum_{q=1}^{N_p} \boldsymbol{C}_q \right\rangle \dot{\boldsymbol{X}} + \boldsymbol{F}_M e^{j\omega t}, \quad \boldsymbol{C}_q = \boldsymbol{F}_E^q \boldsymbol{k}_d^q \boldsymbol{N}_T^q \tag{4.13}$$

Equation (4.13) expresses the FE equations of motion of the smart annular plate where the electrically induced actuation force is modeled as active damping force using the velocity feedback control strategy. The final forms of the equations of motion can be written as,

$$\boldsymbol{M}\ddot{\boldsymbol{X}} + \boldsymbol{C}\dot{\boldsymbol{X}} + \boldsymbol{K}\boldsymbol{X} = \boldsymbol{F}_M e^{j\omega t}$$

$$\boldsymbol{K} = (\boldsymbol{K}_b + \boldsymbol{K}_s),\ \boldsymbol{C} = \left\langle \sum_{q=1}^{N_p} \boldsymbol{C}_q \right\rangle \tag{4.14}$$

4.5 Estimation of active damping within the smart plate

The damping in a structural system is generally estimated by the parameters like damping ratio, loss factor, quality factor etc. All these damping parameters are defined for a single-degree-of-freedom (SDOF) system. In case of multi-degrees-of-freedom (MDOF) system, the same damping parameters can also be utilized for the individual mode of vibration only if the MDOF system can be expressed by a set of SDOF systems corresponding to the normal modes of the (MDOF) system. The damping parameter in every mode of vibration or SDOF system is then called as modal damping parameter. This modal damping parameter is normally evaluated at the corresponding resonant frequency as its primary importance is to limit the peak amplitude at resonance. However, the present MDOF system (Eq. (4.13)) may not be decoupled into a set of SDOF systems mainly because of the form of the corresponding damping matrix. In order to estimate the modal damping parameter under this circumstance, it may be assumed that the peak amplitude at a resonant frequency is affected only by the corresponding normal mode (Papagiannopoulos and Hatzigeorgiou, 2011). On the basis of this assumption, a typical mode (say, i^{th} mode) of vibration of the present MDOF system at the corresponding resonant frequency (ω_i) can be represented by the following SDOF system,

$$\begin{gathered} m_i\ddot{\alpha}_i + c_i\dot{\alpha}_i + k_i\alpha_i = p_i e^{j\omega_i t} \\ m_i = \boldsymbol{\varphi}_i^{\mathrm{T}}\boldsymbol{M}\boldsymbol{\varphi}_i,\ c_i = \boldsymbol{\varphi}_i^{\mathrm{T}}\mathbf{C}\boldsymbol{\varphi}_i,\ k_i = \boldsymbol{\varphi}_i^{\mathrm{T}}\boldsymbol{K}\boldsymbol{\varphi}_i,\ p_i = \boldsymbol{\varphi}_i^{\mathrm{T}}\boldsymbol{F}_M \end{gathered} \tag{4.15}$$

where, the vector $\boldsymbol{\varphi}_i$ represents the nodal displacements of the i^{th} normal mode. Equation (4.15) can also be expressed at the resonant frequency (ω_i) as,

$$m_i\ddot{\alpha}_i + (k_i + jc_i\omega_i)\alpha_i = p_i e^{j\omega_i t} \tag{4.16}$$

From Eq. (4.16), the modal loss factor (η_i) of the system can be obtained as,

$$\eta_i = (c_i\omega_i)/k_i \tag{4.17}$$

The active damping corresponding to a mode of vibration of the smart annular plate can be estimated using Eq. (4.17).

4.6 Present strategy for optimal configuration of actuator-patches

The active damping-capability of every PFC actuator is estimated in terms of the modal loss factor (Eq. (4.17)) after determination of the optimal size and locations of its patches for a mode of vibration under study. A mode of vibration of the overall plate is presently denoted by the radial and circumferential mode numbers as, m and n, respectively. Generally, two kinds of mode-shapes appear in the natural vibration of an annular plate with regard to its circular symmetry. One is the symmetric mode-shape ($n = 0$) and other one is the asymmetric mode-shape ($n > 0$). For every asymmetric mode-shape, there is a similar second mode-shape that is orthogonal to the first one with an angular shift of $\pi / 2n$. The couple of mode-shapes appear at the same natural frequency of every asymmetric mode due to the exchange of sine and cosine functions in the circumferential coordinate (θ) (Amabili, 2008). For these two similar mode-shapes, the only difference between the corresponding optimal configurations of the actuator-patches would be an angular shift of $\pi / 2n$. So, the optimal configuration of actuator-patches can be decided by taking any one of the couple of mode-shapes in an asymmetric mode. In the following section, two typical symmetric (Fig. 4.5(a)) and asymmetric (Fig. 4.5(b)) mode-shapes of the smart annular plate are considered, and a methodology in deciding optimal size and locations of actuator-patches for each of the mode-shapes is demonstrated.

4.6.1 Initial configuration of the smart annular plate

It may be observed from Fig. 4.5 that every mode-shape is comprised of certain numbers of positive and negative half sine-waves along each of the radial and circumferential directions. These positive and negative half sine-waves are of uniform dimensions along radial/circumferential direction, and they also appear alternatively in both the orthogonal directions. Following the radial and circumferential boundaries of the half sine-waves, the top surface of the host annular plate is divided into equal number of sectors as shown in Figs. 4.5(a) and 4.5(b) by the dash-lines. Basically, the sectors of half sine-waves are created following the nodes of the mode-shape. The PFC actuator is first taken in layer-form over the top surface of the substrate plate and then divided in the form of patches following the boundaries (dash-lines) of the sectors. These patches are considered to be uniformly separated in a little gap along both the radial and circumferential directions. For a flexure mode of deformation of an annular plate, generally, the mechanically induced in-plane normal stresses appear with significant magnitudes at the locations of anti-nodes. The extension mode PFC actuators provide electrically induced in-plane normal forces against these mechanical stresses at the host plate-surface on which they (PFCs) are attached. So, the initial configuration of the smart plate is taken by providing actuator-material around the anti-nodes or by separating the actuator-layer following the nodes. The mechanical stress at a point of a sector is in opposite phase to that (phase) of the same stress at similar points within the consecutive sectors. So, for effective use of the PFC patches, every patch is supposed to act against the time-varying mechanical stresses around its location by taking the feedback of

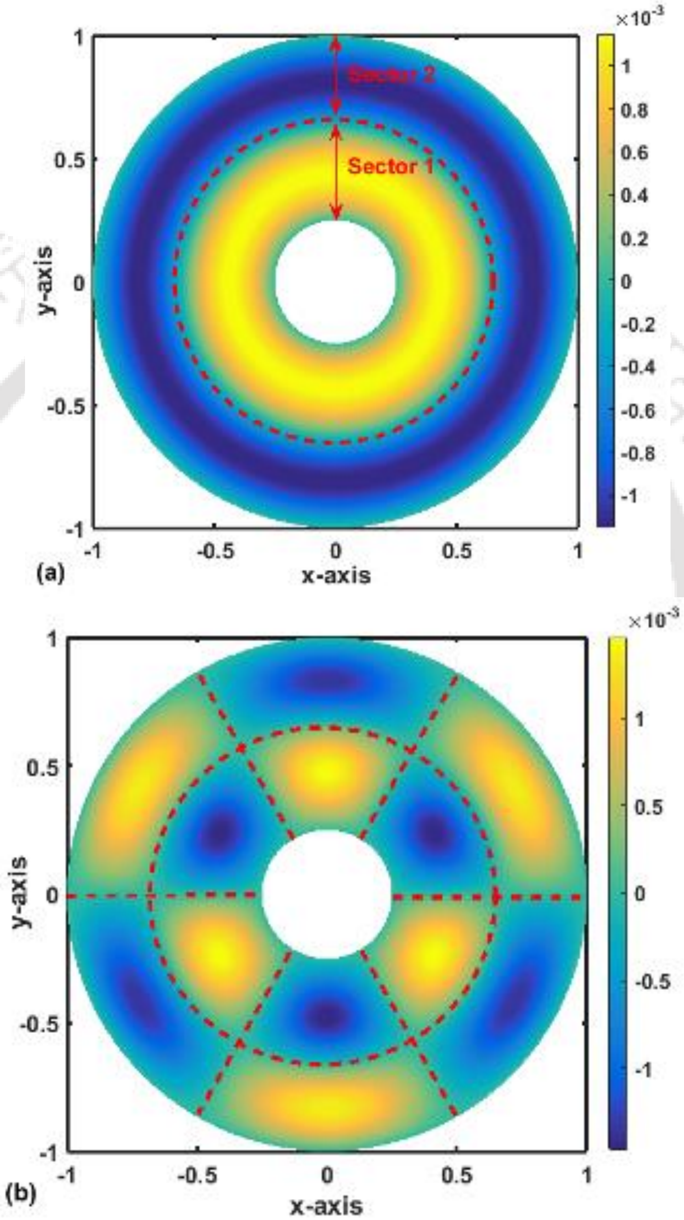

Fig. 4.5 Typical (a) symmetric and (b) asymmetric mode-shapes of the annular plate along with the separated sectors (by dash-lines) of half sine-waves.

local velocity at the anti-node of the corresponding sector. As the velocity in any sector/PFC patch appears with its maximum value at the corresponding anti-node, this point/node is chosen for the feedback of local velocity. However, this initial configuration of the actuator-patches is to be modified for optimal size and location of every actuator-patch within the corresponding sector. It should be noted here that all the sectors are made uniformly, and the actuator-patches act in a uniform manner against the mechanical stresses within the corresponding sectors. So, any one of the sectors can be taken as the representative sector to study the actuation characteristics of the actuator-patches. Also, the optimal size and locations of actuator-patches within the corresponding sectors can be decided based on this representative sector that is presented in the next section.

4.6.2 Optimal configuration of a typical/representative sector

According to the aforesaid initial configuration of the smart annular plate, every PFC patch almost covers the area (in $r\theta$ plane) of the corresponding sector. So, the initial PFC patch within a sector is presently denoted as PFC sector-layer. The optimal size and location of the actuator-patch within a sector are decided on the basis of the importance of the actuator-material at every point over its (sector) $r\theta$ plane. The corresponding tests over a set of points on a PFC sector-layer (representative sector-layer) are carried out without alteration of reaming sector-layers. A typical test-point is taken over the top surface of the PFC sector-layer, and a differential area on the same surface around the test-point is selected such that its (differential area) edges are in parallel to those of the sector-layer. The material of the PFC actuator over this differential area is then removed in such a manner that the PFC sector-layer has a differential hole throughout its thickness around the test-point. Keeping the radial and circumferential spans of the differential area as constant parameters, the test-point is moved at different points/locations over the $r\theta$ plane of the sector-layer. At any location of the test-point along with the differential hole, the remaining area of the PFC sector-layer is a constant area. So, the volume of the PFC sector-layer does not change when the test-point is located at different points. For every location of the test-point, the modal loss factor of the overall plate corresponding to its (plate) mode of vibration is evaluated, and the magnitude of the loss factor is noted along with the location/coordinate (r,θ) of the test-point. The evaluated magnitudes of modal loss factor are then plotted as altitudes against the corresponding locations (r,θ) of the test-point over the $r\theta$ plane of the sector-layer. These altitudes constitute a surface of modal loss factor over the $r\theta$ plane of the sector-layer.

Physically, the removal of differential PFC material from an important location/point significantly affects the control-capability of the PFC sector-layer, and it is implied by the decrease of the corresponding magnitude of modal loss factor. Similarly, if the differential PFC material is removed from an unimportant point/location of a PFC sector-layer, then there would be no significant change in the corresponding magnitude of the modal loss factor. According to this analogy, the projected points on the $r\theta$ plane from the troughs of the aforesaid surface of loss factor signify the important locations of the PFC material. Consequently, the area around a projected point on the $r\theta$ plane is the important zone for the PFC material. After determination of important and unimportant zones over the plane of the sector-layer, the optimal size of the important zone can be decided based on the rate of change of loss factor in every space coordinate (r,θ). Within an important or unimportant zone, loss factor changes in insignificant rate along any of the space coordinates. But, the magnitude of the same parameter significantly differs between these important and unimportant zones. So, there would be a steep rate of change of loss factor at the transition zone which indicates the separation of important zone from the whole area of the sector-layer. The size of the PFC sector-layer can then be reduced according to this separated zone, and it implies optimal size and location of the PFC patch within a sector.

4.7 Numerical results and discussions

In this section, first the patches of individual PFC actuator are optimally configured for each of the fundamental symmetric ($m=1,\ n=0$) and asymmetric ($m=1,\ n=1$) modes of vibration of the overall annular plate. Next, the magnitudes of modal loss factor for these modes of vibration of the overall plate are evaluated using its (smart annular plate) optimal configuration for every PFC actuator. Finally, these results are analyzed for a study on relative damping-capabilities of the PFC actuators. The geometrical and material properties of the host isotropic annular plate are considered as, $r_i = 0.25\,\text{m}$, $r_o = 1\,\text{m}$, $h = 4$ mm,

$E = 70$ GPa, $\upsilon = 0.3$, $\rho = 2700$ kg/m^3. Every PFC actuator (Figs. 4.1 and 4.2) is considered to be comprised of three uniform layers with the layer-thickness of 100 μm. An annular area over the top surface of the host annular plate is considered for distribution of actuator material so that the inner and outer edges of host annular plate are free from the actuator material. The inner (r_i^p) and outer (r_o^p) radii of this annular area are considered as, 0.265 m and 0.985 m, respectively. The material properties of the PFC actuators are illustrated in Table 4.2 while the density of the same PFCs corresponding to their fiber-volume fraction of 40% is taken as 3666 kg/m^3 according to the rule of mixture. All the actuator-patches of every kind of PFCs are considered to operate under the uniform value of control-gain ($k_d^q = k_d$, $q =$ 1,2,3,.... N_p). The inner and outer edges of the host annular plate are considered either as simply-supported edges ($w_o = 0$, $v_o = 0$, $\phi_\theta = 0$) or as fully clamped edges ($w_o = 0$, $u_o = 0$, $v_o = 0$, $\phi_\theta = 0$, $\phi_r = 0$). In order to verify the present FE formulation for an annular plate, the first two natural frequencies of the host annular plate ($h_p \approx 0$, $k_d = 0$) are computed for different boundary conditions. These computed results are illustrated in Table 4.3 together with the similar results available in (Chakraverty et al., 2001). It may be observed from Table 4.3 that the present results are in good agreement with the earlier analytical results (Chakraverty et al., 2001). This comparison verifies the accuracy of the present FE formulation for annular plates.

Table 4.3 Verification of FE formulation for an annular plate ($\lambda_i = \omega_i r_o^2 \sqrt{\rho h/D}$**,** $D = Eh^3/12(1-\upsilon^2)$**,** $h_p \approx 0$**,** $k_d = 0$**, BC: Boundary conditions, CC: Fully clamped plate-edges, SS: Simply-supported plate-edges, Ref. Chakraverty et al., 2001).**

BC	Source	$(r_i/r_o) = 0.2$		$(r_i/r_o) = 0.4$	
		λ_1	λ_2	λ_1	λ_1
CC	Present	36.17	37.76	62.05	63.88
	Ref.	35.12	37.82	61.88	63.04
SS	Present	17.72	20.38	28.40	30.45
	Ref.	16.86	20.47	28.08	30.09

Next, the present formulation for electro-elastic coupling is verified following the same procedure as that is done in the previous chapter (Fig. 3.8, Section 3.3.3).

This comparison verifies the accuracy of the present FE formulation in handling the electro-elastic coupling. In order to achieve sufficient numerical accuracy in the present results, an FE mesh-convergence study is performed considering a layer of LCR actuator over the simply-supported host annular plate. The frequencies of first two natural modes and the corresponding magnitudes of modal loss factor are computed with increasing number of elements in the FE model of the overall plate. These results are presented in Table 4.4. Following these results, the FE mesh of the smart annular plate is decided in the evaluation of subsequent numerical results.

Table 4.4 FE mesh convergence study (ω_i : natural frequency (rad/s), η_i : modal loss factor, m : radial mode number, n : circumferential mode number).

Number of elements	Symmetric mode ($m=1,\ n=0$)		Asymmetric mode ($m=1,\ n=1$)	
	ω_1	η_1	ω_2	η_2
288	117.91	0.1195	131.73	0.1341
540	117.90	0.1199	131.69	0.1341
960	117.90	0.1202	131.68	0.1342
1440	117.90	0.1203	131.68	0.1342
2160	117.90	0.1203	131.68	0.1342

4.7.1 Evaluation of optimal configuration of the smart annular plate

The active damping-capabilities of the PFC actuators are investigated considering fundamental symmetric ($m=1,\ n=0$) and asymmetric ($m=1,\ n=1$) modes of vibration of the annular plate. Figure 4.6 shows the corresponding mode-shapes. For the asymmetric mode ($n=1$), a couple of mode-shapes (Figs. 4.6(b)-(c)) appear which are separated by an angular distance of 90° ($\pi/2n$, $n=$ 1). One (Fig. 4.6(b)) of these couple of mode-shapes is taken for the present study. For every mode (symmetric (Fig. 4.6(a)) and asymmetric (Fig. 4.6(b))), the optimal configuration of the patches of a PFC is determined following the aforesaid procedure in conjunction with the FE model of the overall plate. In the implementation of this procedure, the radial and circumferential spans of the differential hole around the test-point over the representative sector-layer are presently taken as, 0.09 m and 10°, respectively. For a location of the test-point over the representative sector-layer, the corresponding FE mesh of the overall plate is generated following the aforesaid convergence study (Table 4.4), and then the modal loss factor (η) is computed along with a note of the coordinates (r, θ) of the test-point. This computation is repeatedly carried out for a number of locations of the test-point over the sector-layer, and then the surface of the loss factor (η) over the area of the representative sector-layer is constituted. It should be noted here that the size (dimensions) of the differential hole around the test-point can be chosen arbitrarily, but it (size of the hole) remains the same for all locations of the test-point over the sector-layer.

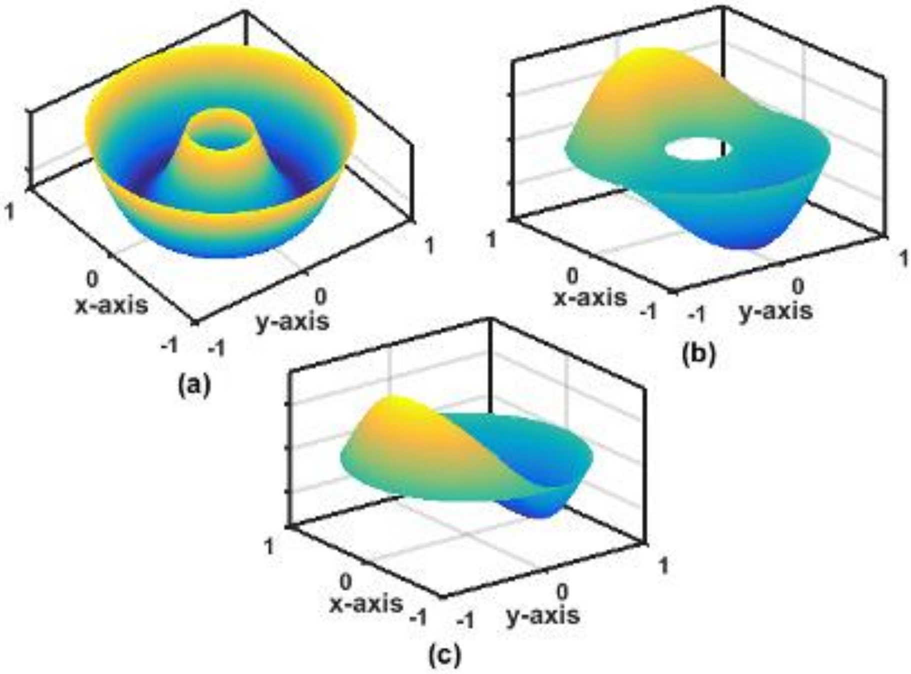

Fig. 4.6 Fundamental (a) symmetric ($m = 1,\ n = 0$), (b)-(c) asymmetric ($m = 1,\ n = 1$) mode-shapes of the simply-supported annular plate.

4.7.1.1 Symmetric mode

The fundamental symmetric mode-shape ($m = 1,\ n = 0$, Fig. 4.6(a)) indicates to consider one initial PFC sector-layer over the top surface of the host annular plate. This initial sector-layer fully covers the annular area (r_i^p = 0.265 m, r_o^p = 0.985 m) over the top surface of host plate that (annular area) is considered for the distribution of actuator material. The test-point is moved over the top surface of this initial sector-layer, and the corresponding surface of the modal loss factor (η) is plotted in Fig. 4.7(a)/Fig. 4.7(c) for the simply-supported/fully clamped annular plate integrated with LCR sector-layer. It may be observed from these figures that the characteristics of the surface of η do not change indicatively for the alteration of boundary conditions. Moreover, these figures reveal the important zone for the LCR-material around the middle point of radial span since η is much affected by removal of the differential LCR material from this location. The LCR actuator acts against the mechanical stress in the radial direction since the major electrically induced actuation force within it appears in this direction. So, the appropriateness of these results (Fig. 4.7(a) and 4.7(c)) for the important location of LCR material can be verified through the distribution of radial stress over the top surface of the host plate. Figure 4.7(b)/4.7(d) shows this distribution of dimensionless radial stress over the top surface of simply-supported/fully clamped host annular plate when it (plate) undergoes the same mode of deformation. The location of the maximum magnitude of radial stress would be the important location for LCR material that is obtained in these results (Figs. 4.7(a) and 4.7(c)). Besides this optimal location of the LCR actuator, its optimal size can be decided following the points of the steep rate of

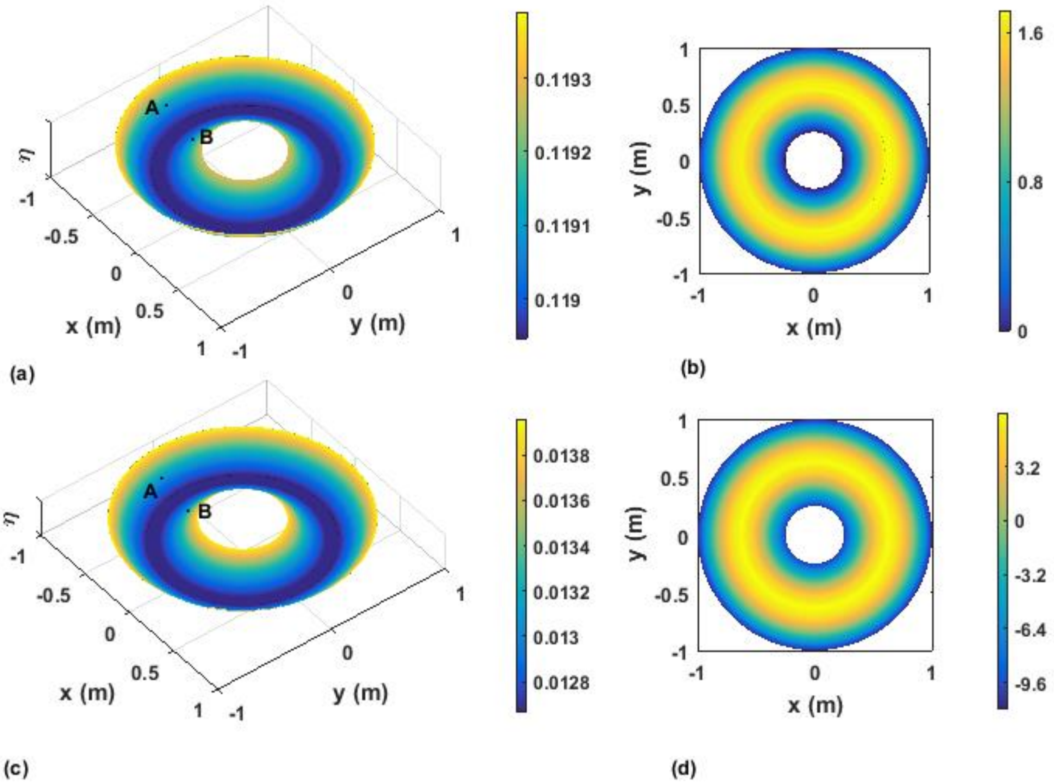

Fig. 4.7 Surface of loss factor (η) over the annular area of LCR sector-layer and the distribution of dimensionless radial stress over the top surface of host annular plate under symmetric mode ($m=1$, $n=0$) of deformation, (a)-(b) simply-supported edges of the plate, (c)-(d) fully clamped edges of the plate ($k_d=100$).

change of η within the transition zone. Presently, the radial locations of these points are identified at the locations A and B (as shown in Fig. 4.7(a)/4.7(c)), and the annular area between these radial points is taken as the optimal size of the LCR actuator.

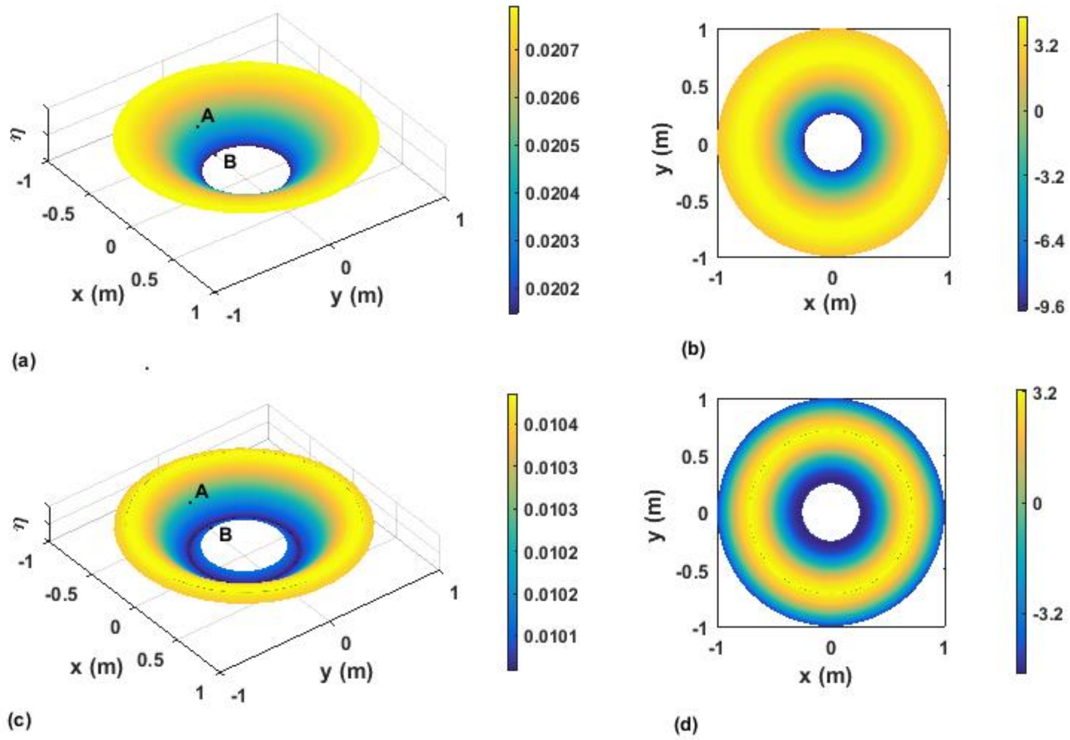

Fig. 4.8 Surface of loss factor (η) over the annular area of LCC sector-layer and the distribution of dimensionless circumferential stress over the top surface of host annular plate under symmetric mode ($m =$ 1, $n =$ 0) of deformation, (a)-(b) simply-supported edges of the plate, (c)-(d) fully clamped edges of the plate ($k_d = 100$).

Similar results for the LCC actuator are illustrated in Fig. 4.8 that indicates its (LCC) optimal location at the inner edge of the simply-supported/fully clamped annular plate. The LCC actuator acts mainly by means of electrically induced actuation force in the circumferential direction. So, its optimal location appears at the location of maximum circumferential stress that occurs at the inner edge of the plate for both kinds of boundary edges of the host plate (Figs. 4.8(b) and 4.8(d)). Besides this optimal location, the optimal size is chosen as an annular area between the inner circumferential boundary of PFC material (point B) and point A within the transition zone (Figs. 4.8(a) and 4.8(c)).

4.7.1.2 Asymmetric mode

According to the asymmetric mode-shape (Fig. 4.6(b)), two identical PFC sector-layers corresponding to two half sine-waves are selected. The inner and outer radial boundaries of these sector-layers are the same boundaries (r_i^p = 0.265 m, r_o^p = 0.985 m) as those are considered for the distribution of actuator material. Also, they are separated at the circumferential locations of 90° and 270° with a gap of 20°. One of these sector-layers within the circumferential locations of 90°

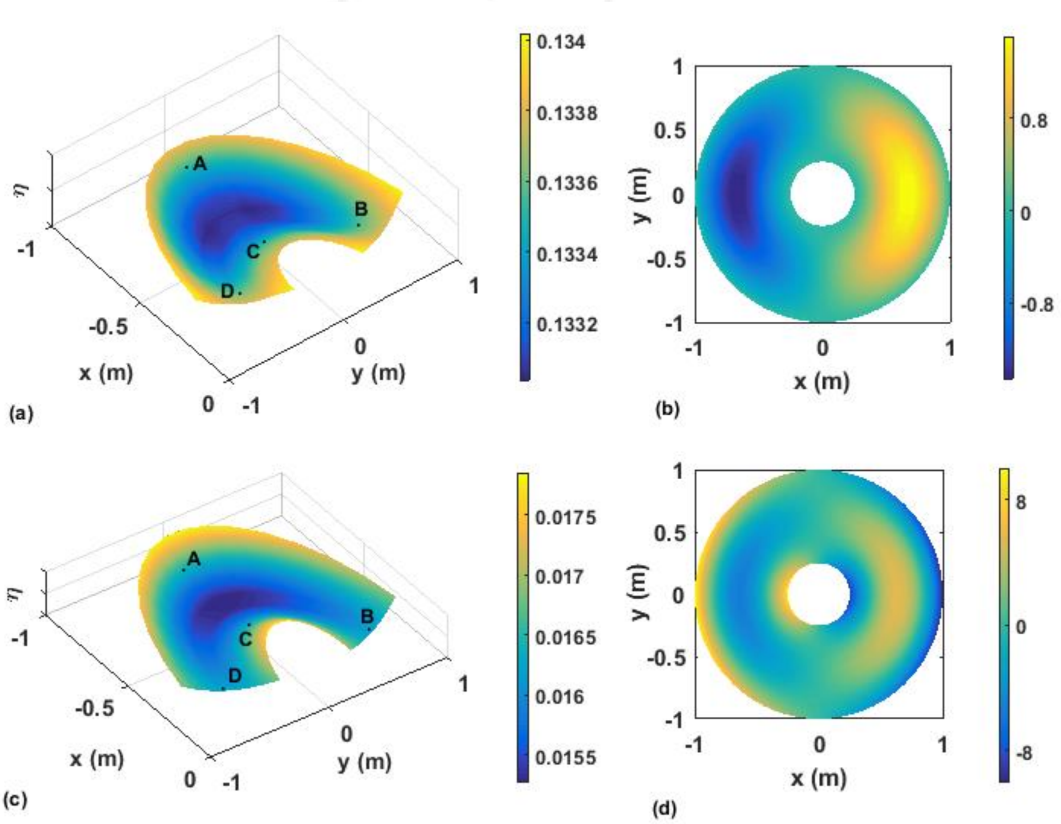

Fig. 4.9 Surface of loss factor (η) over the annular area of representative LCR sector-layer and the distribution of dimensionless radial stress over the top surface of host annular plate under asymmetric mode ($m = 1$, $n = 1$) of deformation, (a)-(b) simply-supported edges of the plate, (c)-(d) fully clamped edges of the plate ($k_d = 100$).

and 270° is taken as the representative sector-layer. In case of the LCR actuator, the surface of the modal loss factor (η) over the area of the representative sector-layer is plotted in Fig. 4.9(a)/Fig. 4.9(c) for simply-supported/fully clamped boundary edges of the host annular plate. It may be observed from these figures that the optimal location of the LCR actuator appears around the middle point of the sector-layer. Similar to the previous case

(Fig. 4.7), this optimal location also coincides with the location of maximum radial stress (Figs. 4.9(b) and 4.9(d)) corresponding to this asymmetric mode of deformation of the annular plate. The optimal size of the LCR actuator-layer is chosen in the form of an annular patch following this optimal location. The corresponding radial and circumferential spans are indicated by the points A, B, C and D in Figure 4.9(a)/4.9(c) for simply supported/fully clamped edges of the substrate plate. These radial (A and C) and circumferential (B and D) points are located following the points of the steep rate of change of η within the transition zone.

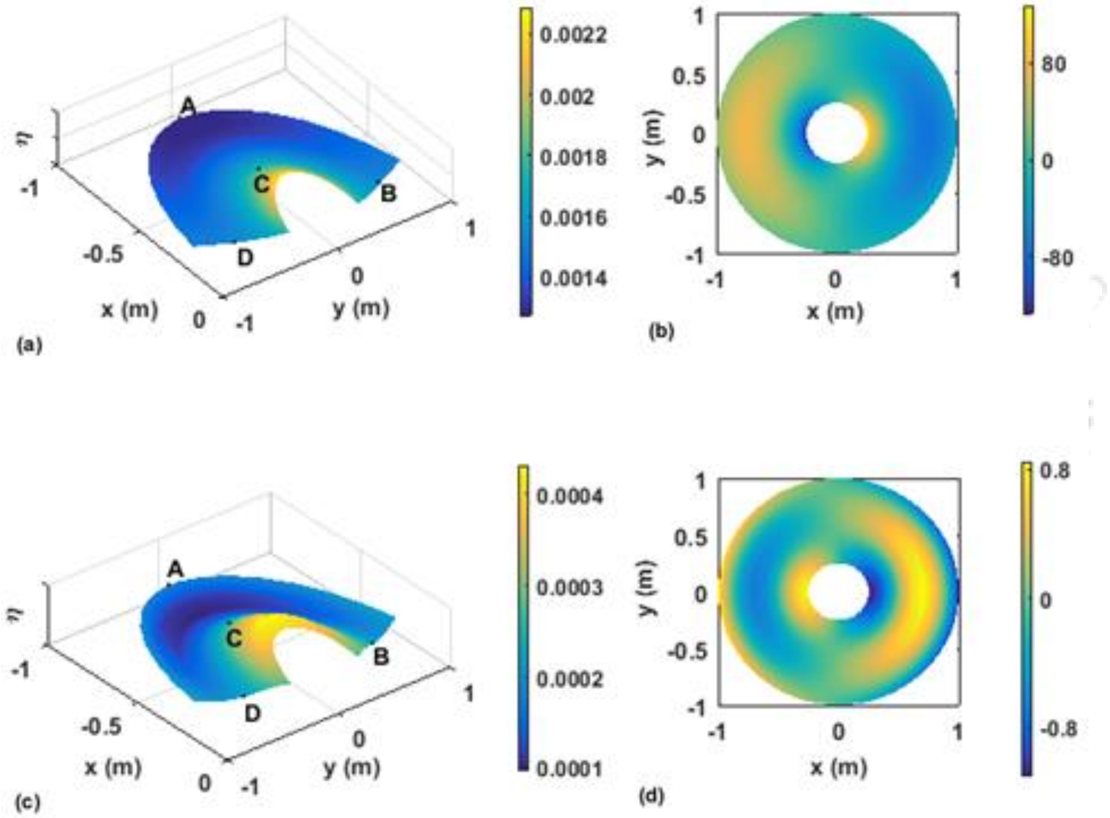

Fig. 4.10 Surface of loss factor (η) over the annular area of representative LCC sector-layer and the distribution of dimensionless circumferential stress over the top surface of host annular plate under asymmetric mode ($m=1$, $n=1$) of deformation, (a)-(b) simply-supported edges of the plate, (c)-(d) fully clamped edges of the plate ($k_d=100$).

For the use of LCC actuator instead of LCR actuator, similar results are illustrated in Fig. 4.10. For the case of simply-supported annular plate, it may be observed from Fig. 4.10(a) that the optimal location of the LCC actuator appears at the outer edge of the host plate. But, it (optimal location) changes a little when the boundary edges of the same host plate are fully clamped edges (Fig. 4.10(c)). Both the locations of LCC actuator appear corresponding to the locations of maximum circumferential stress (Figs. 4.10(b) and 4.10(d)) for the concerned asymmetric mode of deformation of the annular plate. For every kind of boundary conditions, the optimal size of the annular LCC patch is chosen within the points A, B, C and D (Figs. 4.10(a) and 4.10(c)) according to the aforesaid strategy. The control activity of TCR actuator is similar to that of LCR actuator since the major actuation force appears along the radial direction in both the actuators. The optimal size and locations of the TCR patches are also observed as very close to those of LCR patches. Similar observations are also obtained in case of TCC patches when their (TCC patches) size and locations are compared with the same of LCC patches. So, similar results (as in Figs. 4.7-4.10) for TCC and TCR actuators are not furnished here. However, these quantities (size and locations) are tabulated in Table 4.5 for all the PFC actuators.

Table 4.5 Optimal size and locations of PFC patches (BC: boundary conditions, SS: simply-supported boundary condition, CC: fully clamped boundary condition, radial dimensions (r_i^p / r_o^p) are in m; circumferential dimensions ($\theta_{i1}^p / \theta_{o1}^p / \theta_{i2}^p / \theta_{o2}^p$) are in degree and defined as given in Fig. 4.3).

BC	PFC	Symmetric mode $(m = 1,\ n = 0)$				Asymmetric mode $(m = 1,\ n = 1)$					
		r_i^p	r_o^p	θ_{i1}^p	θ_{o1}^p	r_i^p	r_o^p	θ_{i1}^p	θ_{o1}^p	θ_{i2}^p	θ_{o2}^p
SS	LCR	0.40	0.85	0	360	0.40	0.85	295	65	115	245
	LCC	0.265	0.49	0	360	0.40	0.985	290	70	110	250
	TCR	0.40	0.85	0	360	0.40	0.85	295	65	115	245
	TCC	0.265	0.49	0	360	0.40	0.985	290	70	110	250
CC	LCR	0.40	0.85	0	360	0.40	0.85	290	70	110	250
	LCC	0.265	0.58	0	360	0.58	0.985	290	70	110	250
	TCR	0.40	0.85	0	360	0.40	0.85	290	70	110	250
	TCC	0.265	0.58	0	360	0.58	0.985	290	70	110	250

4.7.2 Active damping-capabilities of PFC actuators

The active damping-capability of every PFC actuator is evaluated in this section considering fundamental symmetric and asymmetric modes of vibration of the annular plate. In each mode of vibration, the modal loss factor (η, Eq. (4.17)) for every PFC actuator is computed by taking the optimal configuration (Table 4.5) of its (actuator) patches over the top surface of the host annular plate. For the symmetric mode of vibration of the simply-supported/fully clamped overall annular plate, Fig. 4.11(a)/Fig. 4.11(b) illustrates the variations of modal loss factor (η) with the control-gain (k_d) for different actuators (LCR/LCC/TCR/TCC). It may be observed from Fig. 4.11(a) and 4.11(b) that the active damping within the overall plate remains almost the same for both kinds of boundary conditions although there is a little more damping in the overall plate with the simply-supported edges. It may also be observed that the active damping in the overall plate linearly increases with the increase of the control-gain for all the actuators. The maximum magnitude of the gradient of this linear increase of active damping appears in case of LCR actuator, and thus it (LCR) is the most effective/potential actuator for control of the fundamental symmetric mode of vibration of the annular plate. Similar results for fundamental asymmetric mode are illustrated in Fig. 4.12. The characteristics of these results (Fig. 4.12) are similar to those of the previous results (Fig. 4.11). So, it may be concluded that the LCR actuator is the most effective one among all the aforesaid cylindrically orthotropic PFC actuators for control of both the symmetric and asymmetric modes of vibration of the simply-supported/fully clamped annular plate. Although this conclusion is made on the basis of the fundamental symmetric and asymmetric modes of vibration of the annular plate, it is expected to hold for all the symmetric and asymmetric modes of vibration since similar representative sector (Fig. 4.5) appears in symmetric/asymmetric

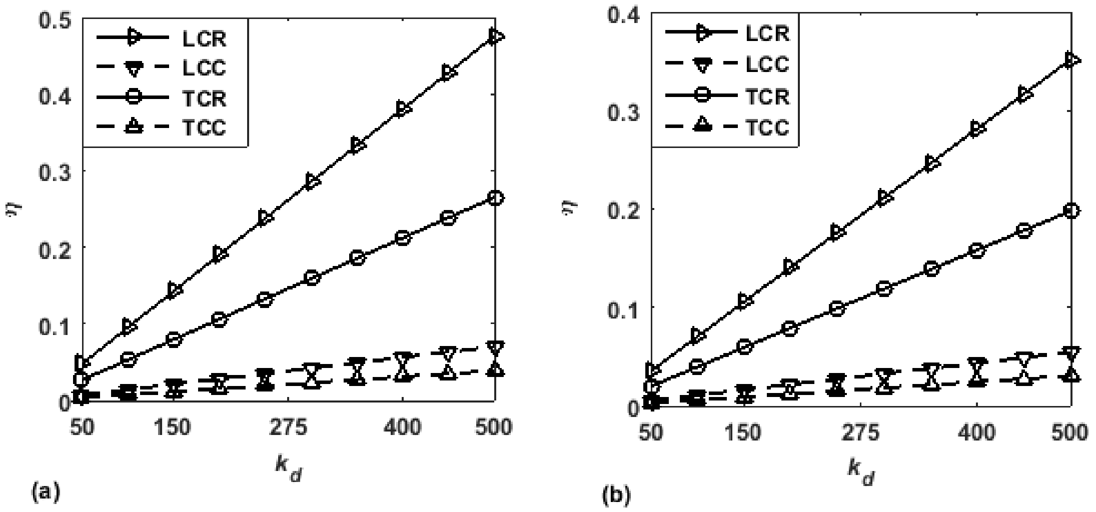

Fig. 4.11 Variation of modal loss factor (η) with the control-gain (k_d) for fundamental symmetric mode ($m = 1$, $n = 0$) of vibration of the (a) simply-supported or (b) fully clamped overall annular plate.

mode-shape of higher circumferential (n) and radial (m) mode numbers. It may also be noted here that the aforesaid conclusion for potential actuator may not stand for other kinds of plane structure in the cylindrical coordinate frame since this conclusion depends on several aspects of the problem like geometrical properties, material properties, kind of boundary conditions etc. But, this procedure can be followed for any kind of smart plate in the cylindrical coordinate frame for deciding its optimal configuration and also in the selection of potential actuator for effective control of its vibration.

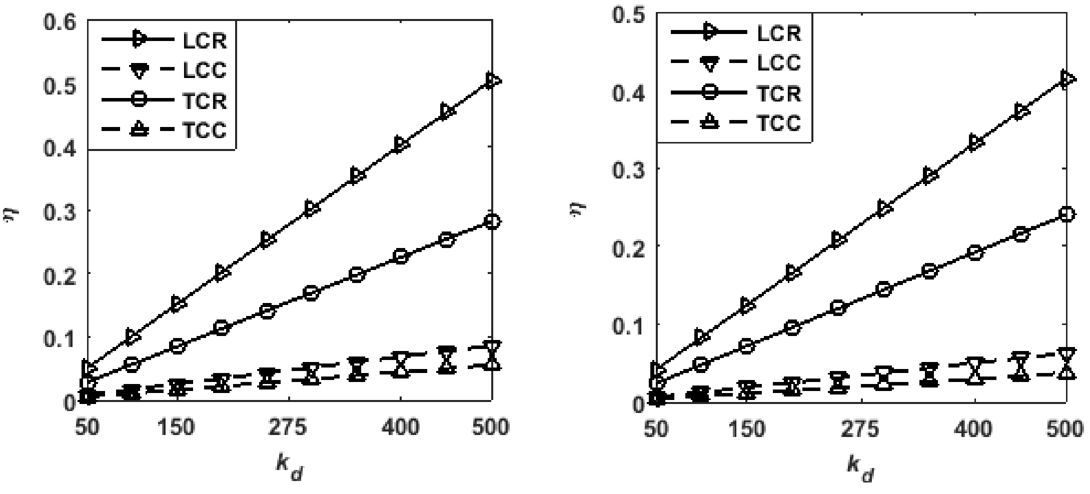

(a) (b)

Fig. 4.12 Variation of modal loss factor (η) with the control-gain (k_d) for fundamental asymmetric mode ($m = 1$, $n = 1$) of vibration of the (a) simply-supported or (b) fully clamped overall annular plate.

4.8 Conclusions

In this chapter, four kinds of PFC actuators are presented for effective control of vibration of plane structures of revolution, and a comparative study on their control-capabilities is performed to identify the potential one in control of vibration of simply-supported/fully clamped isotropic annular plate. These PFC actuators are designated in abbreviated forms of LCR, LCC, TCR and TCC according to their constructional features where the first, second and third letters indicate poling direction of fibers (longitudinal (L) or transverse (T)), continuous fibers (C) and fiber-reinforcement (radial (R)/circumferential(C)), respectively. All the actuators are used in the form of patches which are integrated over the top surface of the host annular plate. For effective utilization of every PFC actuator, its patches are configured to act as smart dampers through the feedback of local velocity according to the velocity feedback control strategy. Additionally, the geometrical and material properties of all the PFC actuators are taken in a uniform manner for the comparative study on their (actuators) control/damping capabilities. According to these properties of the actuators, the relations between the driving electric field and the applied voltage are evaluated for all the actuators through the FE model of the corresponding microstructures (Chapter 2). On the basis of these electrical relations, velocity feedback control law and first-order shear deformation (FSDT) theory, an FE model of the smart annular plate is derived for the comparative study on the control-capabilities of the different PFC actuators.

The comparative study on the smart damping capabilities of the actuators is presented considering fundamental symmetric and asymmetric modes of vibration of the annular plate. For every mode of vibration, the patches of each actuator are first optimally configured (size and locations) through the proposition of a new methodology in conjunction with the FE model of the smart annular plate. These optimal configurations of the smart annular plate for different PFC actuators are then utilized in the evaluation of their (PFCs) modal damping capabilities. The suitability of the present methodology in deciding optimal configuration of PFC patches is substantiated with reference to the distributions of mechanical stresses within the host plate. The modal damping capabilities of the PFC actuators are evaluated in terms of the modal loss factor. From these results, it is observed that the LCR and TCR actuators possess significant control/damping capabilities in control of vibration of simply-supported/fully clamped annular plate. The damping capabilities of all the actuators (LCR, LCC, TCR and TCC) linearly vary with the velocity feedback control-gain. The maximum magnitude of the gradient of this linear variation of damping capability arises in case of LCR actuator, and hence it (LCR) is the most effective PFC actuator in control of vibration of simply-supported/fully clamped annular plate.

CHAPTER

5

An annular PFC actuator for shear mode piezoelectric actuation of plane structures of revolution

5.1 Introduction

In the previous chapters (Chapter 2, Chapter 3 and Chapter 4), an extension mode SPFC/CPFC is designed in the cylindrical coordinates, and its actuation capability is substantiated in control of vibration of an isotropic annular plate. In this chapter, it is intended to achieve a PFC actuator for efficient shear mode piezoelectric actuation of plane structures of revolution. The literature review (Chapter 1) shows a good number of studies on the design as well as control capability of the shear mode PFC actuator. In all these studies, the principal material coordinate system of the shear mode PFC actuator is taken as the rectangular coordinate system. According to this principal material coordinate system, the transverse planes of the electrically induced shear forces at different points within the domain of the shear mode PFC actuator are parallel to each other. So, these existing shear mode PFC actuators may not provide effective actuation of structural deformation/vibration where the actuation forces are required in the cylindrical coordinates. It shows the need of a shear mode PFC actuator that is specially designed in the cylindrical coordinates for effective shear mode piezoelectric actuation of plane structures of revolution like annular/circular plates. Similar work has not been observed in the literature, and thus a shear mode PFC actuator in the cylindrical coordinates is designed in this chapter.

The actuation force in the existing shear mode PFC actuator appears due to its active layer that is a 2-2 PFC lamina as shown in Fig. 5.1(a). This 2-2 PFC lamina is comprised of the longitudinally poled (P) piezoelectric fibers and the polymer matrix. The electrically induced transverse shear stress appears in the xz-plane of the 2-2 PFC lamina due to a transversely applied electric field. To achieve similar transverse shear stress on the rz-plane in the cylindrical coordinate system, the geometric construction of the 2-2 PFC lamina can be modified according to the reference coordinate system as illustrated in Fig.

5.1(b). In this modified structure of the 2-2 PFC lamina, the width of the piezoelectric fibres along the circumferential (θ) direction increases with the increasing radius. So, the flexibility and conformability of the 2-2 PFC lamina may decrease indicatively especially for a large radial span of interest. Moreover, the variation of cross-sectional area of the fibres may raise practical difficulties in the fabrication of the actuator since the cross-sectional dimensions of the fibres are generally defined in micro-scale. In view of these discrepancies, the 2-2 PFC lamina can be made using the traditional piezoelectric fibres as shown in Fig. 5.1(c). Within this 2-2 PFC lamina (Fig. 5.1(c)), the longitudinally poled piezoelectric fibres are reinforced along the radial direction, and the fibres are periodically distributed along the circumferential direction. According to this arrangement of the fibres, the PFC lamina is expected to have sufficient flexibility and conformability. Also, the difficulties in the fabrication of the composite lamina are expected to decrease. But, a disadvantage of reduced fibre volume fraction (FVF) of the composite appears. The cross-sectional area (in θz-plane) of the composite lamina increases with the increasing radius, while the cross-sectional area of any of the fibres remains constant. So, the magnitudes of

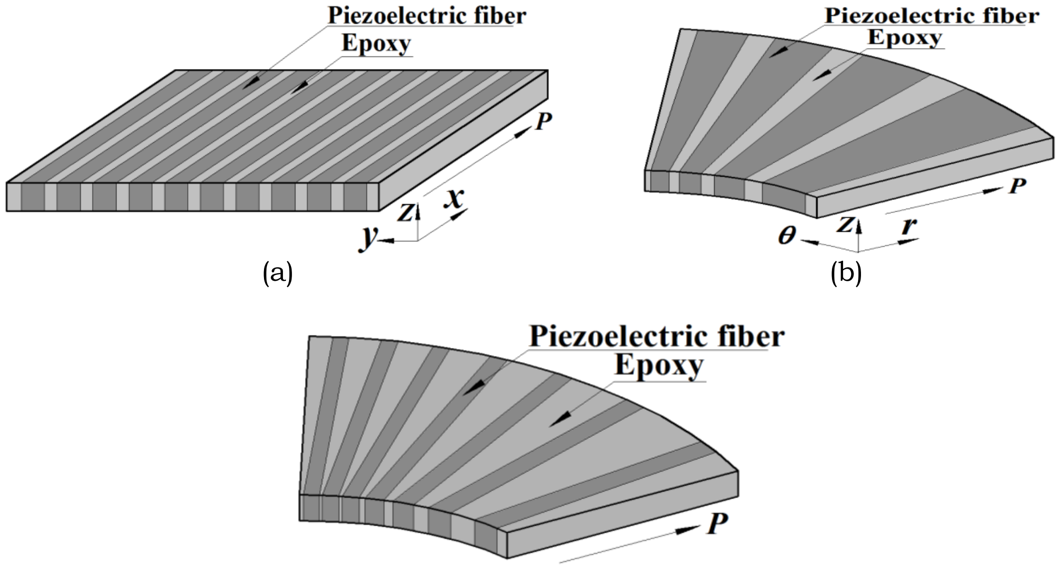

(a)

(b)

(c)

Fig. 5.1 Schematic diagrams of a 2-2 PFC layer in (a) Cartesian and (b)-(c) Cylindrical coordinate systems.

the effective electro-elastic coefficients are expected to decrease with the increasing radius. This fact may result in reduced control capability of the annular PFC actuator. To alleviate this discrepancy, the overall radial span of interest may be divided into a number of divisions, and then the annular PFC lamina is to be designed for every division of small radial length.

The electrically induced transverse shear force within the 2-2 PFC lamina arises due to the external electric field across its (lamina) thickness. Now, for an assigned value of this external electric field, the required voltage increases with the increase of the thickness of the 2-2 PFC lamina. Also, the structural rigidity of the PFC lamina increases for its higher thickness. So, the 2-2 PFC lamina would be made with a small thickness. As this small thickness of the 2-2 PFC lamina may cause insufficient control force in its (2-2 PFC lamina) structural applications, several laminae may be used in the form of a laminate. Following the same, the present shear mode PFC actuator is constructed by taking two 2-2 PFC layers.

In the following sections, the constructional features of the present shear mode PFC actuator are first presented. Next, the varying effective electro-elastic properties of the PFC actuator are estimated by employing the Uniform Fields Model (UFM) (Bent and Hagood, 1997). Subsequently, an FE procedure is developed for the numerical homogenization of the shear mode PFC actuator. The numerical results illustrate the varying effective properties of the PFC actuator. These effective properties are analysed, and an appropriate geometric configuration of the annular PFC actuator is addressed in order to have improved magnitude of the main piezoelectric coefficient (e_{35}).

5.2 Constructional features of the present shear mode PFC actuator

The present shear mode PFC actuator is constructed in the form of a thin laminated annular disc. The laminate is considered to be comprised of two 2-2 PFC layers (L_1 (Fig. 5.2(a)), five electrode layers (L_3), four thin epoxy layers (L_2) and two thick epoxy layers (L_4). Figure 5.2(a) illustrates the stacking sequence of these layers. The thin/thick epoxy layers (L_2 and L_4) are utilised to bind the active layers (L_1) and the electrode layers (L_3) in such a manner that the top and bottom surfaces of every active layer are integrated with the electrode layers. The external electric field is applied by specifying the electric potentials of the electrode layers over the top and bottom surfaces of every active layer. These prescribed electric potentials of the top and bottom electrode layers are denoted

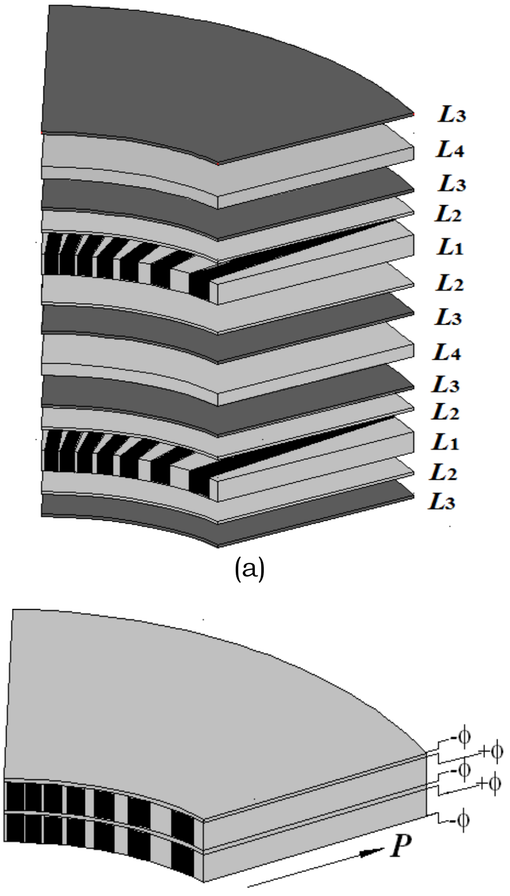

(a)

(b)

Fig. 5.2 Schematic diagrams of (a) stacking sequence of different layers of the annular PFC actuator and (b) laminate of shear mode PFC actuator.

by, $+\phi$ and $-\phi$, respectively. As the dielectric constants of the thin epoxy layer (L_2) are of small magnitudes, the magnitude of the driving electric field in the active layer is lesser than the magnitude of the applied electric field across the top and bottom electrodes of the active layer. So, it is recommended to laminate the layers at a high pressure and a high temperature (Lin et al., 2016) in such a manner that the thin epoxy layers (L_2) become extremely thin layers after lamination. Consequently, it would also be ensured that the thick epoxy layers (L_4) can provide sufficient transverse gap between any two consecutive electrodes of different electric potentials ($-\phi$ and $+\phi$). Under these aspects of lamination, presently the thin epoxy layer is considered as a negligibly thin layer within the laminate so that the electrodes are in almost direct contact with the surfaces of the active layers. Also, the elastic effects of the electrode layers are not accounted for estimation of the effective properties of the laminate since the thickness of the electrode layers is very small in comparison to the thickness of the active layer. By these considerations, a sector of the annular PFC actuator is schematically shown in Fig. 5.2(b).

5.3 Effective properties of the shear mode PFC actuator

According to the geometrical features of the laminate (Fig. 5.2(b)), a part of its thickness between any two consecutive electrodes of the same electric potential ($-\phi$) repeatedly appears along the thickness direction. Based on this feature of the laminate, a representative volume (RV) is selected as shown in Fig. 5.3(a).

This RV is comprised of an active (2-2 PFC) layer and an epoxy layer. The fibre within the active (2-2 PFC) layer of the RV is centrally located, and all the phases within the RV are assumed to be perfectly bonded to each other. The top and bottom electrode-surfaces of the RV are considered to be grounded while the external electric field is applied across the thickness of the active layer by specifying a non-zero electric potential over the electrode-surface between the active layer and the epoxy layer. It may be observed from the geometry of the RV that the cross-sectional area of the RV (in θz -plane) increases with the increasing radius, while the cross-sectional area of the fibre remains constant. So, the effective electro-elastic properties of the RV vary along the radial direction. These varying properties are presently estimated using a concept of asymptotically homogeneous layers/volumes for homogenization of the functionally graded materials (Reiter and Dvorak, 1997). Following this concept (Reiter and Dvorak, 1997), the radial span $(r_o - r_i)$ of the RV is divided into a number (N) of radial divisions ($k = 1,2,3,.. N$) of identical radial length ($\Delta r = (r_o - r_i)/N$) as shown in Fig. 5.3(b). The radial length (Δr) of these divisions is very small ($\Delta r << (r_o - r_i)$) in comparison to the radial span $(r_o - r_i)$ of the RV. The volume of the RV is divided into a number (N) of sub-volumes following the radial divisions. A typical sub-volume is shown in Fig. 5.4(a). Every sub-volume contains a continuous piezoelectric fibre and has certain FVF. The sub-volumes

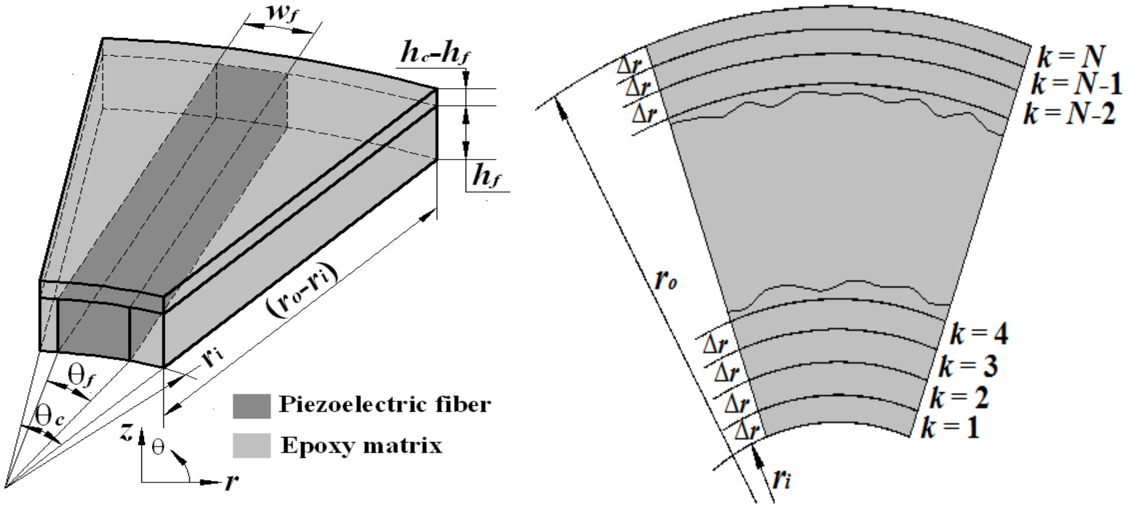

(a) (b)

Fig. 5.3(a) Representative volume (RV) of the shear mode PFC actuator (Fig. 5.2(b)) and (b) a horizontal plane of RV with radial divisions of identical radial length (Δr).

within the radial span of the RV are assumed as the macroscopically homogeneous volumes. By this assumption, the effective properties of the RV at a radial location within its radial span are considered as the effective properties of a sub-volume at that radial location. So, the properties of the RV at any radial location can be obtained by determining the effective properties of the sub-volumes of different FVFs. In the following sections, the closed-form expressions for the effective coefficients of the sub-volumes (Fig. 5.4(a)) are derived. In parallel, an FE procedure is developed for numerical homogenization of the sub-volumes.

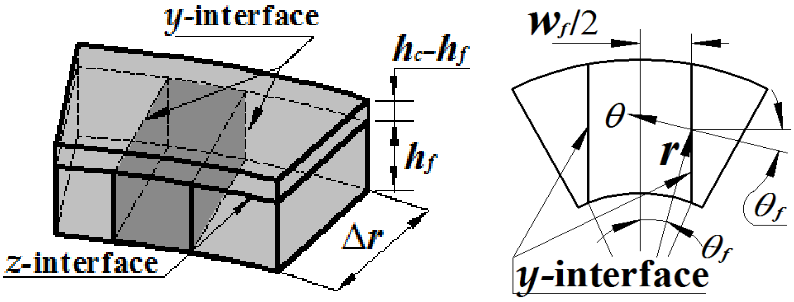

(a) (b)

Fig. 5.4(a) Schematic diagram of a typical sub-volume and (b) a horizontal plane of the active (2-2 PFC) layer of the sub-volume.

5.3.1 Effective properties of a typical sub-volume

For the linear electro-elastic behaviour of the longitudinally poled piezoelectric fibre, the constitutive relations (Cady, 1946) is given in Eq. (2.1). The same relations can be written in terms of the matrices and vectors as,

$$\boldsymbol{\sigma}=\left(\boldsymbol{C\varepsilon}-\boldsymbol{e}^{\mathrm{T}}\boldsymbol{E}\right),\ \boldsymbol{D}=\left(\boldsymbol{e\varepsilon}+\boldsymbol{\in}\,\boldsymbol{E}\right),\ \boldsymbol{\sigma}=\left\{\sigma_r\quad \sigma_\theta\quad \sigma_z\quad \tau_{\theta z}\quad \tau_{rz}\quad \tau_{r\theta}\right\}^{\mathrm{T}},$$

$$\boldsymbol{\varepsilon}=\left\{\varepsilon_r\quad \varepsilon_\theta\quad \varepsilon_z\quad \gamma_{\theta z}\quad \gamma_{rz}\quad \gamma_{r\theta}\right\}^{\mathrm{T}},\ \boldsymbol{E}=\left\{E_r\quad E_\theta\quad E_z\right\}^{\mathrm{T}},$$

$$\boldsymbol{D}=\left\{D_r\quad D_\theta\quad D_z\right\}^{\mathrm{T}},$$

$$\boldsymbol{C}=\begin{bmatrix} C_{11} & C_{12} & C_{13} & 0 & 0 & 0 \\ C_{12} & C_{22} & C_{23} & 0 & 0 & 0 \\ C_{13} & C_{23} & C_{33} & 0 & 0 & 0 \\ 0 & 0 & 0 & C_{44} & 0 & 0 \\ 0 & 0 & 0 & 0 & C_{55} & 0 \\ 0 & 0 & 0 & 0 & 0 & C_{66} \end{bmatrix},\quad \boldsymbol{e}=\begin{bmatrix} e_{11} & e_{12} & e_{13} & 0 & 0 & 0 \\ 0 & 0 & 0 & 0 & 0 & e_{26} \\ 0 & 0 & 0 & 0 & e_{35} & 0 \end{bmatrix},$$

$$\boldsymbol{\epsilon}=\begin{bmatrix}\epsilon_{11} & 0 & 0\\ 0 & \epsilon_{22} & 0\\ 0 & 0 & \epsilon_{33}\end{bmatrix} \tag{5.1}$$

where, σ_r / ε_r, $\sigma_\theta / \varepsilon_\theta$ and σ_z / ε_z are the normal stresses/strains along the r, θ and z directions, respectively; $\tau_{r\theta} / \gamma_{r\theta}$, τ_{rz} / γ_{rz} and $\tau_{\theta z} / \gamma_{\theta z}$ are the shear stresses/strains on the $r\theta$, rz and θz planes, respectively; D_r / E_r, D_θ / E_θ and D_z / E_z are the electric displacements/electric fields along the r, θ and z directions, respectively; C_{ij} are the elements of the stiffness matrix ($\boldsymbol{C}$); ϵ_{ij} are the elements of the dielectric matrix ($\boldsymbol{\epsilon}$); e_{lj} are the elements of the piezoelectric matrix ($\boldsymbol{e}$). According to the present arrangement of the electrodes within the volume of the PFC actuator (Fig. 5.2(b)), a dominant electric field (E_z) or electric displacement (D_z) is imposed along the thickness direction (z). So, it may be assumed that (Trindade and Benjeddou, 2011), $E_r = E_\theta = 0$ or $D_r = D_\theta = 0$, and the constitutive relations (Eq. (5.1)) can be reduced as,

$$\boldsymbol{\sigma}=\left(\boldsymbol{C\varepsilon}-\boldsymbol{e}^{\mathrm{T}}E_z\right),\ \boldsymbol{D}=\left(\boldsymbol{e\varepsilon}+\epsilon_{33}E_z\right),$$

$$\boldsymbol{C}=\begin{bmatrix}C_{11} & C_{12} & C_{13} & 0 & 0 & 0\\ C_{12} & C_{22} & C_{23} & 0 & 0 & 0\\ C_{13} & C_{23} & C_{33} & 0 & 0 & 0\\ 0 & 0 & 0 & C_{44} & 0 & 0\\ 0 & 0 & 0 & 0 & C_{55} & 0\\ 0 & 0 & 0 & 0 & 0 & C_{66}\end{bmatrix},\ \boldsymbol{e}=\begin{bmatrix}0 & 0 & 0 & 0 & e_{35} & 0\end{bmatrix} \tag{5.2}$$

These constitutive relations can also be written in a compact form for any of the materials within the PFC actuator as,

$$\begin{Bmatrix}\boldsymbol{\sigma}^p\\ D_z^p\end{Bmatrix}=\boldsymbol{C}^p\begin{Bmatrix}\boldsymbol{\varepsilon}\\ \text{-}E_z\end{Bmatrix},$$

$$\boldsymbol{C}^p=\begin{bmatrix}C_{11}^p & C_{12}^p & C_{13}^p & 0 & 0 & 0 & 0\\ C_{12}^p & C_{22}^p & C_{23}^p & 0 & 0 & 0 & 0\\ C_{13}^p & C_{23}^p & C_{33}^p & 0 & 0 & 0 & 0\\ 0 & 0 & 0 & C_{44}^p & 0 & 0 & 0\\ 0 & 0 & 0 & 0 & C_{55}^p & 0 & e_{35}^p\\ 0 & 0 & 0 & 0 & 0 & C_{66}^p & 0\\ 0 & 0 & 0 & 0 & e_{35}^p & 0 & -\epsilon_{33}^p\end{bmatrix} \tag{5.3}$$

In Eq. (5.3), the superscript (p) denotes piezoelectric fibre or epoxy matrix as per its value as 1 or 2, respectively. The effective properties of the sub-volume (Fig. 5.4(a)) can be estimated theoretically by applying statistically homogeneous kinematic fields (strain and electric fields) over its (sub-volume) volume provided that the continuities of the field quantities are to be satisfied (Aboudi et al., 2013). These continuities are (Aboudi et al., 2013): (a) the displacement and electric potential fields are to be continuous within the domain of the heterogeneous sub-volume, (b) the tractions and the normal component of the electric displacement are to be continuous at every interphase surface within the heterogeneous sub-volume.

For the present PFC actuator, the electric fields in the active (2-2 PFC) layer and the epoxy layer of the sub-volume (Fig. 5.4(a)) are prescribed through the fully electrode-surfaces. Since the electric fields are specified over the phases of different materials, the continuity of the normal component (D_z) of the electric displacement field at the z-interface (Fig. 5.4(a)) may not appear. But, the continuities of the following tractions on the z-interface would appear for homogenization of the sub-volume by means of applying statistically homogeneous kinematic fields,

$$\overset{z}{T_r} = \tau_{zr}\,,\ \overset{z}{T_\theta} = \tau_{z\theta}\,,\ \overset{z}{T_z} = \sigma_z \tag{5.4a}$$

At any radius (r), the angle between the normal to the y-interface (Fig. 5.4 (b)) and the θ-axis is denoted by, θ_f. This angle (θ_f) equals to, $\sin^{-1}\left(w_f / 2r\right)$. Since the value of w_f is very small (in microscale) in comparison to the radius (r) at any point on the y-interface (Fig. 5.4(b)), it may be assumed that, $(w_f / 2r) \approx 0$. So, the components of the unit normal to the y-interface may be considered as, $n_r \approx 0$, $n_\theta \approx 1$, $n_z = 0$. The corresponding tractions over the y-interface are given in Eq. (5.4b), while there would be no normal component of the electric displacement field according to the constitutive relations (Eq. 5.3).

$$\overset{\theta}{T_r} = \tau_{\theta r}\,,\ \overset{\theta}{T_\theta} = \sigma_\theta\,,\ \overset{\theta}{T_z} = \tau_{\theta z} \tag{5.4b}$$

The stress components ($\tau_{\theta r}$, σ_θ, $\tau_{\theta z}$, Eq. (5.4b)) are to be continuous at the y-interface for the homogenization of the sub-volume by means of applying statistically homogeneous kinematic fields.

5.3.2 Effective properties of the sub-volume using UFM

In this section, the closed-form expressions for the effective coefficients of the sub-volume (Fig. 5.4(a)) are derived using UFM. The sub-volume is assumed to be comprised of an active layer ($L = 1$) and a pure epoxy layer ($L = 2$) as shown in Fig. 5.5(a). The active layer ($L = 1$) is the 2-2 PFC layer of the sub-volume as illustrated in Fig. 5.5(b). The active (2-2 PFC) layer is first homogenised, and then it is taken as a homogeneous layer within the sub-volume (Fig. 5.5(a)) for deriving the closed-form expressions of its (sub-volume) effective coefficients. For homogenisation of the 2-2 PFC layer, the representative volume element (RVE) is chosen as the volume of the active layer (Fig. 5.5(b)) within the sub-volume (Fig. 5.5(a)). Following the continuities of tractions (Eq. (5.4b)) on the interphase surfaces of the RVE, the stress components ($\tau_{\theta r}$, σ_θ and $\tau_{\theta z}$) are assumed to be distributed uniformly over the volume of the RVE. The fibre/matrix phase is continuously distributed on the rz –plane (Fig. 5.5(b)). So, the strain components (ε_r, ε_z and γ_{rz}) are also assumed to be distributed uniformly over the volume of the RVE. The external electric field is applied through the top and bottom fully electrode-surfaces of the RVE (Fig. 5.5(b)). So, the electric field (E_z) is uniformly distributed throughout the volume of the RVE. According to these uniform fields, the constitutive relations (Eq. (5.3)) for the fibre and matrix phases can be written as,

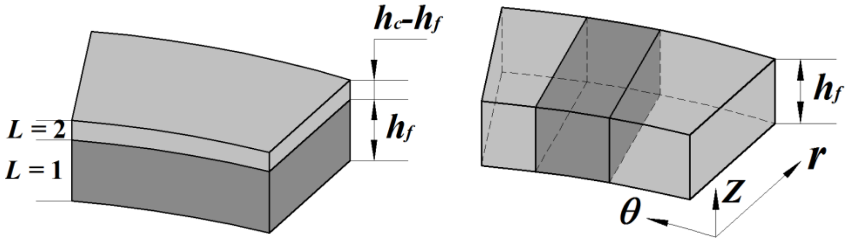

(a) (b)

Fig. 5.5 (a) A typical sub-volume of RV and (b) the 2-2 PFC layer within the sub-volume.

$$\mathfrak{I}^p = A^p \mathfrak{R}, \; \mathfrak{I}^p = \left\{ \sigma_r^p \quad \sigma_z^p \quad \tau_{rz}^p \quad \varepsilon_\theta^p \quad \gamma_{\theta r}^p \quad \gamma_{\theta z}^p \quad D_z^p \right\}^{\mathrm{T}},$$
$$\mathfrak{R} = \left\{ \sigma_\theta \quad \tau_{r\theta} \quad \tau_{\theta z} \quad \varepsilon_r \quad \varepsilon_z \quad \gamma_{rz} \quad E_z \right\}^{\mathrm{T}}, \; p = 1 \text{ or } 2 \tag{5.5a}$$

In Eq. (5.5a), the elements of the vector ($\mathfrak{R}$) are the uniform field components within the RVE. According to the rule of mixtures, the field components ($\sigma_r, \sigma_z, \tau_{rz}, \varepsilon_\theta, \gamma_{\theta r}, \gamma_{\theta z}, D_z$) within the RVE can be assumed as,

$$\mathfrak{I}=\left(v_f\mathfrak{I}^1+v_m\mathfrak{I}^2\right),\ \mathfrak{I}=\left\{\sigma_r\quad \sigma_z\quad \tau_{rz}\quad \varepsilon_\theta\quad \gamma_{\theta r}\quad \gamma_{\theta z}\quad D_z\right\}^{\mathrm{T}} \tag{5.5b}$$

where, v_f and v_m are the volume fractions of the fibre ($p=1$) and matrix ($p=2$) phases of RVE, respectively. Now, Eq. (5.5a) is introduced in Eq. (5.5b) for each of the phases, and then the resulting expression is simplified in the form of Eq. (5.2). The corresponding analytical expressions for the effective coefficients of the 2-2 PFC layer are obtained as,

$$C_{22}^a=\frac{C_{22}^fC_{22}^m}{v_fC_{22}^m+v_mC_{22}^f}\ ,\ C_{12}^a=C_{22}^a\left(\frac{v_fC_{12}^f}{C_{22}^f}+\frac{v_mC_{12}^m}{C_{22}^m}\right)\ ,$$

$$C_{23}^a=C_{22}^a\left(\frac{v_fC_{23}^f}{C_{22}^f}+\frac{v_mC_{23}^m}{C_{22}^m}\right),$$

$$C_{44}^a=\frac{C_{44}^fC_{44}^m}{v_fC_{44}^m+v_mC_{44}^f}\ ,\ C_{66}^a=\frac{C_{66}^fC_{66}^m}{v_fC_{66}^m+v_mC_{66}^f}\ ,\ C_{55}^a=\left(v_fC_{55}^f+v_mC_{55}^m\right)\ ,$$

$$C_{11}^a=\frac{(C_{12}^a)^2}{C_{22}^a}+v_fC_{11}^f+v_mC_{11}^m-\frac{v_f(C_{12}^f)^2}{C_{22}^f}-\frac{v_m(C_{12}^m)^2}{C_{22}^m}\ ,\ e_{35}^a=\left(v_fe_{35}^f+v_me_{35}^m\right),$$

$$C_{33}^a=\frac{(C_{23}^a)^2}{C_{22}^a}+v_fC_{33}^f+v_mC_{33}^m-\frac{v_f(C_{23}^f)^2}{C_{22}^f}-\frac{v_m(C_{23}^m)^2}{C_{22}^m}\ ,$$

$$\in_{33}^a=\left(v_f\in_{33}^f+v_m\in_{33}^m\right),$$

$$C_{13}^a=\frac{C_{12}^aC_{23}^a}{C_{22}^a}+v_fC_{13}^f+v_mC_{13}^m-\frac{v_fC_{12}^fC_{23}^f}{C_{22}^f}-\frac{v_mC_{12}^mC_{23}^m}{C_{22}^m} \tag{5.5c}$$

In Eq. (5.5c), the superscript $f\ /\ m\ /\ a$ denotes a coefficient of the fibre/matrix/2-2 PFC. As per these homogenised properties (Eq. (5.5c)) of the 2-2 PFC layer, it is taken as a homogeneous layer within the sub-volume (Fig. 5.5(a)), and the closed-form expressions for the effective coefficients of the sub-volume are derived. Following the continuities of tractions (Eq. (5.4a)) at the interlayer surface of the sub-volume (Fig. 5.5(a)), it is assumed that the stress components (τ_{zr}, $\tau_{z\theta}$ and σ_z) are uniformly distributed throughout the domain of the sub-volume. Since the layers of the sub-volume are continuously distributed on the $r\theta$-plane, the strain components (ε_r, ε_θ and $\gamma_{r\theta}$) are also assumed to be distributed uniformly over the domain of the sub-volume. As the top and bottom electrodes of the sub-volume are grounded, the homogeneous electric fields (E_z^L) in the active layer ($L=1$) and the epoxy layer ($L=2$) are related by, $E_z^2 = r_a E_z^1$ ($r_a = -h_f / (h_c - h_f)$). According to these uniform fields, Eq. (5.5a) can be written for this case as,

$$\mathfrak{I}^L = \boldsymbol{A}^L \mathfrak{R},\ \mathfrak{I}^L = \left\{ \sigma_r^L \quad \sigma_\theta^L \quad \tau_{r\theta}^L \quad \varepsilon_z^L \quad \gamma_{\theta z}^L \quad \gamma_{rz}^L \quad D_z^L \right\}^{\mathrm{T}},$$

$$\mathfrak{R} = \left\{ \sigma_z \quad \tau_{z\theta} \quad \tau_{rz} \quad \varepsilon_r \quad \varepsilon_\theta \quad \gamma_{r\theta} \quad E_z^1 \right\}^{\mathrm{T}},\ L = 1 \text{ or } 2 \tag{5.6a}$$

In order to determine the effective coefficients of the sub-volume with respect to the applied electric field across the thickness of the active layer ($L = 1$), the corresponding field (E_z^1) is kept within the vector ($\mathfrak{R}$) of uniform field components. Consequently, the electric field (E_z^2) within the epoxy layer is accounted in terms of the electric field (E_z^1) in the active layer by means of including the ratio (r_a) within the matrix ($\boldsymbol{A}^L$) for the epoxy layer ($L = 2$). Using Eq. (5.6a), the same procedure as that is carried out in the previous case is followed, and the closed-form expressions for the effective coefficients of the sub-volume are obtained with respect to the electric field across the thickness of the active layer as,

$$\bar{C}_{33} = \frac{C_{33}^a C_{33}^{ep}}{v_a C_{33}^{ep} + v_{ep} C_{33}^a},\ \bar{C}_{13} = \bar{C}_{33}\left(\frac{v_a C_{13}^a}{C_{33}^a} + \frac{v_{ep} C_{13}^{ep}}{C_{33}^{ep}} \right),$$

$$\bar{C}_{23} = \bar{C}_{33}\left(\frac{v_a C_{23}^a}{C_{33}^a} + \frac{v_{ep} C_{23}^{ep}}{C_{33}^{ep}} \right),$$

$$\bar{C}_{12} = \frac{\bar{C}_{13}\bar{C}_{23}}{\bar{C}_{33}} + (v_a C_{12}^a + v_{ep} C_{12}^{ep}) - \frac{v_a C_{13}^a C_{23}^a}{C_{33}^a} - \frac{v_{ep} C_{13}^{ep} C_{23}^{ep}}{C_{33}^{ep}},$$

$$\bar{C}_{44} = \frac{C_{44}^a C_{44}^{ep}}{v_a C_{44}^{ep} + v_{ep} C_{44}^a},\ \bar{C}_{55} = \frac{C_{55}^a C_{55}^{ep}}{v_a C_{55}^{ep} + v_{ep} C_{55}^a},\ \bar{C}_{66} = v_a C_{66}^a + v_{ep} C_{66}^{ep},$$

$$\bar{e}_{35} = \bar{C}_{55}\left(\frac{v_a e_{35}^a}{C_{55}^a} + \frac{r_a v_{ep} e_{35}^{ep}}{C_{55}^{ep}} \right),$$

$$\bar{C}_{11} = \frac{\bar{C}_{13}^{\,2}}{\bar{C}_{33}} + (v_a C_{11}^a + v_{ep} C_{11}^{ep}) - \frac{v_a (C_{13}^a)^2}{C_{33}^a} - \frac{v_{ep} (C_{13}^{ep})^2}{C_{33}^{ep}},$$

$$\bar{C}_{22} = \frac{\bar{C}_{23}^{\,2}}{\bar{C}_{33}} + (v_a C_{22}^a + v_{ep} C_{22}^{ep}) - \frac{v_a (C_{23}^a)^2}{C_{33}^a} - \frac{v_{ep} (C_{23}^{ep})^2}{C_{33}^{ep}},$$

$$\bar{\in}_{33} = (v_a \in_{33}^a + v_{ep} r_a \in_{33}^{ep}) + \frac{v_a (e_{35}^a)^2}{C_{55}^a} + \frac{v_{ep} r_a (e_{35}^{ep})^2}{C_{55}^{ep}} - \frac{(\bar{e}_{35})^2}{\bar{C}_{55}} \tag{5.6b}$$

where, v_a and v_{ep} are the volume fractions of the active (2-2 PFC) layer ($L =$ 1) and the epoxy layer ($L =$ 2), respectively; the overbar denotes the effective coefficients of the sub-volume.

5.3.3 FE model of the sub-volume

The effective coefficients of the sub-volume (Fig. 5.4(a)) are also estimated by deriving its FE model. A similar FE model is derived in Section 2.4, and that is modified here due to the reduced field components (Eq. (5.2)) in the sub-volume. The linear strain-displacement and electric field-potential relations at any point within the sub-volume can be written as,

$$\begin{Bmatrix} \boldsymbol{\varepsilon} \\ -E_z \end{Bmatrix} = \boldsymbol{L}\boldsymbol{d} \ , \ \boldsymbol{d} = \{u \quad v \quad w \quad \phi\}^{\mathrm{T}} \tag{5.7}$$

where, u, v and w are the displacements at any point within the sub-volume along the r, θ and z directions, respectively; ϕ is the electric potential at any point within the sub-volume; $\boldsymbol{L}$ is an operator matrix as given in Eq. (5.8).

$$\boldsymbol{L} = \begin{bmatrix} \frac{\partial}{\partial r} & \frac{1}{r} & 0 & 0 & \frac{\partial}{\partial z} & \frac{1}{r}\frac{\partial}{\partial \theta} & 0 \\ 0 & \frac{1}{r}\frac{\partial}{\partial \theta} & 0 & \frac{\partial}{\partial z} & 0 & 0 & \frac{\partial}{\partial r} - \frac{1}{r} \\ 0 & 0 & \frac{\partial}{\partial z} & \frac{1}{r}\frac{\partial}{\partial \theta} & \frac{\partial}{\partial r} & 0 & 0 \\ 0 & 0 & 0 & 0 & 0 & 0 & \frac{\partial}{\partial z} \end{bmatrix}^{\mathrm{T}} \tag{5.8}$$

According to Eq. (5.3), the first variation of the electro-elastic internal energy (δU) of the sub-volume can be written as (Tiersten, 1969),

$$\delta U = \sum_{p=1}^{2} \left(\int_{V^p} \left\langle \begin{Bmatrix} \delta \boldsymbol{\varepsilon} \\ -\delta E_z \end{Bmatrix}^{\mathrm{T}} \boldsymbol{C}^p \begin{Bmatrix} \boldsymbol{\varepsilon} \\ -E_z \end{Bmatrix} \right\rangle dV^p \right) \tag{5.9}$$

where, δ is an operator for the first variation; V^p is the volume of fibre phase ($p = 1$) or matrix phase ($p = 2$) within the sub-volume. For deriving the FE model of the sub-volume (Fig. 5.4(a)), its volume is discretized by 27-node isoparametric elements. The edges of a typical element are in parallel to the axes of the reference cylindrical coordinate system. A typical element is made of either fibre or matrix material. The electro-elastic state vector ($\boldsymbol{d}$) at any point within a typical element can be written in terms of the shape function matrix ($\boldsymbol{N}$) and the elemental nodal electro-elastic state vector ($\boldsymbol{d}^{\boldsymbol{e}}$) as given in Eq. (2.38).

$$\boldsymbol{d} = \boldsymbol{N}\boldsymbol{d}^{\boldsymbol{e}} \tag{2.38}$$

Introducing Eq. (5.7) in Eq. (5.9) and then using Eq. (2.38), the first variation of the elemental electro-elastic internal energy (δU^e) can be obtained as,

$$\delta U^e = (\delta \boldsymbol{d}^e)^{\mathrm{T}} \left\langle \boldsymbol{K}^e \boldsymbol{d}^e \right\rangle, \ \boldsymbol{K}^{\boldsymbol{e}} = \int_{V_e^p} \left(\boldsymbol{N}^{\mathrm{T}} \ \boldsymbol{L}^{\mathrm{T}} \ \boldsymbol{C}^p \ \boldsymbol{L} \ \boldsymbol{N} \right) dV_e^p \tag{5.10}$$

where, V_e^p is the elemental volume within the fibre phase ($p = 1$) or the matrix phase ($p = 2$). Assembling the elemental equations (Eq. (5.10)), the expression for the electro-elastic internal energy of the sub-volume can be obtained as given in Eq. (2.40).

$$\delta U = (\delta \boldsymbol{X})^{\mathrm{T}} \left\langle \boldsymbol{K}\,\boldsymbol{X} \right\rangle \tag{2.40}$$

The kinematic boundary conditions over the boundary surface of the sub-volume are implemented following the same procedure as discussed in Section 2.4, and the corresponding reduced form of Eq. (2.40) can be obtained as given in Eq. (2.43).

$$\boldsymbol{K}_r \, \boldsymbol{X}_r = -\sum_{i=1}^{N_b} \boldsymbol{P}_i X_i \tag{2.43}$$

The solution of Eq. (2.43) provides the nodal electro-elastic state vector ($\boldsymbol{X}$) for an applied kinematic boundary condition over the boundary surface of the sub-volume. This solution ($\boldsymbol{X}$) can then be utilised for computation of the volume-average field quantities using Eq. (2.18).

5.3.4 Effective coefficients of the sub-volume using FE formulation

According to the present arrangement of the electrodes and the corresponding assignment of electric potentials, the active layer and the epoxy layer within the sub-volume are subjected to the homogeneous electric fields of different magnitudes. Among these electric fields, the field (E_z^2) in the epoxy layer has no effect on the elastic behaviour of the sub-volume. But, the same field (E_z^2) contributes to the electric displacement (D_z) in the sub-volume. The volume-average electric displacement ($\bar{D}_z$) over the volume of the sub-volume can be written according to the rule of mixture as,

$$\bar{D}_z = (h_f / h_c)(\boldsymbol{e}^1 \bar{\boldsymbol{\varepsilon}}^1 + \in_{33}^1 E_z^1) + \left\langle (h_c - h_f)/h_c \right\rangle \in_{33}^2 E_z^2 \tag{5.11}$$

where, the superscript 1/2 indicates a quantity for the active/epoxy layer; $\bar{\boldsymbol{\varepsilon}}^1$ is the volume-average strain vector over the volume of the active layer. Using the relation ($E_z^2 = r_a E_z^1$) between the electric fields (E_z^1 and E_z^2), Eq. (5.11) can be expressed as,

$$\bar{D}_z = (h_f / h_c)\left[\boldsymbol{e}^1 \bar{\boldsymbol{\varepsilon}}^1 + \in_{33}^1 E_z^1 \left\langle 1 - (\in_{33}^2 / \in_{33}^1) \right\rangle \right] \tag{5.12}$$

As per the geometry of the sub-volume and the material properties of the constituents, the magnitude of $\in_{33}^2$ is about hundred times lesser than the magnitude of $\in_{33}^1$. So, the electric field (E_z^2) in the epoxy layer has a negligibly small effect on the electro-elastic behaviour of the sub-volume. Now, if the electric field in the epoxy layer is assumed to be equal to the electric field in the active layer, then it is expected that there would be no indicative change of the volume-average electric displacement ($\bar{D}_z$) of the sub-volume since the magnitude of E_z^1 is much lesser than the magnitude of E_z^2 according to their relation ($E_z^2 = r_a E_z^1$, $r_a = -h_f / (h_c - h_f)$, $h_f >> (h_c - h_f)$). On the basis of this observation, the electric field throughout the domain of the sub-volume may be assumed as equal to the electric field in the active layer, and thus the effective coefficients of the sub-volume are presently determined by applying zero or non-zero electric field across the thickness of the active layer.

The effective coefficients of the sub-volume are determined by applying seven sets of kinematic boundary conditions over its (sub-volume) boundary surface. These sets of boundary conditions over the six sides of the boundary surface of the sub-volume are illustrated in Table 5.1. A side of the boundary surface is denoted by the corresponding outward normal direction. So, the six sides of the boundary surface of the sub-volume are presented by, $-r$, $+r$, $-\theta$, $+\theta$, $-z$ and $+z$. For every set of boundary conditions (first column of Table 5.1), one strain/electric field component appears with a non-zero value (second column of Table 5.1). The corresponding effective coefficients are determined by computing the volume-average stress and electric displacement components over the volume of the sub-volume (third column of Table 5.1). In Table 5.1, the radial coordinate of the middle point of the sub-volume is denoted by, r_c. The applied electric potentials over the top, bottom and interlayer fully electrode-surfaces are denoted by, ϕ_t, ϕ_b and ϕ_a, respectively. The superscript $\bar{E}/\bar{\varepsilon}$ denotes zero electric field /strain field. The superscript (0) indicates a specified value of the applied homogeneous strain component. The superscript a indicates the electric field across the thickness (h_f) of the active (2-2 PFC) layer. The overbar indicates volume-average field quantity or effective coefficient.

Table 5.1 Kinematic boundary conditions and the effective coefficients of a typical sub-volume (BCs: boundary conditions, NC-S/E: non-zero strain or electric field components).

BCs	NC-S/E	Effective coefficients
$u\vert_{\pm r} = \pm\varepsilon_r^0 \Delta r / 2$, $v\vert_{\pm\theta} = 0$, $w\vert_{\pm z} = 0$	$\bar{\varepsilon}_r = \varepsilon_r^0$	$\left\{\bar{C}_{11}^{\bar{E}} \quad \bar{C}_{21}^{\bar{E}} \quad \bar{C}_{31}^{\bar{E}}\right\}^{\mathrm{T}} = \left\{\bar{\sigma}_r \quad \bar{\sigma}_\theta \quad \bar{\sigma}_z\right\}^{\mathrm{T}} / \bar{\varepsilon}_r$
$u\vert_{\pm r} = 0$, $w\vert_{\pm z} = 0$, $v\vert_{\pm\theta} = \pm\varepsilon_\theta^0 r_c \theta_c / 2$	$\bar{\varepsilon}_\theta = \varepsilon_\theta^0$	$\left\{\bar{C}_{12}^{\bar{E}} \quad \bar{C}_{22}^{\bar{E}} \quad \bar{C}_{32}^{\bar{E}}\right\}^{\mathrm{T}} = \left\{\bar{\sigma}_r \quad \bar{\sigma}_\theta \quad \bar{\sigma}_z\right\}^{\mathrm{T}} / \bar{\varepsilon}_\theta$
$u\vert_{\pm r} = 0$, $v\vert_{\pm\theta} = 0$, $w\vert_{\pm z} = \pm\varepsilon_z^0 h_c / 2$	$\bar{\varepsilon}_z = \varepsilon_z^0$	$\left\{\bar{C}_{13}^{\bar{E}} \quad \bar{C}_{23}^{\bar{E}} \quad \bar{C}_{33}^{\bar{E}}\right\}^{\mathrm{T}} = \left\{\bar{\sigma}_r \quad \bar{\sigma}_\theta \quad \bar{\sigma}_z\right\}^{\mathrm{T}} / \bar{\varepsilon}_z$
$w\vert_{\pm\theta} = \pm\gamma_{\theta z}^0 r_c \theta_c / 4$, $v\vert_{\pm z} = \pm\gamma_{\theta z}^0 h_c / 4$	$\bar{\gamma}_{\theta z} = \gamma_{\theta z}^0$	$\bar{C}_{44}^{\bar{E}} = \bar{\tau}_{\theta z} / \bar{\gamma}_{\theta z}$
$w\vert_{\pm r} = \pm\gamma_{rz}^0 \Delta r / 4$, $u\vert_{\pm z} = \pm\gamma_{rz}^0 h_c / 4$, $\phi_t = \phi_b = \phi_a = 0$	$\bar{\gamma}_{rz} = \gamma_{rz}^0$	$\bar{C}_{55}^{\bar{E}} = \bar{\tau}_{rz} / \bar{\gamma}_{rz}$, $\bar{e}_{35}^{\bar{E}} = \bar{D}_z / \bar{\gamma}_{rz}$
$v\vert_{\pm r} = \pm\gamma_{r\theta}^0 \Delta r / 4$, $u\vert_{\pm\theta} = \pm\gamma_{r\theta}^0 r_c \theta_c / 4$	$\bar{\gamma}_{r\theta} = \gamma_{r\theta}^0$	$\bar{C}_{66}^{\bar{E}} = \bar{\tau}_{r\theta} / \bar{\gamma}_{r\theta}$
$w\vert_{\pm r} = 0$, $u\vert_{\pm z} = 0$, $\phi_t = \phi_b = 0$, $\phi_a = 1$	$\bar{E}_z^a = 1/h_f$	$\bar{\epsilon}_{33}^{\bar{\varepsilon}} = \bar{D}_z / \bar{E}_z^a$, $\bar{e}_{35}^{\bar{\varepsilon}} = \bar{\tau}_{rz} / \bar{E}_z^a$

5.4 Results and discussions

In this section, first the present analytical and numerical procedures for homogenization of the sub-volumes are verified. Then, the effective electro-elastic coefficients of the shear mode PFC actuator are evaluated for its (actuator) different radial spans. The material properties of the epoxy matrix are taken as (Trindade and Benjeddou, 2011), $E = 2.9$ GPa, $\nu = 0.3$ and $\epsilon = 4.25\epsilon_0$ (

E , ν and ϵ_0 are Young's modulus, Poisson's ratio and vacuum permittivity, respectively). Unless otherwise mentioned, the piezoelectric fibres are considered to be made of PZT5H (Erturk and Inman, 2011). The corresponding properties of the longitudinally poled piezoelectric fibres are: C_{11} = 117.4 GPa, C_{22} = 127.2 GPa, C_{12} = 84.64 GPa, C_{23} = 80.21 GPa, C_{44} = 23.4 GPa, C_{66} = 22.99 GPa, e_{35} = 17.034 C/m^2, ϵ_{33}= 15.09 nF/m.

5.4.1 Verification of the present homogenisation procedures

Since a similar shear mode PFC actuator (in cylindrical coordinates) is not available in the literature, the present FE procedure for the numerical homogenization of the PFC actuator is first verified by taking the RVE (Fig. 5.5(b)) of the active (2-2 PFC) layer in the Cartesian coordinate system. If the radial and circumferential spans of the RVE are of small values, then a high value of the inner radius yields its (RVE) geometry similar to that in the Cartesian coordinate system. The material and geometrical properties of this RVE are taken from (Benjeddou and Al-Ajmi, 2011; Trindade and Benjeddou 2011) and the magnitudes of the effective coefficients are evaluated using the present FE procedure. These results are illustrated in Table 5.2 together with the similar analytical and FE results available in the literature (Benjeddou and Al-Ajmi, 2011; Trindade and Benjeddou, 2011). It may be observed from Table 5.2 that the present FE results are in good agreement with the available analytical/FE results (Benjeddou and Al-Ajmi, 2011; Trindade and Benjeddou 2011). This comparison verifies the present FE procedure for estimation of the effective coefficients of the 2-2 PFC layer. Next, for the construction of the RVE (Fig. 5.5(b)) in the cylindrical coordinate system, the magnitudes of the effective coefficients are computed using the present FE procedure. The magnitudes of the same effective coefficients are also computed using the present analytical expressions (Eq. (5.5c)). These results are illustrated in Table 5.3 (Shear mode 2-2 PFC in cylindrical coordinate system) for an FVF (v_f) and other geometrical properties of the RVE (Fig. 5.5(b)) as, $v_f = 0.8$, r_i = 0.2 m, $(r_o - r_i)$ = 500 µm, h_f = 500 µm, $h_c = h_f$, $w_f = h_f / 5$, $\theta_f = \sin^{-1}\left(w_f / 2r_i\right)$, $\theta_c = \theta_f / 0.8$. It may be observed from Table 5.3 (Shear mode 2-2 PFC in cylindrical coordinate system) that the results obtained from the FE procedure are very close to the results obtained from the analytical expressions. This comparison verifies the numerical accuracy in the present computation of effective coefficients of the shear mode 2-2 PFC (Fig. 5.5(b)). Next, The magnitudes of the effective coefficients of a typical sub-volume (Fig. 5.4(a)) are computed using the present FE procedure. These results are illustrated in Table 5.3 (Sub-volume of the shear mode PFC actuator). The FVF (v_f) and other geometrical properties of the sub-volume are taken as, $v_f = 0.76$, $r_i =$ 0.2 m, $(r_o - r_i) =$ 500 μm, $h_f =$ 500 μm, $h_c = h_f / 0.95$, $w_f = h_f / 5$, $\theta_f = \sin^{-1}\left(w_f / 2r_i\right)$, $\theta_c = \theta_f / 0.8$. Table 5.3 also contains the magnitudes of the same effective coefficients obtained from the present analytical expressions (Eq. (5.6b)).It may be observed from these results that the FE results are in excellent agreement with the analytical results, and thus the numerical accuracy in the present computation of effective coefficients of a typical sub-volume is verified. The FE results (Table 5.3) for the effective properties of the sub-volume are obtained by applying zero or non-zero homogeneous electric field across the thickness of the active (2-2 PFC) layer. These FE results are verified with the analytical results (Table 5.3), and this verification infers that the numerical homogenization of the sub-volume may be carried out by assuming the electric field in the active layer as the effective electric field within the domain of the sub-volume. For further verification of the present numerical homogenization procedure due to this consideration of the effective electric field, an electric field ($E_z^a = -V_a / h_f$, $V_a = (\phi_a - \phi_b)$, $\phi_b = \phi_t = 0$) is

Table 5.2 Verification of the present FE procedure for homogenization of the 2-2 PFC layer.

Parameters	FE results (ANSYS) (Trindade and Benjeddou, 2011)	UFM (Benjeddou and Al-Ajmi, 2011)	Present FE
E_1 or E_2 (GPa)	50.09	52.76	52.74
E_3 (GPa)	20.52	22.49	22.72
G_{23} or G_{13} (GPa)	6.49	5.89	6.49
ν_{12}	0.43	0.59	0.51
ν_{13} or ν_{23}	0.2	0.19	0.1
e_{15} (C/m^2)	3.13	2.84	3.13
$\in_{11}^T$ (nF/m)	14.85	14.85	14.85

applied across the thickness of the 2-2 PFC layer within the heterogeneous sub-volume. The corresponding volume-average free shear strain (γ_{rz}) over the volume of the heterogeneous sub-volume is computed using the FE model of the RVE. In parallel, an electric field with the same magnitude of the previous applied electric field ($E_z^a = -V_a / h_f$) is applied across the thickness (h_c) of the homogenised sub-volume by assuming a potential difference (V_c) as, $V_c = -E_z^a h_c$. The material properties of the homogenised sub-volume are taken from the FE results as presented in Table 5.3 and the volume-average free shear strain (γ_{rz}) over the volume of the asymptotically homogeneous sub-volume is computed using the FE model. These results are illustrated in Table 5.4 for three different values of the applied electric field ($E_z = E_z^a$). It may be observed from Table 5.4 that the magnitude of the volume-average free strain (γ_{rz}) of the heterogeneous sub-volume is very close to that of the homogenised sub-volume for any value of the applied electric field. This comparison study shows that the applied electric field across the thickness of the active (2-2 PFC) layer may be assumed as the effective electric field within the domain of the sub-volume, and the

Table 5.3 Magnitudes of the effective coefficients of the shear mode 2-2 PFC or a typical sub-volume of the shear mode PFC actuator ($\bar{C}_{ij}$ in GPa, $\bar{e}_{ij}$ in C/m^2, $\bar{\epsilon}_{ij}$ in 1e-9 F/m).

Shear mode 2-2 PFC in cylindrical coordinate system			Sub-volume of the shear mode PFC actuator	
Coefficients	UFM	FE	UFM	FE
$\bar{C}_{11}$	56.15	56.05	47.49	47.42
$\bar{C}_{22}$	17.38	17.31	16.15	16.27
$\bar{C}_{33}$	67.99	67.89	37.31	36.55
$\bar{C}_{44}$	4.68	4.67	4.026	4.085
$\bar{C}_{55}$	18.61	18.59	10.425	10.320
$\bar{C}_{66}$	4.67	5.02	4.824	4.899
$\bar{C}_{12}$	10.74	10.69	8.543	8.629
$\bar{C}_{13}$	31.55	31.49	17.24	16.96
$\bar{C}_{23}$	10.26	10.21	6.132	6.216
$\bar{e}_{35}$	13.62	13.61	7.25	7.17
$\bar{\epsilon}_{33}$	12.08	12.07	15.92	15.91

homogenization of the sub-volume may be carried out on the basis of this electric field.

Table 5.4 Verification of the volume-average free shear strain (γ_{rz}) (PFC-Hom: Homogenised sub-volume, PFC-Het: Heterogeneous sub-volume).

E_z (Volt/m)	Free strain (γ_{rz}) of PFC-Het	Free strain (γ_{rz}) of PFC-Hom
100e3	0.694e-4	0.691e-4
200e3	1.389e-4	1.382e-4
300e3	2.084e-4	2.073e-4

5.4.2 Effective properties of the shear mode PFC actuator

The varying properties of the RV (Fig. 5.3(a)) are determined by evaluating the effective coefficients of the sub-volumes (Fig. 5.3(b)) of different FVFs. Presently, a radial span of the RV is chosen between the inner (r_i) and the outer (r_o) radii of, 0.2 m and 1 m, respectively. This radial span is divided into four equal radial divisions which are denoted by, S_1, S_2, S_3 and S_4 following the outward radial direction. The RV is first designed with the inner and outer radii of the overall radial span (S ($r_i = 0.2$ m, $r_o = 1$ m) and it is denoted by RV^{S}. Next, it (RV) is redesigned for every radial sector ($S_1 / S_2 / S_3 / S_4$) within the corresponding inner and outer radial coordinates. These RVs for four divisions (S_1, S_2, S_3, S_4) are denoted by RV^{S1}, RV^{S2}, RV^{S3} and RV^{S4}. The maximum FVF at the inner radius of any RV is taken as 0.76 while the other geometric properties are taken as, h_f = 500 μm, $h_c = h_f / 0.95$, $w_f = h_f / 5$, $\theta_f = \sin^{-1}\left(w_f / 2r_i\right)$, $\theta_c = \theta_f / 0.8$. For any of the RVs, the sub-volumes (Fig. 5.3(b)) are generated by taking a radial span (Δr) of 500 μm and the FVFs of the sub-volumes are plotted in Fig. 5.6 against the radial coordinates of their middle points. It may be observed from Fig. 5.6 that the FVF of RV^{S} (S) decreases significantly with the increasing radius and reaches to its (FVF) minimum value at the outer radius. Similar nature of variation of FVF also appears for other RVs (RV^{S1}, RV^{S2}, RV^{S3}, RV^{S4}). But, the rate of change of the FVF with the increasing radius decreases when the inner radius of an RV increases.

For any of the RVs, the sub-volumes appear in a large number because of the small radial length ($\Delta r =$ 500 μm). The effective properties of each of these sub-

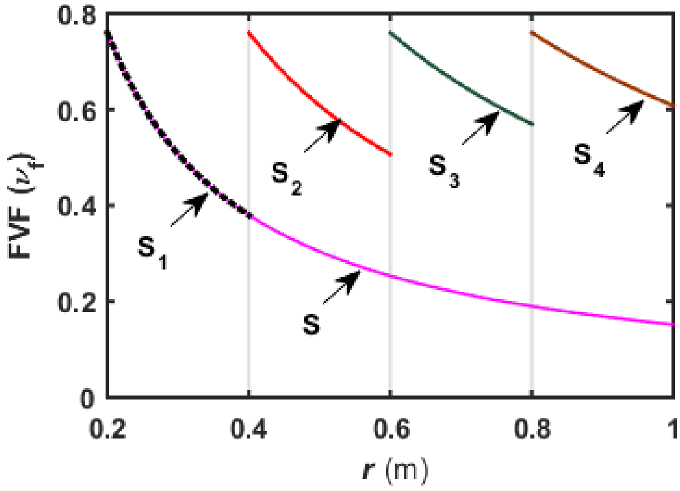

Fig. 5.6 Variations of FVF with radial coordinate for the RVs.

-volumes are to be computed separately. So, a large computational time is required, especially for computation of the effective coefficients using the FE procedure. In order to reduce the computational time, the computation is carried out by taking the sub-volumes at an interval of 2 cm along the radial direction. The corresponding magnitudes of the effective coefficients ($\bar{C}_{11}$, $\bar{e}_{35}$, $\bar{\epsilon}_{33}$) are plotted in Fig. 5.7 for two different materials of the piezoelectric phase (PZT5H or PZT5A) (Erturk and Inman, 2011). The magnitudes of the effective coefficients of a sub-volume are plotted against the radial coordinate of its middle point. It may be observed from Fig. 5.7 that the effective coefficients of an RV vary following the same nature of variation of the corresponding FVF (Fig. 5.6). The improved magnitudes of $\bar{e}_{35}$ and $\bar{\epsilon}_{33}$ can be obtained by the use of PZT5H instead of PZT5A. It is important to observe from Fig. 5.7(b) that the rate of change of the magnitude of $\bar{e}_{35}$ is significantly lesser for RV^{S4} than that for RV^{S1}. Also, the magnitude of $\bar{e}_{35}$ increases indicatively when the RV^{S} is divided into four radial divisions as RV^{S1}, RV^{S2}, RV^{S3} and RV^{S4}. So, the annular PFC actuator would be designed with small radial length for the improved magnitude of its main piezoelectric coefficient ($\bar{e}_{35}$), and it can be followed through the division of the radial span of interest. For the mathematical modelling of this shear mode annular PFC actuator, its varying effective electro-elastic coefficients are expressed as the polynomials of radial coordinate. These polynomials are given in Tables 5.5, 5.6 and 5.7 where

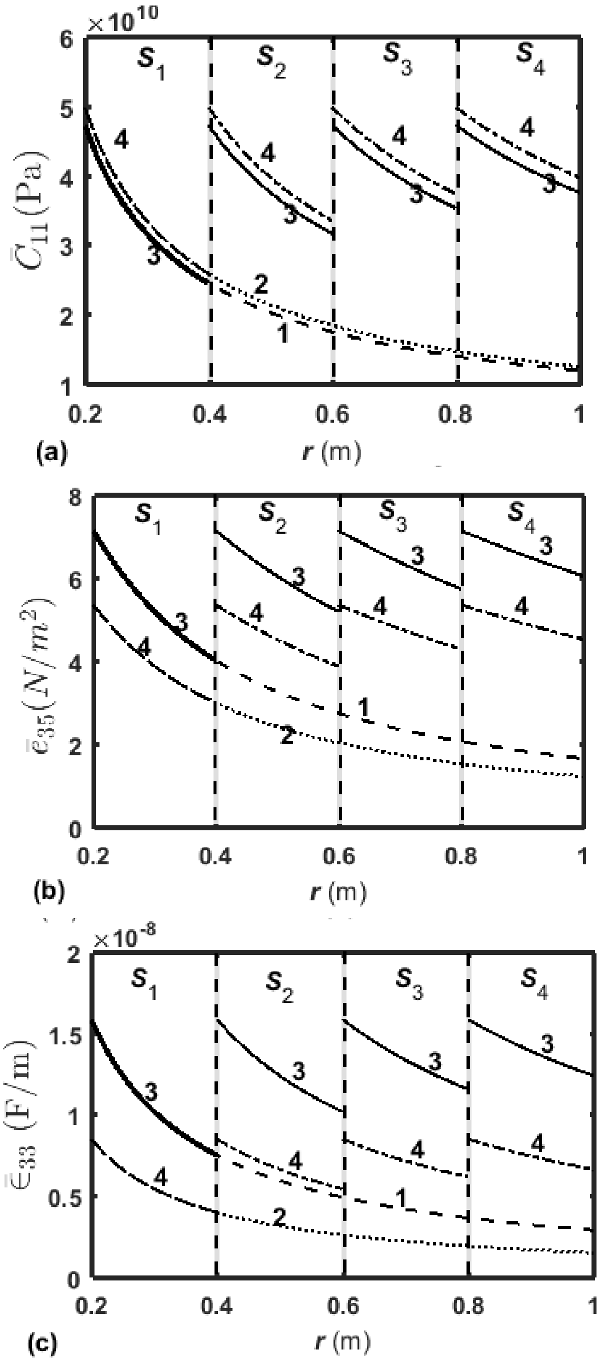

Fig. 5.7 Variations of the effective coefficients ((a) $\bar{C}_{11}$, (b) $\bar{e}_{35}$, (c) $\bar{\epsilon}_{33}$) with the radial coordinate for the different RVs (1: RV^S with PZT5H fibre; 2: RV^S with PZT5A fibre; 3: RV^{S1} /RV^{S2} /RV^{S3} /RV^{S4} with PZT5H fibre; 4: RV^{S1} / RV^{S2} / RV^{S3} / RV^{S4} with PZT5A).

the effective coefficients (C_{ij} , e_{35} , ϵ_{33}) for RV^S, RV^{S1}, RV^{S2}, RV^{S3} and RV^{S4} are denoted by the superscript 0, 1, 2, 3 and 4, respectively. The varying density of the PFC actuator is also computed by implementing the rule of mixtures for each of the sub-volumes, and the same are furnished in Table 5.8.

5.5 Conclusions

In this chapter, a shear mode PFC actuator in the form of a thin laminated annular disc is proposed for shear piezoelectric actuation of the plane structures of revolution. The primary component layer of this annular PFC actuator is made of 2-2 PFC in the shape of a very thin annular disc. The longitudinally poled piezoelectric fibres in the 2-2 PFC layer of the annular actuator are oriented along the radial direction while the fibres are periodically distributed in the circumferential direction. Every 2-2 PFC layer is supposed to be activated by supplying the external electric field across its thickness so that the annular PFC actuator produces electrically induced shear stress in the transverse plane of radial and axial coordinates. The effective electro-elastic properties of this shear mode PFC actuator vary along the radial direction mainly for the arrangement of fibres in the 2-2 PFC layer. These varying properties are determined by dividing the volume of RV of the PFC actuator into a large number of sub-volumes of different FVFs. The physical dimensions of the sub-volumes are taken in microscale, and thus these sub-volumes are assumed as the macroscopically homogeneous volumes. The effective properties of the RV at a point within its (RV) domain are considered as the effective properties of the sub-volume at that location. So, the varying properties of the RV/PFC actuator are determined by estimating the effective properties of the sub-volumes. The closed-form expressions for the effective coefficients of the sub-volumes are derived. An FE procedure is developed for numerical homogenization of the sub-volumes. The FE results for the effective coefficients are verified with the similar analytical results. From the results, it is observed that the main piezoelectric coefficient (e_{35}) has an indicative magnitude at the inner radius of the annular PFC actuator. But, the magnitude of this coefficient decreases at a significant rate as the radius increases. So, the overall radial span of interest is divided into four equal divisions, and the annular PFC actuator is redesigned for every radial division with a small radial length. The corresponding results reveal indicatively improved magnitude of the main piezoelectric coefficient (e_{35}) at any radius within the radial span of interest. Thus, this actuator may be a potential shear mode PFC actuator for active control of plane structures of revolution provided that it is to be designed with the appropriate radial dimensions.

Table 5.5 Stiffness coefficients of the shear mode annular PFC actuator.

C_{11}^{0}	1.4503e12 r^6 -5.8575e12 r^5 +9.7021e12 r^4 -8.4839e12 r^3 +4.1919e12 r^2 -1.1555e12 r +1.648e11
C_{11}^{1}	3.3022e14 r^6 -6.533e14 r^5 +5.3876e14 r^4 -2.3796e14 r^3 +5.9849e13 r^2 -8.2991e12 r +5.4293e11
C_{11}^{2}	6.0254e13 r^6 -1.9233e14 r^5 +2.5635e14 r^4 -1.8296e14 r^3 +7.401e13 r^2 -1.6232e13 r +1.5682e12
C_{11}^{3}	-3.7827e12 r^5 +1.4191e13 r^4 -2.1432e13 r^3 +1.6364e13 r^2 -6.3901e12 r +1.0748e12
C_{11}^{4}	-1.5881e11 r^3 +5.0302e11 r^2 -5.666e11 r +2.6014e11
C_{22}^{0}	-7.3283e12 r^7 +3.3148e13 r^6 -6.2714e13 r^5 +6.4245e13 r^4 -3.8461e13 r^3 +1.3469e13 r^2 -2.568e12 r +2.1383e11
C_{22}^{1}	-1.584e14 r^5 +2.5848e14 r^4 -1.6828e14 r^3 +5.4771e13 r^2 -8.955e12 r +5.9983e11
C_{22}^{2}	-1.2104e12 r^3 +2.0327e12 r^2 -1.1548e12 r +2.3041e11
C_{22}^{3}	-6.6076e11 r^3 +1.5389e12 r^2 -1.2129e12 r +3.3275e11
C_{22}^{4}	1.4482e12 r^4 -5.6168e12 r^3 +8.2243e12 r^2 -5.4057e12 r +1.36e12
C_{33}^{0}	4.8877e11 r^6 -2.0572e12 r^5 +3.5885e12 r^4 -3.3543e12 r^3 +1.8116e12 r^2 -5.6569e11 r +9.8937e10
C_{33}^{1}	-2.0428e14 r^6 +3.4827e14 r^5 -2.4069e14 r^4 +8.5232e13 r^3 -1.5741e13 r^2 +1.2267e12 r +2.5738e10
C_{33}^{2}	-1.5649e12 r^5 +4.2377e12 r^4 -4.7072e12 r^3 +2.7528e12 r^2 -9.027e11 r +1.6602e11
C_{33}^{3}	- 7.3379e11 r^5 +2.7051e12 r^4 -4.032e12 r^3 +3.0797e12 r^2 -1.2531e12 r +2.5716e11
C_{33}^{4}	7.523e10 r^4 -3.0304e11 r^3 +4.8246e11 r^2 -3.8191e11 r +1.5768e11
C_{12}^{0}	1.2738e12 r^6 -4.9966e12 r^5 +7.9526e12 r^4 -6.5668e12 r^3 +2.9696e12 r^2 -7.0165e11 r +7.1237e10
C_{12}^{1}	-8.5569e13 r^5 +1.3962e14 r^4 -9.0895e13 r^3 +2.9586e13 r^2 -4.8393e12 r +3.2421e11
C_{12}^{2}	- 6.5377e11 r^3 +1.0986e12 r^2 - 6.25e11 r +1.2467e11
C_{12}^{3}	-3.5707e11 r^3 +8.3189e11 r^2 -6.5619e11 r +1.8e11
C_{12}^{4}	-2.1736e11 r^3 +6.4728e11 r^2 -6.5232e11 r +2.2754e11
C_{13}^{0}	5.059e11 r^6 -2.0436e12 r^5 +3.3854e12 r^4 -2.9606e12 r^3 +1.463e12 r^2 -4.0355e11 r +5.7977e10
C_{13}^{1}	6.8673e13 r^6 -1.5227e14 r^5 +1.3851e14 r^4 -6.6533e13 r^3 +1.7966e13 r^2 -2.6434e12 r +1.8202e11
C_{13}^{2}	1.0037e12 r^4 -2.2317e12 r^3 +1.9e12 r^2 -7.5319e11 r +1.314e11
C_{13}^{3}	4.3237e11 r^4 -1.3221e12 r^3 +1.5413e12 r^2 -8.2742e11 r +1.8811e11

C_{13}^{4}	$2.2112e11\, r^{4} -8.6155e11\, r^{3} +1.2765e12\, r^{2} -8.6534e11\, r +2.4285e11$
C_{23}^{0}	$7.4152e11\, r^{6} -2.9127e12\, r^{5} +4.6445e12\, r^{4} -3.8456e12\, r^{3} +1.7464e12\, r^{2} -4.157e11\, r +4.3566e10$
C_{23}^{1}	$-4.9697e13\, r^{5} +8.1063e13\, r^{4} -5.2765e13\, r^{3} +1.7179e13\, r^{2} -2.8136e12\, r +1.901e11$
C_{23}^{2}	$-1.1833e13\, r^{5} +3.1713e13\, r^{4} -3.4077e13\, r^{3} +1.8385e13\, r^{2} -4.9971e12\, r +5.5371e11$
C_{23}^{3}	$9.1556e11\, r^{4} -2.7721e12\, r^{3} +3.1687e12\, r^{2} -1.6276e12\, r +3.2217e11$
C_{23}^{4}	$-1.2669e11\, r^{3} +3.7747e11\, r^{2} -3.8107e11\, r +1.3437e11$
C_{44}^{0}	$4.7381e11\, r^{6} - 1.8652e12\, r^{5} + 2.9822e12\, r^{4} - 2.4774e12\, r^{3} + 1.1296e12\, r^{2} - 2.7014e11\, r + 2.8454e10$
C_{44}^{1}	$-2.7215e13\, r^{5} + 4.4691e13\, r^{4} - 2.9328e13\, r^{3} + 9.6453e12\, r^{2} - 1.6e12\, r + 1.1012e11$
C_{44}^{2}	$1.1198e12\, r^{4} - 2.4648e12\, r^{3} + 2.0511e12\, r^{2} - 7.6967e11\, r + 1.1287e11$
C_{44}^{3}	$- 1.7422e12\, r^{5} + 6.5502e12\, r^{4} - 9.8982e12\, r^{3} + 7.5301e12\, r^{2} - 2.8941e12\, r + 4.5429e11$
C_{44}^{4}	$-6.8754e11\, r^{5} + 3.3114e12\, r^{4} - 6.4119e12\, r^{3} + 6.2501e12\, r^{2} - 3.0763e12\, r + 6.1691e11$
C_{55}^{0}	$2.9293e10\, r^{6} - 1.4552e11\, r^{5} + 3.0291e11\, r^{4} - 3.4292e11\, r^{3} + 2.2897e11\, r^{2} - 9.1157e10\, r + 2.1709e10$
C_{55}^{1}	$-4.141e13\, r^{6} + 7.515e13\, r^{5} - 5.6204e13\, r^{4} + 2.2082e13\, r^{3} - 4.7353e12\, r^{2} + 4.9014e11\, r - 6.4125e9$
C_{55}^{2}	$3.2259e11\, r^{5} - 8.7523e11\, r^{4} + 9.358e11\, r^{3} - 4.7767e11\, r^{2} + 1.0021e11\, r + 5.8832e9$
C_{55}^{3}	$6.99e10\, r^{5} - 2.7044e11\, r^{4} + 4.1568e11\, r^{3} - 3.1018e11\, r^{2} + 1.0131e11\, r + 1.0341e9$
C_{55}^{4}	$2.0143e10\, r^{5} - 1.0166e11\, r^{4} + 2.0446e11\, r^{3} - 2.0073e11\, r^{2} + 8.7805e10\, r - 1.0922e9$
C_{66}^{0}	$7.5084e11\, r^{6} - 2.9416e12\, r^{5} + 4.6742e12\, r^{4} - 3.8509e12\, r^{3} + 1.7356e12\, r^{2} - 4.0786e11\, r + 4.1107e10$
C_{66}^{1}	$-5.2314e13\, r^{5} + 8.525e13\, r^{4} - 5.5406e13\, r^{3} + 1.7993e13\, r^{2} - 2.9329e12\, r + 1.9535e11$
C_{66}^{2}	$- 3.9307e11\, r^{3} + 6.5842e11\, r^{2} - 3.7274e11\, r + 7.379e10$
C_{66}^{3}	$9.7479e11\, r^{4} - 2.9476e12\, r^{3} + 3.3626e12\, r^{2} - 1.7213e12\, r + 3.3751e11$
C_{66}^{4}	$- 1.3324e11\, r^{3} + 3.9562e11\, r^{2} - 3.9701e11\, r + 1.3754e11$

Table 5.6 Piezoelectric coefficients of the shear mode annular PFC actuator

e_{35}^{0}	$- 31.165\, r^{5} + 117.8\, r^{4} - 180.87\, r^{3} + 144.84\, r^{2} - 64.475\, r + 15.544$
e_{35}^{1}	$427.71\, r^{5} - 647.53\, r^{4} + 322.92\, r^{3} - 17.867\, r^{2} - 38.816\, r + 13.968$
e_{35}^{2}	$251.23\, r^{5} - 681.62\, r^{4} + 728.79\, r^{3} - 372.01\, r^{2} + 78.041\, r + 3.7131$
e_{35}^{3}	$54.437\, r^{5} - 210.62\, r^{4} + 323.73\, r^{3} - 241.56\, r^{2} + 78.896\, r - 0.063275$
e_{35}^{4}	$- 8.5651\, r^{4} + 32.3\, r^{3} - 42.413\, r^{2} + 17.347\, r + 7.4119$

Table 5.7 Dielectric coefficients of the shear mode annular PFC actuator.

$\in_{33}^{0}$	$- 2.1024e\text{-}7\, r^{5} + 7.3423e\text{-}7\, r^{4} - 1.0173e\text{-}6\, r^{3} + 7.0968e\text{-}7\, r^{2} - 2.599e\text{-}7\, r + 4.6425e\text{-}8$

$\in_{33}^{1}$	4.9524e-5 r^{6} - 9.673e-5 r^{5} + 7.9607e-5 r^{4} - 3.5685e-5 r^{3} + 9.3596e-6 r^{2} - 1.419e-6 r + 1.1125e-7
$\in_{33}^{2}$	1.7572e-6 r^{6} -6.0591e-6 r^{5} +8.8664e-6 r^{4} -7.1105e-6 r^{3} +3.3517e-6 r^{2} -9.1491e-7 r +1.2857e-7
$\in_{33}^{3}$	-1.5588e-7 r^{5} +6.4047e-7 r^{4} - 1.0839e-6 r^{3} +9.6094e-7 r^{2} -4.6451e-7 r +1.1194e-7
$\in_{33}^{4}$	-4.5261e-8 r^{5} +2.4007e-7 r^{4} -5.2487e-7 r^{3} +6.015e-7 r^{2} - 3.7582e-7 r +1.1687e-7

Table 5.8 Density of the shear mode annular PFC actuator

ρ^{o}	r^{6} -4.0897e5 r^{5} +6.9574e5 r^{4} -6.3035e5 r^{3} +3.2706e5 r^{2} -96773 r +16316
ρ^{1}	5.3869e6 r^{6} -1.1289e7 r^{5} +1.0046e7 r^{4} -4.9199e6 r^{3} +1.4318e6 r^{2} -2.4756e5 r +24794
ρ^{2}	2.6183e5 r^{6} -9.1591e5 r^{5} +1.3686e6 r^{4} -1.1324e6 r^{3} +5.6027e5 r^{2} -1.6577e5 r +28405
ρ^{3}	35898 r^{6} -1.7587e5 r^{5} +3.6865e5 r^{4} -4.2857e5 r^{3} +2.9844e5 r^{2} -1.2448e5 r +30046
ρ^{4}	8118.9 r^{6} -51147 r^{5} +1.3795e5 r^{4} -2.065e5 r^{3} +1.8527e5 r^{2} -99637 r +30988

CHAPTER

6

Active control of vibration of annular plates using a new shear mode PFC actuator with cylindrically periodic microstructure

6.1 Introduction

A new PFC actuator in cylindrical coordinates is designed in the previous chapter (Chapter 5) for shear mode piezoelectric actuation of plane structures of revolution. Its actuation capability is studied in this chapter by means of utilizing it in control of vibration of an annular plate. The overall study is carried out by proposing a smart annular sandwich plate with the embedded patches of the shear mode PFC actuator. The primary objective in this proposition of a smart annular sandwich plate is to achieve equal attenuation of all the modes of vibration of the plate within a frequency domain. The patches are embedded within the core of the sandwich plate, and every patch is supposed to counteract the mechanically induced transverse shear stress around its location by means of the feedback of local velocity. In this use of the velocity feedback control law for the shear mode PFC actuator, a fruitful strategy is proposed to utilize all the patches in an equal manner for effective control of vibration of the smart sandwich plate. For the analysis, an FE model of the smart annular sandwich plate is developed based on the layer-wise shear deformation theory, and the forced frequency responses for the plate are evaluated. These results illustrate the control power of the shear mode PFC actuator (Chapter 5) and also the suitability of the present strategy for configuring the smart annular plate.

6.2 Present smart annular sandwich plate

For active control of vibration of plates using the shear mode piezoelectric actuator, the overall smart plate is generally made in the form of the sandwich plate where the piezoelectric actuator is located in the core (Baillargeon and Vel, 2005a; Raja et al., 2011). If the piezoelectric actuator is used in the form of the patch, then a complex geometric configuration of the core arises. However, it may be achieved by embedding the patches within the traditional core of foam (Baillargeon and Vel, 2005b). Following the same procedure, the present annular sandwich plate is constructed by taking the material of the core as foam, and the patches of the shear mode PFC actuator are embedded within this foam layer. A schematic diagram of this smart annular sandwich plate is presented in Fig. 6.1. The inner/outer radius and the thickness of the overall annular plate are denoted by, r_i / r_o and h, respectively. The thicknesses of the top/bottom face layer and the core are indicated by, h_f and h_c, respectively. The thickness of the patches is the same as that is for the core.

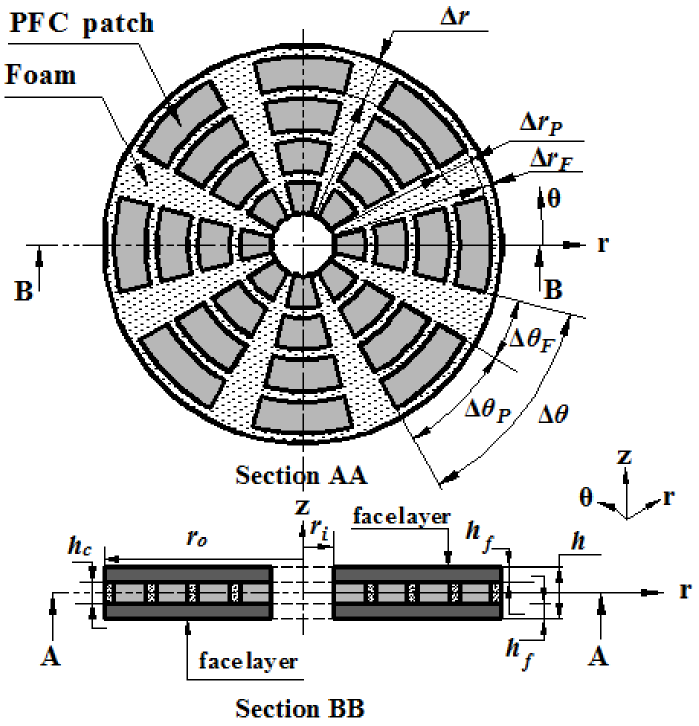

Fig. 6.1 Schematic diagram of the smart annular sandwich plate.

For effective control of structural deformation/vibration using a piezoelectric actuator in the form of the patch, it is generally recommended to locate the patches within the domain of the overall structure in an appropriate manner. The present shear mode PFC actuator counteracts the mechanically induced transverse shear stress within the overall plate, and this transverse shear stress appears with its maximum value at the nodes of any bending mode shape of vibration of the plate. So, the appropriate locations of the patches may be chosen as the nodes of the bending mode shape of vibration of the plate under study. But, the number and locations of the nodes change as the mode shape of the plate alters during its vibration within a range of operating frequency. So, it is a little difficult to decide appropriate locations of the patches over the plane of the annular plate. Presently, a strategy for the arrangement of the patches is proposed by taking the identical patches in the shape of annular-sector. The corresponding configuration of the patches is demonstrated in Fig. 6.1. The circumferential span of the annular plate is divided into a number (n_θ) of equal divisions. Similarly, the radial span $(r_o - r_i)$ of the same plate is divided into a number (n_r) of equal radial divisions. These divisions yield identical annular-sectors over the plane of the plate with the radial and circumferential spans of, $\Delta r = (r_o - r_i)/n_r$ and $\Delta\theta = 2\pi/n_\theta$, respectively. In every annular-sector, one patch is provided with the radial and circumferential lengths of, Δr_p and $\Delta\theta_p$, respectively. The corresponding radial (Δr_F) and circumferential ($\Delta\theta_F$) gaps in every sector are filled by the foam ($\Delta\theta = (\Delta\theta_p + \Delta\theta_F)$, $\Delta r = (\Delta r_p + \Delta r_F)$) (Fig. 6.1). The gaps ($\Delta r_F, \Delta\theta_F$) are very small in comparison to the in-plane dimensions of the patches ($\Delta\theta_p > \Delta\theta_F$, $\Delta r_p > \Delta r_F$). The main purpose of making this configuration of the core is to provide a sufficient number of patches around every node for any mode of vibration of the plate within an operating frequency-range of interest. If the operating frequency-range includes the modes of higher radial mode numbers, then the number (n_r) of divisions of the radial span $(r_o - r_i)$ is to be increased. Similarly, the number (n_θ) of divisions of the circumferential span (2π) is to be increased when the operating frequency-range includes the modes of higher circumferential mode numbers. For the increased number of radial/circumferential divisions, there would be no discrepancy in achieving effective actuation of the modes of lower radial/circumferential mode numbers. So, the number of radial/circumferential divisions is to be decided based on the maximum radial/circumferential mode number within the operating frequency-range of interest. Now, the mechanically induced transverse shear stress does not appear uniformly over the plane of the annular plate for any of its bending modes of vibration. So, it is required to activate the patches in an appropriate manner such that every patch can effectively counteract the mechanically induced transverse shear stress around its location. In order to achieve it according to the velocity feedback control strategy, every patch is equipped with a velocity sensor. For a typical patch, the velocity sensor is located on the top surface of the overall plate corresponding to the middle point of the plane of the patch. With this location of the velocity sensor, every patch is supposed to counteract the time-varying transverse shear stress around its location by taking the feedback of local velocity. According to this arrangement of the patches and velocity sensors, all the bending modes of vibration of the smart plate are expected to be attenuated effectively, and it is verified in the later section of this chapter. The control capability of the shear mode PFC actuator (Chapter 5) is investigated through this arrangement of its (PFC) patches where the PFC actuator is utilized with its two different geometric configurations separately.

For the first geometric configuration of the annular PFC actuator (as indicated by line 1/2 in Fig. 5.7), its inner and outer radii are equal to those of the host plate. The patches are made by dividing the plane of this annular PFC actuator, and the material of the patches is denoted by PFC#1. For the second geometric configuration of the PFC actuator (as indicated by line 3/4 in Fig. 5.7), the patches within a radial division ($S_1 / S_2 / S_3 / S_4$, Fig. 5.7) are made by dividing the plane of the corresponding part of the annular PFC actuator. In this second case, the material of the patches is denoted by PFC#2.

6.3 FE model of the smart annular sandwich plate

The middle plane of the overall annular plate is taken as the reference plane, and the centre of this annular plane is the origin of the reference cylindrical coordinate system ($r\theta z$). The kinematics of deformation of the overall annular plate is defined according to the layer-wise deformation theory. As per this theory, the displacements, u^k, v^k and w^k at any point within a layer (k) of the overall annular plate along the r, θ and z directions, respectively, can be written in Taylor series as follows,

$$u^k = u_0^k + \sum_{i=1}^{\infty} \xi_i^k \phi_i^k \ , \ v^k = v_0^k + \sum_{i=1}^{\infty} \xi_i^k \beta_i^k \ , \ w^k = w_0 \tag{6.1}$$

where, the superscript k indicates the bottom, middle and top layers as per its values as 1, 2 and 3, respectively; i indicates the number of terms in the Taylor series; u_0^k and v_0^k are the displacements at any point on the reference plane of the k^{th} layer along the r and θ directions, respectively; w_0 is the transverse displacement at any point on the middle plane of the overall plate; ξ_i^k is the thickness coordinate of i^{th} term for k^{th} layer; ϕ_i^k and β_i^k are the i^{th} order derivatives of u^k and v^k, respectively, with respect to the thickness coordinate (z)

at the reference plane of k^{th} layer. For any bending mode of deformation of the overall plate, the transverse shear stress ($\tau_{rz} / \tau_{\theta z}$) appears with an indicative magnitude at the middle plane of the plate. So, the deformation of the core ($k = 2$) is defined by the cubic polynomial ($i = 3$) of the thickness coordinate (z) as,

$$u^2 = u_0 + \sum_{i=1}^{3} \xi_i^2 \phi_i^2 \, , \;\; v^2 = v_0 + \sum_{i=1}^{3} \xi_i^2 \beta_i^2 \, , \;\; w^2 = w_0 \tag{6.2}$$

where, u_0 / v_0 is the translational displacement at any point on the middle plane of the plate along the r / θ direction and the thickness coordinates are, $\xi_1^2 = z$, $\xi_2^2 = (z)^2$ and $\xi_3^2 = (z)^3$. For any bending mode of deformation of the sandwich plate, the transverse shear stress ($\tau_{rz} / \tau_{\theta z}$) appears within the thin face layers with a small magnitude. So, the deformations of these layers ($k = 1$, 3) can be defined according to the first-order shear deformation theory (FSDT) as,

$$u^1 = u^2\Big|_{z=-h_c/2} + \xi_1^1 \phi_1^1 \, , \;\; v^1 = v^2\Big|_{z=-h_c/2} + \xi_1^1 \beta_1^1 \, , \;\; w^1 = w_0 \tag{6.3a}$$

$$u^3 = u^2\Big|_{z=h_c/2} + \xi_1^3 \phi_1^3 \, , \;\; v^3 = v^2\Big|_{z=h_c/2} + \xi_1^3 \beta_1^3 \, , \;\; w^3 = w_0 \tag{6.3b}$$

where, the reference planes for the bottom ($k = 1$) and top ($k = 3$) layers are taken as the corresponding interlayer surfaces. So, the thickness coordinates are, $\xi_1^1 = (z + h_c / 2)$ and $\xi_1^3 = (z - h_c / 2)$. The thickness of the overall plate is very small in comparison to its in-plane dimensions. So, the state of stress at any point within the overall plate may be assumed as $\sigma_z = 0$. According to this assumption, the state of stress and the state of strain at any point within a layer (k) can be written as,

$$\begin{gathered}\boldsymbol{\sigma}_b^k = \left\{ \sigma_r^k \quad \sigma_\theta^k \quad \tau_{r\theta}^k \right\}^{\mathrm{T}} , \; \boldsymbol{\sigma}_s^k = \left\{ \tau_{rz}^k \quad \tau_{\theta z}^k \right\}^{\mathrm{T}} , \; \boldsymbol{\varepsilon}_b^k = \left\{ \varepsilon_r^k \quad \varepsilon_\theta^k \quad \gamma_{r\theta}^k \right\}^{\mathrm{T}} , \\ \boldsymbol{\varepsilon}_s^k = \left\{ \gamma_{rz}^k \quad \gamma_{\theta z}^k \right\}^{\mathrm{T}} \end{gathered} \tag{6.4}$$

According to Eqs. (6.2) and (6.3), the displacements at any point within a layer (k) can be expressed by a generalized displacement vector ($\boldsymbol{d}$) as,

$$\boldsymbol{d}^k = \left\{ u^k \quad v^k \quad w^k \right\}^{\mathrm{T}} = \mathbf{Z}^k \boldsymbol{d} \, ,$$

$$\boldsymbol{d} = \left\{ u_0 \quad v_0 \quad w_0 \quad \phi_1^1 \quad \beta_1^1 \quad \phi_1^2 \quad \beta_1^2 \quad \phi_1^3 \quad \beta_1^3 \quad \phi_2^2 \quad \beta_2^2 \quad \phi_3^2 \quad \beta_3^2 \right\}^{\mathrm{T}}$$

$$\boldsymbol{Z}^k = \begin{bmatrix} 1 & 0 & 0 & z_1^k & 0 & z_2^k & 0 & z_3^k & 0 & z_4^k & 0 & z_5^k & 0 \\ 0 & 1 & 0 & 0 & z_1^k & 0 & z_2^k & 0 & z_3^k & 0 & z_4^k & 0 & z_5^k \\ 0 & 0 & 1 & 0 & 0 & 0 & 0 & 0 & 0 & 0 & 0 & 0 & 0 \end{bmatrix} \tag{6.5}$$

According to this displacement field, the strain-displacement relations can be written as,

$$\boldsymbol{\varepsilon}_b^k = \left(\boldsymbol{\varepsilon}_b^0 + z_1^k\boldsymbol{\kappa}_b^1 + z_2^k\boldsymbol{\kappa}_b^2 + z_3^k\boldsymbol{\kappa}_b^3 + z_4^k\boldsymbol{\kappa}_b^4 + z_5^k\boldsymbol{\kappa}_b^5\right),$$

$$\boldsymbol{\varepsilon}_s^k = \left(\boldsymbol{\varepsilon}_s^0 + {}^d z_1^k\boldsymbol{\kappa}_s^1 + {}^d z_2^k\boldsymbol{\kappa}_s^2 + {}^d z_3^k\boldsymbol{\kappa}_s^3 + {}^d z_4^k\boldsymbol{\kappa}_s^4 + {}^d z_5^k\boldsymbol{\kappa}_s^5\right),$$

$$\boldsymbol{\varepsilon}_b^0 = \partial_b^0\{u_0 \quad v_0 \quad w_0\}^{\mathrm{T}},\ \boldsymbol{\kappa}_b^1 = \partial_b^1\left\{\phi_1^{\ 1} \quad \beta_1^{\ 1}\right\}^{\mathrm{T}},\ \boldsymbol{\kappa}_b^2 = \partial_b^1\left\{\phi_1^{\ 2} \quad \beta_1^{\ 2}\right\}^{\mathrm{T}},$$

$$\boldsymbol{\kappa}_b^3 = \partial_b^1\left\{\phi_1^{\ 3} \quad \beta_1^{\ 3}\right\}^{\mathrm{T}},\ \boldsymbol{\kappa}_b^4 = \partial_b^1\left\{\phi_2^{\ 2} \quad \beta_2^{\ 2}\right\}^{\mathrm{T}},\ \boldsymbol{\kappa}_b^5 = \partial_b^1\left\{\phi_3^{\ 2} \quad \beta_3^{\ 2}\right\}^{\mathrm{T}},$$

$$\boldsymbol{\varepsilon}_s^0 = \partial_s^0\{u_0 \quad v_0 \quad w_0\}^{\mathrm{T}},\ \boldsymbol{\kappa}_s^1 = \partial_s^1\left\{\phi_1^{\ 1} \quad \beta_1^{\ 1}\right\}^{\mathrm{T}},\ \boldsymbol{\kappa}_s^2 = \partial_s^1\left\{\phi_1^{\ 2} \quad \beta_1^{\ 2}\right\}^{\mathrm{T}},$$

$$\boldsymbol{\kappa}_s^3 = \partial_s^1\left\{\phi_1^{\ 3} \quad \beta_1^{\ 3}\right\}^{\mathrm{T}},\ \boldsymbol{\kappa}_s^4 = \partial_s^1\left\{\phi_2^{\ 2} \quad \beta_2^{\ 2}\right\}^{\mathrm{T}},\ \boldsymbol{\kappa}_s^5 = \partial_s^1\left\{\phi_3^{\ 2} \quad \beta_3^{\ 2}\right\}^{\mathrm{T}}$$

$$\partial_b^0 = \begin{bmatrix} \frac{\partial}{\partial r} & 0 & 0 \\ \frac{1}{r} & \frac{1}{r}\frac{\partial}{\partial \theta} & 0 \\ \frac{1}{r}\frac{\partial}{\partial \theta} & \left(\frac{\partial}{\partial r} - \frac{1}{r}\right) & 0 \end{bmatrix},\ \partial_b^1 = \begin{bmatrix} \frac{\partial}{\partial r} & 0 \\ \frac{1}{r} & \frac{1}{r}\frac{\partial}{\partial \theta} \\ \frac{1}{r}\frac{\partial}{\partial \theta} & \left(\frac{\partial}{\partial r} - \frac{1}{r}\right) \end{bmatrix},\ \partial_s^0 = \begin{bmatrix} 0 & 0 & \frac{\partial}{\partial r} \\ 0 & 0 & \frac{1}{r}\frac{\partial}{\partial \theta} \end{bmatrix},\ \partial_s^1 = \begin{bmatrix} 1 & 0 \\ 0 & 1 \end{bmatrix} \tag{6.6}$$

In Eqs. (6.5) and (6.6), the parameters $\left(z_i^k,\ {}^d z_i^k\right)$ for the layers ($k = 1,\ 2,\ 3$) are,

$$\text{Layer 1 } (k=1)\text{: } z_1^1 = \left(z - h_2\right),\ z_2^1 = h_2,\ z_3^1 = 0,\ z_4^1 = (h_2)^2,\ z_5^1 = (h_2)^3,\ {}^d z_1^1 = 1$$
$$,\ {}^d z_2^1 = 0,\ {}^d z_3^1 = 0,\ {}^d z_4^1 = 0,\ {}^d z_5^1 = 0$$
$$\text{Layer 2 } (k=2)\text{: } z_1^2 = 0,\ z_2^2 = z,\ z_3^2 = 0,\ z_4^2 = (z)^2,\ z_5^2 = (z)^3,\ {}^d z_1^2 = 0,$$
$${}^d z_2^2 = 1,\ {}^d z_3^2 = 0,\ {}^d z_4^2 = 2z,\ {}^d z_5^2 = 3(z)^2$$
$$\text{Layer 3 } (k=3)\text{: } z_1^3 = 0,\ z_2^3 = h_3,\ z_3^3 = \left(z - h_3\right),\ z_4^3 = (h_3)^2,\ z_5^3 = (h_3)^3,$$
$${}^d z_1^3 = 0,\ {}^d z_2^3 = 0,\ {}^d z_3^3 = 1,\ {}^d z_4^3 = 0,\ {}^d z_5^3 = 0 \tag{6.7}$$

where, h_k and h_{k+1} are the thickness coordinates of the bottom and top surfaces of k^{th} layer, respectively. The strain-displacement relations in Eq. (6.6) can also be written in a compact form as follows,

$$\boldsymbol{\varepsilon}_b^k = \boldsymbol{Z}_b^k\partial_b\boldsymbol{d},\ \boldsymbol{\varepsilon}_s^k = \boldsymbol{Z}_s^k\partial_s\boldsymbol{d}$$

$$\boldsymbol{Z}_b^k = \begin{bmatrix} \boldsymbol{I}_3 & z_1^k\boldsymbol{I}_3 & z_2^k\boldsymbol{I}_3 & z_3^k\boldsymbol{I}_3 & z_4^k\boldsymbol{I}_3 & z_5^k\boldsymbol{I}_3 \end{bmatrix}$$

$$\boldsymbol{Z}_s^k = \begin{bmatrix} \boldsymbol{I}_2 & {}^d z_1^k \boldsymbol{I}_2 & {}^d z_2^k \boldsymbol{I}_2 & {}^d z_3^k \boldsymbol{I}_2 & {}^d z_4^k \boldsymbol{I}_2 & {}^d z_5^k \boldsymbol{I}_2 \end{bmatrix}$$

$$\partial_b = \begin{bmatrix} \partial_b^0 & 0 & 0 & 0 & 0 & 0 \\ 0 & \partial_b^1 & 0 & 0 & 0 & 0 \\ 0 & 0 & \partial_b^1 & 0 & 0 & 0 \\ 0 & 0 & 0 & \partial_b^1 & 0 & 0 \\ 0 & 0 & 0 & 0 & \partial_b^1 & 0 \\ 0 & 0 & 0 & 0 & 0 & \partial_b^1 \end{bmatrix}, \ \partial_s = \begin{bmatrix} \partial_s^0 & 0 & 0 & 0 & 0 & 0 \\ 0 & \partial_s^1 & 0 & 0 & 0 & 0 \\ 0 & 0 & \partial_s^1 & 0 & 0 & 0 \\ 0 & 0 & 0 & \partial_s^1 & 0 & 0 \\ 0 & 0 & 0 & 0 & \partial_s^1 & 0 \\ 0 & 0 & 0 & 0 & 0 & \partial_s^1 \end{bmatrix} \tag{6.8}$$

where, $\boldsymbol{I}_2 / \boldsymbol{I}_3$ is the unit matrix of the size $(2\times 2)/(3\times 3)$. The face layers are considered to be made of an isotropic material. The corresponding constitutive relations under the plane stress assumption can be written as,

$$\boldsymbol{\sigma}_b^k = \boldsymbol{C}_b^k \boldsymbol{\varepsilon}_b^k, \ \boldsymbol{\sigma}_s^k = \boldsymbol{C}_s^k \boldsymbol{\varepsilon}_s^k$$
$$\boldsymbol{C}_b^k = \frac{E^k}{1-(\nu^k)^2} \begin{bmatrix} 1 & \nu^k & 0 \\ \nu^k & 1 & 0 \\ 0 & 0 & (1-\nu^k)/2 \end{bmatrix}, \ \boldsymbol{C}_s^k = \frac{E^k}{2(1+\nu^k)} \begin{bmatrix} 1 & 0 \\ 0 & 1 \end{bmatrix} \tag{6.9}$$

where, E^k and ν^k are Young's modulus and Poisson's ratio, respectively, for the face layers ($k=1,3$). Since the foam at the core ($k=2$) is also an isotropic material, similar constitutive relations (as in Eq. (6.9)) also appear for the foam.

The annular PFC actuator (Chapter 5) is comprised of several active layers. The top and bottom surfaces of every active layer are fully electrode-surfaces, and the external electric field is applied by specifying the voltage (V) across the thickness (h_a) of the active layer or the electrode-surfaces. So, the electric field components (E_r, E_θ, E_z) at any point within the actuator may be assumed as, $E_z = -V/h_a$, $E_r = E_\theta = 0$. Under this applied electric field, a transverse shear stress (τ_{rz}) induces within the PFC actuator due to its effective piezoelectric coefficient (e_{35}). Accordingly, the constitutive relations under the plane stress assumption can be written as (Chapter 5),

$$\boldsymbol{\sigma}_b^k = \boldsymbol{C}_b^k(r)\boldsymbol{\varepsilon}_b^k, \ \boldsymbol{\sigma}_s^k = \boldsymbol{C}_s^k(r)\boldsymbol{\varepsilon}_s^k - \boldsymbol{e}_s^k(r)E_z, \ D_z^k = \left\langle \boldsymbol{e}_s^k(r) \right\rangle^{\mathrm{T}} \boldsymbol{\varepsilon}_s^k + \epsilon_{33}^k(r)E_z \tag{6.10}$$

where, the superscript k indicates the layer ($k=2$) at the core of the plate, and the property matrices ($\boldsymbol{C}_b^k(r)$, $\boldsymbol{C}_s^k(r)$ and $\boldsymbol{e}_s^k(r)$) are as follows,

$$\boldsymbol{C}_b^k = \begin{bmatrix} \bar{C}_{11}^k(r) & \bar{C}_{12}^k(r) & 0 \\ \bar{C}_{12}^k(r) & \bar{C}_{22}^k(r) & 0 \\ 0 & 0 & C_{66}^k(r) \end{bmatrix},\ \boldsymbol{C}_s^k = \begin{bmatrix} C_{55}^k(r) & 0 \\ 0 & C_{44}^k(r) \end{bmatrix},\ \boldsymbol{e}_s^k = \begin{Bmatrix} e_{35}^k(r) \\ 0 \end{Bmatrix},$$

$$\bar{C}_{11}^k(r) = C_{11}^k(r) - \left\langle C_{13}^k(r) \right\rangle^2 / C_{33}^k(r),\ \bar{C}_{12}^k(r) = C_{12}^k(r) - \left\langle C_{13}^k(r) C_{23}^k(r) \right\rangle / C_{33}^k(r),$$

$$\bar{C}_{22}^k(r) = C_{22}^k(r) - \left\langle C_{23}^k(r) \right\rangle^2 / C_{33}^k(r),\ k = 2 \tag{6.11}$$

In Eq. (6.11), $C_{ij}^k(r)$ $(i, j = 1,2,\ldots,6)$, $\in_{ij}^k(r)$ $(i, j = 1,2,3)$ and $e_{35}^k(r)$ are the stiffness, dielectric and piezoelectric coefficients of the PFC actuator, respectively; D_z^k is the electric displacement along the thickness (z) direction.

For deriving the FE model of the smart annular sandwich plate, the plane of the plate is discretized by nine-node isoparametric elements in such a manner that the edges of any element are in parallel to the radial and circumferential axes of the reference cylindrical coordinate system. The core of a typical element is either made of foam or made of PFC actuator. So, two different elemental stacking sequences appear in the FE mesh. The first one (Element 1) has the core of foam and the second one (Element 2) has the core of PFC actuator. The displacement vector $(\boldsymbol{d})$ at any point within an element can be written in terms of the shape function matrix $(\boldsymbol{N})$ and the elemental nodal displacement vector $(\boldsymbol{d}_e)$ as follows,

$$\boldsymbol{d} = \boldsymbol{N}\boldsymbol{d}_e \tag{6.12}$$

Using Eq. (6.12), the strain-displacement relations (Eq. (6.8)) and the displacement vector $(\boldsymbol{d}^k)$ (Eq. (6.5)) for an element can be expressed as,

$$\boldsymbol{\varepsilon}_b^k = \boldsymbol{Z}_b^k \boldsymbol{B}_b \boldsymbol{d}_e,\ \boldsymbol{B}_b = \boldsymbol{\partial}_b \boldsymbol{N},\ \boldsymbol{\varepsilon}_s^k = \boldsymbol{Z}_s^k \boldsymbol{B}_s \boldsymbol{d}_e,\ \boldsymbol{B}_s = \boldsymbol{\partial}_s \boldsymbol{N},\ \boldsymbol{d}^k = \boldsymbol{Z}^k \boldsymbol{N}\boldsymbol{d}_e \tag{6.13}$$

The overall annular plate is considered to operate under a transverse harmonic point load $(p(r,\theta,z,t))$ at a point (r_L, θ_L, z_L). For the corresponding vibration of the overall annular plate, the first variations of the total potential energy (δT_p^e) and the total kinetic energy (δT_k^e) of a typical element at an instant of time (t) can be written as,

$$\delta T_p^e = \int_{r_i^e}^{r_o^e} \int_{\theta_i^e}^{\theta_o^e} \left\{ \sum_{k=1}^{3} \int_{h_k}^{h_{k+1}} \left[(\delta \boldsymbol{\varepsilon}_b^k)^{\mathrm{T}} \boldsymbol{\sigma}_b^k + (\delta \boldsymbol{\varepsilon}_s^k)^{\mathrm{T}} \boldsymbol{\sigma}_s^k \right] dz - \int_{h_k}^{h_{k+1}} \delta E_z D_z^k \Big|_{k=2} dz \right\} r\, d\theta\, dr - Q_p \tag{6.14}$$

$$Q_p = \left\langle (\delta w_0) p \right\rangle_{r_L,\theta_L,z_L}$$

$$\delta T_k^e = \int_{r_i^e}^{r_0^e} \int_{\theta_i^e}^{\theta_0^e} \left\langle \sum_{k=1}^{3} \int_{h_k}^{h_{k+1}} \left\{ \delta \dot{u}^k \quad \delta \dot{v}^k \quad \delta \dot{w}^k \right\} \rho^k \left\{ \dot{u}^k \quad \dot{v}^k \quad \dot{w}^k \right\}^{\mathrm{T}} dz \right\rangle r d\theta dr \tag{6.15}$$

where, δ is an operator for the first variation; r_i^e / θ_i^e and r_0^e / θ_0^e are the inner and outer radial/circumferential boundaries of an element, respectively. In Eq. (6.14), the last term appears for the elements which are subjected to the applied mechanical point load. Using Eqs. (6.5), (6.8), (6.9), (6.10) and (6.13) in Eqs. (6.14) and (6.15), the simplified elemental expressions for δT_p^e and δT_k^e can be obtained as follows,

$$\delta T_p^e = \int_{r_i^e}^{r_0^e} \int_{\theta_i^e}^{\theta_0^e} \left\{ \delta \boldsymbol{d}_e^{\mathrm{T}} \left[\left\langle \boldsymbol{B}_b^{\mathrm{T}} \boldsymbol{A}_b(r) \boldsymbol{B}_b + \boldsymbol{B}_s^{\mathrm{T}} \boldsymbol{A}_s(r) \boldsymbol{B}_s \right\rangle \boldsymbol{d}_e - \left\langle \boldsymbol{B}_s^{\mathrm{T}} \boldsymbol{A}_e(r) \right\rangle E_z \right] \right\} r d\theta dr - \delta \boldsymbol{d}_e^{\mathrm{T}} \boldsymbol{P}_e(t) \tag{6.16}$$

$$\delta T_k^e = \int_{r_i^e}^{r_0^e} \int_{\theta_i^e}^{\theta_0^e} \left\{ \delta \dot{\boldsymbol{d}}_e^{\mathrm{T}} \left[\boldsymbol{N}^{\mathrm{T}} \boldsymbol{m}(r) \boldsymbol{N} \right] \dot{\boldsymbol{d}}_e \right\} r d\theta dr \tag{6.17}$$

where, $\boldsymbol{P}_e(t)$ is a column matrix for the elemental nodal transverse loads. In Eq. (6.16) and (6.17), the rigidity matrices ($\boldsymbol{A}_b(r), \boldsymbol{A}_s(r)$), electro-elastic coupling vector ($\boldsymbol{A}_e(r)$) and mass matrix per unit area ($\boldsymbol{m}(r)$) are to be formed according to the elemental stacking sequences (Element 1 and Element 2) as follows,

$$\begin{gathered} \boldsymbol{A}_b(r) = \sum_{k=1}^{3} \int_{h_k}^{h_{k+1}} \left[(\boldsymbol{Z}_b^k)^{\mathrm{T}} \boldsymbol{C}_b^k(r) \boldsymbol{Z}_b^k \right] dz, \quad \boldsymbol{A}_s(r) = \sum_{k=1}^{3} \int_{h_k}^{h_{k+1}} \left[(\boldsymbol{Z}_s^k)^{\mathrm{T}} \boldsymbol{C}_s^k(r) \boldsymbol{Z}_s^k \right] dz, \\ \boldsymbol{m}(r) = \sum_{k=1}^{3} \int_{h_k}^{h_{k+1}} \left[(\boldsymbol{Z}^k)^{\mathrm{T}} \rho^k(r) \boldsymbol{Z}^k \right] dz, \quad \boldsymbol{A}_e(r) = \int_{h_k}^{h_{k+1}} \left[(\boldsymbol{Z}_s^k)^{\mathrm{T}} \boldsymbol{e}_s^k(r) \right]_{k=2} dz \end{gathered} \tag{6.18}$$

In Eq. (6.18), the electro-elastic coupling vector ($\boldsymbol{A}_e(r)$) is a null vector for the elements with the core of foam (Element 1). The governing equations of motion of the overall annular plate are derived employing Hamilton's principle as given in Eq. (3.36).

$$\int_{t_1}^{t_2} \left(\delta T_p^e - \delta T_k^e \right) dt = 0 \tag{3.36}$$

Introducing Eqs. (6.16) and (6.17) in Eq. (3.36), the governing equations of motion for a typical element can be obtained as,

$$\boldsymbol{M}^e \ddot{\boldsymbol{d}}_e + \boldsymbol{K}^e \boldsymbol{d}_e = \boldsymbol{P}_e + \boldsymbol{P}_E^e E_z$$

$$\begin{gathered}\boldsymbol{M}^e=\int_{r_i^e}^{r_0^e}\int_{\theta_i^e}^{\theta_0^e}\left[\boldsymbol{N}^{\mathrm{T}}\boldsymbol{m}(r)\boldsymbol{N}\right]rd\theta dr\,,\\ \boldsymbol{K}^e=\int_{r_i^e}^{r_0^e}\int_{\theta_i^e}^{\theta_0^e}\left[\boldsymbol{B}_b{}^{\mathrm{T}}\boldsymbol{A}_b(r)\boldsymbol{B}_b+\boldsymbol{B}_s{}^{\mathrm{T}}\boldsymbol{A}_s(r)\boldsymbol{B}_s\right]rd\theta dr\,,\\ \boldsymbol{P}_E^e=\int_{r_i^e}^{r_0^e}\int_{\theta_i^e}^{\theta_0^e}\left[\boldsymbol{B}_s{}^{\mathrm{T}}\boldsymbol{A}_e(r)\right]rd\theta dr\end{gathered}\tag{6.19}$$

Assembling the elemental equations (Eq. (6.19)), the following global equations of motion for the overall annular plate can be obtained,

$$\boldsymbol{M}\ddot{\boldsymbol{X}}+\boldsymbol{K}\boldsymbol{X}=\boldsymbol{P}_M+\sum_{s=1}^{n_p}\boldsymbol{P}_E^s E_z^s\tag{6.20}$$

where, $\boldsymbol{M}$ and $\boldsymbol{K}$ are the global mass and stiffness matrices, respectively; $\boldsymbol{X}$ is the global nodal displacement vector; $\boldsymbol{P}_M$ is the global nodal mechanical load vector; n_p is the total number of patches of the shear mode PFC actuator; $\boldsymbol{P}_E^s$ and E_z^s are the electromechanical coefficient vector and the applied electric field, respectively for the s^{th} patch of the shear mode PFC actuator.

6.3.1 Implementation of control strategy

Every patch of the shear mode PFC actuator is activated by taking the feedback of local transverse velocity. The local transverse velocity ($\dot{w}_s$) for s^{th} patch is sensed at its middle point and fed back to it in the form of the electric field (E_z^s) as follows,

$$E_z^s=\mp k_d^s\dot{w}_s\tag{6.21}$$

where, k_d^s is the velocity feedback control-gain for s^{th} actuator-patch. The transverse velocity ($\dot{w}_s$) corresponding to the s^{th} patch can be expressed in terms of the global velocity vector ($\dot{\boldsymbol{X}}$) as,

$$\dot{w}_s=\boldsymbol{T}_s\dot{\boldsymbol{X}}\tag{6.22}$$

where, $\boldsymbol{T}_s$ is a row matrix that indicates the element of $\dot{\boldsymbol{X}}$ corresponding to the transverse velocity at the middle point of s^{th} patch. Introducing Eqs. (6.21) and (6.22) in Eq. (6.20), the following expression can be obtained,

$$\boldsymbol{M}\ddot{\boldsymbol{X}}+\boldsymbol{K}\boldsymbol{X}=\boldsymbol{P}_M\mp\left(\sum_{s=1}^{n_p}\boldsymbol{C}_s\right)\dot{\boldsymbol{X}},\ \boldsymbol{C}_s=(\boldsymbol{P}_E^s k_d^s\boldsymbol{T}_s)\tag{6.23}$$

For any bending mode shape of the annular plate, the sign of the transverse shear stress (τ_{rz}) at a node is opposite to that at a consecutive node. The corresponding change of sign of the stress (τ_{rz}) occurs at the anti-node between the consecutive nodes. So, for effective actuation of the annular plate at any instant of time, the direction of the externally applied electric field (E_z^s) is to be reversed at the anti-nodes along the radial direction. Now, the transverse velocity does not change its sign at the same locations (anti-nodes). So, as per the velocity feedback control law (Eq. (6.21)), the reversal in the direction of the applied electric field can be achieved by altering the sign (positive/negative) of the control-gain ($+k_d^S / -k_d^S$). Since this alteration of the sign of the control-gain appears along the radial direction due to the transverse plane of actuation in radial and thickness coordinates, it can be implemented by making a number of radial groups of the patches. Presently, the number of radial groups is taken as n_r following the radial divisions in the arrangement of the patches. Every radial group is distributed throughout the circumference of the annular plate having the number of patches as n_θ. The radial-groups are denoted as, $g = 1, 2, 3, \ldots\ n_r$ following the outward radial direction. The control-gains for the patches within a group (g) are assigned with the same sign, while it (sign) changes over the groups according to the modes of vibration under study. By this strategy, Eq. (6.23) is written as,

$$\boldsymbol{M}\ddot{\boldsymbol{X}} + \boldsymbol{K}\boldsymbol{X} = \boldsymbol{P}_M - \left(\sum_{g=1}^{n_r} S_g \boldsymbol{C}_g\right)\dot{\boldsymbol{X}},\ \boldsymbol{C}_g = \sum_{s=1}^{n_\theta} \left(\boldsymbol{P}_E^s\left(\left|k_d^s\right|\right)\boldsymbol{T}_s\right)_g \qquad (6.24)$$

where, S_g indicates the sign of the control-gain for the g^{th} group of patches (S_g = +1 or -1), and the subscript g in the expression of $\boldsymbol{C}_g$ indicates the patches within a group ($g = 1, 2, \ldots n_r$). Equation (6.24) can also be written in a simplified form as,

$$\boldsymbol{M}\ddot{\boldsymbol{X}} + \boldsymbol{C}\dot{\boldsymbol{X}} + \boldsymbol{K}\boldsymbol{X} = \boldsymbol{P}_M,\ \boldsymbol{C} = \sum_{g=1}^{n_r} S_g \boldsymbol{C}_g \qquad (6.25)$$

6.4 Results and discussions

In this section, the frequency responses of the smart annular sandwich plate are evaluated for investigating the control capability of the shear mode annular PFC actuator. The inner and the outer edges of the overall annular plate are considered as the simply-supported edges. The face layers of the sandwich plate are considered to be made of Aluminum ($E = 70$ GPa, $\nu = 0.3$, $\rho =$ 2700 kg/m^3). The properties of foam at the core are taken as, $E = 35.3$ MPa, $\nu = 0.383$. The inner radius (r_i), outer radius (r_o) and thickness (h) of the overall annular plate are taken as, 0.2 m, 1 m and 4 mm, respectively. The two different geometric configurations of the annular PFC actuator are utilized separately. In the first geometric configuration of the annular PFC actuator (line/2 in Fig. 5.7), its inner and outer radii are, 0.2 m and 1 m, respectively. In the second one, the radial dimensions for the four divisions/parts of the PFC actuator (line 3/4 in Fig. 5.7) are taken as, $r_i = 0.2$ m, $r_1 = 0.4$ m, $r_2 = 0.6$ m, $r_3 = 0.8$ m and $r_o = 1$ m. For any of the two geometric configurations of the annular PFC actuator, it is considered to be made of four active layers. Every active layer has a thickness (h_e) of 0.5 mm, while the total thickness of the actuator or the core is 2.104 mm. According to these geometrical properties and a maximum FVF of 0.76, the varying properties of the PFC actuator for any of its geometrical configurations are given in Tables 5.5, 5.6, 5.7 and 5.8. Using the first (PFC#1) or second (PFC#2) geometric configuration of the annular PFC actuator, the patches are arranged with the geometrical properties of, $n_r = 4$, $n_\theta = 8$, $\Delta\theta_F = 2^{\circ}$, $\Delta r_F = 5$ mm.

In order to verify the present FE formulation, first, the natural frequencies of the annular plate are evaluated considering negligibly small thickness ($h_c \approx 0$) of the core with the deactivated patches. These results are compared with the similar analytical results (Singh and Chakraverty, 1993) for an identical isotropic annular plate. This comparison is illustrated in Table 6.1. It may be observed from this table

Table 6.1 Verification of the present FE formulation (Ref.: Singh and Chakraverty, 1993).

Source	Dimensionless natural frequency		
	$r_i / r_o = 0.2$	$r_i / r_o = 0.4$	$r_i / r_o = 0.6$
Simply-supported edges of the isotropic annular plate			
Present FE	16.729	28.10	62.156
Ref.	16.72	28.08	62.12
Fully clamped edges of the isotropic annular plate			
Present FE	34.617	62.103	140.03
Ref.	34.61	61.87	139.6

that the present FE results are in good agreement with the similar analytical results (Singh and Chakraverty, 1993). This comparison infers the accuracy of the present FE formulation in handling the vibration of the annular plate.

To verify the present FE formulation for handling the electro-elastic coupling within the PFC actuator, the annular PFC actuator is taken at the core while the face layers are considered to have a negligibly small thickness ($h_f \approx 0$). So, the overall annular plate becomes as an annular piezoelectric disc that is made of the present annular PFC actuator with its first geometric configuration. This annular PFC disc is freed at its inner and outer edges, and the free transverse shear strain (γ_{rz}) due to an applied electric field (E_z) is computed by the analytical expression as, $\gamma_{rz} = \langle e_{35}(r)/C_{55}(r) \rangle E_z$. These analytical results at different points in the plane ($r\theta$-plane) of the annular disc are plotted in Fig. 6.2 (blue points). The distribution of the similar free strain (γ_{rz}) over the plane of the annular disc is also evaluated using the present FE formulation, and this result is plotted in the same figure (Fig. 6.2, surface plot). It may be observed from Fig. 6.2 that the present FE results are in good agreement with the similar analytical results. This comparison shows the accuracy of the present FE formulation in handling the electro-elastic coupling within the PFC actuator.

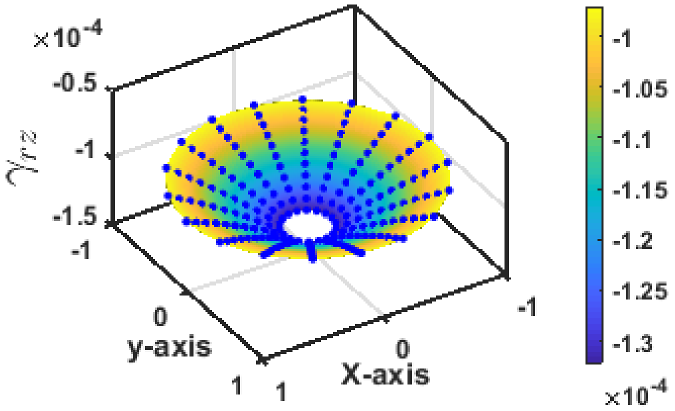

Fig. 6.2 Distribution of the electrically induced free transverse shear strain (γ_{rz}) over the plane of the annular PFC actuator with its first geometric configuration (surface plot: present FE results, point plot: analytical results, V = 100 volt, $E_z = -V/h_e$).

For the results in Fig. 6.2, the annular PFC actuator is taken with its first geometric configuration. If the actual configuration of its patches (PFC#1) at the core of the annular sandwich plate is considered (Fig. 6.1), then the distribution of the electrically induced transverse shear strain (γ_{rz}) over the middle plane of the overall simply-supported annular plate is illustrated in Fig. 6.3(a). It may be observed from Fig. 6.3(a) that the electrically induced strain (γ_{rz}) appears with its maximum magnitude at the inner edge ($r = r_i$) and decreases with the increasing radius. This distribution of γ_{rz} (Fig. 6.3(a)) appears following the nature of variation of the piezoelectric shear coefficient ($e_{35}(r)$, line 1 in Fig. 5.7) for the first geometric configuration of the annular PFC actuator. For its (PFC actuator) design with the second geometric configuration, similar distribution of the electrically induced shear strain (γ_{rz}) over the middle plane of the overall annular plate is illustrated in Fig. 6.3(b). In contrast to the previous result (Fig. 6.3(a)), the result in Fig. 6.3(b) illustrates that all the patches (PFC#2) experience almost the same electrically induced shear strain (γ_{rz}, Fig. 6.3(b)). Also, the magnitude of this shear strain (γ_{rz}, Fig. 6.3(b)) is very close to the maximum magnitude of the similar strain (γ_{rz}) in Fig. 6.3(a). Thus, it is expected that the annular PFC actuator would have superior actuation capability when it is used in the form of its second geometric configuration instead of the first one. This estimation is further verified through the subsequent analysis of frequency responses of the smart annular plate.

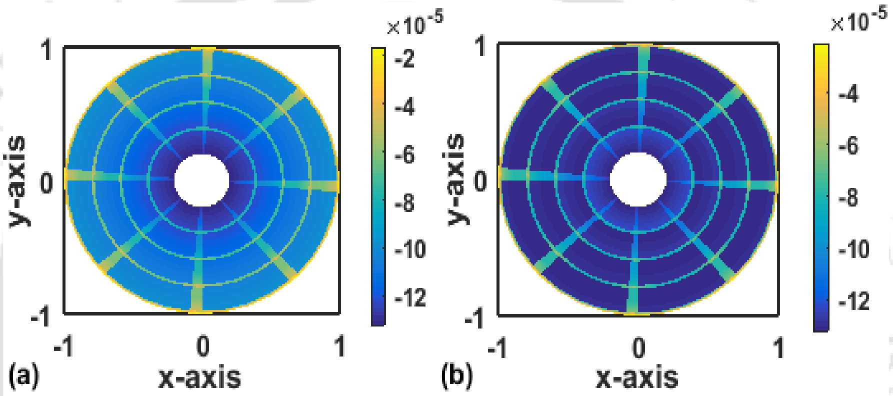

Fig. 6.3 Distribution of the electrically induced shear strain (γ_{rz}) at the middle plane of the simply-supported annular sandwich plate for the material of patches as (a) PFC#1 or (b) PFC#2 (V = 100 volt, $E_z = -V/h_e$).

The simply-supported annular sandwich plate is considered to be subjected to a harmonic transverse point load ($p(r,\theta,z,t) = p(0.6,\pi/4,h/2)\,e^{j\omega t}$) ($j = \sqrt{-1}$, p is the amplitude of the transverse harmonic load). The corresponding frequency responses of the overall annular plate are evaluated within a range of the operating frequency (ω). This frequency-range includes first four bending modes of vibration of the plate. These modes are of fundamental radial mode number ($m=1$), while they are separated by the different circumferential mode numbers (n) as 0, 1, 2, 3. Since these modes are of fundamental radial mode number ($m=1$), there is only one anti-node along the radial direction, and it lies at the middle of the radial span of the annular plate. Following this location of an anti-node within the radial span of the annular plate, the aforesaid control strategy is implemented over the four groups ($n_r = 4$) of patches. The control-gains for the patches within inner two radial groups ($g=1$, 2) are assigned with the same sign, while it (sign) is reversed for the patches within the outer two radial groups ($g=3$, 4) since the anti-node appears at the middle of the four groups of patches.

Since the mechanically induced transverse shear stress (τ_{rz}) appears with its maximum magnitude at the nodes of a bending mode shape of the plate, the electrically induced shear stress is primarily required at the locations of the nodes. But, the velocity around a node appears with a very low magnitude. So, for achieving effective actuation according to the velocity feedback control strategy (Eq. (6.21)), the control-gains are to be assigned with high values for the patches around every node. Concurrently, the control-gains for the patches around every anti-node would be assigned with small values since the velocity at this location appears with a high magnitude. In this assignment of control-gains, the main purpose is to supply the external electric field to the patches in an equal manner such that all the patches can be utilized effectively to control the vibration of the overall plate. The corresponding variation in the value of control-gain arises along the radial direction because of the plane (rz-plane) of the electrically induced transverse shear stress/strain within the patches. So, presently the values of the control-gains are assigned following the groups of the patches. For every radial group (g), the average ($\bar{\dot{w}}^g_{\max}$) of the magnitudes ($\left|{}^q\dot{w}^g_{\max}\right|$) of maximum transverse velocities (${}^q\dot{w}^g_{\max}$, $q=$ 1,2,... N_m) for all (N_m) the modes of vibration within the operating frequency-range is taken as,

$$\bar{\dot{w}}^g_{\max} = \frac{1}{N_m}\sum_{q=1}^{N_m}\left|{}^q\dot{w}^g_{\max}\right|,\; g=1,2,\ldots\ldots\ldots n_r \tag{6.26}$$

In the present analysis, the natural modes of the fundamental radial mode number ($m=1$) are considered. So, one half-sine wave appears with two nodes at the inner and outer edges of the annular plate. For this characteristic of the mode shapes of interest, the maximum velocity-magnitude at the inner group ($g=1$) is very close to that at the outer group ($g=4$). The same circumstance also appears for the inner groups ($g=2,3$). So, the average velocity-magnitudes (Eq. (6.26)) for the groups of the patches are reduced as,

$$\bar{\dot{w}}_{\max}^{1/4}=(\bar{\dot{w}}_{\max}^{1}+\bar{\dot{w}}_{\max}^{4})/2,\quad \bar{\dot{w}}_{\max}^{2/3}=(\bar{\dot{w}}_{\max}^{2}+\bar{\dot{w}}_{\max}^{3})/2 \tag{6.27}$$

According to Eq. (6.27), the average of maximum velocity-magnitudes within the inner or outer radial groups ($g=1$ and 4) is assumed as $\bar{\dot{w}}_{\max}^{1/4}$, while $\bar{\dot{w}}_{\max}^{2/3}$ implies the same for the inner radial groups ($g=2$ and 3). Now, to activate all the groups (g) of patches with almost the same magnitude of the external electric field (E_z), the following relation can be obtained according to Eq. (6.21),

$$\left(k_d^{1/4}/k_d^{2/3}\right)=\left(\bar{\dot{w}}_{\max}^{2/3}/\bar{\dot{w}}_{\max}^{1/4}\right)=k_d^r \tag{6.28}$$

where, $k_d^{1/4}$ and $k_d^{2/3}$ are the control-gains corresponding to the velocity-magnitudes $\bar{\dot{w}}_{\max}^{1/4}$ and $\bar{\dot{w}}_{\max}^{2/3}$, respectively. For any natural bending mode of vibration of the plate, the maximum velocity appears at the same location as that is for the maximum displacement. So, the ratio (k_d^r) can also be written in terms of the average of maximum displacement-magnitudes as, $k_d^r=(\bar{w}_{\max}^{2/3}/\bar{w}_{\max}^{1/4})$. Following the same procedure as illustrated through Eqs. (6.26) and (6.27), the displacement-magnitudes ($\bar{w}_{\max}^{2/3}$, $\bar{w}_{\max}^{1/4}$) can be computed from the normalized mode shapes of the natural modes within the operating frequency range. Using the corresponding value of k_d^r, the values of the control-gains can be assigned by specifying the value of any one. Presently, $k_d^{1/4}$ is specified as, $k_d^{1/4}=k_d$ and it is followed for assigning the control-gains for all the groups ($g=1,2,3,4$) as, $k_d^1=k_d$, $k_d^4=k_d$, $k_d^2=k_d/k_d^r$ and $k_d^3=k_d/k_d^r$. It may be noted here that the assignment of the values of control-gains is a little difficult task since all the patches are to be activated in an equal manner under the circumstance of their different velocities. This difficulty can be simplified by the aforesaid strategy where the value of one of the control-gains is to be prescribed. The fruitfulness of this strategy is numerically verified in the following results.

Figure 6.4 illustrates the variation of the maximum displacement-amplitude ($W_{\max} = w_{\max} / h$) of the annular sandwich plate within a frequency-range when the patches are either made of PFC#1 or made of PFC#2. For every material (PFC#1 or PFC#2), the decrease of $W_{\max}$ (in percent, $\%A$) at a resonance for an increase of the control-gain (k_d from 10e6 to 20e6) is also tabulated in Table 6.2.

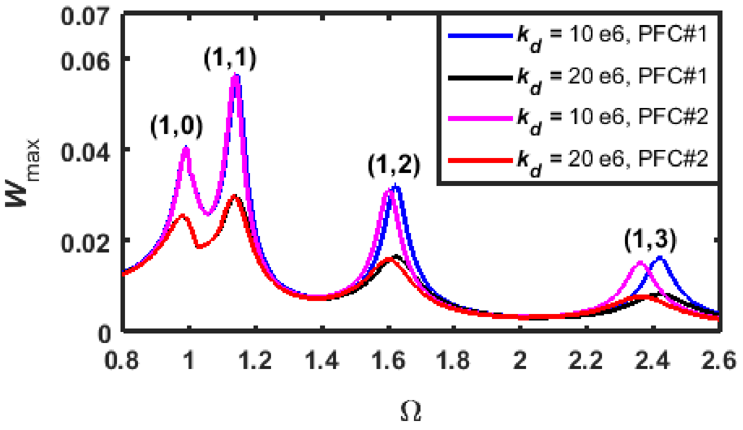

Fig. 6.4 Variation of the maximum displacement-amplitude of the annular sandwich plate within a frequency-range when the patches are made of either PFC#1 or PFC#2 ($\Omega = \omega / \omega_{(1,0)}$, $p =$ 1 N, $\omega_{(1,0)}$ is the fundamental natural frequency).

Table 6.2 Maximum displacement-amplitude ($W_{\max} = w_{\max} / h$) at every resonant frequency and the decrease ($\%A$) of $W_{\max}$ for an increase of the control-gain (k_d).

PFC	k_d	$m=1, n=0$		$m=1, n=1$		$m=1, n=2$		$m=1, n=3$	
		$W_{\max}$	$\%A$	$W_{\max}$	$\%A$	$W_{\max}$	$\%A$	$W_{\max}$	$\%A$
PFC#1	10e6	0.0406	36.94	0.0564	47.34	0.0323	49.22	0.0163	50.30
	20e6	0.0256		0.0297		0.0164		0.0081	
PFC#2	10e6	0.0405	37.03	0.0562	47.15	0.0312	50.00	0.0152	49.34
	20e6	0.0255		0.0297		0.0156		0.0077	

It may be observed from Fig. 6.4 that the displacement-amplitudes at the resonances (n, $m = 1$) can be controlled effectively using any of the materials (PFC#1 or PFC#2) for the patches. Also, the displacement-amplitudes at the resonances are attenuated almost in the equal manner ($\%A$, Table 6.2) although a little difference appears at the first resonance ($n = 0,\ m = 1$). This result (%A, Table 6.2) infers the fruitfulness of the present arrangement of the patches for achieving equal attenuation of all the modes of vibration of the plate.

Figure 6.5 illustrates the variation of the maximum voltage-amplitude ($V^g_{\max}$) for each of the groups ($g = 1, 2, 3, 4$) of the patches corresponding to the responses in Fig. 6.4. For any value of the control-gain, it may be observed from Fig. 6.5 that all the groups of the patches (PFC#1 or PFC#2) are activated with almost the same value of the maximum voltage-amplitude. So, all the groups of patches are equally utilized for attenuation of vibration of the annular sandwich plate. This result (Fig. 6.5) shows the suitability of the present strategy for assigning the values of the control-gains under the circumstance of different velocities over the patches.

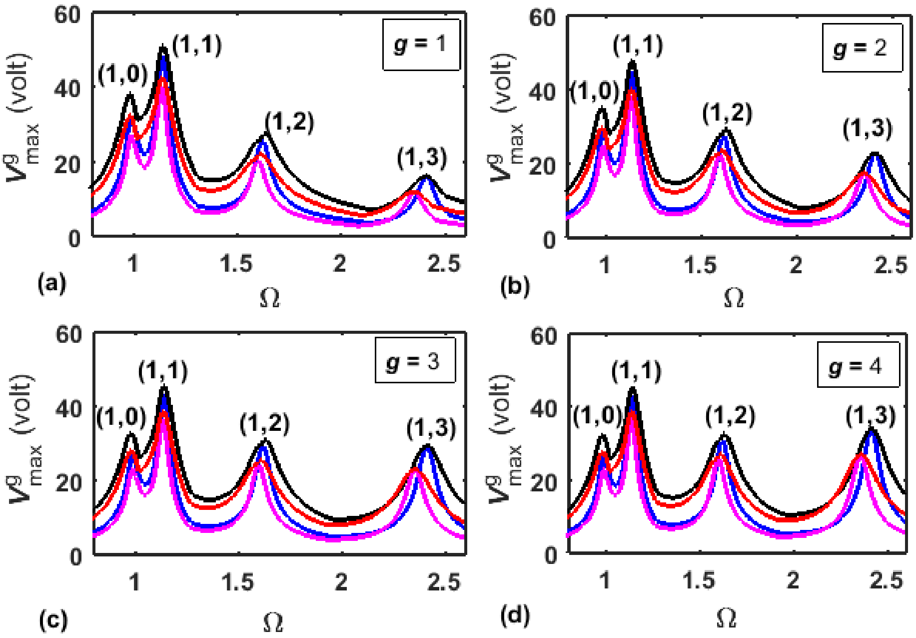

Fig. 6.5 Variation of the maximum voltage-amplitude for every radial group (g) of patches corresponding to the frequency responses in Fig. 6.4 (the colors of the lines mean the same as those are in Fig. 6.4).

It is important to observe from Fig. 6.4 that the change in the geometric configuration (PFC#1 or PFC#2) of the annular PFC actuator does not have the indicative effect on its control capability for the first two modes ($m = 1, n = 0,1$) of vibration. But, for the higher modes ($m = 1, n = 2,3$), the annular PFC actuator has superior control capability when the patches are made from its (PFC actuator) second geometric configuration (PFC#2). In order to explain this observation, the distribution of the mechanically induced shear stress (τ_{rz}) over the middle plane of the sandwich plate is illustrated in Fig. 6.6 for each of the bending modes ($m=1, n=0,1,2,3$). In this result, the material of the deactivated patches is taken either as PFC#1 or as PFC#2. For the first two modes ($m=1, n=0,1$), it may be observed from Figs. 6.6(a), 6.6(b), 6.6(e) and 6.6(f) that the magnitude of the stress (τ_{rz}) at the inner edge of the plate is indicatively higher than that at the outer edge of the same plate. But this difference decreases at a higher mode (Figs. 6.6(c), 6.6(d), 6.6(g) and 6.6(h)). So, for the first two modes of vibration, the actuation force is primarily required at the inner edge of the plate. But, for the higher modes of vibration, the control forces are required at both the inner and outer edges of the annular plate. Now, from the results in Fig. 6.3, the PFC actuator with its first geometric configuration (PFC#1) can provide indicative actuation force at the inner edge only, while the same PFC actuator with its second geometric configuration (PFC#2) can provide indicative actuation force at any radial location. Thus, both the geometric configurations of the PFC actuator can provide effective control of first two modes of vibration of the smart plate. But, for effective control of any modes of vibration of the smart plate, the PFC actuator would be taken with its second geometric configuration. By this observation, further results are evaluated by taking the second geometric configuration of the annular PFC actuator.

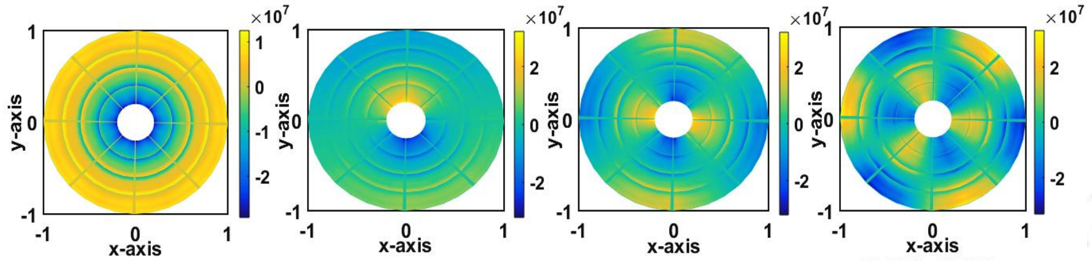

(a) PFC: PFC#2, *m*=1, *n* = 0

(b) PFC: PFC#2, *m*=1, *n* = 1

(c) PFC: PFC#2, *m*=1, *n* = 2

(d) PFC: PFC#2, *m*=1, *n* = 3

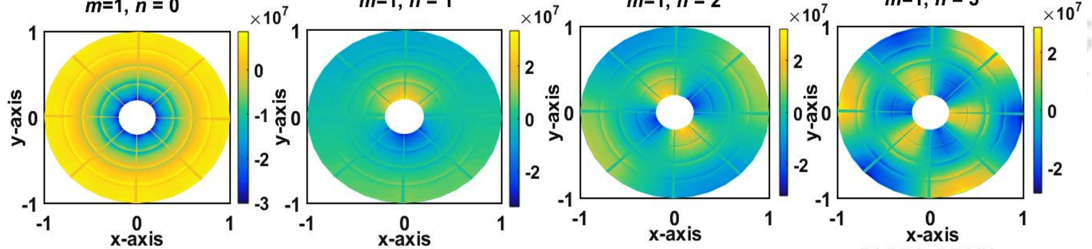

(e) PFC: PFC#1, *m*=1, *n* = 0

(f) PFC: PFC#1, *m*=1, *n* = 1

(g) PFC: PFC#1, *m*=1, *n* = 2

(h) PFC: PFC#1, *m*=1, *n* = 3

Fig. 6.6 Distributions of the shear stress (τ_{rz}) over the middle plane of the overall annular plate for its different bending modes ($m=1$) of vibration.

Figure 6.7(a) illustrates the variation of the maximum displacement-amplitude ($W_{\max}$) of the annular sandwich plate within a frequency-range when the patches are made from the present annular PFC actuator (PFC#2) or from the annular disc of the traditional monolithic shear piezoelectric actuator (PZT5H). The corresponding variations of the maximum voltage-amplitude ($V_{\max}^{g}$, $g = 1$) are also presented in Fig. 6.7(b). It may be observed from Fig. 6.7 that the present PFC actuator possesses better control capability than that of the monolithic piezoelectric actuator (PZT5H), while both the actuators require almost equal control-voltage at any value of the control-gain. In addition to this improved control capability, the present shear mode PFC actuator also possesses greater flexibility and conformability due to its polymer constituent. So, the present shear mode PFC actuator may be a potential actuator for active control of vibration of the plane structures of revolution.

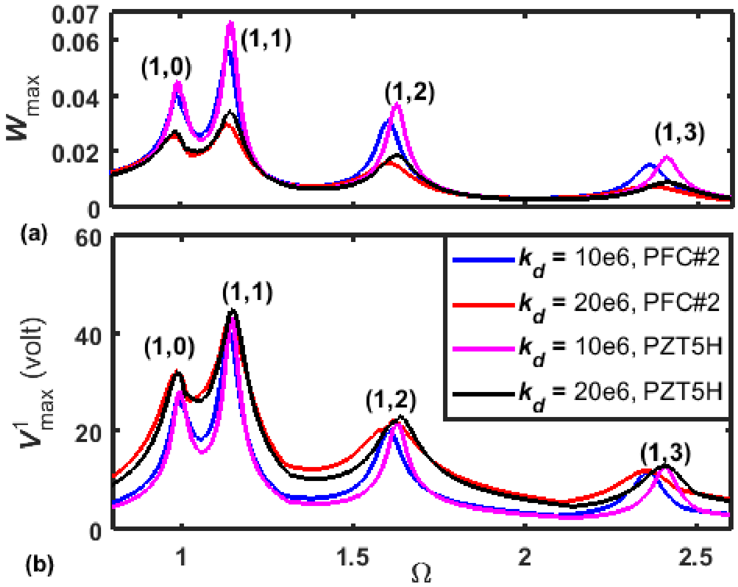

Fig. 6.7(a) Variations of the maximum displacement-amplitude ($W_{\max}$) of the annular sandwich plate within a frequency-range and (b) the corresponding variations of the maximum voltage-amplitude within the first radial group ($g = 1$) of the patches ($\Omega = \omega / \omega_{(1,0)}$, $p =$ 1 N).

Figure 6.8 illustrates the frequency responses of the overall annular plate for the use of two radial groups instead of four radial groups of the patches. The middle two radial groups ($g = 2$, 3) in the aforesaid arrangement of the patches (n_r = 4) are removed, while the inner ($g = 1$) and outer ($g = 4$) radial groups are retained. It may be observed from this result (Fig. 6.8) that there is no significant change in the controlled response of the overall annular plate for the removal of middle two radial groups ($g = 2, 3$) of patches. It occurs since the actuation force is primarily required around the nodes of the mode shape of vibration. Now, the nodes for the present modes ($m = 1$) of vibration of the plate appear at its (plate) edges. So, the removal of the patches ($g = 2, 3$) around the anti-node does not have much effect on the controlled response of the annular sandwich plate. This result indicates to locate the groups of the patches only around the nodes of the mode shape of vibration.

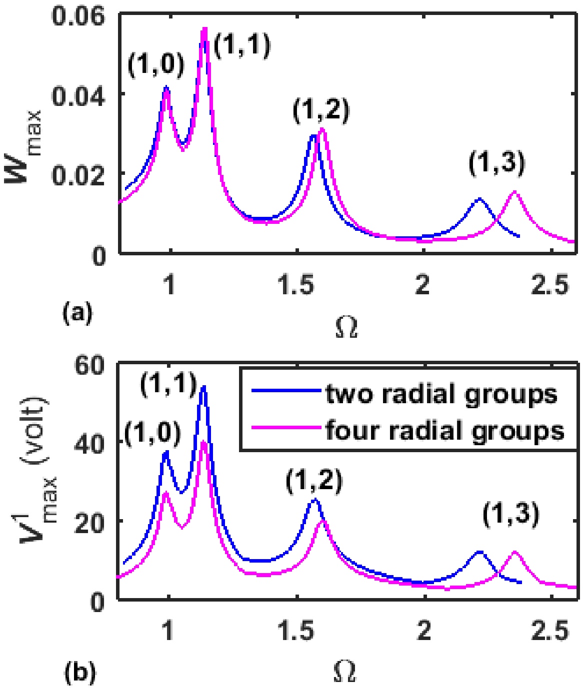

Fig. 6.8 Variations of (a) the maximum displacement-amplitude ($W_{\max}$) and (b) the corresponding maximum voltage-amplitude within the first radial group ($g = 1$) for the use of two radial groups ($g = 1$ and 4) instead of four radial groups ($g = 1,2,3,4$) of the patches (PFC#2, $\Omega = \omega / \omega_{(1,0)}$, $p =$ 1 N).

In order to investigate the effect of the control-gain (k_d) on the controlled frequency response of the overall plate, the value of the control-gain (k_d) is varied with a constant value of the load-amplitude (p). Figures 6.9(a) and 6.9(b) illustrate the corresponding variations of the maximum displacement-amplitude and the maximum voltage-amplitude (at $g = 1$), respectively at the second resonant frequency ($m = 1, n = 1$). For any value of the load-amplitude (p), it may be observed from Fig. 6.9(a) that the displacement-amplitude significantly decreases as the control-gain increases. Although this reduction of the displacement-amplitude requires higher control-voltage (Fig. 6.9(b)), the rate of increase of the control-voltage is much lesser than the rate of decrease of the displacement-amplitude. So, an indicative reduction of the displacement-amplitude can be achieved by a small

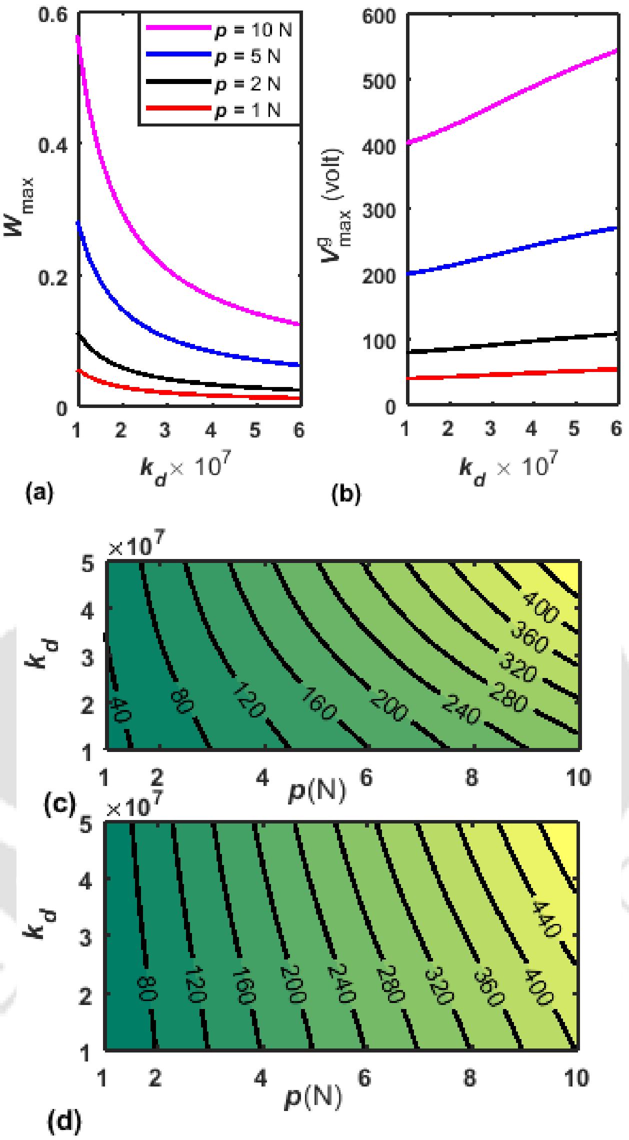

Fig. 6.9(a) Variations of the maximum transverse displacement-amplitude at the second resonance with the control-gain, (b) the corresponding variations of the maximum voltage-amplitude ($V^g_{\max}$, $g=1$); (c)-(d) contours of the maximum voltage-amplitude ($V^g_{\max}$, $g=1$) at the (c) first ($m=1, n=0$) and (d) second ($m=1, n=1$) resonances (PFC: PFC#2).

increase of the control voltage. Although this advantage can be obtained by increasing the control-gain (k_d) at a load-amplitude (p), but this increase of the control-gain (k_d) is limited to its (k_d) certain value due to the constraint of permissible applied voltage/electric field for the PFC actuator. In order to obtain the limiting value of the control-gain at a load-amplitude, presently the contours of the maximum voltage-amplitude ($V_{\max}^{g}$, $g=1$) are plotted within a two-dimensional domain of the control-gain and the load-amplitude as demonstrated in Figs. 6.9(c) and 6.9(d) for first two resonances. A line within the domain is a line of constant voltage-amplitude. So, the line of the permissible voltage can easily be marked within the domain. For instance, let the permissible voltage is 200 volt. The line of 200 volt divides the overall domain into the left and right sub-domains. Then, the feasible values of the control-gain corresponding to a load-amplitude lie within the left sub-domain. Using similar contour plot of the maximum voltage-amplitude at a resonance of interest, the feasible values of the control-gain at a load-amplitude can be decided graphically for that resonance. The plot in Fig. 6.9(c) or 6.9(d) is a graphical representation of the relation among the control-gain, load-amplitude and voltage-amplitude.

6.5 Conclusions

In this chapter, the control capability of a new shear mode annular PFC actuator (Chapter 5) is investigated for active control of vibration of an annular plate. This annular PFC actuator is proposed in Chapter 5 with its (PFC) two different geometric configurations. In the first one, the inner and outer radii of the annular PFC actuator are the same as those are for the host annular plate. In the second one, the radial span of the host annular plate is divided into four equal divisions, and the annular PFC actuator is designed for every radial division of small radial length. For each of the geometric configurations of the annular PFC actuator, its control capability is investigated by means of constructing an annular sandwich plate. The radial and circumferential spans of the annular PFC actuator are evenly divided to form the patches in the shape of annular-sector, and then the patches are embedded within the core of foam according to the coordinates of their (patches) radial and circumferential edges. A fruitful strategy in deciding the in-plane dimensions of the patches is proposed for having the equal attenuation of all the modes of vibration of the plate within a range of the operating frequency. Every patch counteracts the mechanically induced transverse shear stress around its location by taking the feedback of local velocity. In this use of the velocity feedback control law for the shear mode PFC actuator, a new strategy is proposed to utilize all the patches effectively for control of any mode of vibration of the overall annular plate.

For the analysis of the smart annular sandwich plate, an FE model is developed based on the layer-wise shear deformation theory. This FE model is first verified for handling the electro-elastic responses of the smart annular plate. Then, the frequency responses of the smart plate are evaluated within an operating frequency-range that includes its (smart plate) first four bending modes of vibration. These results exhibit indicative control capability of the present shear mode annular PFC actuator for active control of vibration of annular plates. The actuation capability of the present shear mode PFC actuator is higher than that of the traditional monolithic shear piezoelectric actuator (PZT5H). The annular PFC actuator possesses superior control capability when it is used with its second geometric configuration instead of the first one. It is observed that all the modes of vibration of the plate within a frequency domain are attenuated in almost equal manner. This observation infers the suitability of the present strategy in deciding the in-plane dimensions of the patches. A graphical methodology is also proposed for deciding the limiting values of the control-gain in the use of the velocity feedback control strategy for shear piezoelectric actuation of structural vibration.

CHAPTER
7
Active-passive damping characteristics of a smart annular sandwich plate using a new shear mode PFC actuator

7.1 Introduction

A shear mode annular PFC actuator is designed in Chapter 5, and its performance in control of vibration of an annular plate is investigated in the previous chapter (Chapter 6). In this chapter, a study on the performance of this shear mode annular PFC actuator in the ACLD treatment of vibration of an annular plate is carried out. It may be noted here that the ACLD treatment is a popular hybrid damping treatment as its extensive application for different kinds of engineering structures has been addressed in the literature (Chapter 1). In all these applications of the ACLD treatment, the extension mode piezoelectric actuators are utilized. However, the utilization of the shear mode piezoelectric actuators for this (ACLD) active-passive damping treatment has not yet been observed, and thus it is attempted in this chapter by the use of the present shear mode PFC actuator (Chapter 5) in the suppression of vibration of an annular plate. There are basically two objectives of this study. The first one is to study the damping characteristics of the ACLD treatment for the use of the shear mode piezoelectric actuator. The second one is to investigate the performance of the present shear mode annular PFC actuator in the ACLD treatment of annular plates. The overall study is carried out by proposing an ACLD arrangement at the core of a host annular sandwich plate. The ACLD layer is made in the form of a laminate with two different stacking sequences. In the first one, the viscoelastic layer is constrained between two identical shear mode piezoelectric layers. In the next one, the shear mode piezoelectric layer is kept between two identical viscoelastic layers, while the viscoelastic layers are constrained between the face layers. The shear mode piezoelectric layer is made using the annular PFC actuator (Chapter 5) in the form of a piezo-foam layer that is similar to the smart core of the annular sandwich plate in the previous chapter (Chapter 6). The actuator patches in the piezo-foam layer are activated following the same strategy as that is presented in Chapter 6 particularly for control of several modes of vibration of the overall smart annular plate. An FE model of the overall annular sandwich plate is developed based on the layer-wise shear deformation theory, and its (overall plate) active-passive damping characteristics are studied according to the aforesaid objectives.

7.2 Smart annular sandwich plate

In order to enhance the viscoelastic damping in an annular sandwich plate with the core of viscoelastic material, the shear mode annular PFC actuator (Chapter 5) is utilized in the form of the patch. In this use of the patches of the annular PFC actuator, a strategy for the arrangement of the patches on the plane of the annular plate is proposed in Section 6.2 for effective utilization of the patches in control of all the modes of vibration of a host annular plate. Following this strategy, the patches in the shape of the annular-sector are made by means of dividing the radial and circumferential spans of the annular piezoelectric actuator and the patches are embedded within a foam layer according to the coordinates of their (patches) radial and circumferential boundaries. The foam layer is in the shape of a thin annular disc with the same dimensions as those are for the annular piezoelectric actuator. A schematic diagram of this piezo-foam layer is illustrated in Fig. 7.1. The geometrical properties of the piezo-foam layer are indicated by the same symbols (Δr, Δr_p, Δr_F, n_r, $\Delta\theta$, $\Delta\theta_p$, $\Delta\theta_F$, n_θ) as those are in the previous piezo-foam layer (Fig. 6.1). The inner (r_i) and outer (r_o) radii of the piezo-foam layer are equal to those of the host annular plate. This piezo-foam layer is utilized along with the viscoelastic layers at the core of an annular sandwich plate. The piezo-foam and the viscoelastic

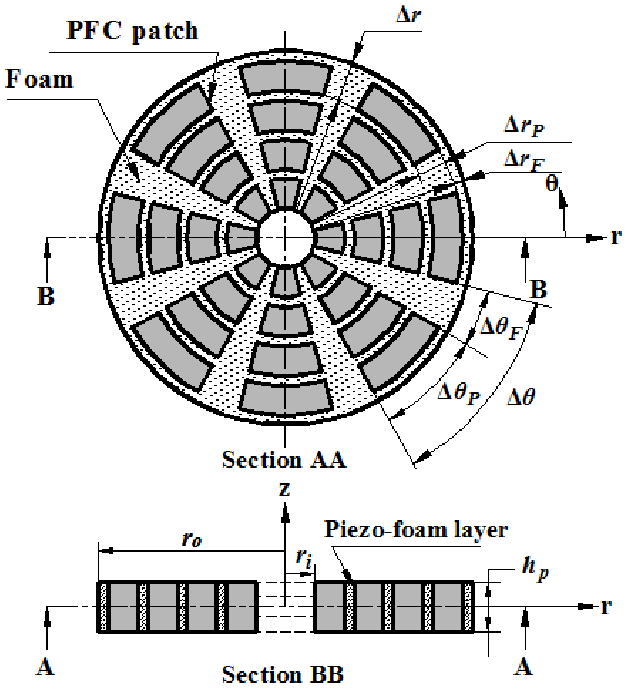

Fig. 7.1 Schematic diagram of the piezo-foam layer in the shape of a thin annular disc.

layers are stacked at the core in two different stacking sequences. In the first one, one viscoelastic layer is sandwiched between two identical piezo-foam layers. A diametric cross-section of the corresponding annular sandwich plate is shown in Fig. 7.2(a), and this configuration of the overall annular plate is denoted by CONFIG#1. In the second one, one piezo-foam layer is sandwiched between two identical viscoelastic layers as a corresponding diametric cross-section of the overall annular plate is shown in Fig. 7.2(b). This second configuration of the overall laminated annular plate is denoted by CONFIG#2. The thicknesses of the overall plate and the face layers are denoted by h and h_f, respectively. The thickness ($h_v/2$) of the viscoelastic layers in CONFIG#2 is half of the thickness (h_v) of the similar layer in CONFIG#1. In like manner, the thickness ($h_p/2$) of the piezo-foam layers in CONFIG#1 is half of the thickness (h_p) of the similar layer in CONFIG#2.

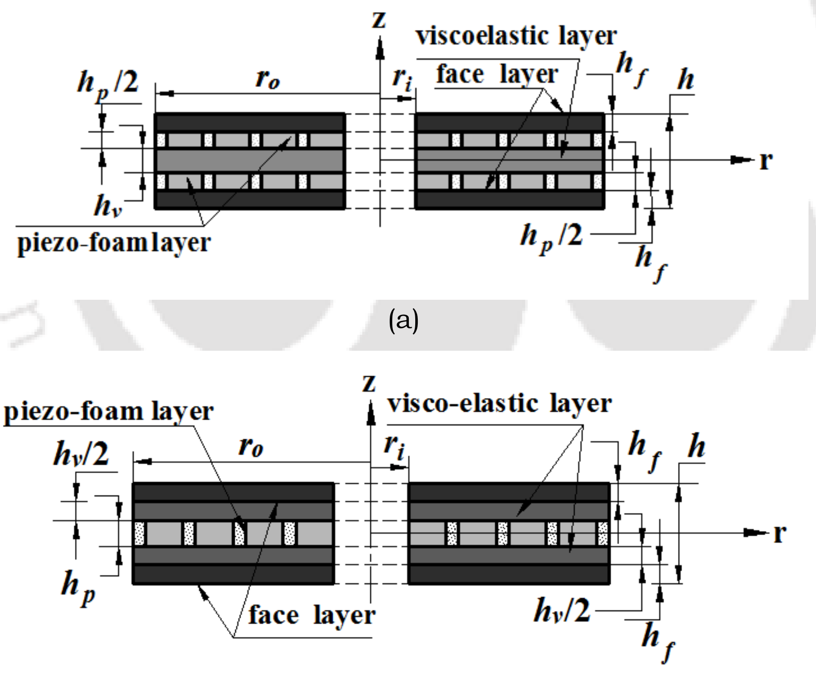

(a)

(b)

Fig. 7.2 Schematic diagrams of the diametric cross-sections of the overall annular plate with (a) the viscoelastic (CONFIG#1) or (b) the piezo-foam (CONFIG#2) layers at the core.

For effective control of any mode of vibration of the overall annular plate, the earlier strategy (Chapter 6) for activation of the patches is followed. According to this strategy, every patch is activated by taking the feedback of local velocity, and thus the velocity sensors are located on the top surface of the overall plate following the in-plane coordinates of middle points of the patches. The present shear mode annular PFC actuator is utilized with any of its two different geometric configurations (Fig. 5.7). In the use of the annular PFC actuator with its first geometric configuration (line 1/2 in Fig. 5.7), it is made with the inner (r_i) and outer (r_o) radii of application/host plate and the patches are made by dividing the radial and circumferential spans of this annular PFC actuator. The corresponding material of the patches is denoted by PFC#1. For the second geometric configuration of the annular PFC actuator (line 3/4 in Fig. 5.7), it is made in four parts by means of dividing the radial span (r_o - r_i) of application into four equal divisions. The patches within a radial division are made by dividing the radial and circumferential spans of the corresponding part of the annular PFC actuator, and the material of the patches is denoted by PFC#2.

7.3 FE formulation for the annular sandwich plate

The middle plane of the smart annular sandwich plate is taken as the reference plane, and the origin of the reference cylindrical coordinate system ($r\theta z$) is located at the centre of the annular reference plane. The displacements u^k, v^k and w^k at any point within a layer (k) along the r, θ and z directions, respectively, can be written according to Eq. (6.1).

$$u^k = u_0^k + \sum_{i=1}^{\infty} \xi_i^k \phi_i^k \;,\; v^k = v_0^k + \sum_{i=1}^{\infty} \xi_i^k \beta_i^k \;,\; w^k = w_0 \tag{6.1}$$

In this use of Eq. (6.1) for the present smart annular plate, the superscript k indicates the layers of the overall plate according to its value as 1, 2, 3, 4 and 5 starting from the bottom layer as, $k=1$. For a bending mode of deformation of the overall plate (Fig. 7.2), the transverse shear stresses appear with their maximum magnitudes around the middle plane of the plate. So, the kinematics of deformation for the layers ($k=2,3,4$) at the core is defined by the cubic polynomial of the thickness coordinate (z) as,

$$u^3 = u_0 + \sum_{i=1}^{3} \xi_i^3 \phi_i^3 \,,\; v^3 = v_0 + \sum_{i=1}^{3} \xi_i^3 \beta_i^3 \,,\; w^3 = w_0 \;\text{ for }\; k=3 \tag{7.1a}$$

$$u^2 = u^3\Big|_{z=h_3} + \sum_{i=1}^{3} \xi_i^2 \phi_i^2 \quad , \; v^2 = v^3\Big|_{z=h_3} + \sum_{i=1}^{3} \xi_i^2 \beta_i^2 \, , \; w^2 = w_0 \;\text{ for }\; k = 2 \tag{7.1b}$$

$$u^4 = u^3\Big|_{z=h_4} + \sum_{i=1}^{3} \xi_i^4 \phi_i^4 \quad , \; v^4 = v^3\Big|_{z=h_4} + \sum_{i=1}^{3} \xi_i^4 \beta_i^4 \, , \; w^4 = w_0 \;\text{ for }\; k = 4 \tag{7.1c}$$

where, h_k and h_{k+1} are the thickness coordinates of the bottom and top surfaces of k^{th} layer, respectively. Similar to Eq. (6.3) for the previous annular sandwich plate (Chapter 6), the kinematics of deformation of the face layers are defined according to the first-order shear deformation theory (FSDT) as,

$$u^1 = u^2\Big|_{z=h_2} + \xi_1^1 \phi_1^1 \, , \; v^1 = v^2\Big|_{z=h_2} + \xi_1^1 \beta_1^1 \, , \; w^1 = w_0 \;\text{ for }\; k = 1 \tag{7.1d}$$

$$u^5 = u^4\Big|_{z=h_5} + \xi_1^5 \phi_1^5 \, , \; v^5 = v^4\Big|_{z=h_5} + \xi_1^5 \beta_1^5 \, , \; w^5 = w_0 \;\text{ for }\; k = 5 \tag{7.1e}$$

In order to express the layer-wise displacements in a simplified manner, a generalized displacement vector ($\boldsymbol{d}$) is defined as,

$$\begin{aligned} \boldsymbol{d} = \{ & u_0 \quad v_0 \quad w_0 \quad \phi_1^1 \quad \beta_1^1 \quad \phi_1^2 \quad \beta_1^2 \quad \phi_1^3 \quad \beta_1^3 \quad \phi_1^4 \quad \beta_1^4 \quad \phi_1^5 \quad \beta_1^5 \quad \phi_2^2 \\ & \beta_2^2 \quad \phi_2^3 \quad \beta_2^3 \quad \phi_2^4 \quad \beta_2^4 \quad \phi_3^2 \quad \beta_3^2 \quad \phi_3^3 \quad \beta_3^3 \quad \phi_3^4 \quad \beta_3^4 \}^{\mathrm{T}} \end{aligned} \tag{7.2}$$

Using this generalized displacement vector, the layer-wise displacements are expressed as,

$$u^k = \boldsymbol{Z}_u^k \boldsymbol{d} \, , \; v^k = \boldsymbol{Z}_v^k \boldsymbol{d} \, , \; w^k = \boldsymbol{Z}_w^k \boldsymbol{d} \tag{7.3}$$

where $\boldsymbol{Z}_u^k$, $\boldsymbol{Z}_v^k$ and $\boldsymbol{Z}_w^k$ are the row matrices of thickness coordinates corresponding to the displacements u^k, v^k and w^k, respectively. These row matrices are in the size of (1×25), and the nonzero elements of these row matrices are as follows,

$$\begin{aligned} & Z_{u1}^k = 1, \; Z_{u4}^k = z_1^k \, , \; Z_{u6}^k = z_2^k \, , \; Z_{u8}^k = z_3^k \, , \; Z_{u10}^k = z_4^k \, , \; Z_{u12}^k = z_5^k \, , \\ & Z_{u14}^k = z_6^k \, , \; Z_{u16}^k = z_7^k \, , \; Z_{u18}^k = z_8^k \, , \; Z_{u20}^k = z_9^k \, , \; Z_{u22}^k = z_{10}^k \, , \; Z_{u24}^k = z_{11}^k \end{aligned} \tag{7.4a}$$

$$\begin{aligned} & Z_{v2}^k = 1, \; Z_{v5}^k = z_1^k \, , \; Z_{v7}^k = z_2^k \, , \; Z_{v9}^k = z_3^k \, , \; Z_{v11}^k = z_4^k \, , \; Z_{v13}^k = z_5^k \, , \\ & Z_{v15}^k = z_6^k \, , \; Z_{v17}^k = z_7^k \, , \; Z_{v19}^k = z_8^k \, , \; Z_{v21}^k = z_9^k \, , \; Z_{v23}^k = z_{10}^k \, , \; Z_{v25}^k = z_{11}^k \, , \end{aligned} \tag{7.4b}$$

$$Z_{w3}^k = 1 \tag{7.4c}$$

In Eqs. (7.4a)-(7.4c), Z_{ui}^{k}, Z_{vi}^{k} and Z_{wi}^{k} are the elements at the i^{th} column of $\mathbf{Z}_u^k$, $\mathbf{Z}_v^k$ and $\mathbf{Z}_w^k$, respectively, and the thickness coordinates $(z_i^k, i = 1,2,....11)$ for different layers are as follows,

$$\begin{aligned}
z_1^k\Big|_{k=1,2,3,4,5} &= (z-h_2)\big|_{k=1}, 0\big|_{k=2}, 0\big|_{k=3}, 0\big|_{k=4}, 0\big|_{k=5} \\
z_2^k\Big|_{k=1,2,3,4,5} &= (h_2-h_3)\big|_{k=1}, (z-h_3)\big|_{k=2}, 0\big|_{k=3}, 0\big|_{k=4}, 0\big|_{k=5} \\
z_3^k\Big|_{k=1,2,3,4,5} &= h_3\big|_{k=1}, h_3\big|_{k=2}, z\big|_{k=3}, h_4\big|_{k=4}, h_4\big|_{k=5} \\
z_4^k\Big|_{k=1,2,3,4,5} &= 0\big|_{k=1}, 0\big|_{k=2}, 0\big|_{k=3}, (z-h_4)\big|_{k=4}, (h_5-h_4)\big|_{k=5} \\
z_5^k\Big|_{k=1,2,3,4,5} &= 0\big|_{k=1}, 0\big|_{k=2}, 0\big|_{k=3}, 0\big|_{k=4}, (z-h_5)\big|_{k=5} \\
z_6^k\Big|_{k=1,2,3,4,5} &= (h_2-h_3)^2\Big|_{k=1}, (z-h_3)^2\Big|_{k=2}, 0\big|_{k=3}, 0\big|_{k=4}, 0\big|_{k=5} \\
z_7^k\Big|_{k=1,2,3,4,5} &= {h_3}^2\Big|_{k=1}, {h_3}^2\Big|_{k=2}, z^2\Big|_{k=3}, {h_4}^2\Big|_{k=4}, {h_4}^2\Big|_{k=5} \\
z_8^k\Big|_{k=1,2,3,4,5} &= 0\big|_{k=1}, 0\big|_{k=2}, 0\big|_{k=3}, (z-h_4)^2\Big|_{k=4}, (h_5-h_4)^2\Big|_{k=5} \\
z_9^k\Big|_{k=1,2,3,4,5} &= (h_2-h_3)^3\Big|_{k=1}, (z-h_3)^3\Big|_{k=2}, 0\big|_{k=3}, 0\big|_{k=4}, 0\big|_{k=5} \\
z_{10}^k\Big|_{k=1,2,3,4,5} &= {h_3}^3\Big|_{k=1}, {h_3}^3\Big|_{k=2}, z^3\Big|_{k=3}, {h_4}^3\Big|_{k=4}, {h_4}^3\Big|_{k=5} \\
z_{11}^k\Big|_{k=1,2,3,4,5} &= 0\big|_{k=1}, 0\big|_{k=2}, 0\big|_{k=3}, (z-h_4)^3\Big|_{k=4}, (h_5-h_4)^3\Big|_{k=5}
\end{aligned} \tag{7.5}$$

According to Eq. (7.3), the displacement at any point in a layer (k) can be written in a compact form as follows,

$$\mathbf{d}^k = \mathbf{Z}^k \mathbf{d}, \quad \mathbf{d}^k = \left\{ u^k \quad v^k \quad w^k \right\}^{\mathrm{T}}, \quad \mathbf{Z}^k = \left\{ \begin{matrix} \mathbf{Z}_u^k \\ \mathbf{Z}_v^k \\ \mathbf{Z}_w^k \end{matrix} \right\} \tag{7.6}$$

The thickness of the annular sandwich plate is very small in comparison to its in-plane dimensions. So, the state of stress at any point within the overall plate is assumed as $\sigma_z = 0$. Accordingly, the state of stress and the state of strain at any point in the overall plate can be written following Eq. (6.4).

$$\boldsymbol{\sigma}_b^k = \left\{ \sigma_r^k \quad \sigma_\theta^k \quad \tau_{r\theta}^k \right\}^{\mathrm{T}}, \; \boldsymbol{\sigma}_s^k = \left\{ \tau_{rz}^k \quad \tau_{\theta z}^k \right\}^{\mathrm{T}}, \; \boldsymbol{\varepsilon}_b^k = \left\{ \varepsilon_r^k \quad \varepsilon_\theta^k \quad \gamma_{r\theta}^k \right\}^{\mathrm{T}}, \quad \boldsymbol{\varepsilon}_s^k = \left\{ \gamma_{rz}^k \quad \gamma_{\theta z}^k \right\}^{\mathrm{T}} \tag{6.4}$$

According to the displacement field in Eq. (7.3), the strain-displacement relations can be written as,

$$\boldsymbol{\varepsilon}_b^k = \mathbf{Z}_b^k \partial_b \mathbf{d}\ ,\ \ \boldsymbol{\varepsilon}_s^k = \mathbf{Z}_s^k \partial_s \mathbf{d}$$

$$\mathbf{Z}_b^k = \begin{bmatrix} \mathbf{I}_3 & z_1^k \mathbf{I}_3 & z_2^k \mathbf{I}_3 & z_3^k \mathbf{I}_3 & z_4^k \mathbf{I}_3 & z_5^k \mathbf{I}_3 & z_6^k \mathbf{I}_3 & z_7^k \mathbf{I}_3 \\ z_8^k \mathbf{I}_3 & z_9^k \mathbf{I}_3 & z_{10}^k \mathbf{I}_3 & z_{11}^k \mathbf{I}_3 \end{bmatrix}$$

$$\mathbf{Z}_s^k = \begin{bmatrix} \mathbf{I}_2 & \frac{\partial z_1^k}{\partial z}\mathbf{I}_2 & \frac{\partial z_2^k}{\partial z}\mathbf{I}_2 & \frac{\partial z_3^k}{\partial z}\mathbf{I}_2 & \frac{\partial z_4^k}{\partial z}\mathbf{I}_2 & \frac{\partial z_5^k}{\partial z}\mathbf{I}_2 & \frac{\partial z_6^k}{\partial z}\mathbf{I}_2 & \frac{\partial z_7^k}{\partial z}\mathbf{I}_2 \\ \frac{\partial z_8^k}{\partial z}\mathbf{I}_2 & \frac{\partial z_9^k}{\partial z}\mathbf{I}_2 & \frac{\partial z_{10}^k}{\partial z}\mathbf{I}_2 & \frac{\partial z_{11}^k}{\partial z}\mathbf{I}_2 \end{bmatrix}$$

$$\partial_b = \begin{bmatrix} \partial_b^0 & 0 & 0 & . & . & . & 0 \\ 0 & \partial_b^1 & 0 & . & . & . & 0 \\ 0 & 0 & \partial_b^1 & . & . & . & . \\ . & . & & . & & & . \\ . & . & & & . & & . \\ . & . & & & & . & . \\ 0 & 0 & 0 & . & . & . & \partial_b^1 \end{bmatrix},$$

$$\partial_s = \begin{bmatrix} \partial_s^0 & 0 & 0 & . & . & . & 0 \\ 0 & \partial_s^1 & 0 & . & . & . & 0 \\ 0 & 0 & \partial_s^1 & . & . & . & . \\ . & . & & . & & & . \\ . & . & & & . & & . \\ . & . & & & & . & . \\ 0 & 0 & 0 & . & . & . & \partial_s^1 \end{bmatrix},$$

$$\partial_b^0 = \begin{bmatrix} \frac{\partial}{\partial r} & 0 & 0 \\ \frac{1}{r} & \frac{1}{r}\frac{\partial}{\partial \theta} & 0 \\ \frac{1}{r}\frac{\partial}{\partial \theta} & \left(\frac{\partial}{\partial r} - \frac{1}{r}\right) & 0 \end{bmatrix},\ \partial_b^1 = \begin{bmatrix} \frac{\partial}{\partial r} & 0 \\ \frac{1}{r} & \frac{1}{r}\frac{\partial}{\partial \theta} \\ \frac{1}{r}\frac{\partial}{\partial \theta} & \left(\frac{\partial}{\partial r} - \frac{1}{r}\right) \end{bmatrix},$$

$$\partial_s^0 = \begin{bmatrix} 0 & 0 & \frac{\partial}{\partial r} \\ 0 & 0 & \frac{1}{r}\frac{\partial}{\partial \theta} \end{bmatrix},\ \partial_s^1 = \begin{bmatrix} 1 & 0 \\ 0 & 1 \end{bmatrix} \tag{7.7}$$

In Eq. (7.7), $\boldsymbol{I}_2 / \boldsymbol{I}_3$ is the unity matrix of size $((2\times2)/(3\times3))$, and the derivatives of the thickness coordinates $(z_i^k, i=1,2,....11)$ are as follows,

$$
\begin{aligned}
\left.\frac{\partial z_1^k}{\partial z}\right|_{k=1,2,3,4,5} &= 1|_{k=1}, 0|_{k=2}, 0|_{k=3}, 0|_{k=4}, 0|_{k=5}, \\
\left.\frac{\partial z_2^k}{\partial z}\right|_{k=1,2,3,4,5} &= 0|_{k=1}, 1|_{k=2}, 0|_{k=3}, 0|_{k=4}, 0|_{k=5} \\
\left.\frac{\partial z_3^k}{\partial z}\right|_{k=1,2,3,4,5} &= 0|_{k=1}, 0|_{k=2}, 1|_{k=3}, 0|_{k=4}, 0|_{k=5}, \\
\left.\frac{\partial z_4^k}{\partial z}\right|_{k=1,2,3,4,5} &= 0|_{k=1}, 0|_{k=2}, 0|_{k=3}, 1|_{k=4}, 0|_{k=5} \\
\left.\frac{\partial z_5^k}{\partial z}\right|_{k=1,2,3,4,5} &= 0|_{k=1}, 0|_{k=2}, 0|_{k=3}, 0|_{k=4}, 1|_{k=5}, \\
\left.\frac{\partial z_6^k}{\partial z}\right|_{k=1,2,3,4,5} &= 0|_{k=1}, 2(z-h_3)|_{k=2}, 0|_{k=3}, 0|_{k=4}, 0|_{k=5} \\
\left.\frac{\partial z_7^k}{\partial z}\right|_{k=1,2,3,4,5} &= 0|_{k=1}, 0|_{k=2}, 2z|_{k=3}, 0|_{k=4}, 0|_{k=5}, \\
\left.\frac{\partial z_8^k}{\partial z}\right|_{k=1,2,3,4,5} &= 0|_{k=1}, 0|_{k=2}, 0|_{k=3}, 2(z-h_4)|_{k=4}, 0|_{k=5} \\
\left.\frac{\partial z_9^k}{\partial z}\right|_{k=1,2,3,4,5} &= 0|_{k=1}, \left.3(z-h_3)^2\right|_{k=2}, 0|_{k=3}, 0|_{k=4}, 0|_{k=5}, \\
\left.\frac{\partial z_{10}^k}{\partial z}\right|_{k=1,2,3,4,5} &= 0|_{k=1}, 0|_{k=2}, \left.3z^2\right|_{k=3}, 0|_{k=4}, 0|_{k=5} \\
\left.\frac{\partial z_{11}^k}{\partial z}\right|_{k=1,2,3,4,5} &= 0|_{k=1}, 0|_{k=2}, 0|_{k=3}, \left.3(z-h_4)^2\right|_{k=4}, 0|_{k=5}
\end{aligned}
\tag{7.8}
$$

The face layers are considered to be made of an isotropic material. The foam and the viscoelastic materials are also isotropic materials. So, the constitutive relations for these materials under the plane stress assumption can be written according to Eq. (6.9).

$$\boldsymbol{\sigma}_b^k = \boldsymbol{C}_b^k \boldsymbol{\varepsilon}_b^k \,,\ \boldsymbol{\sigma}_s^k = \boldsymbol{C}_s^k \boldsymbol{\varepsilon}_s^k$$

$$\boldsymbol{C}_b^k = \frac{E^k}{1-(v^k)^2}\begin{bmatrix} 1 & v^k & 0 \\ v^k & 1 & 0 \\ 0 & 0 & (1-v^k)/2 \end{bmatrix},\ \boldsymbol{C}_s^k = \frac{E^k}{2(1+v^k)}\begin{bmatrix} 1 & 0 \\ 0 & 1 \end{bmatrix} \qquad (6.9)$$

Equation (6.9) shows the constitutive relations for an isotropic material within the k^{th} layer. The viscoelastic material is presently modelled in complex stiffness method. So, the stiffness matrices ($\boldsymbol{C}_b^k$ and $\boldsymbol{C}_s^k$) in Eq. (6.9) are the complex matrices for the viscoelastic material. The constitutive relations for the shear mode annular PFC actuator under the plane stress assumption are given in Eq. (6.10).

$$\boldsymbol{\sigma}_b^k = \boldsymbol{C}_b^k(r)\boldsymbol{\varepsilon}_b^k \,,\ \boldsymbol{\sigma}_s^k = \boldsymbol{C}_s^k(r)\boldsymbol{\varepsilon}_s^k - \boldsymbol{e}_s^k(r)E_z \,,\ D_z^k = \left\langle \boldsymbol{e}_s^k(r) \right\rangle^{\mathrm{T}} \boldsymbol{\varepsilon}_s^k + \epsilon_{33}^k(r)E_z \qquad (6.10)$$

In the use of Eq. (6.10) for the present plate, the superscript k indicates the piezo-foam layer in the overall laminated plate, while the constitutive relations are for the PFC patches within the piezo-foam layer.

The FE mesh of the smart annular sandwich plate is created by dividing the radial and circumferential spans of the plane of the plate. Every element is in the shape of the annular-sector with the edges in parallel to the radial and circumferential axes of the reference cylindrical coordinate system. As the patches of the annular PFC actuator are embedded within the foam layer, two different elemental stacking sequences appear in the FE mesh of the overall annular plate for each of its configurations (CONFIG#1 (Figs. 7.2(a)) and CONFIG#2 (Fig. 7.2(b))). For the first configuration of the annular plate (CONFIG#1 (Figs. 7.2(a))), the two different elemental stacking sequences are shown in Figs. 7.3(a) and 7.3(b) by the names of Element 1 and Element 2. Similarly, Figs. 7.3(c) and 7.3(d) show Element 3 and Element 4, respectively, for the two different elemental stacking sequences in the FE mesh of the second configuration of the annular plate (CONFIG#2 (Fig. 7.2(b)).

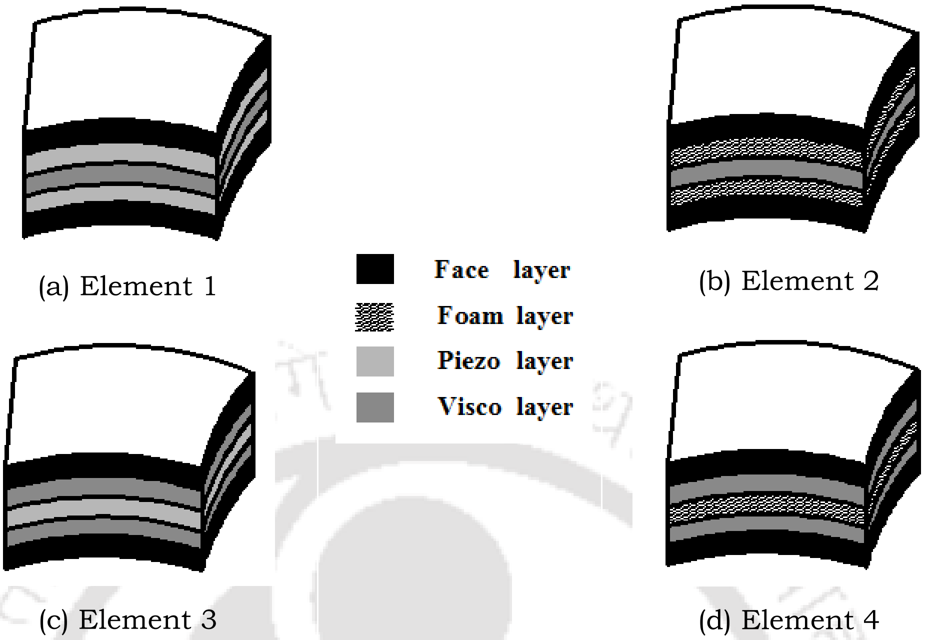

(a) Element 1 (b) Element 2

(c) Element 3 (d) Element 4

Fig. 7.3 Elemental stacking sequences for two different configurations of the smart annular plate (Fig. 7.2).

At any point within a typical element, the generalized displacement vector $(\boldsymbol{d})$ can be written in terms of the shape function matrix $(\boldsymbol{N})$ and the elemental nodal displacement vector $(\boldsymbol{d}_e)$ as given in Eq. (6.12).

$$\boldsymbol{d} = \boldsymbol{N}\boldsymbol{d}_e \tag{6.12}$$

The strain displacement relations (Eq. (7.7)) and the displacements (Eq. (7.6)) at any point within a typical element can be expressed as,

$$\begin{gathered} \boldsymbol{\varepsilon}_b^k = \boldsymbol{Z}_b^k \boldsymbol{B}_b \boldsymbol{d}_e\,,\ \ \boldsymbol{\varepsilon}_s^k = \boldsymbol{Z}_s^k \boldsymbol{B}_s \boldsymbol{d}_e\,,\ \ \boldsymbol{d}^k = \boldsymbol{Z}^k \boldsymbol{N}\boldsymbol{d}_e \\ \boldsymbol{B}_b = \boldsymbol{\partial}_b \boldsymbol{N}\,,\ \ \boldsymbol{B}_s = \boldsymbol{\partial}_s \boldsymbol{N} \end{gathered} \tag{7.9}$$

The smart annular sandwich plate is considered to operate under a transversely distributed harmonic load $p(r,\theta,z,t)$. For the corresponding vibration of the plate, the first variations of the total potential energy (δT_p^e) and the total kinetic energy (δT_k^e) for an element at any instant of time can be written as (Tiersten, 1969),

$$\delta T_p^e = \int_{A_e} \left\{ \sum_{k=1}^{5} \int_{h_k}^{h_{k+1}} \left[\delta \boldsymbol{\varepsilon}_b^{k^{\mathrm{T}}} \boldsymbol{\sigma}_b^k + \delta \boldsymbol{\varepsilon}_s^{k^{\mathrm{T}}} \boldsymbol{\sigma}_s^k \right] dz - \sum_{k=2,k\neq 3}^{4} \int_{h_k}^{h_{k+1}} \delta E_z D_z^k \, dz - Q_p \right\} dA_e \tag{7.10}$$

$$Q_p = (\delta w^k)\, p(r,\theta,\frac{h}{2},t)\Big|_{k=5}$$

$$\delta T_k^e = \int_{A_e} \left\{ \sum_{k=1}^{5} \int_{h_k}^{h_{k+1}} \left\{ \delta \dot{u}^k \quad \delta \dot{v}^k \quad \delta \dot{w}^k \right\} \rho^k \left\{ \delta \dot{u}^k \quad \delta \dot{v}^k \quad \delta \dot{w}^k \right\}^{\mathrm{T}} dz \right\} dA_e \tag{7.11}$$

where, ρ^k is the mass density of k^{th} layer; A_e is the elemental area over the plate; δ is an operator for the first variation. In Eq. (7.10), the energy due to the electric displacement (D_z^k) is written for Element 1 (Fig. 7.3(a)). For other elements (Element 2, Element 3 and Element 4 in Fig. 7.3), this energy would be computed according to the location of the piezoelectric layers within the elemental stacking sequence. Using Eqs. (6.9), (6.10), (7.6), (7.7) and (7.9) in Eqs. (7.10) and (7.11), the expressions of δT_p^e and δT_k^e can be written as,

$$\delta T_p^e = \int_{A_e} \delta \boldsymbol{d}_e^{\mathrm{T}} \left\langle \left[\boldsymbol{B}_b^{\mathrm{T}} \boldsymbol{A}_b(r) \boldsymbol{B}_b + \boldsymbol{B}_s^{\mathrm{T}} \boldsymbol{A}_s(r) \boldsymbol{B}_s \right] \boldsymbol{d}_e - \boldsymbol{B}_s^{\mathrm{T}} \boldsymbol{A}_e(r) E_z - Q_{pe} \right\rangle \, dA_e$$

$$Q_{pe} = \boldsymbol{N}^{\mathrm{T}} \boldsymbol{A}_p\, p(r,\theta,\frac{h}{2},t) \tag{7.12}$$

$$\delta T_k^e = \int_{A_e} \left[\delta \dot{\boldsymbol{d}}_e^{\mathrm{T}} \left\langle \boldsymbol{N}^{\mathrm{T}} \boldsymbol{m}(r) \boldsymbol{N} \right\rangle \dot{\boldsymbol{d}}_e \right] \, dA_e \tag{7.13}$$

In Eqs. (7.12) and (7.13), the rigidity matrices $(\boldsymbol{A}_b(r), \boldsymbol{A}_s(r))$, electro-elastic coupling vector $(\boldsymbol{A}_e(r))$, mechanical load coefficient ($\boldsymbol{A}_p$) and mass per unit area ($\boldsymbol{m}(r)$) of the overall plate are,

$$\boldsymbol{A}_b(r) = \sum_{k=1}^{5} \int_{h_k}^{h_{k+1}} \left(\boldsymbol{Z}_b^{k\,\mathrm{T}} \boldsymbol{C}_b^k(r) \boldsymbol{Z}_b^k \right) dz\,, \quad \boldsymbol{A}_s(r) = \sum_{k=1}^{5} \int_{h_k}^{h_{k+1}} \left(\boldsymbol{Z}_s^{k\,\mathrm{T}} \boldsymbol{C}_s^k(r) \boldsymbol{Z}_s^k \right) dz\,,$$

$$\boldsymbol{A}_e(r) = \sum_{k=2,k\neq 3}^{4} \int_{h_k}^{h_{k+1}} \left(\boldsymbol{Z}_s^{k\,\mathrm{T}} \boldsymbol{e}_s^k(r) \right) \, dz\,, \quad \boldsymbol{m}(r) = \sum_{k=1}^{5} \int_{h_k}^{h_{k+1}} \left((\boldsymbol{Z}^k)^{\mathrm{T}} \rho^k(r) \boldsymbol{Z}^k \right) dz\,,$$

$$\boldsymbol{A}_p = \left\langle (\boldsymbol{Z}^k)^{\mathrm{T}} \{0 \quad 0 \quad 1\}^{\mathrm{T}} \right\rangle \Big|_{k=5} \tag{7.14}$$

Equations (7.12) and (7.13) can also be simplified as,

$$\delta T_p^e = \delta \boldsymbol{d}_e^{\mathrm{T}} \left(\boldsymbol{K}_b^e + \boldsymbol{K}_s^e - \boldsymbol{P}_E^e E_z - \boldsymbol{P}_e \right),$$

$$\boldsymbol{K}_b^e = \int_{A_e} \left(\boldsymbol{B}_b^{\mathrm{T}} \boldsymbol{A}_b(r) \boldsymbol{B}_b \right) \, dA_e\,, \quad \boldsymbol{K}_s^e = \int_{A_e} \left(\boldsymbol{B}_s^{\mathrm{T}} \boldsymbol{A}_s(r) \boldsymbol{B}_s \right) \, dA_e\,,$$

$$\boldsymbol{P}_E^e = \int_{A_e} \left(\boldsymbol{B}_s{}^{\mathrm{T}} \boldsymbol{A}_e(r)\right) \; dA_e \,, \quad \boldsymbol{P}_e = \int_{A_e} \left(\boldsymbol{N}^{\mathrm{T}} \boldsymbol{A}_p p(r,\theta,\frac{h}{2},t)\right) \; dA_e \tag{7.15}$$

$$\delta T_k^e = \delta \dot{\boldsymbol{d}}_e{}^{\mathrm{T}} \left(\boldsymbol{M}^e\right) \dot{\boldsymbol{d}}_e \,,$$

$$\boldsymbol{M}^e = \int_{A_e} \left(\boldsymbol{N}^{\mathrm{T}} \boldsymbol{m}(r) \boldsymbol{N}\right) \; dA_e \tag{7.16}$$

The governing equations of motion for the smart annular sandwich plate is obtained employing the extended Hamilton’s principle as given in Eq. (3.36). Introducing Eq. (7.15) and (7.16) in Eq. (3.36), the elemental equations of motion can be obtained as,

$$\boldsymbol{M}^e \ddot{\boldsymbol{d}}_e + \boldsymbol{K}\boldsymbol{d}_e = \boldsymbol{P}_e + \boldsymbol{P}_E^e E_z \,, \quad \boldsymbol{K} = \left(\boldsymbol{K}_b^e + \boldsymbol{K}_s^e\right) \tag{7.17}$$

Assembling the elemental equations of motion, the global equations of motion for the overall annular plate can be obtained in the form of Eq. (6.20).

$$\boldsymbol{M}\ddot{\boldsymbol{X}} + \boldsymbol{K}\boldsymbol{X} = \boldsymbol{P}_M + \sum_{s=1}^{n_p} \boldsymbol{P}_E^s E_z^s \tag{6.20}$$

Recalling Eq. (6.20), the symbol n_p indicates the number of patches while the symbols $\boldsymbol{P}_E^S$ and E_z^S stand for the electro-elastic coupling coefficient vector and applied electric field, respectively, for the S^{th} patch.

7.3.1 Control strategy

Every actuator patch (S) of the PFC actuator is activated by supplying the external electric field (E_z^S) in proportion to the transverse velocity ($\dot{w}_s$) at its middle point. It can be expressed by Eq. (6.21) as,

$$E_z^s = \mp k_d^s \dot{w}_s \tag{6.21}$$

The transverse velocity ($\dot{w}_s$) is expressed in terms of the global nodal velocity vector ($\dot{\boldsymbol{X}}$) according to Eq. (6.22), and the equations of motion for the smart annular sandwich plate can be derived in the form of Eq. (6.23).

$$\dot{w}_s = \boldsymbol{T}_s \dot{\boldsymbol{X}} \tag{6.22}$$

$$\boldsymbol{M}\ddot{\boldsymbol{X}} + \boldsymbol{K}\boldsymbol{X} = \boldsymbol{P}_M \mp \left(\sum_{s=1}^{n_p} \boldsymbol{C}_s\right) \dot{\boldsymbol{X}} \,, \quad \boldsymbol{C}_s = (\boldsymbol{P}_E^s k_d^s \boldsymbol{T}_s) \tag{6.23}$$

Now, following the same control strategy as discussed in Section 6.3.1, a group of patches is defined by taking the patches with the identical radial boundaries, and the corresponding groups of patches are denoted by, $g = 1,2,3,\ldots\ n_r$ starting from the innermost group as, $g = 1$. The control-gains (k_d^s) for the patches in a group are assigned with the same sign, while it (sign) varies over the groups of patches following the locations of the anti-nodes in the radial direction for the modes of vibration under study. According to this strategy, the governing equations of motion are reduced in the form of Eq. (6.24) or Eq. (6.25).

$$\boldsymbol{M}\ddot{\boldsymbol{X}} + \boldsymbol{K}\boldsymbol{X} = \boldsymbol{P}_M - \left(\sum_{g=1}^{n_r} S_g \boldsymbol{C}_g\right)\dot{\boldsymbol{X}}, \quad \boldsymbol{C}_g = \sum_{s=1}^{n_\theta}(\boldsymbol{P}_E^s(|k_d^s|)\boldsymbol{T}_s)_g \tag{6.24}$$

$$\boldsymbol{M}\ddot{\boldsymbol{X}} + \boldsymbol{C}\dot{\boldsymbol{X}} + \boldsymbol{K}\boldsymbol{X} = \boldsymbol{P}_M, \quad \boldsymbol{C} = \sum_{g=1}^{n_r} S_g \boldsymbol{C}_g \tag{6.25}$$

7.4 Results and discussions

In this section, the active-passive damping characteristics of the smart annular sandwich plate are studied by means of evaluating its frequency responses using the present FE formulation. The FE formulation in this chapter is a modified form of that in the previous chapter. This modification of the FE formulation is required due to the inclusion of the viscoelastic layer and the corresponding modified form of the layer-wise shear deformation theory. This modified FE formulation as well as the corresponding FE code are presently verified following the same procedures as those were carried out in the previous chapter. First, a negligibly small thickness of the core ($h_v \approx 0$, $h_c \approx 0$) is considered, and the natural frequencies of the simply-supported/fully clamped annular plate are computed for different radial coordinates of its inner and outer edges.

Table 7.1 Verification of the present FE formulation by computation of the dimensionless natural frequencies ($\lambda_i = \omega_i r_o^2\sqrt{\rho h/D}$, $D = Eh^3/12(1-\upsilon^2)$, $k_d = 0$**) of the annular plate.**

Source	$r_i/r_o = 0.2$	$r_i/r_o = 0.4$	$r_i/r_o = 0.6$	$r_i/r_o = 0.8$
Simply-supported edges of the annular plate				
Present FE	16.727	28.081	62.12	246.66
Chakraverty et al., 2001	16.72	28.08	62.12	247
Fully-clamped edges of the annular plate				
Present FE	34.604	61.837	139.4	558.8
Chakraverty et al., 2001	34.61	61.87	139.6	559.1

These results are illustrated in Table 7.1 together with the similar analytical results for an identical isotropic annular plate (Chakraverty et al., 2001). It may be observed from Table 7.1 that the present FE results are in good agreement with the available analytical results (Chakraverty et al., 2001), and this comparison verifies the present FE formulation for handling the vibration of an annular plate. Next, the piezo-foam layer is considered to be fully made of a monolithic piezoelectric actuator (PZT5H). Concurrently, the face layers and the viscoelastic layers within the overall annular plate are considered as the negligibly thin layers ($h_f \approx 0$, $h_v \approx 0$) so that the overall plate becomes like a thin annular piezoelectric disc. The poling direction of this piezoelectric annular disc is the radial direction, while the external electric field is applied across its thickness. For different values of the externally applied transverse electric field, the corresponding magnitudes of the free transverse shear strain (γ_{rz}) of the annular piezoelectric disc are computed by the closed-form expression as, $\gamma_{rz} = \langle e_{35} / C_{55} \rangle E_z$. Similar results are also computed using the present FE formulation, and these FE results are compared with the analytical results in Table 7.2. It may be observed from Table 7.2 that the FE results are in excellent agreement with the analytical results thus verifying the present FE formulation for handling the electro-elastic coupling in the shear piezoelectric actuator.

Table 7.2 Verification of the present FE formulation for handling the electro-elastic coupling in the shear piezoelectric actuator.

E_z (volt/m)	Free transverse shear strain (γ_{rz})	
	Present FE	Analytical
1e5	5.8452e-5	5.839e-5
2e5	1.1681e-4	1.168e-4
4e5	2.3354e-4	2.336e-4

For evaluation of the frequency responses of the smart annular sandwich plate (Figs. 7.1 and 7.2), its geometrical properties are considered as, $r_i = 0.2$ m, $r_o = 1$ m, n_r = 4, Δr_F = 10 mm, n_θ = 8, $\Delta\theta_F = 5^0$. Unless otherwise mentioned, the thickness (h) of the overall annular plate, total thickness (h_v) of the viscoelastic layers and total thickness (h_p) of the piezo-foam layers are considered as, 6 mm, 1 mm and 2.104 mm, respectively. Within the total thickness ($h_p = 2.104$) of the annular PFC actuator, four 2-2 PFC layers are considered, and each of these 2-2 PFC layers is of a thickness (h_e) of 0.5 mm.

The material properties of the face layers and foam are taken as those were considered in the previous analysis (Section 6.4). The Young's modulus, Poisson's ratio and density of the viscoelastic material are considered as, 20(1+1 j) MPa ($j = \sqrt{-1}$), 0.3 and 1140 kg/m^3, respectively. As stated in Section 7.2, the two different geometric configurations (Fig. 5.7) of the shear mode annular PFC actuator are utilized separately. For the first geometric configuration (PFC#1) (line 1/2 in Fig. 5.7) of the annular PFC actuator, its inner and outer radii are the same as those ($r_i = 0.2$ m, $r_o = 1$ m) are for the overall annular plate. In the second geometric configuration of the annular PFC actuator (PFC#2) (line 3/4 in Fig. 5.7), the radial coordinates for its four radial divisions/parts are considered as, $r_i = 0.2$ m, $r_1 = 0.4$ m, $r_2 = 0.6$ m, $r_3 =$ 0.8 m and $r_o = 1$ m. The varying material properties of the annular PFC actuator for each of its configurations are given in Tables 5.5, 5.6, 5.7 and 5.8.

As discussed in Section 6.4, the mechanically induced transverse shear stress (τ_{rz}) appears with its maximum/minimum magnitude at the node/anti-node of any bending mode of deformation/vibration of the overall plate. Consequently, the velocity appears with a low/high magnitude around the node/anti-node. So, for efficient control of vibration of the overall plate according to the velocity feedback control law, the value of the control-gain is to be varied along the radial direction. Presently, four groups of patches ($n_r = 4$) are considered following the arrangement of the patches, and the modes under study are of the fundamental radial mode number. So, following the same procedure as that is presented in Section 6.4, the control-gains for the patches in the inner ($g = 1$) and outer ($g =$ 4) groups are assigned with a uniform value, and it is parametrically denoted by k_d. Consequently, the control-gains for the patches in the inner two groups ($g =$ 2, 3) are assigned as, k_d / k_d^r, where k_d^r is defined as $k_d^r = (\bar{w}_{\max}^{2/3} / \bar{w}_{\max}^{1/4})$ (Section 6.4). As one anti-node appears at the middle of the radial span for the study with the fundamental radial mode number, the control-gains for the inner two groups ($g = 1$, 2) of patches are assigned with the same sign. Concurrently, the control-gains for the outer two groups ($g = 3$, 4) of patches are assigned with the opposite sign. With this assignment of the control-gains, the frequency responses of the simply-supported overall annular plate are evaluated by applying a transversely distributed harmonic load on its top surface as,

$$p(r,\theta,t) = p\langle 1+\cos(\theta)\rangle e^{j\omega t} \tag{7.18}$$

where, p is the load-amplitude and ω is the operating frequency. For presenting the results, the transverse displacement-amplitude at a point ($(r_o - r_i)/2, 0, h/2$) is evaluated at every frequency (ω) of excitation. Also, the maximum voltage-amplitude in every group of patches is computed for estimating the required control-voltage.

In order to verify the fruitfulness of the present control strategy, the variations of the displacement-amplitude with the frequency of excitation are illustrated in Fig. 7.4(a) by taking three different cases in assigning the signs of control-gains corresponding to the groups of patches. In the first ($+k_d$) or second ($-k_d$) case (Fig. 7.4(a)), all the control-gains over the groups of patches are assigned with the positive or negative sign, respectively. For the third case ($\pm k_d$), Fig. 7.4(a), the sign of the control-gain for a group is assigned according to the aforesaid strategy. For any of the cases, the overall annular plate is taken with its first configuration (CONFIG#1, Fig. 7.2(a)) while the annular PFC actuator is taken with its first geometric configuration (PFC#1).

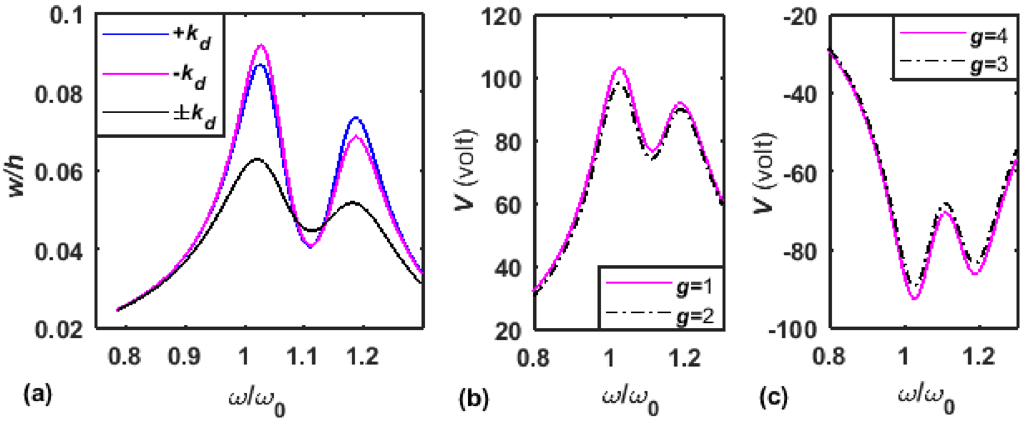

Fig. 7.4(a) Variations of dimensionless displacement-amplitude (w/h) with the frequency of excitation, (b)-(c) variation of maximum voltage in each of the groups corresponding the response for $\pm k_d$ in (a) (k_d = 10e6, $p = 10$ N/m², ω_0 is the fundamental natural frequency).

It may be observed from this figure that a significant improvement in the attenuation of vibration of the smart annular sandwich plate can be achieved by assigning the signs of the control-gains over the groups ($g = 1,2,3,4$) according to the present strategy (third case, $\pm k_d$) instead of any of the other ones (first ($+k_d$) and second ($-k_d$) cases). This result (Fig. 7.4(a)) verifies the fruitfulness of the present strategy for assigning the sign of the control-gains over the groups of patches. For the response of the overall plate corresponding to the third case (curve for $\pm k_d$ in Fig. 7.4(a)), the variation of maximum voltage in every group of patches is illustrated in Figs. 7.4(b) and 7.4(c). It may be observed from these figures (Figs. 7.4(b)-(c)) that the sign of the voltage in inner groups ($g = 1$, 2) is opposite to that in the outer groups ($g = 3$, 4). This appears following the assigned sign of the control-gains over the groups. More importantly, there is insignificant difference among the magnitudes of the voltages in the groups of patches. It implies effective utilization of all the groups of patches for active control of vibration of the overall annular plate, and it is obtained due to the present strategy in assigning the values of the control-gains over the groups of patches. The results in Figs. 7.4(b) and 7.4(c) indicate the fruitfulness of the present strategy for assigning the values of the control-gains.

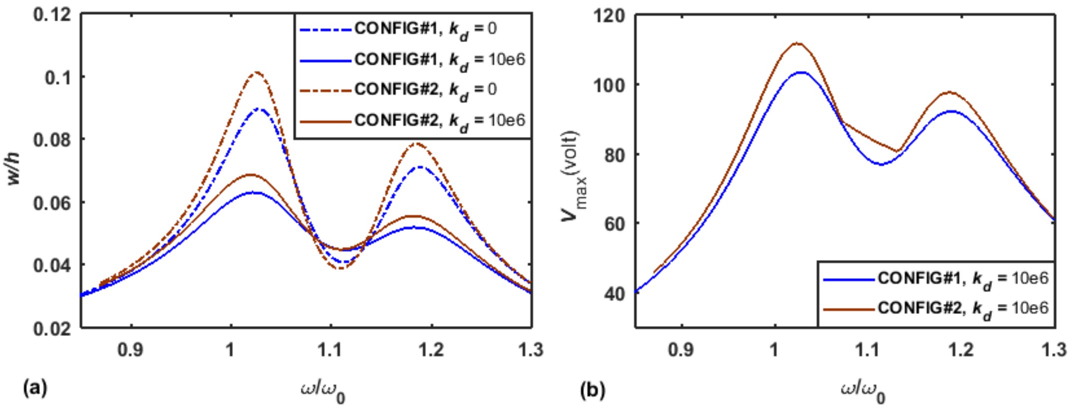

Fig. 7.5 Variations of (a) the dimensionless transverse displacement-amplitude and (b) the corresponding maximum voltage-amplitude at inner group ($g = 1$) with the frequency of excitation for two different configurations of the overall annular plate ($p = 10$ N/m², PFC: PFC#2).

Figure 7.5(a) illustrates the variations of the dimensionless transverse displacement-amplitude with the frequency of excitation for each of the two different configurations (CONFIG#1 and CONFIG#2, Fig. 7.2) of the smart annular sandwich plate. The corresponding variations of the maximum control-voltage in the inner group ($g = 1$) are also illustrated in Fig. 7.5(b). For these responses, the annular PFC actuator is taken with its second geometric configuration (PFC#2). It may be observed from Fig. 7.5(a) that the damping in the overall plate increases significantly with the increasing value of the control gain for any of the configurations (CONFIG#1/CONFIG#2). But, for any value of the control-gain, the amount of damping within the overall plate is more in case of CONFIG#1 than that in case of CONFIG#2. This improvement of damping in the smart plate appears with a lesser control voltage (Fig. 7.5(b)) although the value of the control-gain (k_d) remains the same for both the configurations (CONFIG#1/CONFIG#2).

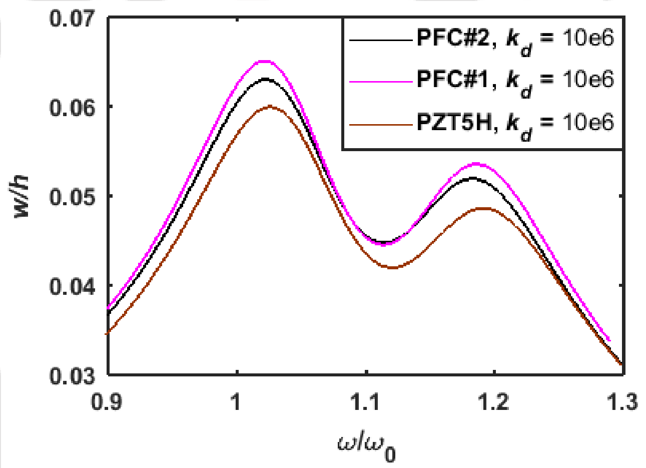

Fig. 7.6 Variation of dimensionless transverse displacement-amplitude with the frequency of excitation when the material of the patches is either of PFC#1, PFC#2 and shear PZT5H (p = 10 N/m^2).

Figure 7.6 illustrates the variations of the dimensionless transverse displacement-amplitude with the operating frequency when the patches are either made of the present PFC actuator or made of the conventional monolithic shear piezoelectric actuator (PZT5H). The annular PFC actuator is taken with its first (PFC#1) or second (PFC#2) geometric configuration, and the overall annular plate is made with its first configuration (CONFIG#1, Fig. 7.2(a)). It may be observed from this figure that the annular PFC actuator possesses superior control capability when it is made with its second geometric configuration (PFC#2) instead of the first one (PFC#1). For any of the geometric configurations (PFC#1 and (PFC#2)) of the annular PFC actuator, its actuation capability is a little lesser than that of the monolithic shear piezoelectric actuator (PZT5H). It may be noted by recalling the results in Fig. 6.7 that the actuation capability of the annular PFC actuator is greater than that of the monolithic shear piezoelectric actuator (PZT5H) when the actuators are used without viscoelastic layer. However, a small difference between the actuation capabilities of the actuators (PFC#2 and PZT5H) appears (Fig. 7.6), and it may not be an important issue in the applications of the PFC actuator while it (PFC) possesses the advantages of greater flexibility and conformability.

In order to verify the enhancement of damping in the smart sandwich annular plate due to the inclusion of a viscoelastic layer, the frequency responses of the overall annular plate are evaluated with or without consideration of the viscoelastic layer at the core.

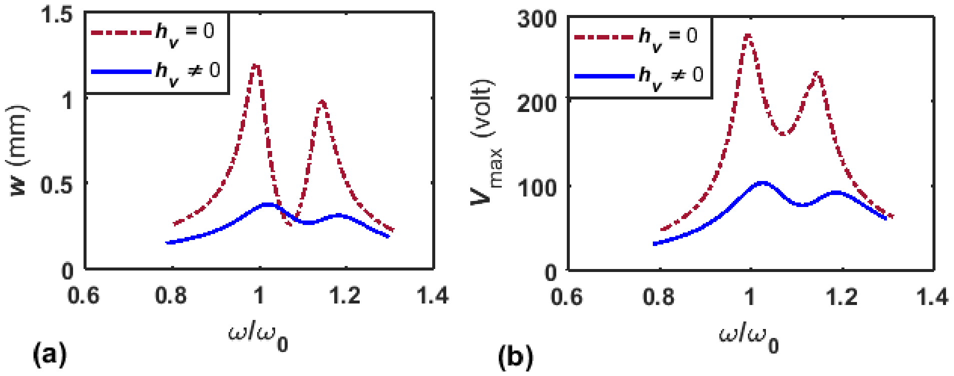

Fig. 7.7 Variations of (a) the transverse displacement-amplitude and (b) the corresponding maximum control-voltage (in $g = 1$) with the frequency of excitation (k_d = 10e6, $p = 10$ N/m², PFC: PFC#2).

Figure 7.7 illustrates these responses which are evaluated for the constant values of the control-gain and the load-amplitude. The overall plate is taken with its first geometric configuration (CONFIG#1), and the material for the patches in the piezo-foam layer is considered as PFC#2. Since the thickness of the overall plate differs due to the presence ($h_v = 1$ mm) and the absence ($h_v = 0$) of the viscoelastic layer, the transverse displacement-amplitude is presented in Fig. 7.7(a) with its absolute value. It may be observed from Fig. 7.7 that the damping in the overall annular plate significantly improves due to the inclusion of the viscoelastic layer. Also, this improved damping is achieved by supplying indicatively lesser control-voltage. Thus, it would always be preferred to utilize the shear mode PFC actuator along with the viscoelastic material in order to have efficient damping in the overall plate at the expense of a reasonably small control-voltage. In this application of the shear mode PFC actuator, the thickness (h_v) of the viscoelastic layer is an important parameter in the design of the overall annular plate.

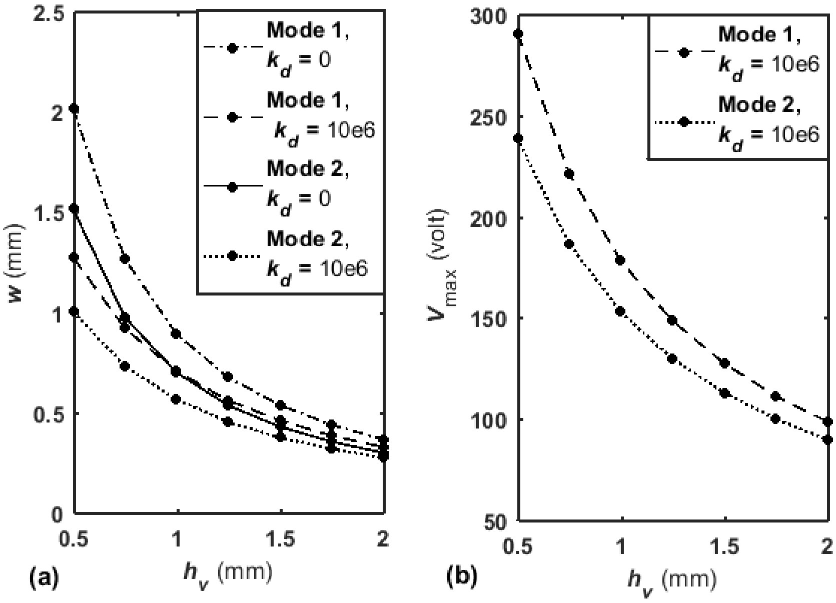

Fig. 7.8 Variations of (a) the transverse displacement-amplitude and (b) the corresponding maximum control-voltage (in $g=1$) with the thickness (h_v) of the viscoelastic layer of the overall annular plate with the first configuration (CONFIG#1) ($p=10$ N/m², PFC: PFC#2).

Figure 7.8(a) illustrates the variations of the transverse displacement-amplitude with the thickness of the viscoelastic layer for the first (Mode 1) and second (Mode 2) resonances. The thickness (h_v) of the viscoelastic layer is varied without altering the thicknesses of the face layers and the piezo-foam layers. So, the thickness (h) of the overall annular plate varies, and thus the corresponding variations of the transverse displacement-amplitude are presented with its absolute value. The overall plate is taken with its first configuration (CONFIG#1), and every piezo-foam layer is considered to be made of one 2-2 PFC layer with a thickness ($h_p/2$) of 0.526 mm. It may be observed from Fig. 7.8(a) that the displacement-amplitude decreases indicatively with an increase of the control gain (k_d from 0 to 10e6) for any thickness of the viscoelastic layer. But, this active action of the piezo-foam layer decreases with the increase of the thickness of the viscoelastic layer even though the displacement-amplitude decreases at a significant rate with the increase of the thickness of the viscoelastic layer. So, the displacement-amplitude can be attenuated efficiently using a viscoelastic layer of high thickness without any actuator or piezo-foam layer. But, if the viscoelastic layer of high thickness is not permitted in the design of the annular plate, then the piezo-foam layer may be utilized with a viscoelastic layer of small thickness. In this use of the piezo-foam layer, the viscoelastic layer with a too small thickness may cause the requirement of a high voltage (Fig. 7.8(b)) for attenuation of the vibration amplitude. So, the thickness of the thin viscoelastic layer may be selected in an optimal manner with certain bound of the required control-voltage. This bound of the applied/required control-voltage may be chosen as the permissible applied voltage for the shear mode annular PFC actuator.

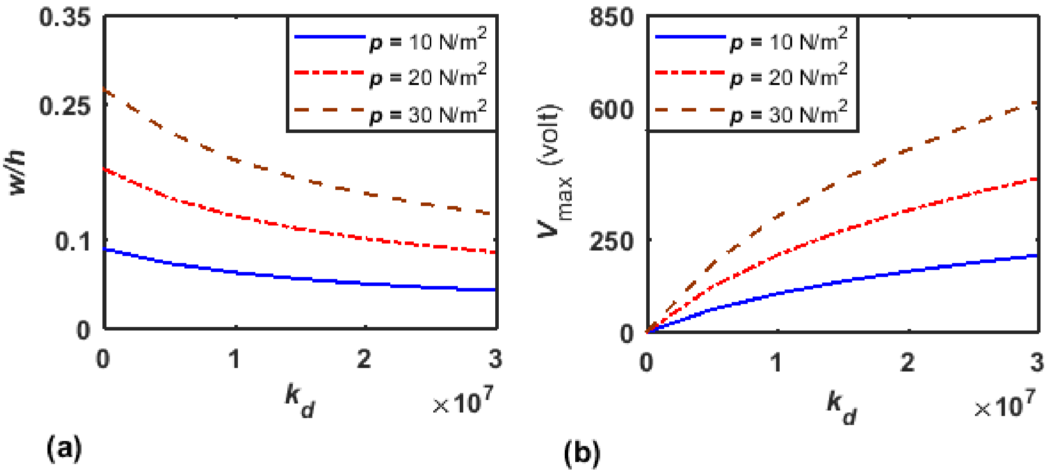

Fig. 7.9 Variations of (a) the dimensionless transverse displacement-amplitude and (b) the corresponding maximum control-voltage (at $g = 1$) with the control-gain (k_d) at the first resonant frequency of vibration (PFC: PFC#2, overall annular plate: CONFIG#1).

Figure 7.9 illustrates the variations of the dimensionless transverse displacement-amplitude (at the first resonant frequency) and the corresponding maximum control-voltage (at $g = 1$) with the control-gain (k_d) for three different values of the load-amplitude (p). For a load-amplitude, it may be observed from Fig. 7.9(a) that the displacement-amplitude decreases with the increase of the control-gain, and the corresponding control-voltage increases. It is important to observe from Fig. 7.9(b) that the control-voltage increases with the increasing control-gain at a higher rate when the load-amplitude increases. So, the control-voltage may exceed the permissible voltage for the PFC actuator, and it indicates a limiting value of the control-gain at a load-amplitude. In order to find this bound of the control-gain at a load-amplitude, the contours of the maximum control-voltage within a two-dimensional domain of the control-gain and load-amplitude are plotted in Figs. 7.10(a) and 7.10(b) for the first (Mode 1) and second (Mode 2) resonances, respectively.

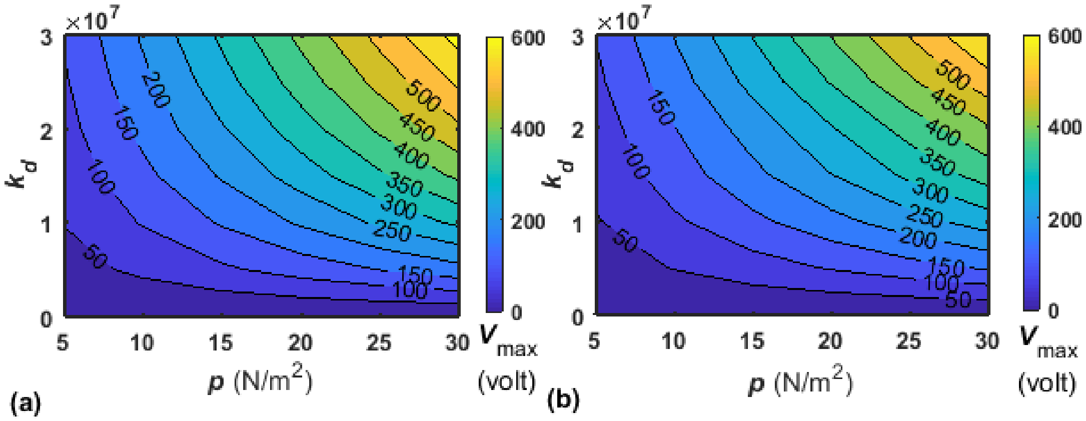

Fig. 7.10 Contours of maximum control-voltage (at $g = 1$) within the two-dimensional domain of control-gain (k_d) and load-amplitude (p) at the (a) first and (b) second resonant frequencies (PFC: PFC#2, Overall plate: CONFIG#1).

A line in this two-dimensional domain signifies a line of constant voltage. So, the line of the permissible applied voltage for the annular PFC actuator can be identified in this two-dimensional domain of the control-gain and the load-amplitude. Corresponding to this line of the permissible voltage, the overall domain can be divided into two-sub-domains. One of these sub-domains contains the feasible values of the control-gain for any applied load-amplitude. For instance, let the permissible voltage is 200 volt. The line of 200 volt divides the domain into the top and bottom sub-domains. The bottom sub-domain contains the feasible values of the control-gain for any load-amplitude. It may be noted from the results in Fig. 7.10 that a high value of the control-gain can be assigned for a low load-amplitude and vice versa. It infers the utility of the PFC actuator only for the low load-amplitudes.

7.5 Conclusions

In this chapter, the active-passive damping characteristics of a smart annular sandwich plate are investigated using a shear mode annular PFC actuator that is designed in Chapter 5. The face layers of the annular sandwich plate are made of an isotropic material, while the core is comprised of viscoelastic and piezo-foam layers in two different stacking sequences. In the first one, a viscoelastic layer is sandwiched between two identical piezo-foam layers. Conversely, a piezo-foam layer is sandwiched between two identical viscoelastic layers in the second one. The corresponding configurations of the overall annular plate are denoted by CONFIG#1 and CONFIG#2. The piezo-foam layer is comprised of the patches of the annular PFC actuator where the patches are embedded within the foam layer. The patches are made by dividing the annular PFC actuator following the same strategy as that is presented in Chapter 6. Every patch is considered to be activated with the feedback of its own transverse velocity. So, the velocity sensors are located at the top surface of the overall plate corresponding to the in-plane coordinates of the middle points of the patches. In this use of the velocity feedback control law, the previous strategy (Chapter 6) is followed for the assignment of control-gains corresponding to the patches. Based on this control strategy and the layer-wise shear deformation theory, a closed-loop FE model of the smart annular sandwich plate is developed, and its (overall plate) controlled frequency responses are evaluated. These results exhibit significant improvement of the damping in the overall annular plate for the use of viscoelastic layer along with the shear mode annular PFC actuator. But the thickness of the viscoelastic layer is to be chosen in an optimal manner for efficient utilization of the annular PFC actuator. It is observed that the active-passive damping in the smart annular sandwich plate increases when it is made with its first configuration (CONFIG#1) instead of its second configuration (CONFIG#2). Also, the overall plate possesses superior active-passive damping when the patches are made from the second geometric configuration (PFC#2) of the annular PFC actuator instead of its first one (PFC#1). For any of these geometric configurations of the PFC actuator, its (PFC) performance for inducing the active-passive damping in the overall annular plate is a little lesser than that in case of the use of a conventional monolithic shear piezoelectric actuator (PZT5H) in the same manner.

CHAPTER

8

Conclusions and scope for future work

8.1 Conclusions

This dissertation deals with the active control of flexural vibration of annular plates through the design of extension/shear mode piezoelectric fiber composite (PFC) actuators in the cylindrical coordinates. First, a cylindrically orthotropic piezoelectric fiber composite (PFC) is designed for having a flexible extension mode piezoelectric actuator in control of plane structures of revolution. The PFC is in the shape of a thin annular disc and comprised of unidirectional short or continuous piezoelectric fibers. The longitudinally poled short/continuous piezoelectric fibers are oriented along the radial direction so that the extension mode piezoelectric actuation appears along the radial direction in response to an externally applied coaxial electric field. The PFC with the short or continuous form of the unidirectional piezoelectric fibers is denoted by short piezoelectric fiber composite (SPFC) or continuous piezoelectric fiber composite (CPFC), respectively. The effective electro-elastic properties of both the SPFC and CPFC are estimated by developing an FE procedure, and the electromechanical behaviour of the cylindrically orthotropic SPFC/CPFC is studied with special attention to the significant changes in the electro-elastic behaviour of the cylindrically orthotropic PFC due to the unidirectional short/discontinuous fibers instead of the continuous ones. For efficient utilization of the SPFC/CPFC as a material of distributed actuator in control of bending modes of deformation/vibration of the plane structures of revolution, an arrangement of surface-electrodes over the top and bottom surfaces of the annular SPFC/CPFC disc is proposed. Based on this arrangement of the surface-electrodes, the SPFC/CPFC is utilized in the form of the patch to investigate its (SPFC/CPFC) performance in control of flexural vibration of an annular plate. The patches of the SPFC/CPFC actuator are attached to the top surface of the host plate and act as the damping elements to attenuate the forced harmonic vibration of the smart annular plate. The corresponding controlled frequency responses of this smart annular plate are evaluated by developing an FE model, and the actuation capabilities of the SPFC and CPFC actuators are illustrated. Concurrently, a comparative study on the actuation capabilities of SPFC and CPFC actuators is presented. This comparison study is further extended by taking the poling direction of the fibers in the cylindrically orthotropic CPFC either as radial (longitudinal) or as thickness (transverse) direction. For each of these longitudinal and transverse poling directions of the piezoelectric fibers in the CPFC, the fibers are oriented either in radial or in the circumferential direction so that four kinds of cylindrically orthotropic CPFCs appear based on the orientation and poling direction of the fibers. The arrangement of surface-electrodes for each of these CPFCs is illustrated, and their control capabilities are evaluated following the same host plate and control strategy as those are considered in the previous case of SPFC/CPFC actuator. But, the patches of each of the CPFC actuators are configured over the host plate-surface in an optimal manner through the proposition of a new numerical methodology for optimal size and locations of piezoelectric distributed actuators. On the basis of this methodology, the patches of every CPFC actuator are attached to the top surface of the host annular plate, and the capability of every CPFC actuator in inducing the active damping in the smart annular plate are quantified to address the best one among the four kinds of CPFC actuators.

Besides the extension mode SPFC/CPFC actuator, a shear mode PFC actuator is also designed in the cylindrical coordinates. It is made in the form of a thin laminated annular disc that is mainly comprised of two or more 2-2 PFC layers. The 2-2 PFC layer is composed of conventional piezoelectric fibers which are oriented in the radial direction and evenly spaced in the circumferential coordinate. The external electric field acts along the transverse direction of the longitudinally poled piezoelectric fibers, and the electrically induced shear force within the annular actuator appears in the transverse plane of radial and axial coordinates. The cylindrically periodic microstructure within this shear mode PFC actuator yields its radially varying electro-elastic properties. These varying properties are determined theoretically by means of dividing the volume of the corresponding representative volume (RV) into a large number of micro-volumes with different fiber volume fractions (FVFs). Every micro-volume is homogenized by developing an FE procedure. The closed-form expressions for the effective coefficients of the micro-volumes are also derived, and the properties at a point within the domain of RV are considered as the effective properties of the micro-volume at that point. An analysis of these varying properties of RV is performed, and two different geometric configurations of the shear mode annular PFC actuator are addressed for having its improved actuation capability. The performance of this PFC actuator with any of its two different geometric configurations is investigated for active control of vibration of an annular plate. In this investigation, the annular PFC actuator is divided into the patches in the shape of the annular-sector. These patches are embedded in the host annular plate by means of making a smart annular sandwich plate. A fruitful strategy for the arrangement of the patches in the annular plane of the plate is proposed to have the equal attenuation of all the bending modes of vibration of the smart annular sandwich plate. Concurrently, a useful scheme is also presented for efficient utilization of all the patches of the shear mode PFC actuator according to the velocity feedback control law. Based on these strategies in configuring the smart annular sandwich plate, the frequency responses of the overall plate are evaluated by deriving an FE model, and the control activities of the patches of the shear mode annular PFC actuator are studied. This study is further extended by adding the viscoelastic layers at the core of the smart annular sandwich plate for investigating the performance of the shear mode PFC actuator in the ACLD treatment. The following main conclusions may be drawn from the work carried out in this thesis.

1. A new cylindrically orthotropic unidirectional short (discontinuous)/continuous piezoelectric fiber composite (SPFC/CPFC) actuator is designed in the shape of a thin annular disc for active control of plane structures of revolution. The longitudinally poled short/continuous piezoelectric fibers within this SPFC/CPFC are oriented along the radial direction. The effective electro-elastic properties of this SPFC/CPFC are evaluated by developing an FE procedure, and it is observed that one effective piezoelectric coefficient (e_{11}, 1 for radial direction) appears with an indicative magnitude while other similar coefficients have negligibly small magnitudes. It is also observed that the use of short fibers (SPFC) instead of continuous fibers (CPFC) causes the lesser magnitude of e_{11}. To alleviate this issue, an analysis of the effective properties of the SPFC is carried out, and the appropriate geometrical properties of its (SPFC) microstructure are decided with an objective of the improved magnitude of the effective coefficient (e_{11}). On the basis of this effective coefficient (e_{11}), the SPFC/CPFC may be utilized as a material of extension mode piezoelectric actuator in the cylindrical

coordinate frame provided that an external electric field is to be supplied along the radial direction. In order to supply this electric field for the use of the SPFC/CPFC as a distributed actuator, an arrangement of surface-electrodes over the top and bottom surfaces of the annular smart composite disc is presented. This arrangement of surface-electrodes is proposed in such a manner that several SPFC/CPFC discs may be used in a laminate form for achieving sufficient actuation force in a structural application.

2. The control capability of the cylindrically orthotropic SPFC/CPFC actuator is substantiated through the evaluation of frequency responses of an annular plate integrated with four identical patches of the same (SPFC/CPFC) actuator. The patches of the SPFC/CPFC actuator are activated according to the negative velocity feedback control strategy so as to achieve smart damping in the overall smart annular plate. A closed-loop FE model of the overall smart annular plate is developed in order to evaluate its (overall plate) controlled frequency responses. These responses exhibit indicative performance of both the actuators (SPFC/CPFC) in inducing smart damping within the overall plate. It is observed that the control power of the SPFC actuator is a little more than that of the CPFC actuator although the magnitude of the concerned coefficient (e_{11}) for SPFC is lesser than that for CPFC. Additionally, the cylindrically orthotropic SPFC possesses the advantages of greater flexibility and conformability. So, the present SPFC actuator may be a potential extension mode piezoelectric actuator in control of vibration of plane structures of revolution.

3. Four kinds of cylindrically orthotropic extension mode CPFC actuators are addressed for active control of vibration of plane structures of revolution, and a comparative study on their control capabilities is performed to identify the potential ones in control of vibration of simply-supported/fully clamped annular plate. These CPFC actuators are designated in abbreviated forms of LCR, LCC, TCR and TCC according to their constructional features where the first, second and third letters indicate poling direction of fibers (longitudinal (L) or transverse (T)), continuous fibers (C) and fiber-reinforcement (radial (R)/circumferential(C)), respectively. All these CPFC actuators are taken with the identical thickness, constituent materials and fiber volume faction. With

these identical material and geometrical properties, the patches of every CPFC actuator are optimally configured over the top surface of a simply-supported/fully clamped annular plate, and the capabilities of the CPFC actuators in inducing active damping in the smart annular plate are quantified by supplying uniform magnitude of external electric field (for all the CPFC actuators). This result reveals indicative control-capabilities of LCR and TCR actuators.

4. A novel numerical methodology is proposed for optimal size and locations of the patches of extension mode piezoelectric actuator over the surface of an annular plate. This methodology can be utilized for efficient attenuation of symmetric/asymmetric bending modes of vibration of an annular plate in conjunction with the FE procedure.
5. A new PFC actuator is designed in the cylindrical coordinates for shear mode piezoelectric actuation of plane structures of revolution. The effective electro-elastic properties of this shear mode annular PFC actuator vary in the radial direction due to the use of conventional piezoelectric fibers in its (PFC) cylindrically periodic microstructure. These varying effective properties are theoretically evaluated by developing an FE procedure, and also by deriving the corresponding closed-form expressions using UFM. From these results, it is observed that the main piezoelectric coefficient (e_{35}) (for the shear mode actuation) has an indicative magnitude at the inner radius of the annular PFC actuator. But, the magnitude of this coefficient (e_{35}) decreases at a significant rate as the radius increases. So, the overall radial span of interest is divided into four equal divisions, and the annular PFC actuator is redesigned for every radial division with a small radial length. The corresponding results reveal improved magnitude of the main piezoelectric coefficient (e_{35}) at any radius within the radial span of interest. Thus, this actuator may be a promising shear mode PFC actuator for active control of plane structures of revolution provided that it is to be designed with the appropriate radial dimensions.
6. The study on the performance of the new shear mode annular PFC actuator in control of vibration of an annular plate reveals its indicative control

capability. It is found that the control capability of the present shear mode PFC actuator is more than that of the conventional monolithic shear mode piezoelectric (PZT5H) actuator. Additionally, the present shear mode PFC actuator possesses greater flexibility and conformability. So, it may be a potential shear mode piezoelectric actuator in control of plane structures of revolution.

7. A fruitful strategy in deciding the in-plane dimensions of the patches of the shear mode annular PFC actuator is proposed for having the equal attenuation of all the modes of vibration of an annular plate within a range of the operating frequency. Every patch of the shear mode PFC actuator is supposed to counteract the mechanically induced transverse shear stress around its location by taking the feedback of local velocity. In this use of the velocity feedback control law for the shear mode PFC actuator, a new strategy is proposed to utilize all the patches effectively for control of any mode of vibration of the overall annular plate.

8. The active-passive damping characteristics of a smart annular sandwich plate are studied using the shear mode annular PFC actuator. A piezo-foam layer is made by embedding the patches of the shear mode PFC actuator within a foam layer. This piezo-foam layer is utilized along with the viscoelastic layers in two different stacking sequences. In the first one, a viscoelastic layer is sandwiched between two piezo-foam layers (CONFIG#1). Conversely, a piezo-foam layer is sandwiched between two viscoelastic layers (CONFIG#2). Every patch of the shear mode PFC actuator is considered to be activated with the feedback of its own transverse velocity, and the corresponding forced frequency responses of the overall annular plate are evaluated by developing an FE model based on the layer-wise shear deformation theory. These results exhibit a significant improvement of the damping in the plate for the use of viscoelastic layers along with the shear mode annular PFC actuator. But the thickness of the viscoelastic layer is an important parameter for efficient utilization of the annular PFC actuator. It is observed that the active-passive damping in the smart annular sandwich plate increases when it is made with its first configuration (CONFIG#1) instead of its second configuration (CONFIG#2). It is also found that the

performance of the shear mode PFC actuator for inducing the active-passive damping in the annular sandwich plate is a little lesser than that in case of the use of a conventional monolithic shear piezoelectric actuator (PZT5H) in the same manner.

8.2 Scope for future work

Although the objectives of this thesis have been fulfilled by the contributions presented in the preceding chapters of this dissertation, further research may still be pursued for the development of smart annular/circular plates. Some of the future works which may be readily undertaken in line with the present work are as follows.

1. Development of an extension mode PFC actuator in cylindrical coordinates using the convectional piezoelectric fibers.

2. The issue of optimizing the thickness of the viscoelastic layers for effective utilization of the shear mode annular PFC actuator.

3. Performance of the extension mode SPFC/CPFC in the active constrained damping treatment of an annular plate.

4. The experimental verifications of the theoretical models developed in this thesis are also an important scope for further research work.

References

Aboudi J 1998 Micromechanical prediction of the effective coefficients of thermo-piezoelectric multiphase composites. *Journal of Intelligent Material Systems and Structures* **9** 713-22

Aboudi J, Arnold S M, Bednarcyk B A 2013 *Micromechanics of Composite Materials* (New York: Academic Press)

Agrawal B N and Treanor K E 1999 Shape control of a beam using piezoelectric actuators. *Smart Materials and .Structures* **8** 729-40

Aldraihem O J and Khdeir A A 2000 Smart beams with extension and thickness-shear piezoelectric actuators. *Smart Materials and Structures* **9** 1-9

Aldraihem O J and Wetherhold R C 1997 Mechanics and control of coupled bending and twisting vibration of laminated beams. *Smart Materials and Structures* **6** 123-33

Alibeigloo A 2017 Thermo elasticity solution of functionally graded, solid, circular, and annular plates integrated with piezoelectric layers using the differential quadrature method. *Mechanics of Advanced Materials and Structures*, DOI: 10.1080/15376494.2017.1308585

Amabili M 2008 *Nonlinear vibrations and stability of shells and plates*. (Cambridge University Press: New York)

Arafa M and Baz A 2000a Dynamics of active piezoelectric damping composites. *Composites Part B: Engineering* **3** 255-64

Arafa M and Baz A 2000b Energy dissipation characteristics of active piezoelectric damping composites. Composites Science and Technology **60** 2759-68

Araújo A L et al. 2016 Vibration analysis of laminated soft core sandwich plates with piezoelectric sensors and actuators. *Composite Structures* **151** 91-8

Aravinda Kumar M S, Panda S and Chakraborty D 2015 Harmonically excited nonlinear vibration of heated functionally graded plates integrated with piezoelectric composite actuator. *Journal of Intelligent Material Systems and Structures* **26** 931-51

Aravinda Kumar M S, Panda S and Chakraborty D 2016 Piezo-vioscoelastically damped nonlinear frequency response of functionally graded plates with a heated plate surface. *Journal of Vibration and Control* **22** 320-43

Azvine B, Tomlinson G R and Wynne R J 1995 Use of active constrained-layer damping for controlling resonant vibration. *Smart Materials and Structures* **4** 1-6

Azzouz M S, Mei C, Bevan J S and Ro J J 2001 Finite element modeling of MFC/AFC actuators and performance of MFC. *Journal of Intelligent Material Systems and Structures* **12** 601–12

Bailey T and Hubbard J E 1985 Distributed piezoelectric-polymer active vibration control of a cantilever beam. *Journal of Guidance, Control, and Dynamics* **8** 605–11

Baillargeon B P and Vel S S 2005a Exact solution for the vibration and active damping of composite plates with piezoelectric shear actuators. *Journal of Sound and Vibration* **282** 781-804

Baillargeon B P and Vel S S 2005b Active vibration suppression of sandwich beams using piezoelectric shear actuators: experiments and numerical simulations. *Journal of Intelligent Material Systems and Structures* **16** 517-30

Balamurugan V and Narayanan S 2001 Shell finite element for smart piezoelectric composite plate/shell structures and its application to the study of active vibration control. *Finite Elements in Analysis and Design* **37** 713-38

Balamurugan V and Narayanan S 2002 Finite element formulation and active vibration control study on beams using smart constrained layer damping (SCLD) treatment. Journal of Sound and Vibration **249** 227-50

Balamurugan V, Manikandan B and Narayanan S 2007 A higher order finite element modeling of piezolaminated smart composite plates and its application to active vibration control. *International Journal of Computational Methods* **4** 141-62

Bambill D V, La Malfa S, Rossit C A and Laura P A A 2004 Analytical and experimental investigation on transverse vibrations of solid, circular and annular plates carrying a concentrated mass at an arbitrary position with marine applications. *Ocean Engineering* **31** 127-38

Barkanov E, Gluhih S and Kovalov A 2008 Optimal design of the active twist for helicopter rotor blades with C-spar. *Mechanics of Advanced Materials and Structures* **15** 325-34

Batra R C and Geng T S 2002 Comparison of active constrained layer damping by using extension and shear mode piezoceramic actuators. *Journal of Intelligent Material Systems and Structures* **13** 349-67

Batra R C, Liang X Q and Yang J S 1996 The vibration of simply supported rectangular elastic plate due to piezoelectric actuators. *International Journal of Solids and Structures* **33** 1597-618

Baz A 1997 Optimization of energy dissipation characteristics of active constrained layer damping. *Smart Materials and Structures* **6** 360-68

Baz A and Chen T 2000 Control of axi-symmetric vibrations of cylindrical shells using active constrained layer damping. *Thin-Walled Structures* **36** 1-20

Baz A and Poh S 1988 Performance of an active control system with piezoelectric actuators. *Journal of Sound and Vibration* **126** 327-43

Baz A and Poh S 1990 Experimental implementation of the modified independent modal space control method. *Journal of Sound and Vibration* **139** 133-49

Baz A and Ro J 1993 Partial treatment of flexible beams with active constrained layer damping. *ASME Applied Mechanics Division-Publications-AMD* **167** 61-80

Baz A and Ro J 1995 Optimum design and control of active constrained layer damping. *Transactions-ASME Journal of Mechanical Design* **117** 135-44

Baz A and Ro J 1996 Vibration control of plates with active constrained layer damping. *Smart Materials and Structures* **5** 272-80

Baz A and Tempia A 2004 Active piezoelectric damping composites. Sensors and Actuators A: Physical **112** 340–50

Benjeddou A and Al-Ajmi M 2011 Analytical Homogenizations of piezo-ceramic shear macro-fiber composites *Proc. IUTAM Symposium on Multiscale Modelling of Fatigue, Damage and Fracture in Smart Materials Systems* ed M Kuna and A Ricoeur (Dordrecht: Springer) 229-42

Benjeddou A and Deu D F 2001b Piezoelectric Transverse Shear Actuation and Sensing of Plates, Part -2: Application and Analysis. *Journal of Intelligent Material Systems and Structures* **12** 451-67

Benjeddou A and Deu J F 2001a Piezoelectric transverse shear actuation and sensing of plates, Part 1: A three-dimensional mixed state space formulation. *Journal of Intelligent Material Systems and Structures* **12** 435-49

Benjeddou A, Trindade M A and Ohayon R 1997 A Unified Beam Finite Element Model For Extension and Shear Piezoelectric Actuation Mechanisms *Journal of Intelligent Material Systems and Structures* **8** 1012-25

Bent A A 1999 Active fiber composite material systems for structural control applications. *Proc. SPIE 3674, Smart Structures and Materials 1999: Industrial and Commercial Applications of Smart Structures Technologies* **166** (July, 1999)

Bent A A and Hagood N W 1997 Piezoelectric fiber composites with interdigitated electrodes. *Journal of Intelligent Material Systems and Structures* **8** 903–19

Benveniste Y 1993 Universal relations in piezoelectric composites with eigenstress and polarization fields, Part I: Binary media-Local fields and effective behavior. *Transactions-ASME Journal of Applied Mechanics* **60** 265-69

Benveniste Y 1994 On the micromechanics of fibrous piezoelectric composites. *Mechanics of materials* **18** 183-93

Benveniste Y and Dvorak G J 1992 Uniform fields and universal relations in piezoelectric composites. *Journal of Mechanics and Physics of Solids* **40** 1295–312

Berger H et al. 2005b An analytical and numerical approach for calculating effective material co-efficients of piezoelectric fiber composites. *International Journal of Solids and Structures* **42** 5692–714

Berger H et al. 2006 Unit cell models of piezoelectric fiber composites for numerical and analytical calculation of effective properties. *Smart Materials and Structures* **15** 451-68

Berger H et al. 2010 A numerical homogeniztzation technique for piezoelectric composites with arbitrary fiber distribution. *11th Pan-American Congress of Applied Mechanics* January 04-08, Foz do Iguaçu, PR, Brazil.

Berger H, et al. 2005a Calculation of effective coefficients for piezoelectric fiber composites based on a general numerical homogenization technique. *Composite Structures* **71** 397–400

Berger H, Kari S, Gabbert U, Rodríguez-Ramos R, Bravo-Castillero J, and Guinovart-Díaz R 2005c A comprehensive numerical homogenisation technique for calculating effective coefficients of uniaxial piezoelectric fibre composites. *Materials Science and Engineering A* **412** 53–60

Bilgen O, et al. 2011 Macro-fiber composite actuators for flow control of a variable camber airfoil. *Journal of Intelligent Material Systems and Structures* **22** 81-91

Bilgen O, Kochersberger K B, Inman D J and Ohanian O J 2010 Macro-fiber composite actuated simply supported thin airfoils. *Smart Materials and Structures* **19** 055010

Bing J, Fang D and Hwang K 1997b The effective properties of piezocomposites, Part II: The effective electro-elastic moduli. *Acta Mechanica Sinica* **13** 347-54

Bowen C R and Kara H 2002 Pore anisotropy in 3–3 piezoelectric composites. *Materials Chemistry and Physics* **75** 45–9

Bowen C R, Perry A, Kara H and Mahon S W 2001 Analytical modelling of 3–3 piezoelectric composites. *Journal of European Ceramic Society* **21** 1463–67

Brenner R, Bravo-Castillero J and Mesejo Léon D 2012 Investigation of the effective response of 2-1-2 piezoelectric composites. *Procedia IUTAM* **3** 292-300

Brischetto S and Carrera E 2012 Coupled thermo-electro-mechanical analysis of smart plates embedding composite and piezoelectric layers. *Journal of Thermal Stresses* **35** 766–804

Brockmann T H and Lammering R 2006 Beam finite elements for rotating piezoelectric fiber composite structures. *Journal of Intelligent Material Systems and Structures* **17** 431-48

Bruant I, Coffignal G, Lene F and Verge M 2001 Active control of beam structures with piezoelectric actuators and sensors: modeling and simulation. *Smart Materials and Structures* **10** 404–8

Buffum D and Fleeter S 1986 Aerodynamic performance of an annular flat plate airfoil cascade with nonuniform inlet velocity. *AIAA journal* **24** 270-77

Burke S E and Hubbard J E 1987 Active vibration control of a simply supported beam using spatially distributed actuator. *IEEE Control Systems Magazine* **3** 25–30

Cady W G 1946 *Piezoelectricity* (McGraw-Hill: New York)

Cao L, Mantell S and Polla D 2001 Design and simulation of an implantable medical drug delivery system using microelectromechanical systems technology. *Sensors and Actuators A: Physical* **94** 117-25

Cesnik C E and Shin S 2001 On the modeling of integrally actuated helicopter blades. *International Journal of Solids and Structures* **38** 1765–1789

Cha Y, Abdolhamidi S and Porfiri M 2015 Energy harvesting from underwater vibration of an annular ionic polymer metal composite. *Meccanica* **50** 2675-90

Chakraverty S, Bhat R B and Stiharu I 2001 Free vibration of annular elliptic plates using boundary characteristic orthogonal polynomials as shape functions in the Rayleigh-Ritz method. *Journal of Sound and Vibration* **241** 521-39

Challagulla K S and Venkatesh T A 2009 Electromechanical response of 2-2 layered piezoelectric composites: A micromechanical model based on the asymptotic homogenization method. *Philosophical Magazine* **89** 1197-222

Chambion B et al. 2011 Optimization of the piezoelectric response of 0–3 composites: a modeling approach. *Smart Materials and Structures* **20** 115006

(8pp)

Chan H L W and Unsworth J 1989 Simple model for piezoelectric ceramic/polymer 1-3 composites used in ultrasonic transducer applications. IEEE Transactions on Ultrasonics, Ferroelectrics and Frequency Control **36** 434-41

Chandrashekhara K and Tenneti R 1995 Thermally induced vibration suppression of laminated plates with piezoelectric sensors and actuators. *Smart Materials and Structures* **4** 281-90

Chang-Qing C, Xiao-Ming W and Ya-Peng S 1996 Finite element approach of vibration control using self-sensing piezoelectric actuators. *Computers and Structures* **60** 505-12

Chantalakhana C and Stanway R 2000 Active constrained layer damping of plate vibrations: a numerical and experimental study of modal controllers. *Smart Materials and Structures* **9** 940-52

Chattopadhyay A and Seeley C E 1994 Multiobjective design procedure for control of structures using piezoelectric materials. *Journal of Intelligent Material Systems and Structures* **5** 403-41

Chattopadhyay A, Gu H, Beri R and Nam C 2001 Modeling segmented active constrained layer damping using hybrid displacement field. *AIAA Journal* **39** 480-86

Chattopadhyay A, Kim J S and Liu Q 2002 Aeromechanical stability analysis and control of smart composite rotor blades. Journal of Sound and Vibration **8** 847-60

Chaudhry Z and Rogers C 1995 Actuators for smart structures. *Fiber optic smart structures(A 95-34976 09-39), New York, NY, John Wiley & Sons, Inc. (Wiley Series in Pure and Applied Optics)* 497-536

Chee C Y K 2000 Static shape control of laminated composite plate smart structure using piezoelectric actuators. PhD thesis, The University of Sydney

Chee C Y K, Tong L and Steven G P 1999 A mixed model for composite beams with piezoelectric actuators and sensors. *Smart Materials and Structures* **8** 417–32

Chen T 1996 Effective properties of platelet reinforced piezocomposites. *Composites Part B: Engineering* **27** 467-74

Chen T and Baz A 1996 Performance characteristics of active constrained layer damping versus passive constrained layer damping with active control. *Smart Structures and Materials* 256-268 (May 31)

Chia C Y 1980 *Non-linear Analysis of Plates.* (McGraw-Hill: New York)

Choi S C, Park J S and Kim J H 2006 Active damping of rotating composite thin walled beams using MFC actuators and PVDF sensors. *Composite Structures* **76** 362-74

Choi S C, Park J S and Kim J H 2007 Vibration control of pre-twisted rotating composite thin-walled beams with piezoelectric fiber composites. *Journal of Sound and Vibration* **300** 176-96

Clauser H R 1968 Modern materials concepts make structure key to progress. *Materials Engineering* **68** 38–42

Clauser H R 1975 From static to dynamic materials in design. ASME Journal of *Mechanical Engineering* **97** 20–6

Cook A C and Vel S S 2012 Multiscale analysis of laminated plates with integrated piezoelectric fiber composite actuators. *Composite Structures* **94** 322-36

Cook R D, Malkus D S, Plesha M E, Witt R J 2001 *Concepts and Applications of Finite Element Analysis* (Wiley: New York)

Cotoni V, Masson P and Cĉté F 2006 A finite element for piezoelectric multilayered Plates: Combined higher-order and piecewise linear C° formulation. *Journal of Intelligent Material Systems and Structures* **17** 155-66

Crawley E F and Lazarus K B 1991 Induced Strain Actuation of Isotropic and Anisotropic Plates. *AIAA Journal* **29** 944-51

Crawley E F and Luis J D 1987 Use of piezoelectric actuators as elements of intelligent structures. *AIAA Journal* **25** 1373–85

Crawley E F, Luis J De, Hagood N W and Anderson E H F 1988 Development of piezoelectric technology for applications in control of intelligent structures. *Proceedings of the American Control Conference*, Atlanta, USA 1890–96

Dano M L and Julliere B 2007 Active control of thermally induced distortion in composite structures using macro fiber composite actuators. *Smart Materials and .Structures* **16** 2315-22

Dash P and Singh B N 2009 Nonlinear free vibration of piezoelectric laminated composite plate. *Finite Elements in Analysis and Design* **45** 686-94

Della C N and D Shu 2008 The performance of 1-3 piezoelectric composites with a porous non-piezoelectric matrix. *Acta Materialia* **56** 754–61

Della C N and Shu D 2007 On the performance of 1–3 piezoelectric composites with a passive and active matrix. *Sensors and Actuators A: Physical* **140** 200-6

Deraemaeker A and Nasser H 2010 Numerical evaluation of the equivalent properties of Macro Fiber Composite (MFC) transducers using periodic homogenization. *International Journal of Solids and Structures* **47** 3272–85

Deraemaeker A, Benelechi S, Benjeddou A and Preumont A 2007 Analytical and numerical computation of homogenized properties of MFCs : Application to a composite boom with MFC actuators and sensors. *Proc. III ECCOMAS Thematic Conference on Smart Structures and Materials* Gdansk Poland July

Deraemaeker A, Nasser H, Benjeddou A and Preumont A 2009 Mixing rules for the piezoelectric properties of macro fiber composites. *Journal of Intelligent Material Systems and Structures* **20** 1475 -82

Djojodihardjo H, Jafari M, Wiriadidjaja S and Ahmad K A 2015 Active vibration suppression of an elastic piezoelectric sensor and actuator fitted cantilevered beam configurations as a generic smart composite structure. *Composite Structures* **132** 848-63

Dong S, Uchino K, Li L and Viehland D 2007 Analytical solutions for the transverse deflection of a piezoelectric circular axisymmetric unimorph actuator. *IEEE Transactions of Ultrasonics and Ferroelectrics and Frequency control* **54** 1240-48

Dongyu X, Peng D, Jingxiao W, Pengkun H, Shifeng H and Xin C 2016 Design and properties of Gaussian-type 1–3 piezoelectric composites. *Composite Structures*, Volume **140** 213-16

Dongyu X, Xin C Hongda G, Fan L and Shifeng H 2015 Design, fabrication and properties of 1-3 piezoelectric ceramic composites with varied piezoelectric phase distribution *Ceramics International* **41** 9433-42

Dube G P, Kapuria S and Dumir P C 1996a Exact piezothermoelastic solution of simply-supported circular cylindrical panel in cylindrical bending. *Archive of Applied Mechanics* **66** 537-54

Dube G P, Kapuria S and Dumir P C 1996b Exact piezothermoelastic solution of simply-supported orthotropic flat panel in cylindrical bending. *International Journal of Mechanical Sciences* **38** 1161-77

Dunn M L and Taya M 1993 Micromechanics predictions of the effective electroelastic moduli of piezoelectric composites. *International Journal of Solids and Structures* **30** 161–75

Ebrahimi F and Rastgoo A 2008 Free vibration analysis of smart annular FGM plates integrated with piezoelectric layers. *Smart Materials and Structures* **17** 015044 (13pp)

Ebrahimi F, Rastgoo A and Atai A A 2009 A theoretical analysis of smart moderately thick shear deformable annular functionally graded plate. *European Journal of Mechanics-A/Solids* **28** 962-73

Elshafei M A and Alraiess F 2013 Modeling and analysis of smart piezoelectric beams using simple higher order shear deformation theory. *Smart Materials and .Structures* **22** 035006

Erturk A and Inman D J 2011 *Piezoelectric energy harvesting* (Wiley: New York)

Eynbeygui M and Aghdam M M 2015 A micro-mechanical study on the electro-elastic behavior of piezoelectric fiber-reinforced composites using the element-free Galerkin method *Acta Mechanica* **226** 3177-94

Fakri N, Azrar L and El Bakkali L 2003 Electroelastic behavior modeling of piezoelectric composite materials containing spatially oriented reinforcements. *International Journal of Solids and Structures* **40** 361-84

Fallah N and Ebrahimnejad M 2014 Finite volume analysis of adaptive beams with piezoelectric sensors and actuators. *Applied Mathematical Modeling* **38** 722-37

Forward R L 1981 Electronic damping of orthogonal bending modes in a cylindrical mast experiment. *Journal of Spacecraft and Rockets* **18** 11–17

Fox C H J, Chen X and McWilliam S 2007 Analysis of the deflection of a circular plate with an annular piezoelectric actuator. *Sensors and Actuators A: Physical* **133** 180-94

Fu P, Liu H and Chu X 2017 An efficient multiscale computational formulation for geometric nonlinear analysis of heterogeneous piezoelectric composite. *Composite Structures* **167** 191-206

Furukawa T 1989 Piezoelectricity and pyroelectricity in polymers. *IEEE Transactions of Electrical Insulation* **24** 375–95

Gabbert U and Schulz I 1996 Optimal placement of piezoelectric actuators in vibration control of adaptive structures. *Proceedings of ASME International Mechanical Engineering Congress and Exposition* **DE 93** 271-77

Gamble L L and Inman D J 2017 Yaw Control of a Smart Morphing Tailless Aircraft Concept. In *Advances in Science and Technology* **101** 127-32 Trans Tech Publications.

Ganapathi M, Patel B P and Touratier M 2004 A C1 finite element for flexural and torsional analysis of rectangular piezoelectric laminated/sandwich composite beams. *International Journal for Numerical Methods in Engineering* **61** 584-610

Gandhi F and Munsky B E 2000 Comparison of the mechanism and effectiveness of position and velocity feedback in active constrained-layer damping treatments. In *Proceedings of the SPIE The International Society for Optical Engineering* **3989** 61-72 April

Gao J X and Liao W H 2005 Vibration analysis of simply supported beams with enhanced self-sensing active constrained layer damping treatments. *Journal of Sound and Vibration* **280** 329-57

Gentilman R L et al. 1994 Fabrication and properties of 1-3 PZT-polymer composites. *No. CONF-931142 - American Ceramic Society* Westerville, OH (United States)

Ghasemi-Nejhad M N, Pourjalali S, Uyema M and Yousefpour A 2006 Finite element method for active vibration suppression of smart composite structures using piezoelectric materials. *Journal of Thermoplastic Composite Materials* **19** 309-52

Ghoneim H 1993 Electromechanical surface damping using constrained layer and shunted piezoelectric. *North American Conference on Smart Structures and Materials*. *International Society for Optics and Photonics* 1993.

Ghoneim H 1996 Application of the electromechanical surface damping to the vibration control of a cantilever plate. *Transactions of ASME Journal of Vibration and Acoustics* **118** 551-57

Giannopoulos G and Vantomme J 2005 A fully thermoelectromechanically coupled FE analysis for the dynamic behavior of smart plates using discrete-layer kinematics. *Proceedings of SPIE-The International Society for Optical Engineering* **5757** 420-31

Glushanin S V and Topolov V Y 2003 Predicting the piezoelectric response of novel anisotropic 1–2 type composites. *Technical Physics Letters* **29** 316-19

Gopinath T, Raja S and Ikeda T 2011a Active Flutter control of Composite Plate with Embedded and Surface Bonded Piezoelectric Composites *Active and Passive Smart Structures and Integrated Systems,* (*Proc. of SPIE*) ed M N Ghasemi-Nejhad (San Diego, California USA, March 6, 2011) **7797** 1-10

Gopinath T, Raja S and Ikeda T 2011b Finite element formulation of laminated plate with flexible piezoelectric actuators and vibration control analysis. In *SPIE Smart Structures and Materials+ Nondestructive Evaluation and Health Monitoring* (**797707** 01 - 10) International Society for Optics and Photonics.

Gopinathan M and Pajunen G A 1995 Model reference control of vibrations in flexible smart structures. *Proceedings of IEEE Conference on Decision and Control* **4** 3551-56

Görnandt A and Gabbert U 2002 Finite element analysis of thermopiezoelectric smart structures *Acta Mechanica* **154** 129-40

Guennam A E and Luccioni B M 2006 FE modeling of a closed box beam with piezoelectric fiber composite patches. *Smart Materials and Structures* **15** 1605-15

Guo X, et al. 2017 Nonlinear Dynamic Analysis of Macrofiber Composites Laminated Shells. *Advances in Materials Science and Engineering* **2017 Article ID: 4073591 17 pp**.

Gupta S S, Patel B P, Ganapathi M, Umapathy M and Bhave S Y 1996 Non-linear dynamic analysis of laminated pates/shells with piezoelectric sensors and actuators. In *Proceedings of SPIE's symposium on Smart Materials, Structures and MEMS* (pp. 11-14).

Gupta V, Sharma M, Thakur N and Singh S P 2011 Active vibration control of a smart plate using a piezoelectric sensor–actuator pair at elevated temperatures. *Smart Materials and .Structures* **20** 105023 (13pp)

Hagood N W and Flotow V A 1991 Damping of structural vibrations with piezoelectric materials and passive electrical networks. *Journal of Sound and Vibration* **146** 243-68

Hanagud S, Obal M W and Calise A J 1992 Optimal vibration control by the use of piezoceramic sensors and actuators. *Journal of Guidance, Control and Dynamics* **15** 1199- 206

Hasin Z 1965 Viscoelastic behavior of heterogeneous media. *Journal of Applied Mechanics* **32** 630-36

Hasin Z 1970 Complex moduli of viscoelastic composites-I, general theory and application to particulate composites. *International Journal of Solids and Structures* **6** 539-52

He L-H 1998 Axisymmetric response of circular plates with piezoelectric layers: an exact solution. *International Journal of Mechanical Sciences* **40** 1265-79

Herdic P C et al. 2005 The vibro-acoustic response and analysis of a full-scale aircraft fuselage section for interior noise reduction. *The Journal of the Acoustical Society of America* **117** 3667-78

Heyliger P and Saravanos D A 1995 Exact free-vibration analysis of laminated plates with embedded piezoelectric layers. *The Journal of the Acoustical Society of America* **98** 1547-57

High J W and Wilkie W K 2003 Method of fabricating NASA-standard macro-fiber composite piezoelectric actuators. *In: National Aeronautics and Space Administration*, Langley Research Center.

Ho C H, Poon Y M and Shin F G 2006 New explicit formulas for the effective piezoelectric coefficients of binary 0-3 composites. *Journal of Electroceramics* **16** 283-88

Huang J H and Kuo W S 1996 Micromechanics determination of the effective properties of piezoelectric composites containing spatially oriented short fibers. Acta Materialia **44** 4889-98

Hwang W C and Park H C 1993 Finite element modeling of piezoelectric sensors and actuators. *AIAA Journal* **31** 930-37

Hwang W S, Hwang W and Park HC 1993 Integration of composite structural design with the intelligent system concept. *A1AA/ASME/ASCE/AHS/ASC 34th Structures. Structural Dynamics and Materials Conference La*Jolla CA, 3534-39

Im S and Atluri S N 1989 Effects of a piezoactuator on a finitely deformed beam subjected to general loading. *AIAA Journal* **27** 1801-07

Iyer S and Venkatesh T A 2014 Electromechanical response of (3–0, 3–1) particulate, fibrous, and porous piezoelectric composites with anisotropic constituents: A model based on the homogenization method. *International Journal of Solids and Structures* **51** 1221-34

Jalili N 2010 *Piezoelectric-Based Systems Modeling.* (Piezoelectric-Based Vibration Control) Springer US 183-232

Jayendiran R and Arockiarajan A 2013 Non-linear electromechanical response of 1-3 type piezocomposites. *International Journal of Solids and Structures* **50** 2259-70

Jiang B, Fang D and Hwang K A 1999 Unified model for piezocomposites with non-piezoelectric matrix and piezoelectric ellipsoidal inclusions. *International Journal of Solids and Structures* **36** 2707-33

Jiang C P, Tong Z H and Cheung Y K 2001 A generalized self-consistent method for piezoelectric fiber reinforced composites under antiplane shear. *Mechanics of Materials* **33** 295-308

Jiang J P and Li D X 2008 Finite element formulations for thermopiezoelastic laminated composite plates. *Smart Materials and .Structures* **17** 015027 (13pp)

Kalamkarov A L and Savi M A 2012 Micromechanical modeling and effective properties of the smart grid reinforced composites. *Journal of Brazilian Society of Mechanical Science and Engineering* **XXXIV** 343-51

Kapuria S and Hagedorn P 2007 Unified efficient layerwise theory for smart beams with segmented extension/shear mode, piezoelectric actuators and sensors. *Journal of Mechanics of Materials and Structures* **2** 1267–98

Kapuria S and Yasin M Y 2010 Active vibration control of piezoelectric laminated beams with electroded actuators and sensors using an efficient finite element involving an electric node. *Smart Materials and .Structures* **19** 045019 (15pp)

Kapuria S and Yasin M Y 2013 Active vibration control of smart plates using directional actuation and sensing capability of piezoelectric composites. *Acta Mechanica* **224** 1185-99

Kar-Gupta R and Venkatesh T A 2005 Electromechanical response of 1-3 piezoelectric composites: Effect of poling characteristics. *Journal of Applied Physics* **98** 054102

Kar-Gupta R and Venkatesh T A 2007a Electromechanical response of 1–3 piezoelectric composites: A numerical model to assess the effects of fiber distribution. *Acta Materialia* **55** 1275-92

Kar-Gupta R and Venkatesh T A 2007b Electromechanical response of 1–3 piezoelectric composites: an analytical model. *Acta Materialia* **55** 1093-108

Kar-Gupta R and Venkatesh T A 2008 Electromechanical response of piezoelectric composites: Effects of geometric connectivity and grain size. *Acta Materialia* **56** 3810-23

Kar-Gupta R and Venkatesh T A 2013 Electromechanical response of 2–2 layered piezoelectric composites. *Smart Materials and Structures* **22** 025035

Kari S, Berger H, Rodriguez-Ramos R and Gabbert U 2007 Numerical evaluation of effective material properties of transversely randomly distributed unidirectional piezoelectric fiber composites. *Journal of Intelligent Material Systems and Structures* **18** 361-72

Kim H S, Sohn J W and Choi S B 2011 Vibration control of a cylindrical shell structure using macro fiber composite actuators. *Mechanics Based Design of Structural Machines* **39** 491–506

Kim J, Varadan V V, Varadan V K and Bao X Q 1996 Finite element modeling of a smart cantilever plate and comparison with experiments. *Smart Materials and .Structures* **5** 165-70

Kim S J and Jones J D 1995 Influence of piezo-actuator thickness on the active vibration control of a cantilever beam. *Journal of Intelligent Material Systems and Structures 6* 610-23

Kim Y H and Ha S K 2003 Analysis of a disk-type stator for the piezoelectric ultrasonic motor using impedance matrix. *Journal of Sound and Vibration* **263** 643-63

Ko S H, Park C H, Park H C and Hwang W 2004 Vibration control of an arc type shell using active constrained layer damping. *Smart Materials and Structures* **13** 350-54

Kovalovs A, Barkanov E and Gluhihs S 2007 Active control of structures using macro-fiber composite (MFC). *Journal of Physics: Conference Series* **93** 012034

Kranz B, Benjeddou A and Drossel W G 2013a Enthalpy-based homogenization procedure for composite piezoelectric modules with integrated electrodes *Smart Structures and Systems* **12** 579-94

Kranz B, Benjeddou A and Drossel W G 2013b Numerical and experimental characterizations of longitudinally polarized piezoelectric d15 shear macro-fiber composites. *Acta Mechanica* **224** 2471–87

Kumar A S P, Panda S and Reddy N H 2015 Smart damping of vibration of annular plates by the design of a cylindrically orthotropic piezoelectric fiber-reinforced composite actuator. *Acta Mechanica* **226** 3151-76

Kumar A S P, Panda S and Reddy N H 2017 A comparative study on the smart damping capabilities of cylindrically orthotropic piezoelectric fiber-reinforced composite actuators in vibration control of simply supported/fully clamped isotropic annular plate. *Journal of Intelligent Material Systems and Structures* **28** 1839-59

Kumar N and Singh S P 2009 Vibration and damping characteristics of beams with active constrained layer treatments under parametric variations. *Materials and Design* **30** 4162-74

Kumar N and Singh S P 2012 Vibration control of curved panel using smart damping. *Mechanical Systems and Signal Processing* **30** 232-47

Kumar R 2013 Effective active vibration control of single link flexible manipulator with modified positive position feedback control in the presence of instrumentation phase lead/lag. *Journal of Vibration and Control* **19** 1538-60

Kumar S, Srivastava R and Srivastava R K 2014 Active vibration control of smart piezo cantilever beam using PID controller. *International Journal of Research in Engineering and Technology* **3** 392-99

Kumari P, Nath J K, Dumir P C and Kapuria S 2007 2D Exact solutions for flat hybrid piezoelectric and magnetoelastic angle-ply panels under harmonic load. *Smart Materials and Structures* **16** 1651-61

Kundalwal S I and Ray M C 2016 Smart damping of fuzzy fiber reinforced composite plates using 1-3 piezoelectric composites. *Journal of Vibration and Control* **22** 1526-46

Kuo W S and Huang J H 1997 On the effective electroelastic properties of piezoelectric composites containing spatially oriented inclusions. *International Journal of Solids and Structures* **34** 2445-61

Kwak M K, Heo S and Jeong M 2009 Dynamic modelling and active vibration controller design for a cylindrical shell equipped with piezoelectric sensors and actuators. *Journal of Sound and Vibration* **321** 510–24

Kwak S K, Washington G and Yedavalli R K 1999 Active and passive vibration control of landing gear components. In *Adaptive Structures and Materials Systems-ASME* **59** 269-75, November.

Lai Z, Zhou R C, Xue D Y, Huang J K and Mei C 1993 Suppression of nonlinear panel flutter at elevated temperature with piezoelectric actuators. *AIAA/ASME/ASCE/AHS/ASC 34th Structures, Structural Dynamics and Materials Conference* LaJolla CA **3466-72**

Lazarus K B, Crawley E F and Lin C Y 1996 Multivariable high-authority control of plate-like active structures. *Journal of Guidance Control and Dynamics* **19** 1357-63

Lee H J and Saravanos D A 1995 Layerwise analysis of piezoelectric composite structures in thermal environments. *Proceedings of ASME International Mechanical Engineering Congress and Exposition* San Fransisco CA **95-WA/AD-13**

Lee H J and Saravonos D A 2000 A mixed multi-field finite element formulation for thermopiezoelectric composite shells. *International Journal of Solids and Structures* **37** 4949-67

Lee HJ and Saravanos D A 1997 Generalized finite element formulation for smart multilayered thermal piezoelectric composite plates. *International Journal of Solids and Structures* **34** 3355-71

Li F M et al. 2008 Vibration control of beams with active constrained layer damping. *Smart Materials and Structures* **17** 065036 (9pp)

Li J and Narita Y 2013 Vibration suppression for laminated composite plates with arbitrary boundary conditions. *Mechanics of Composite Materials* **49** 519-30

Li J, Ma Z, Wang Z and Narita Y 2016 Random vibration control of laminated composite plates with piezoelectric fiber reinforced composites. *Acta Mechanica Solida Sinica* **29** 316-27

Li Y, Zheng H, Long S and Wu L 2011 Effects of the piezoelectric phase's geometric properties on effective coefficients of 1–3 piezoelectric composites. *Computational Materials Science* **50** 2135-41

Liew K M et al. 2003b Finite element piezothermoelasticity analysis and the active control of FGM plates with integrated piezoelectric sensors and actuators. *Computational Mechanics* **31** 350-58

Liew K M, He X Q and Kitipornchai S 2004 Finite element method for the feedback control of FGM shells in the frequency domain via piezoelectric sensors and actuators. *Computer Methods in Applied Mechanics and*

Engineering **193** 257-73

Liew K M, Sivashanker S, He X Q and Ng T Y 2003a The modelling and design of smart structures using functionally graded materials and piezoelectrical sensor/actuator patches. *Smart Materials and Structures* **12** 647-55.

Lim Y H, Varadan V V and Varadan V K 2002 Closed loop finite-element modeling of active constrained layer damping in the time domain analysis. *Smart Materials and Structures* **11** 89-97

Lin C H and Muliana A 2013 Micromechanics models for the effective nonlinear electro-mechanical responses of piezoelectric composites. *Acta Mechanica* **224** 1471-92

Lin C H and Muliana A 2014 Micromechanical models for the effective time-dependent and nonlinear electromechanical responses of piezoelectric composites. *Journal of Intelligent Material Systems and Structures* **25** 1306-22

Lin X, Huang S, Zhou K, and Zhang D 2016 The influence of structural parameters on the actuation performance of piezoelectric fiber composites *Materials and Design* **107** 123–9

Liu et al. 2004 Robust control of plate vibration via active constrained layer damping. *Thin-Walled Structures* **42** 427-48

Liu L, Zhang Z and Hua H 2007 Dynamic characteristics of rotating cantilever plates with active constrained layer damping treatments. *Smart Materials and Structures* **16** 1849-56

Lu F, Lin X, Geng H and Huang S 2016 Effects of fiber volume fraction on strain of piezoelectric fiber composites. *International Journal of Materials Research* **107** 573-77

Lu J, Wang P and Zhan Z 2017 Active vibration control of thin-plate structures with partial SCLD treatment. *Mechanical Systems and Signal Processing* **84** 531-50

Mahato P K and Maiti D K 2010 Aeroelastic analysis of smart composite structures in hygro-thermal environment. *Composite Structures* **92** 1027–38

Mahut T, Agbossou A and Pastor J 1998 Dynamic analysis of piezoelectric fiber composite in an active beam using homogenization and finite element methods. *Journal of Intelligent Material Systems and Structures* **9** 1009-16

Maiti D K and Sinha P K 2011 Analysis of smart laminated composites employing piezo embedded super element. *Procedia Engineering* **14** 3268–76

Malgaca L 2010 Integration of active vibration control methods with finite element models of smart laminated composite structures. *Composite Structures* **92** 1651-63

Mallik N and Ray M C 2003 Effective coefficients of piezoelectric fiber reinforced composites. *AIAA Journal* **41** 704–10

Mallik N and Ray M C 2004 Exact solutions for the analysis of piezoelectric fiber reinforced composites as distributed actuators for smart composite plates. *International Journal of Mechanics and Materials in Design* **1** 347–64

Mallik N and Ray MC 2005 Exact solutions for the analysis of piezoelectric fiber reinforced composite as distributed actuators for smart composite plates. *International Journal of Mechanics and Materials in Design* **2** 81–97

Marinaki M, Marinakis Y and Stavroulakis G E 2011 Vibration control of beams with piezoelectric sensors and actuators using particle swarm optimization. *Expert Systems with Applications* **38** 6872–83

Meirovitch L 2007 *Elements of Vibration Analysis.* (New York: McGraw-Hill)

Melnykowycz M, Kornmann X, Huber C, Barbezat M and Brunner A J 2006 Performance of integrated active fiber composites in fiber reinforced epoxy laminates. *Smart Materials and .Structures* **15** 204–12

Mi X, Qin L, Liao Q and Wang L 2017 Electromechanical coupling coefficient and acoustic impedance of 1-1-3 piezoelectric composites. *Ceramics International* **43** 9 7374-77

Miller S E and Hubbard J E 1988 Observability of a Bernoulli-Euler Beam Using PVF$_2$ as a distributed sensor. *Proceedings of 6th VPI & SU/AIAA Symposium on Dynamics and Control of Large Structures* (June 1987)

Moon S H and Kim S J 2001 Active and passive suppressions of nonlinear panel flutter using finite element method. *AIAA Journal* **39** 2042-50

Moon S H, Chwa D and Kim S J 2005 Feedback linearization control for panel flutter suppression with piezoelectric actuators. *AIAA Journal* **43** 2069-72

Narayanan S and Balamurugan V 2003 Finite element modeling of piezolaminated smart structures for active vibration control with distributed sensors and actuators. *Journal of Sound and Vibration* **262** 529-62

Nasser H, Biscani F and Belouettar S 2011 Effect of matrix properties on the overall piezoelectric constants of piezocomposite transducers. *Mechanics of Advanced Materials and Structures* **18** 531-39

Neto M A, Yu W and Roy S 2009 Two finite elements for general composite beams with piezoelectric actuators and sensors. *Finite Elements in Analysis and Design* **45** 295– 304

Nguyen C H and Kornmann X 2006 A comparison of dynamic piezoactuation of fiber-based actuators and conventional PZT patches. *Journal of Intelligent*

Material Systems and Structures **17** 45-55

Nguyen Q and Tong L 2004 Shape control of smart composite plate with non-rectangular piezoelectric actuators. *Composite Structures* **66** 207-14

Ni Q, et al. 2013 Modeling and dynamics analysis of shells of revolution by partially active constrained layer damping treatment. *Acta Mechanica Solida Sinica* **26** 468-79

Odegard G M 2004 Constitutive modeling of piezoelectric polymer pomposities. *Acta Materialia* **52** 5315–30

Padoin E, Fonseca J S O, Perondi E A and Menuzzi O 2015 Optimal placement of piezoelectric macro fiber composite patches on composite plates for vibration suppression. *Latin American Journal of Solids and Structures* **12** 925-47

Panda S 2011 Non-linear analysis of smart annular plates using cylindrically orthotropic piezoelectric fiber-reinforced composite. *Journal of Intelligent Material Systems and Structures* **22** 1789-1801

Panda S and Ray M C 2006 Nonlinear analysis of smart functionally graded plates integrated with a layer of piezoelectric fiber reinforced composite. *Smart Materials and Structures* **15** 1595-1604

Panda S and Ray M C 2008 Active constrained layer damping of geometrically nonlinear vibrations of functionally graded plates using piezoelectric fiber-reinforced composites. *Smart Materials and Structures* **025012** (15pp)

Panda S and Ray M C 2009a Active control of geometrically nonlinear vibrations of functionally graded laminated composite plates using piezoelectric fiber reinforced composites. *Journal of Sound and Vibration* **325** 186-205

Panda S and Ray M C 2009b Control of nonlinear vibrations of functionally graded plates using 1-3 piezoelectric composite. *AIAA Journal* **47** 1421-34

Panda S and Sopan G G 2013 Nonlinear analysis of smart functionally graded annular sector plates using cylindrically orthotropic piezoelectric fiber reinforced composite. *International Journal of Mechanics and Materials in Design* **9** 35–53

Panda S, Reddy N H and Pavan Kumar A S 2015 Design and finite element analysis of a short piezoelectric fiber-reinforced composite actuator. *Archive of Applied Mechanics* **85** 691-711

Pandey A and Arockiarajan A 2017a Performance studies on Macro fiber composite (MFC) under thermal condition using Kirchhoff and Mindlin plate theories. *International Journal of Mechanical Sciences* **130** 416-25

Pandey A and Arockiarajan A 2017b An experimental and theoretical fatigue study on macro fiber composite (MFC) under thermo-mechanical loadings.

European Journal of Mechanics-A/Solids **66** 26-44

Papagiannopoulos G A and Hatzigeorgiou G D 2011 On the use of the half-power bandwidth method to estimate damping in building structures. *Soil Dynamics and Earthquake Engineering* **31** 1075–79

Park C H and Baz A 1999 Vibration control of bending modes of plates using active constrained layer damping. *Journal of Sound and Vibration* **227** 711-34

Park J S and Kim J H 2004 Suppression of aero-thermal large deflections and snap-through behaviors of composite panels using macro fiber composite actuators. *Smart Materials and .Structures* **13** 1448–59

Park J S and Kim J H 2005 Analytical development of single crystal macro fiber composite actuators for active twist rotor blades. *Smart Materials and Structures* **14** 745-53

Park S, Inman D J and Yun C B 2008 An outlier analysis of MFC-based impedance sensing data for wireless structural health monitoring of railroad tracks. *Engineering Structures* **30** 2792–99

Peng X Q, Lam K Y and Liu G R 1998 Active vibration control of composite beams with piezoelectrics: A finite element model with third order theory. *Journal of Sound and Vibration* **209** 635-50

Pettermann H E and Suresh S 2000 A comprehensive unit cell model: a study of coupled effects in piezoelectric 1-3 composites. *International Journal of Solids and Structures* **37** 5447-64

Plagianakos T S and Saravanos D A 2005 Coupled high-order shear layerwise analysis of adaptive sandwich piezoelectric composite beams. *AIAA Journal* **43** 885–94

Plump J M, Hubbard J E and Bailey T 1987 Nonlinear Control of a Distributed System: Simulation and Experimental Results. *Journal of Dynamic Systems, Measurement, and Control* **109** 133-39

Poizat C and Sester M 1999 Effective properties of composites with embedded piezoelectric fibres. *Computational Materials Science* **16** 89-97

Prasath S S and Arockiarajan A 2013 Effective electromechanical response of macro-fiber composite (MFC): analytical and numerical models. *International Journal of Mechanical Sciences* **77** 98–106

Providakis C P, et al. 2008 Comparisons of smart damping treatments based on FEM modeling of electromechanical impedance. *Smart Structures and Systems* **4** 35-46

Qin Q 2005 Micromechanics-BEM Analysis for Piezoelectric Composites.

Tsinghua Science and Technology **10** 30-34

Qiu Z C 2015 Experiments on vibration suppression for a piezoelectric flexible cantilever plate using nonlinear controllers. *Journal of Vibration and Control* **21** 300-19

Qiu Z C, Han J D, Zhang X M, Wang Y C and Wu Z W 2009 Active vibration control of a flexible beam using a non-collocated acceleration sensor and piezoelectric patch actuator. *Journal of Sound and Vibration* **326** 438–55

Raja S and Ikeda T 2008 Concept and electro-elastic modeling of shear actuated fiber composite using micro-mechanics approach. *Journal of Intelligent Material Systems and Structures* **19** 1173-83

Raja S, Ikeda T and Dwarakanathan D 2011 Deflection and vibration control of laminated plates using extension and shear actuated fiber composites. *Smart Materials Research* **Article ID 515942** (15pp)

Raja S, Pashilkar A A, Sreedeep R and Kamesh J V 2006 Flutter control of a composite plate with piezoelectric multilayered actuators. *Aerospace Science Technology* **10** 435-41

Raja S, Prathap G and Sinha P K 2002 Active vibration control of composite sandwich beams with piezoelectric extension-bending and shear actuators. *Smart Materials and Structures* **11** 63-71

Ramesh Kumar K and Narayanan S 2008 Active vibration control of beams with optimal placement of piezoelectric sensors/actuator pairs. *Smart Materials and .Structures* **17** 005008 (15pp)

Rao A K, Matesan K, Bhat M S and Ganguli R 2008 Experimental demonstration of H_∞ control based active vibration suppression in composite fin-tip of aircraft using optimal placed piezoelectric patch actuators. *Journal of Intelligent Material Systems and Structures* **19** 651–69

Rao M N, Tarun S, Schmidt R, Morari M and Schröder K U 2016 Finite element modelling and analysis of piezo-integrated composite structures under large applied electric fields *Smart Materials and Structures* **25** Article ID 055044 (12pp)

Rao S S and Sunar M 1993 Analysis of distributed thermopiezoelastic sensors and actuators in advanced intelligent structures. *AIAA Journal* **31** 1280-86

Ray M C 1998 Optimal control of laminated plates with piezoelectric sensor and actuator layers. *AIAA Journal* **12** 2204-08

Ray et al. 2001 Active constrained layer damping of thin cylindrical shells. *Journal of Sound and Vibration* **240** 921-35

Ray M C 2006a Micromechanics of piezoelectric composites with improved effective piezoelectric constant. *International Journal of Mechanics and*

Materials in Design **3** 361-71

Ray M C 2006b Hybrid damping of smart, functionally graded plates using piezoelectric fiber-reinforced composites. *IEEE transactions on Ultrasonics, Ferroelectrics and Frequency Control* **53** 2152-65

Ray M C and Batra R C 2007a Vertically reinforced 1-3 piezoelectric composites for active damping of functionally graded plates. *AIAA Journal* **45** 1779–83

Ray M C and Batra R C 2007b A single-walled carbon nanotube reinforced 1–3 piezoelectric composite for active control of smart structures. *Smart Materials and Structures* **16** 1936-47

Ray M C and Baz A 1997 Optimization of energy dissipation of active constrained layer damping treatments of plates. *Journal of Sound and Vibration* **208** 391-406

Ray M C and Mallik N 2004b Finite element analysis of smart structures containing piezoelectric fiber-reinforced composite actuator. *AIAA Journal* **42** 1398-405

Ray M C and Mallik N 2005 Performance of smart damping treatment using piezoelectric fiber reinforced composites. *AIAA Journal* **43** 184-93

Ray M C and Pradhan A K 2007 On the use of vertically reinforced 1-3 piezoelectric composites for hybrid damping of laminated composite plates. *Mechanics of Advanced Materials and Structures* **14** 245-61

Ray M C and Reddy J N 2004a Optimal control of thin circular cylindrical laminated composite shells using active constrained layer damping treatment. Smart Materials and Structures **13** 64-72

Ray M C and Reddy J N 2004b Performance of Piezoelectric fiber-reinforced composites for active structural-acoustic control of laminated composite plates. *IEEE transactions on Ultrasonics, Ferroelectrics and Frequency Control* **51** 1477-90

Ray M C and Reddy J N 2005 Active control of laminated cylindrical shells using piezoelectric fiber reinforced composites. *Composites Science and Technology* **65** 1226-36

Ray M C and Sachade H M 2006a Finite element analysis of smart functionally graded plates *International Journal of Solids and Structures* **43** 5468–84

Ray M C and Sachade H M 2006b Exact solutions for the functionally graded plates integrated with a layer of piezoelectric fiber-reinforced composite *ASME Journal of Applied Mechanics* **73** 622–32

Ray M C, Bhattacharya R and Samanta B 1993 Exact solutions for static analysis of intelligent structures. *AIAA Journal* **31** 1684-91

Ray M C, Bhattacharya R and Samantha B 1998 Exact solutions for dynamic analysis of composite plates with distributed piezoelectric layers. *Computers and Structures* **66** 737-43

Ray MC and Mallik N 2004a Active control of laminated composite beams using a piezoelectric fiber reinforced composite layer. *Smart Materials and Structures* **13**146-52

Reader W and Sauter D 1993 Piezoelectric composites for use in adaptive damping concepts. *Proceedings of DAMPING' 93* (pp. GBB-1)

Reddy B A and Ray M C 2007 Optimal control of smart functionally graded plates using piezoelectric fiber reinforced composites. *Journal of Vibration and Control* **13** 795-814

Reiter T and Dvorak G J 1997 Micromechanical models for graded composite materials *Journal of the Mechanics and Physics of Solids* **45** 1281-1302

Ro J and Baz A 2002 Optimum placement and control of active constrained layer damping using modal strain energy approach. *Journal of Vibration and Control* **8** 861-76

Robbins D H and Reddy J N 1991 Analysis of piezoelectrically actuated beam using a layerwise displacement theory *Computers and Structures* **41** 265-79

Robbins Jr D H, Reddy J N 1996 An efficient computational model for the stress analysis of smart plate structures. *Smart Materials and Structures* **5** 353-60

Ruan X, Chou T W, Safari A and Danforth S C 2002 A 3-D connectivity model for effective piezoelectric properties of yarn composites. *Journal of Composite Materials* **36** 1693-708

Sabina F J et al. 2001 Closed-form expressions for the effective coefficients of a fibre-reinforced composite with transversely isotropic constituents. II: Piezoelectric and hexagonal symmetry. *Journal of the Mechanics and Physics of Solids* **49** 1463-79

Saini P, Pandhi A and Darpe A K 2008 An Experimental Study on the Use of Active Constrained Layer Damping for Thin Curved Smart Shell Structures. In *Advances in Science and Technology* **56** 309-14 Trans Tech Publications

Sakthivel A and Arockiarajan A 2011 An effective matrix poling characteristics of 1-3-2 piezoelectric composites. *Sensors and Actuators A: Physical* **167** 34-43

Sakthivel A and Arockiarajan A 2012 Thermo-electro-mechanical response of 1-3-2 piezoelectric composites: effect of fiber orientations. *Acta Mechanica* **223**

1353-69

Sakthivel M and Arockiarajan A 2010 An analytical model for predicting thermo-electro-mechanical response of 1–3 piezoelectric composites. *Computational Materials Science* **48** 759-67

Saravanan C, Ganesan N and Ramamurti V 2001 Semianalytical finite element analysis of active constrained layer damping in cylindrical shells of revolution. *Computers and Structures* **79** 1131-45

Saravanos D A, Heyliger P R, and Hopkins D A 1997 Layerwise mechanics and finite element for the dynamic analysis of piezoelectric composite plates. *International Journal of Solids and Structures* **34** 359-78

Schulz M J, Sundaresan M J, Ghoshal A and Pai P F 2000 Active fiber composites for structural health monitoring. *Proceedings of SPIE **3992**, Smart Structures and Materials 2000: Active Materials: Behavior and Mechanics* 13 (June 14, 2000)

Sekouri E et al. 2002 Modeling of annular plate with piezoelectric actuators for active vibration control. *ASME International Mechanical Engineering Congress and Exposition* **IMECE2002-33936** *Adaptive Structures and Materials Systems* November 17–22, New Orleans, Louisiana

Sekouri E et al. 2004 Modeling of a circular plate with piezoelectric actuators. *Mechatronics* **14** 1007-20

Sergienko V P, Bukharov S N and Kupreev A V 2008 Noise and vibration in brake systems of vehicles. Part 1: Experimental procedures. *Journal of Friction and Wear* **29** 234-41

Sharnappa, Ganesan N and Sethuraman R 2007 Dynamic modeling of active constrained layer damping of composite beam under thermal environment. *Journal of Sound and Vibration* **305** 728-49

Shen I Y 1993 Intelligent constrained layer-An innovative approach (active and passive vibration damping). *Intelligent structures, Materials, and Vibrations* 75-82

Shen I Y 1994 Hybrid damping through intelligent constrained layer treatments. *Journal of Vibration and Acoustics, Transactions of the ASME* **116** 341-49

Shen I Y 1997 Active constrained layer damping treatments for shell structures: A deep-shell theory, some intuitive results, and an energy analysis. *Smart Materials and Structures* **6** 89-101

Shen M H H 1994 Analysis of beams containing piezoelectric sensors and actuators. *Smart Materials and Structures* **3** 439-47

Shi L, Shuai J, Wang X and Xu K 2017 Experimental and numerical investigation of stress in a large-scale steel tank with a floating roof. *Thin-Walled Structures* **117** 25-34

Shi Y et al. 2004 The finite element analysis and experimental study of beams with active constrained layer damping treatments. *Journal of Sound and Vibration* **278** 343-63

Shindo Y, Fumio Narita and Taiki Watanabe 2010 Nonlinear electromechanical fields and localized polarization switching of 1-3 piezoelectric/polymer composites. *European Journal of Mechanics - A/Solids* **29** 647-53

Singh B and Chakraverty S 1993 Transverse vibration of annular circular and elliptic plates using the characteristic orthogonal polynomials in two dimensions *Journal of sound and vibration* **162** 537-546

Smith W A and Auld B A 1991 Modeling 1-3 composites piezoelectrics: Thickness mode oscillations. *IEEE Transactions on Ultrasonics, Ferroelectrics and Frequency Control* **38** 40-47

Smyser C P and Chandrasekhara K 1997 Robust vibration control of composite beams using piezoelectric devices and neural networks. *Smart Materials and Structures* **6** 178-89

Sodano H A, Park G and Inman D J 2004 An investigation into the performance of macro-fiber composites for sensing and structural vibration applications. *Mechanical Systems and Signal Processing* **18** 683-97

Sohn J W, Choi S B and Kim H S 2011 Vibration control of smart hull structure with optimally placed piezoelectric composite actuators. *International Journal of Mechanical Sciences* **53** 647–59

Sohn J W, Choi S B and Lee C H 2009 Active vibration control of smart hull structure using piezoelectric composite actuators. *Smart Materials and Structures* **18** 074004 (14pp)

Sohn J W, Kim H S, Choi S B and Kim K S 2006 Experimental investigation of smart hull structures based on macro fiber composite actuators. *Key Engineering Materials* **326** 1419-22

Sohn, et al. 2007 Vibration suppression of hull structure using macro fiber composite actuators and sensors. *Proceedings of SPIE 6525: Active and Passive Smart Structures and Integrated Systems* 652527-1

Suleman A and Venkayya V B 1995 Simple finite element formulation for a laminated composite plate with piezoelectric layers. *Journal of Intelligent Material Systems and Structures* **6** 776-82

Sun D and Tong L 2003 Effect of debonding in active constrained layer damping patches on hybrid control of smart beams. International Journal of Solids and Structures **40** 1633-51

Suresh Kumar R and Ray M C 2012 Active constrained layer damping of smart laminated composite sandwich plates using 1-3 piezoelectric composites. *International Journal Mechanics and Materials in Design* **8** 197-218

Tan P and Liyong Tong 2001b Micromechanics models for non-linear behavior of piezo-electric fiber reinforced composite materials. *International Journal of Solids and Structures* **38** 8999-9032

Tan P and Tong L 2001a Micro-electromechanics models for piezoelectric-fiber-reinforced composite materials. *Composites Science and Technology* **61** 759-69

Tarazaga P A, Inman D J and Wilkie W K 2007 Control of a space rigidizable inflatable boom using macro-fiber composite actuators. *Journal of Vibration and Control* **13** 935-50

Tauchert T R 1992 Piezothermoelastic behavior of a laminated plate. *Journal of Thermal Stresses* **15** 25-37

Thakkar D and Ganguli R 2004 Helicopter vibration reduction in forward flight with induced-shear based piezoceramic actuation. *Smart Materials and Structures* **13** 599-608

Thornburgh R P, Chattopadhyay A and Ghoshal A 2004 Transient vibration of smart structures using a coupled piezoelectric mechanical theory. *Journal of Sound and Vibration* **274** 53-72

Tiersten H F 1969 *Linear Piezoelectric Plate Vibrations.* (New York: Plenum)

Tomlinson G R 1996 An overview of active/passive damping techniques employing viscoelastic materials. In *Proceedings of SPIE International Society for Optical Engineering* 656-69 (April)

Trindade M A and Benjeddou A 2011 Finite element homogenization technique for the characterization of d_{15} shear piezoelectric macro-fibre composites. *Smart Materials and Structures* **20** 075012 (17pp)

Trindade M A and Benjeddou A 2012 Parametric Analysis of Effective Material Properties of Thickness-Shear Piezoelectric Macro-Fiber Composites *Journal of the Brazilian Society of Mechanical Sciences and Engineering* **34** (SPE) 352-61

Trindade M A and Benjeddou A 2016 Finite element characterization of multilayer d_{31} piezoelectric macro-fibre composites. *Composite Structures* **151** 47–57

Trindade M A and Maio C E B 2008 Multimodal passive vibration control of sandwich beams with shunted shear piezoelectric materials *Smart Materials and Structures* **17** 00515-24

Tungyang C 1994 Micromechanical estimates of the overall thermoelectroelastic moduli of multiphase fibrous composites. *International Journal of Solids and Structures* **31** 3099-111

Tylikowski A 2001 Control of circular plate vibrations via piezoelectric actuators shunted with a capacitive circuit. *Thin-Walled Structures* **39** 83-94

Tzou H S and Gadre M 1989 Theoretical analysis of a multilayered thin shell coupled with piezoelectric shell actuators for distributed vibration controls. *Journal of Sound and Vibration* **132** 433-50

Tzou H S and Pandita S 1987 A multipurpose dynamic and tactile sensor for robot manipulators. *Journal of Robotic Systems* **4** 719–41

Tzou H S and Ye R 1994 Piezothermoelasticity and precision control of piezoelectric systems: Theory and finite element analysis. *Journal of Vibration and Acoustics* **116** 489-95

Vasques C M A, et al. 2006 Arbitrary active constrained layer damping treatments on beams: Finite element modelling and experimental validation. *Computers and Structures* **84** 1384-1401

Vel S S and Batra R C 2000 Three-dimensional analytical solution for hybrid multilayered piezoelectric plates. *Journal of Applied Mechanics* **67** 558-67

Vel S S and Batra R C 2001a Exact solution for rectangular sandwich plates with embedded piezoelectric shear actuators. *AIAA Journal* **39** 1363-73

Vel S S and Batra R C 2001b Analysis of piezoelectric bimorphs and plates with segmented actuators. *Thin-Walled Structures* **39** 23-44

Vel S S, Mewer R. C and Batra R C 2004 Analytical solution for the cylindrical bending vibration of piezoelectric composite plates. *International Journal of Solids and Structures* **41** 1625-43

Veley D E and Rao S S 1996 A comparison of active, passive and hybrid damping in structural design. *Smart Materials and Structures* **5** 660-71

Wang B 1992 Effective Behavior of Piezoelectric Composites. *ASME Applied Mechanics Review* **47** S112-S121

Wang C M, Nazmul I M and Wang Q 2004 Exact bending solutions of axisymmetric Reissner plates in terms of classical thin plate solutions. *Advances in Structural Engineering* **7** 129-45

Wang X, et al. 2016 Tracking control system design for roll maneuver via active wings using macro fiber composites. In *AIAA Modeling and Simulation Technologies Conference* (p. 4012)

Wang X, et al. 2017 Dynamic shape control of piezocomposite-actuated morphing wings with vibration suppression. *Journal of Intelligent Material Systems and Structures*, DOI: 1045389X17708039.

Wickramasinghe V K and Hagood N W 2004b Material characterization of active fiber composites for integral twist-actuated rotor blade application. *Smart Materials and Structures* **13** 1155-65

Wickramasinghe V.K and Hagood N W 2004a Durability characterization of active fiber composite actuators for helicopter rotor blade applications. J. Aircraft **41** 931–37

William A L 1998 Vibration control of fluid-loaded cylindrical shells using active constrained layer damping *PhD Dissertation Catholic University of America*

Yasin M Y, Ahmad N and Alam M N 2010 Finite element analysis of actively controlled smart plate with patched actuators and sensors *Latin American Journal of Solids and Structures* **7** 227–47

Yu N 1999 On overall properties of smart piezoelectric composites. *Composites Part B: Engineering* **30** 709-12

Yuan L, Xiang Y, Huang Y and Lu J 2010 A semi-analytical method and the circumferential dominant modal control of circular cylindrical shells with active constrained layer damping treatment. *Smart Materials and Structures* **19** 025010 (14pp)

Yuan X, et al. 2017 A novel thickness polarized d15 shear piezoelectric fiber composites, Sensors and Actuators A: Physical **260** 15 185-90

Zemčík R, Rolfes R, Rose M and Teßmer J 2007 High-performance four-node shell element with piezoelectric coupling for the analysis of smart laminated structures. *International Journal for Numerical Methods in Engineering* **70** 934-61

Zhang D and Zheng L 2014 Active vibration control of plate partly treated with ACLD using hybrid control. *International Journal of Aerospace Engineering* **2014** Article ID: **432970** (12pp)

Zhang H Y and Shen Y P 2007 Vibration suppression of laminated plates with 1–3 piezoelectric fiber-reinforced composite layers equipped with interdigitated electrodes. *Composite Structures* **79** 220-28

Zhang S Q et al. 2015 Modeling and simulation of macro-fiber composite layered smart structures. *Composite Structures* **126** 89–100

Zhang S Q et al. 2016 Computation of macro-fiber composite integrated thin-walled structures. *Smart Materials and .Structures IOP Conference Series: Materials Science and Engineering* **137** 012032

Zhen Y, Li J F and Zhang H 2008 Electrical and elastic properties of 1–3 PZT/epoxy piezoelectric composites. *Journal of Electroceramics* **21** 410-13

Zheng L, Zhang D and Wang Y 2011 Vibration and damping characteristics of cylindrical shells with active constrained layer damping treatments. *Smart Materials and Structures* **20** 025008 (9pp)

Zhou M, Sun M, Li M, Xie S and Huang S 2012 Fabrication and properties of 1-3-2 multi-element piezoelectric composite. *Journal of Electroceramics* **28** 139-43

Zippo A, Ferrari G, Amabili M, Barbieri M and Pellicano F 2015 Active vibration control of a composite sandwich plate. *Composite Structures* **128** 100-14

LIST OF PUBLICATIONS

The work presented in this thesis has led to the following publications:

1. Pavan Kumar A S, Panda S and Reddy N H 2015 Smart damping of vibration of annular plates by the design of a cylindrically orthotropic piezoelectric fiber reinforced composite actuator. *Acta Mechanica* **226** 3151-76.

2. Panda S, Reddy N H and Kumar A S P 2015 Design and finite element analysis of a short piezoelectric fiber-reinforced composite actuator. *Archive of Applied Mechanics* **85** 691-711.

3. Pavan Kumar A S, Panda S and Reddy N H 2017 Comparative study on the smart damping capabilities of cylindrically orthotropic piezoelectric fiber-reinforced composite actuators for vibration control of simply supported/fully clamped isotropic annular plate. *Journal of Intelligent Material Systems and Structures* **28** 1839-59.

4. Pavan Kumar A S and Panda S 2017 Electromechanical behavior of a shear mode PFC actuator with cylindrically periodic microstructure. (S*ubmitted in the peer reviewed international journal, Under Review*).

5. Pavan Kumar A S and Panda S 2017 Active-passive damping in an annular sandwich plate using a new shear mode PFC actuator with varying properties in cylindrical coordinates. (*Manuscript is prepared to submit in the peer reviewed international journal*).